FORMATION OF MULTIPLE GIANT PLANETS AND THEIR IMPACT ON THE PROTOPLANETARY DISC STRUCTURE

A PhD manuscript by

Camille Bergez-Casalou

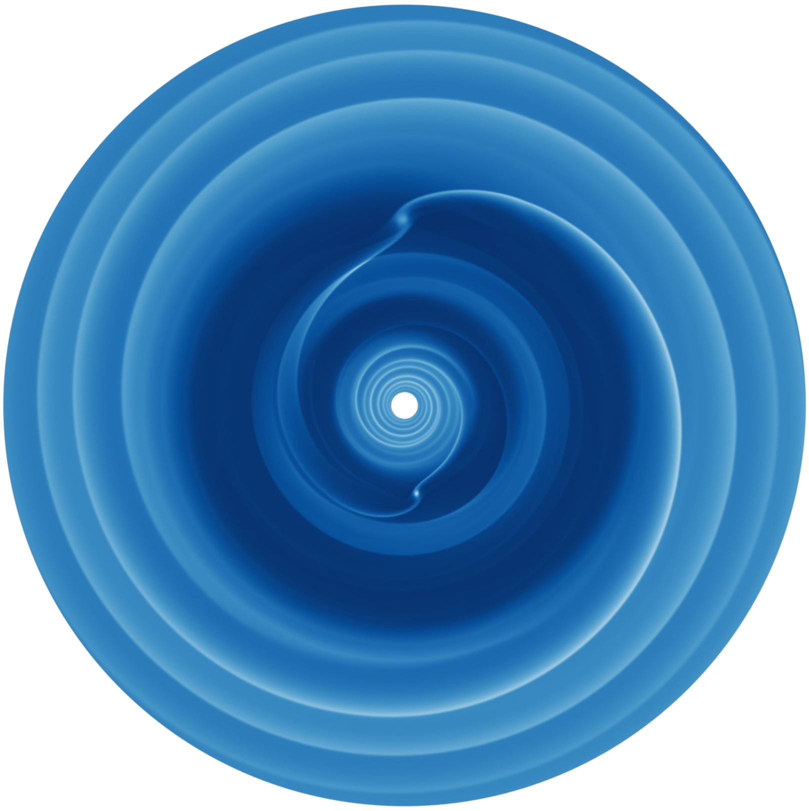

Dissertation

submitted to the
Combined Faculty of Mathematics, Engineering and Natural Sciences
of Heidelberg University, Germany
for the degree of
Doctor of Natural Sciences

Put forward by
Camille Bergez-Casalou
born in: Bordeaux, France

Oral examination: July 13th, 2022

Formation of multiple giant planets and their impact on the protoplanetary disc structure

REFEREES

Dr. Bertram Bitsch
Prof. Dr. Cornelis Dullemond

Abstract

The Solar System, together with some exoplanetary systems, is known to host multiple planets. These planets are believed to be born in discs composed of gas and dust in rotation around forming stars. These discs are called protoplanetary discs. The formation of such planets is studied via different, complementary, methods: theoretically, with the help of both hydrodynamical simulations to analyse the behavior of the fluids in presence of planets and N-body simulations to predict the dynamical interactions between these planets; and observationally with the recent detailed observations of protoplanetary discs.

In this thesis, I use a hydrodynamical approach to investigate the impact of multiple giant planets on the global disc structure. Previous hydrodynamical simulations focus on the local growth of single planets. Here, my collaborators and I start by analysing the impact that a single gas accreting planet has on its surrounding disc at a global scale. I show that the influence of planetary gas accretion on the gas disc structure depends on its viscosity. With that in mind, it is possible, in a second study, to determine how the gas is distributed in a disc hosting two accreting planets. By running long-term hydrodynamical simulations (up to 0.5 Myrs), we find that even if the planets do not start accreting simultaneously, they end up with similar masses. This has an interesting impact on our understanding of planet formation.

Finally, an observational approach is investigated by deriving synthetic ALMA images of the potential parental Solar system protoplanetary disc. I use two different simulation codes to determine the behavior of the gas and the dust in presence of multiple giant planets, before relying on a radiative transfer simulation that predicts how light is emitted from the disc. The resulting image is treated to mimic recent protoplanetary disc observations, allowing us to compare the observable features to known discs. With this project, we provide a way to put the Solar system in perspective with the known observed disc. This comparison allows us to better constrain the formation pathway of giant planets.

To summarize, this thesis uses a theoretical approach to investigate the formation of multiple giant planets in their protoplanetary disc. I finish by discussing several questions addressed in this work. The answers provided can be used as foundations to follow-up studies, improving our understanding of planet formation both theoretically and observationally.

Zusammenfassung

Das Sonnensystem, wie auch einige extrasolare Planetensysteme, beherbergt bekanntlich etliche Planeten. Diese Planeten, so glaubt man, entstehen in sogenannten protoplanetaren Scheiben, welche sich aus Gas und Staub zusammensetzen und um den Mutterstern rotieren. Der Entstehungsprozess solcher Planeten wird durch verschiedene, komplementäre Studien untersucht: theoretische Studien, die einerseits auf hydrodynamischen Simulationen beruhen, um das Verhalten der Gaskomponente in Gegenwart von jungen Planeten zu bestimmen, und die andererseits mit Hilfe von N-Körper-Simulationen die dynamische Wechselwirkung zwischen entstehenden Planeten zu beschreiben versuchen. Die Vorhersagen dieser theoretischen Modelle zielen schließlich darauf ab, sie mit der Beobachtung protoplanetarer Scheiben in Einklang zu bringen.

In der vorliegenden Doktorarbeit verfolge ich einen hydrodynamischen Ansatz, um den Einfluss mehrerer Riesenplaneten auf die globale Struktur einer protoplanetaren Scheibe zu untersuchen. Vorherige hydrodynamische Studien legten dabei den Fokus auf die lokale Masseanhäufung einzelner Planeten. In der folgenden Analyse beginnen wir mit der Untersuchung eines einzelnen durch Gasakkretion wachsenden Planeten und dessen Einfluss auf die globale Struktur der protoplanetare Scheibe. Das Ergebnis zeigt, dass der Einfluss der Gasakkretion auf die Scheibe von deren Viskosität abhängt. Damit ist es möglich, die Gasverteilung einer protoplanetaren Scheibe zu untersuchen, die zwei Planeten enthält. Mit der Durchführung hydrodynamischer Simulationen, die sich über große Zeitskalen erstrecken (bis zu 0,5 Ma), zeigen wir, dass die Planeten, selbst wenn diese nicht gleichzeitig beginnen, Masse anzuhäufen, am Ende ihrer Entwicklung etwa die gleiche finale Masse haben. Dieses Ergebnis liefert einen wichtigen Beitrag zu unserem Verständnis der Planetenentstehung.

Im letzten Teil dieser Arbeit versuchen wir, die Beobachtung einer protoplanetaren Scheibe, die ein möglicher Vorläufer unseres Sonnensystems ist, synthetisch nachzubilden. Ich verwende dabei zwei verschiedene Codes, um das Gas und den Staub in einer Scheibe mit mehreren Riesenplaneten zu simulieren, bevor ein Code für den Strahlungstransport eine synthetische Beobachtung der Scheibe liefert. Damit können wir bestimmte Merkmale mit tatsächlichen Beobachtungen bekannter Scheiben vergleichen. Dies erlaubt einen systematischen Einblick in die mögliche Entstehungsgeschichte unseres heutigen Sonnensystems.

Zusammenfassend finden in dieser Doktorarbeit theoretische Modelle Anwendung, um die Entstehung mehrerer Riesenplaneten in protoplanetaren Scheiben zu untersuchen. Schließlich nehme ich Bezug auf die Fragen, die wir mit dieser Arbeit versuchen zu beantworten. Unsere Ergebnisse können als Basis für künftige Studien dienen, um unser Verständnis der Planetenentstehung zu verbessern.

Résumé

Le Système solaire, ainsi que certains systèmes exoplanétaires, est composé de plusieurs planètes. Les recherches actuelles indiquent que ces planètes sont formées dans des disques de gaz et de poussières en rotation autour d'étoiles naissantes. Ces disques sont appelés disques protoplanétaires. L'étude de la formation planétaire se base sur différentes méthodes complémentaires. D'un point de vue théorique, les simulations hydrodynamiques servent à l'analyse du comportement des fluides en présence ou non de corps en formation, tandis que les simulations à N-corps permettent de détailler les interactions dynamiques entre ces différents corps. D'un point de vue observationnel, les instruments récents permettent de produire des images détaillées des disques protoplanétaires.

Dans cette thèse, j'utilise une approche hydrodynamique pour étudier l'impact de la présence de multiples planètes géantes sur la structure globale de leur disque protoplanétaire. De précédentes études hydrodynamiques se sont concentrées sur l'étude locale de la croissance d'une planète isolée dans le disque. Ici, mes collaborateurs et moi-même commençons par étudier l'impact de l'accrétion de gaz d'une planète isolée sur la structure globale du disque protoplanétaire. Nous trouvons que cet impact dépend de la viscosité du disque. Sachant cela, nous analysons dans une deuxième étude comment le gaz se répartit entre deux planètes accrétant du gaz depuis le même disque. La longue intégration de nos simulations hydrodynamiques (jusqu'à 0.5 Ma) nous permet de conclure que, même si elles ne commencent pas à accréter simultanément, les planètes finissent par avoir des masses similaires. Ce résultat a des conséquences intéressantes concernant l'évolution des systèmes planétaires multiples.

Une approche observationnelle sur la formation planétaire est développée dans un dernier chapitre. Nous simulons des images du potentiel disque protoplanétaire dans lequel le Système solaire s'est formé, tel qu'il aurait pu être observé par le télescope ALMA. Grâce à deux codes différents de simulation, nous avons pu déterminer la répartition du gaz et des poussières dans le disque en présence de multiples planètes géantes. Les profils de poussières sont utilisés comme entrée pour un code de transfert radiatif prédisant la lumière émise par un tel système. Les images ainsi produites sont traitées afin de simuler des observations via le télescope ALMA, nous permettant de comparer les signatures observationnelles à d'autres disques connus. Cette comparaison nous permet de mieux contraindre les conditions de formation des planètes géantes.

Pour conclure, cette thèse se base sur une approche théorique pour étudier la formation de multiples planètes géantes dans leur disque protoplanétaire. Je finis par résumer nos conclusions en apportant une potentielle réponse aux différentes questions abordées au cours de cette thèse. Ces réponses ont vocation à servir de base à de futures études, permettant d'améliorer notre compréhension de la formation planétaire d'un point de vue théorique et observationnel.

À mes parents.

Contents

Abstract i

Zusammenfassung iii

Résumé v

1 Introduction 1
- 1.1 Protoplanetary discs 3
  - 1.1.1 Gas disc structure and evolution 3
  - 1.1.2 Dust dynamics 6
  - 1.1.3 Discs observations 10
- 1.2 Planet-disc interactions 14
  - 1.2.1 Planet formation models 14
  - 1.2.2 Gap formation 17
  - 1.2.3 Migration 18
- 1.3 Planetary systems 20
  - 1.3.1 Solar System 20
  - 1.3.2 Exoplanets 23
- 1.4 Motivations of this thesis 25

2 Numerical methods **27**
- 2.1 Simulating gas disc evolution: `FARGO-2D1D` 28
  - 2.1.1 The `FARGO-2D1D` features 28
  - 2.1.2 Gas accretion routine 30
  - 2.1.3 Gas disc parameters 31
- 2.2 Simulating dust evolution in a gas disc: `TWO-POP-PY` 32
  - 2.2.1 Structure of `TWO-POP-PY` 32
  - 2.2.2 Dust evolution parameters 32
- 2.3 Simulating dust emission to produce synthetic images: `RADMC-3D` 33
  - 2.3.1 Structure of `RADMC-3D` 33
  - 2.3.2 Opacities with `OpTool` 34
  - 2.3.3 Radiative transfer parameters 34

3 Single accreting planet: How is gas accretion impacting the gap depth ? **35**
- 3.1 Motivations 36
- 3.2 Numerical setup 37
- 3.3 Influence of gas accretion 38
  - 3.3.1 Accretion versus non-accretion 38

3.3.2 Influence of different gas accretion rates 41
3.3.3 Influence on the stellar accretion rate 42
3.4 Influence of disc parameters 46
3.4.1 Different aspect ratios 46
3.4.2 Different viscosities 48
3.4.3 Gap-opening mass 52
3.4.4 Migration maps 55
3.5 Discussion 58
3.5.1 Accretion onto the star 58
3.5.2 Implications for observations 58
3.5.3 Implications for the grand tack scenario 60
3.6 Conclusions 60

4 Two accreting planets: How is gas distributed between the planets ? 63
4.1 Motivations 64
4.2 Numerical setup 65
4.3 Influence of the disc viscosity 67
4.3.1 Influence of the turbulent viscosity 67
4.3.2 Influence of the aspect ratio 68
4.3.3 Impact on the planets mass ratio 69
4.4 Single accreting planet compared to two accreting planets 72
4.4.1 Accretion rates and masses comparison 72
4.4.2 Impact on the accretion onto the star 76
4.5 Influence of the planet separation 78
4.5.1 Impact on the mass ratio 78
4.5.2 Impact on the gap opening mass 80
4.6 Influence of delayed accretion 82
4.7 Discussion 83
4.7.1 Accretion onto the star 83
4.7.2 Impact of planet dynamics 84
4.7.3 Implications for the Grand Tack scenario 85
4.7.4 Comparison to exoplanets 85
4.8 Conclusions 89

5 Four fixed planets: How would the Solar System natal protoplanetary disc be observed with ALMA ? 91
5.1 Motivations 92
5.2 Numerical setups 93
5.2.1 Planet configurations 93
5.2.2 Hydro-dynamical setup 94
5.2.3 Dust evolution setup 96
5.2.4 Synthetic image setup 98
5.3 Dust size distributions from `TWO-POP-PY` 100
5.3.1 Solar System configurations 100
5.3.2 Influence of planet mass and Three-Giants configuration 102
5.4 Synthetic images - `RADMC-3D` outputs convolved with Gaussian beams . . . 104
5.4.1 Radial profiles in the Solar System configurations at $\lambda = 1.3$ mm . . 104
5.4.2 Influence of the different masses on the 1.3 mm images 106
5.4.3 Influence of the disc inclinations 107

5.4.4 Influence of the beam size 109
5.5 Discussion 111
5.5.1 Comparisons to known observed discs 111
5.5.2 Comparing to exoplanet populations 112
5.5.3 Features created by traffic jams 113
5.5.4 Impact of time evolution 114
5.5.5 Disc dust mass 116
5.6 Conclusions 120

6 Summary and outlook **123**

A Additional material to Chapter 4 **129**
A.1 Surface density maps 129

B Additional material to Chapter 5 **131**
B.1 Gas hydrodynamical profiles 131
B.2 Impact of the radial gas velocity on the dust distributions 136
B.3 Complementary images 137
B.3.1 Solar System images 137
B.3.2 Images of inclined discs 137

List of Figures **141**

List of Tables **144**

Publication list **145**

Bibliography **147**

Acknowledgements **155**

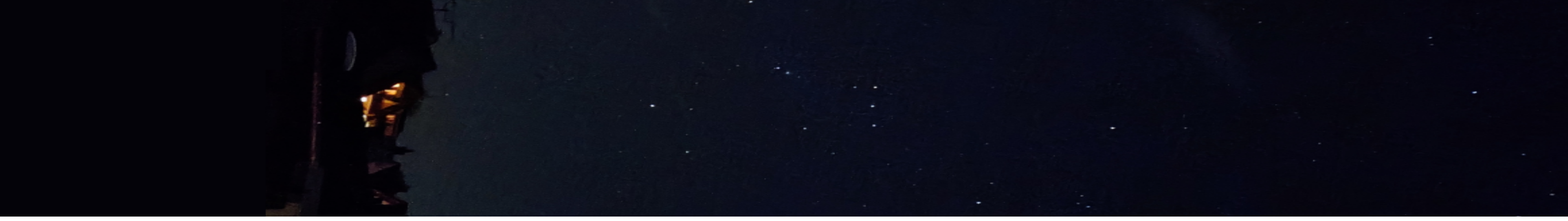

1

Introduction

- Mom, what's that bright star in the sky ?
- This one is not a star my love, that's Venus, often mistaken for a star due to its brightness. So it's a planet even if its nickname is the Evening star.
- Hum I see ... Where do planets come from?

That's a tough question kid. A lot of scientists are trying to answer this question. While astronomy is one of the oldest sciences, we had to wait until the XVII$^{\text{th}}$ century to begin to commonly accept that the Earth and other planets of the Solar system orbit the Sun. Then, the first theories on how the Solar system could have formed started to emerge: for example, Georges-Louis Leclerc, Comte de Buffon (1707-1788) speculated in his *Epoques de la Nature* (1778) that the planets are formed from material ejected from the collision of a giant comet with the Sun. However, this theory has trouble explaining the differences between the planets and the Sun regarding their energy and composition.

Another set of theories, emerging with Kant (1755) and Marquis de Laplace (1796), suggests that the planets originate from the same in-fall of a parent nebula as the Sun. Immanuel Kant (1724-1804) and Pierre-Simon Marquis de Laplace (1749-1827) placed the basis of the modern view of planet formation in these flat gaseous discs in rotation around a forming star that we call nowadays *protoplanetary discs*. Since then, many different studies focused on the description of such discs. Among all these works, we can note some of them that are still used: Safronov (1969) first described the evolution of theses objects, by deriving the equations governing particle growth to form planetesimals (the planets building blocks); Lynden-Bell & Pringle (1974) developed the equations to describe the time evolution of a viscous gaseous disc, and Weidenschilling (1977) and Hayashi (1981) derived the Minimum Mass Solar Nebula (MMSN) profile, estimating the minimal initial distribution in solids in the solar nebula needed to reproduce the distribution of solids observed in the present-day Solar System.

The existence of all these different studies provides context to the complexity of planet formation. Part of this complexity resides in the inter-dependence of many of the formation mechanisms. This first chapter aims at describing the main processes governing planet formation. In order to clarify the complex links between these processes, I show in Fig. 1.1 how the different components interact with each other.

Everything starts from the structure of the protoplanetary disc. In section 1.1, I develop how the gas and dust composing the disc evolve as a function of time and can influence each other's evolution (sections 1.1.1 and 1.1.2). Disc observations presented in section 1.1.3 are used to probe the gas and dust structures, helping to constrain the

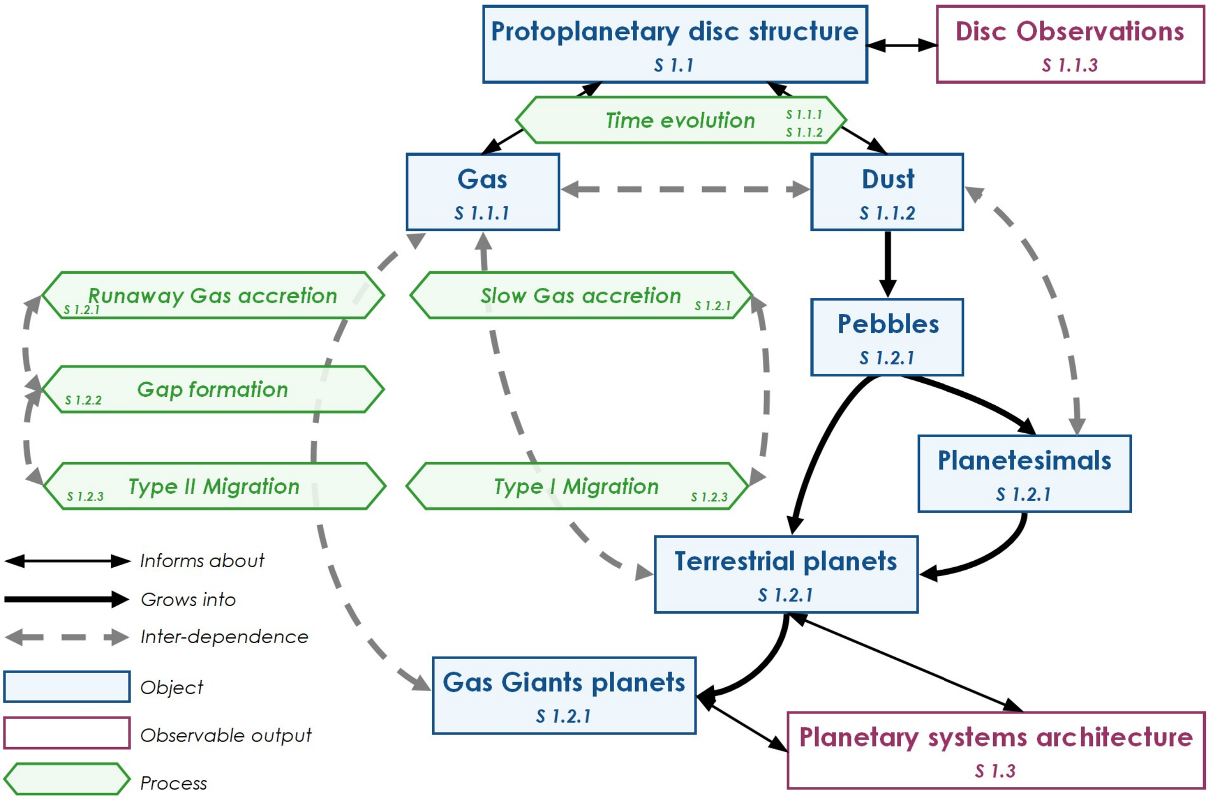

Figure 1.1: Schematic of the connections between the different components and processes studied in this thesis. The objects are marked by blue rectangles while the processes are shown in green hexagons. Two domains of observations that can be used to constrain planet formation are marked by purple rectangles. The different arrows represent the type of connections linking each object and process. Each component is discussed in this introduction, in the section noted in each frame.

theoretical models. Planet formation processes are described in section 1.2, starting from the formation of pebbles by dust growth, leading to the formation of planetesimals and planetary cores (section 1.2.1). All these objects feel the presence of the gas in the disc, resulting in different particle-gas interactions. For the most massive objects (i.e., planetary cores), these interactions include gas accretion (section 1.2.1), gap formation (section 1.2.2) and migration (section 1.2.3), leading to the formation of all kind of different planets, ranging from the terrestrial planets to the giant planets. For example, as these three last processes both depend on and influence the gas distribution, they are all inter-dependent, making their study rather complex. Finally, the output of planet formation is the structure of the resulting planetary system, which can be used to derive constraints on their formation history, as discussed in section 1.3. The Solar system is the most accessible system to study in detail as it is the closest to us (section 1.3.1), but it is also possible to derive constraints from the analysis of the multitude of observed exoplanetary systems (section 1.3.2).

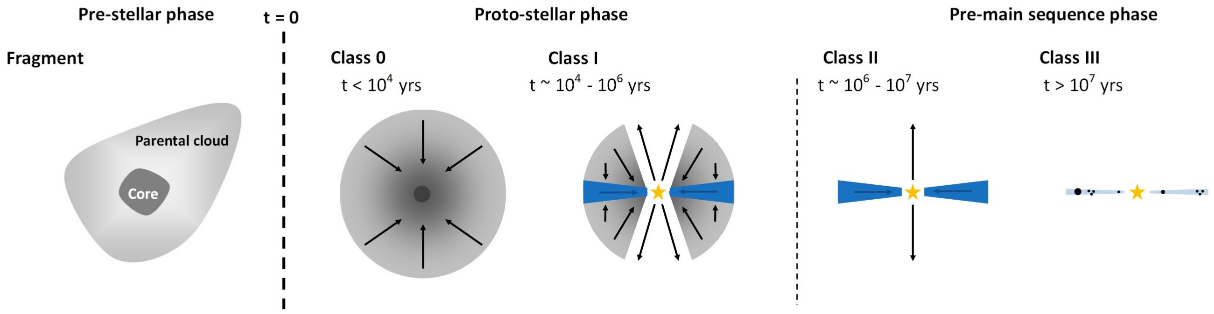

Figure 1.2: Schematic (not to scale) showing the geometry of star-disc systems following the classification scheme for the evolutionary stages of a young stellar object (YSO) according to the Lada sequence (Lada, 1987). In this thesis, I will focus on the stages of planet formation occurring during the Class II phase. Figure adapted from Pohl (2018) and Bhandare (2020).

1.1 Protoplanetary discs

Planets are a by-product of star formation. Stars form from the collapse of molecular clouds, composed of cold, dense molecular gas and dust (see reviews by McKee & Ostriker 2007 and Heyer & Dame 2015). This gravitational collapse can be triggered by the presence of external forces (Ebert, 1955; Bonnor, 1956). To conserve angular momentum during the formation of the protostar, the material contained in the rotating, collapsing primordial cloud forms a disc surrounding the emerging star. This formation process can be divided into different stages, as shown in Fig. 1.2. The pre-stellar phase consists of the formation of an initial core in the parental molecular cloud. Then the star-disc formation mechanism can be divided in four different categories: a class 0 young stellar object corresponds to the moment when the cloud starts collapsing onto the central core. During the class I phase, the star starts to accrete its envelope and creates a disc around it. When the star envelope has mostly dissipated (class II phase), the proto-star enters the pre-main sequence phase, continuing to evolve via the accretion of its protoplanetary disc. The last stage of evolution, called class III phase, leaves a disc depleted of gas, composed only of planets and remaining solid debris (also known as "debris discs").

While recent studies tend to show that planet formation processes may start as early as the Class I phase (Segura-Cox et al., 2020; Cridland et al., 2021), the work presented in this thesis focuses on the stages of planet formation occurring during the Class II phase.

1.1.1 Gas disc structure and evolution

Vertical structure

Once the star-disc system enters the Class II phase, we can assume that the disc reaches an equilibrium state. The vertical structure of the protoplanetary disc can therefore be derived by assuming a hydrostatic equilibrium.

Protoplanetary discs are naturally described by a polar coordinate system. Considering a gas parcel located at distance d from its central star as in Fig. 1.3, the gradient of the gas pressure P_g of a non self-gravitating disc can be written as:

$$\frac{dP_g}{dz} = -\rho_g g_z \tag{1.1}$$

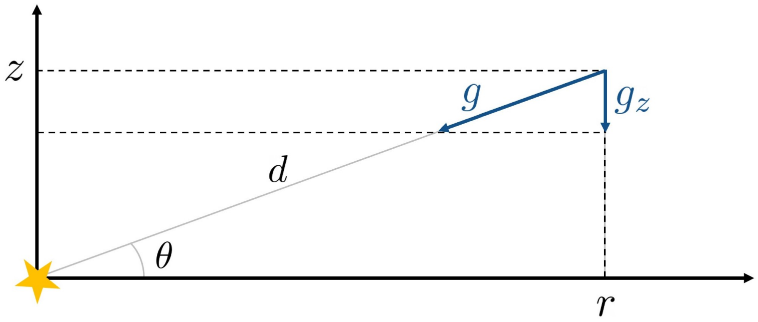

Figure 1.3: Coordinates of a gas parcel in a vertically thin, non self-gravitating, protoplanetary disc. The parcel, located at a distance d from its host star, feels the star gravitational force.

where ρ_g is the gas volume density. From Fig. 1.3, it is clear that the vertical gravitational acceleration g_z can be written as:

$$g_z = g\sin(\theta) = \frac{GM_\star}{d^2}\sin(\theta) = \frac{GM_\star}{d^3}z \tag{1.2}$$

where G is the gravitational constant and $M_\star$ is the mass of the central star.

Considering that protoplanetary discs are vertically thin, $z \ll r$, leading to $d \sim r$:

$$g_z \simeq \frac{GM_\star}{r^3}z \simeq \Omega_k^2 z \tag{1.3}$$

where $\Omega_k = \sqrt{GM_\star/r^3}$ is the keplerian angular frequency.

From now on and for the different projects presented in this thesis, we assume the gas to be vertically isothermal, meaning that its temperature does not dependent on the vertical coordinate. The equation of state is given by $P_g = \rho_g c_s^2$ and depends on the isothermal sound speed c_s which can be written as:

$$c_s = \sqrt{\frac{k_B T}{\mu m_p}} \tag{1.4}$$

Here, k_B is the Boltzmann constant, T is the temperature, μ is the mean molecular weight in units of the proton mass m_p ($\mu \simeq 2.3$ for a fully molecular gas of solar composition). The hydrostatic equilibrium from eq. 1.1 then becomes:

$$c_s^2\frac{d\rho_g}{dz} = -\rho_g \Omega_k^2 z \tag{1.5}$$

The solution to this differential equation is:

$$\rho_g(z) = \rho_{g,(z=0)}\exp\left(\frac{-z^2}{2H_g^2}\right) \tag{1.6}$$

where $H_g = c_s/\Omega_k$ is the vertical disc scale height. From the disc scale height, we can define the disc aspect ratio $h = H/r$. Please note that the notations might differ depending on the author: here H is the vertical disc scale height and h the aspect ratio, while some authors prefer to write it the other way around.

The volume density in the mid-plane (i.e., at $z = 0$) can be expressed as a function of the surface density Σ_g. The surface density of the gas is defined by:

$$\Sigma_g(r,t) = \int_{-\infty}^{+\infty} \rho_g(r,z,t)dz \tag{1.7}$$

Thus, the gas volume density as a function of radius, height and time is given by:

$$\rho_g(r,z,t) = \frac{\Sigma_g(r,t)}{H_g(r)\sqrt{2\pi}} \exp\left(\frac{-z^2}{2H_g^2(r)}\right) \tag{1.8}$$

This description of the gas volume density therefore depends on the radial structure of the time evolving gas surface density $\Sigma_g(r,t)$.

Radial structure

Consider a parcel of gas isolated in orbit around its host star. Such a parcel would stay on a stable orbit, orbiting at a keplerian velocity $v_{\phi,k} = \sqrt{GM_\star/r}$. It has a specific angular momentum l:

$$l = \Omega_k r^2 \Rightarrow l \propto \sqrt{r} \tag{1.9}$$

However, gas parcels present in discs are not isolated. First of all, the gas is subject to its own pressure. The radial pressure gradient is negative in protoplanetary discs, resulting in a gas rotating at a slightly sub-keplerian speed ($v_\phi/v_k \simeq 0.995$). Moreover, the gas present in protoplanetary discs has a specific viscosity. Angular momentum is redistributed by the viscous friction between two gaseous rings in differential rotation. Due to the conservation of angular momentum, a fraction of the gas is accreted towards the star while the other part moves away from it.

The origin for this viscosity is still challenging to explain. If we only consider the molecular viscosity (i.e., viscosity originating from the collisions of the gas molecules), the resulting disc lifetime does not match the observations. For example, taking a typical molecular viscosity for protoplanetary disc surface densities of $\nu \sim 2 \times 10^5$ cm^2/s (Armitage, 2010) leads to a viscous timescale of $\tau_\nu \simeq r^2/\nu \simeq 4 \times 10^{13}$ years at 1 AU. This is at least 6 orders of magnitude longer than the observed disc lifetimes (Pfalzner et al., 2014).

To address that problem, Shakura & Sunyaev (1973) show that turbulent viscosity can reduce the disc lifetime to the order of 10^6 years, which matches the observations better. However, the origin for this turbulence is not well constrained yet. To represent the presence of turbulence, they parametrized the turbulent viscosity with a scaling factor called α. In these so-called α-discs, the viscosity can be expressed as:

$$\nu = \alpha c_s H_g \tag{1.10}$$

With this turbulent viscosity, the viscous timescale can be re-written as $\tau_\nu = \alpha^{-1}h^{-2}\Omega^{-1}$. If we consider a disc lifetime of 10^7 years for a disc of typically 100 AU, with a constant aspect ratio $h = 0.05$, we obtain a value for α of 6×10^{-3}. This rough estimation leads to a rather high value of α when compared to the values derived from observed discs (Dullemond et al., 2018; Flaherty et al., 2018), meaning that obviously, more detailed simulations of the disc evolution is needed to capture the complexity of disc turbulence and distribution of angular momentum.

Now that we know how the gas can be transported towards the central star, we can determine the accretion rate of the disc:

$$\dot{M} = -2\pi r \Sigma_g v_r \tag{1.11}$$

where v_r is the radial velocity of the gas, taken to be negative when flowing towards the star. If we consider a steady-state disc, then the radial velocity can be expressed as a function of the viscosity $v_r = -3\nu/(2r)$. Substituting the steady-state radial velocity in eq. 1.11 gives the accretion rate of a steady-state disc:

$$\dot{M} = 3\pi\nu\Sigma_g = 3\pi\Sigma_g\alpha c_s H_g = 3\pi\Sigma_g\alpha\Omega_k H_g^2 \tag{1.12}$$

Taking a typical example of a disc having a constant aspect ratio $h = 0.05$ with a surface density of $\Sigma_g = 10^3$ g/cm^2 at 1 AU and $\alpha = 10^{-3}$, this gives an accretion rate of $\dot{M} = 1.6 \times 10^{-8}\ M_\odot/\mathrm{yr}$, consistent with the observed values (e.g., Mulders et al., 2017; Rafikov, 2017; Manara et al., 2019).

However, not all discs are in steady state, making the derivation for the evolution of the surface density more complex. By combining the equations for mass and momentum conservation, the surface density evolution is governed by the following differential equation:

$$\frac{\partial\Sigma_g}{\partial t} = \frac{3}{r}\frac{\partial}{\partial r}\left[r^{1/2}\frac{\partial}{\partial r}(\nu\Sigma_g r^{1/2})\right] \tag{1.13}$$

Some studies derived analytical solutions describing Σ_g as a function of time and radius (Lynden-Bell & Pringle, 1974; Pringle, 1981). However, in this thesis, I use numerical integration of the full hydrodynamic equations to determine the evolution of the surface density. In section 2.1 of Chapter 2, I present the hydrodynamical code used to solve for the mass, momentum and energy conservation equations, also called the Navier-Stokes equations.

1.1.2 Dust dynamics

Protoplanetary discs are composed of gas and dust. The relative proportion of dust compared to the gas is described by the dust-to-gas ratio. Even if this ratio is dependent on time and radius, its initial value is estimated to be around 1%. This section presents how the dust evolves in protoplanetary discs. Note that from here, *grains* identify any kind of solids composing the dust in protoplanetary discs. I detail the different terminologies (i.e., *small grains*, *pebbles*, *planetesimals*) in the following section.

Dust radial motion

As mentioned earlier, the gas present in discs evolves on a slightly sub-keplerian orbit due its own pressure. On the other hand, the dust grains do not behave as a viscous fluid, meaning that they would orbit at a keplerian speed if left unperturbed. As the grains and the gas do not evolve at the same speed, the grains feel a head-wind from the surrounding gas (Weidenschilling, 1977; Brauer et al., 2008). This head-wind causes the grains to lose angular momentum, making them drift towards higher pressure gas regions. The gas pressure profile of a smooth disc decreases with radius, making the grains drift to the inner regions of the disc.

The importance of this head-wind on the velocity of the grains depends on their size compared to the disc properties. Small grains that are well coupled to the gas are subject to gas drag: their coupling is so strong that they move with the gas. In contrast, too large grains do not loose enough angular momentum to drift inward. The radial drift efficiency is therefore highly dependent on the grains size. This drift efficiency can be monitored with the Stokes number St. This parameter is the ratio of the stopping time of a particle to the keplerian frequency at a given disc distance. Assuming spherical grains in an Epstein regime near the disc mid-plane of an isothermal disc, the Stokes number is defined by Birnstiel et al. (2012) as:

$$\mathrm{St} = \frac{t_{stop}}{\Omega_k} = \frac{\pi a \rho_s}{2\Sigma_g}, \tag{1.14}$$

where a is the size of the grain and ρ_s is the internal density of the particle. With this parameter, it is therefore possible to determine the total velocity of dust grains $v_{\mathrm{tot,dust}}$ depending on the radial velocity of the gas $v_{r,\mathrm{gas}}$, as derived by Brauer et al. (2008):

$$v_{\mathrm{tot,dust}} = v_{\mathrm{drift,dust}} + v_{\mathrm{drag,dust}} = \frac{|\gamma| c_s^2}{v_k(\mathrm{St} + \mathrm{St}^{-1})} + \frac{v_{r,\mathrm{gas}}}{1 + \mathrm{St}^2} \tag{1.15}$$

where $|\gamma|$ is the pressure profile of the gas disc, c_s is the sound speed and v_k is the keplerian velocity. The total velocity of the dust grain as a function of its Stokes number is shown in Fig. 1.4. Three different categories[1] can be distinguished for the dust grains:

- For $\mathrm{St} \ll 1$, the *small grains* are coupled to the gas, following its motion in the disc.
- For $\mathrm{St} \approx 1$, the *pebbles* are partially coupled to the gas and feel a strong head-wind, leading to an important inward radial drift.
- For $\mathrm{St} \gg 1$, the *planetesimals* are completely decoupled to the gas and their movement is governed by different mechanisms.

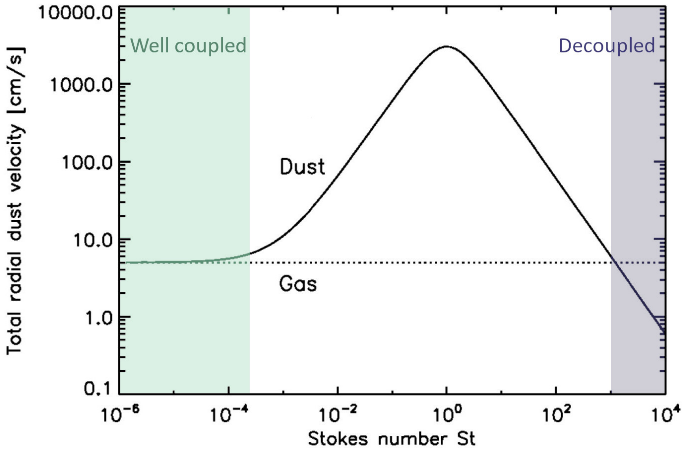

Figure 1.4: Adapted from Brauer et al. (2008): Inward radial velocity of a single dust grain as a function of its Stokes number St (solid line) compared to the gas radial velocity (dotted line). The green area shows the range of St for which the grains are well coupled to the gas while the blue area represents the range of St where the grains are decoupled from the gas.

---

[1] Note that the terminology of each category might vary from one author to the other.

Due to the efficient of dust drift, the growth of particles is limited in the disc. It is possible to determine the maximum grain size a grain can reach before quickly drifting to the inner region depending on the gas and dust properties. Birnstiel et al. (2012) expressed it as:

$$a_{\text{drift}} = f_d \frac{2\Sigma_d v_K^2}{\pi \rho_s |\gamma| c_s^2} \tag{1.16}$$

where $f_d = 0.55$ is a correcting factor, Σ_d is the dust surface density, v_K is the keplerian velocity and $|\gamma| = |d\ln(P)/d\ln(r)|$ is the gas pressure profile of the disc. The dust radial motion can therefore be estimated based on the gas disc properties and the Stokes number of the grains.

Dust vertical distribution

The vertical distribution of grains depend on two main processes: the dust settling, which pushes the larger grains to quickly settle in the mid-plane of the disc; and vertical mixing, which depends on the turbulent diffusion capacity to homogenise the dust distribution above and below the mid-plane.

Considering these two effects, it is possible to determine the dust disc vertical structure as a function of the gas structure and the Stokes number of the grains (Brauer et al., 2008; Birnstiel et al., 2010; Pinilla et al., 2012):

$$H_d = H_g \times \min\left[1, \left(\frac{\alpha}{\min(\mathrm{St}, 1/2)(1+\mathrm{St}^2)}\right)^{1/2}\right] \tag{1.17}$$

where H_d is the dust scale height, H_g is the gas scale height and α is the turbulent viscosity parameter. Therefore, while large grains with $\mathrm{St} \gg 1$ will settle in the mid-plane, the small grains coupled to the gas ($\mathrm{St} \ll 1$) can spread up to the upper layers of the disc.

Dust growth and fragmentation

It is expected that dust grains originating from the interstellar medium and trapped in the protoplanetary disc during its formation are the building blocks from which larger solid bodies grow. These primordial grains of about 0.1μm in size interact with each other mainly by collisions. These collisions can lead to different kind of interactions, as listed by Güttler et al. (2010).

The ability of these collisions to form larger aggregates depends on the composition of the grains (stickiness) but mostly on their relative velocities. The Smoluchowski equation (Smoluchowski, 1916) solves for the collisional evolution of the dust grains depending on their probability to stick together. The final outcome of the collisions therefore depends on the fragmentation velocity v_f, above which the particles cannot grow to larger sizes (Brauer et al., 2008). This limited maximum size can be written as in Birnstiel et al. (2012):

$$a_{\text{frag}} = \frac{2\Sigma_g v_f^2}{3\pi\alpha\rho_s c_s^2}, \tag{1.18}$$

where Σ_g is the gas surface density, v_f is the fragmentation velocity, α is the α-viscosity parameter, ρ_s is the internal density of the grains, and c_s is the sound speed.

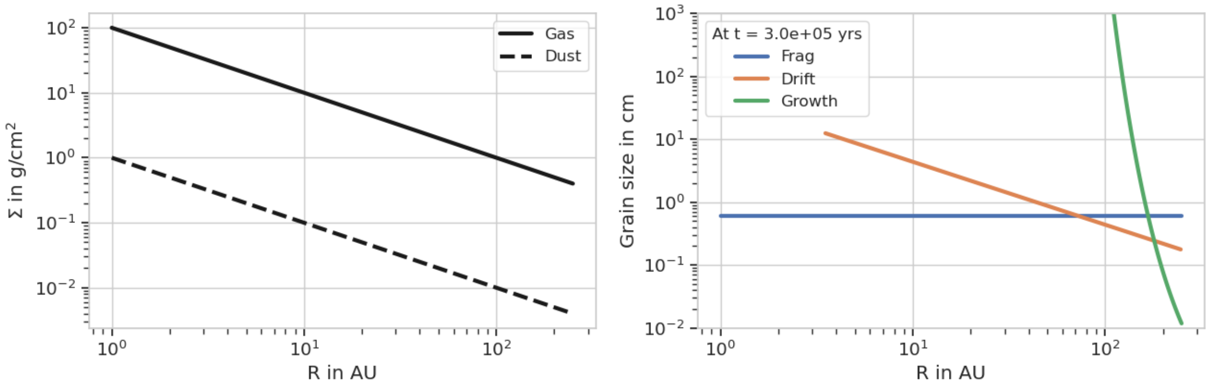

Figure 1.5: Radial dependence of the fragmentation, drift and growth limits. A simple smooth disc profile is taken as example and is shown on the left panel. The gas is represented by the solid black line while the dust is represented with the dashed black line. The right panel shows the maximum size a grain can reach before being limited by the different mechanisms after 3×10^5 yrs: fragmentation (in blue), drift (in orange) and growth (in green).

Regarding the fragmentation velocity v_f, velocities of around ~ 10 m/s are required in simulations to explain the formation of large planetesimals (Drążkowska et al., 2016; Lenz et al., 2019). However, laboratory experiments of dust collisions under physical conditions of protoplanetary discs show that these velocities cannot be that high: they result in $v_f \sim 1$ m/s (Musiolik & Wurm, 2019; Schneider et al., 2019). Pinilla et al. (2021) investigate which conditions are necessary for planet formation to happen with a low fragmentation velocity: it is challenging because it is clear from equation 1.18 that a lower fragmentation velocity yields small grain sizes, if the disc's viscosity is large. Again, the gas disc properties are therefore a key element for dust evolution.

Dust evolution global view

In order to form larger aggregates, the dust particles need to grow before they either drift (eq. 1.16) or fragment (eq. 1.18). Their maximal grain size relies on the balance between each limiting mechanism: $a_{\text{max}} = \min\left(a_{\text{frag}}, a_{\text{drift}}, a_{\text{growth}}\right)$.

It is possible to estimate the growth limit by considering the growth rate resulting from coagulation (Brauer et al., 2008) and the approximate relative velocities of similar sized grains in turbulent motion (Ormel & Cuzzi, 2007). As Birnstiel et al. (2012) shows, this results in a growth limited maximum size written as:

$$t_g = \frac{\Sigma_g}{e_s \Omega_K \Sigma_d} \tag{1.19}$$

$$a_{\text{growth}} = a_0 \times \exp\left(t/t_g\right), \tag{1.20}$$

where e_s is the sticking probability, a_0 is the initial size of all the grains in the disk and t_g is the growth timescale.

Examples of the radial dependence of the limiting sizes described by equations 1.16, 1.18 and 1.20 are shown in Fig.1.5. We consider a density profile described by a simple power law following $\Sigma_g = 10^3 \times (r/1\text{AU})^{-1}$ g/cm^2, with a constant aspect ratio $h = 0.05$. The disc spans from 1 AU to 250 AU and has an α-viscosity of 10^{-3}. The dust profile corresponds to 1% of the gas profile, with an initial dust size $a_0 = 1\mu$m. The grains have an internal density $\rho_s = 1.6$ g/cm^3 and are subject to a typical fragmentation velocity

$v_f = 10$ m/s. The different limiting sizes are shown on the right panel: the dust grains are limited by fragmentation in the inner disc (blue line); after 75 AU, the grains become drift limited (orange line). Lastly, the time of evolution $t = 3 \times 10^5$ years is chosen to show the impact of the growth limit (green line) at early times: the grains located beyond 180 AU did not have time to grow beyond this limit yet.

Equations 1.16, 1.18 and 1.20 show that dust evolution can be derived from the gas evolution, assuming some properties for the dust grains. I present in Chapter 2 a numerical code that solves the time evolution of the dust growth and motion.

Dust trapping in pressure bumps

As mentioned earlier, dust evolution is highly dependent on the gas structure of the disc. Different mechanisms can alter the gas structure: for example, hydrodynamical instabilities can generate vortices where the gas curls on itself at certain locations (e.g., Lovelace et al., 1999; Klahr & Bodenheimer, 2003; Pierens & Lin, 2018; Flores-Rivera et al., 2020); the presence of ice-lines (i.e. locations in the disc where the temperature is high enough for a given material to evaporate) modifies the local structure of the gas(Morbidelli et al., 2015; Wang, 2015); or large bodies such as planetary cores can affect the gas pressure profile (see next section 1.2).

These gas substructures can help prevent the dust disc to be quickly depleted by radial drift. As Brauer et al. (2008) shows, radial drift can empty the disc in grains with St ≈ 1 in less than 1 Myr, which is way faster than the gas disc lifetime. The gas substructures have the capacity to trap particles in pressure bumps (e.g., Brauer et al., 2008; Pinilla et al., 2012; Weber et al., 2018). Radial drift pushes the grains to move to the regions of higher gas pressure. Therefore, when the gas structure presents a local maximum, the drifting grains tend to be trapped in this maximum, called pressure bump. The efficiency of the trapping depends on the amplitude of the bump and on the local turbulence, that acts against the trapping mechanism by radially dissipating the grains (Dullemond et al., 2018).

The dust grains trapped in pressure bumps create local overdensities of dust shaped as rings. Their observation is used to characterize the structure of protoplanetary discs.

1.1.3 Discs observations

The understanding of the protoplanetary discs structure relies in one hand on our ability to model the evolution of this objects, and, on the other hand, on our ability to derive constraints from observations. Recent facilities such as the Atacama Large Millimetre/submillimetre Array (ALMA) or the Spectro-Polarimetric High-contrast Exoplanet REsearch (SPHERE) have granted us with high resolution images of protoplanetary discs, allowing us to revisit our view on disc evolution and planet formation. This section discusses the different emission processes occurring in protoplanetary discs and the kind of constraints that can be derived from their observation.

Radiative transfer

The emission originating from protoplanetary discs can be characterized by the capacity of the disc components to emit, absorb and scatter light. This ability is monitored by the mass-weighted opacity κ_ν of the gas and the dust at a given wavelength ν. Between gas and dust, dust grains are the material that contributes the most to the emission. This originates from their important continuum opacities compared to the gas molecules.

While dust grains are responsible for a large part of the emission, their opacity highly depends on their composition. Laboratory experiments work on deriving these optical characteristics (e.g., Henning & Stognienko, 1996; Draine, 2003; Warren & Brandt, 2008).

The radiative transfer equation aims at quantifying the change in intensity of a radiation transported through a given medium (for a review on dust radiative transfer, see Steinacker et al., 2013). Considering a radiation field described by its intensity $I_\nu(\vec{x},\vec{n})$ at wavelength ν, located in $\vec{x}$ and propagating in the direction $\vec{n}$, the change of intensity due to emission and absorption along a path s (as $\vec{x}(s) = \vec{x_0} + s\vec{n}$) can be written as:

$$\frac{dI_\nu}{ds}(s,\vec{n}) = -\kappa_\nu^{abs}(s)\rho(s)I_\nu(s,\vec{n}) + j_\nu(s) \tag{1.21}$$

where j_ν represents a source term adding radiation to the field and is called the emissivity, and ρ is the density of the medium with an absorbing opacity κ_ν^{abs}. By integrating eq. 1.21 along the path s, the resulting intensity can be expressed as a function of the properties of the medium as:

$$I_\nu(s_1,\vec{n}) = I_\nu(s_0,\vec{n})\exp\left(-\tau_\nu(s_0,s_1)\right) + \int_{s_0}^{s_1} j_\nu(s)\exp\left(-\tau_\nu(s_0,s_1)\right)ds \tag{1.22}$$

where τ_ν is the optical depth, which is defined as the integrated absorption coefficient along the path s:

$$\tau_\nu(s_0,s_1) = \int_{s_0}^{s_1} \rho(s)\kappa_\nu(s)ds \tag{1.23}$$

The optical depth is used to determine the importance of absorption of the initial radiation by the medium:

- in an optically thin case ($\tau \ll 1$), the absorption can be neglected, resulting in an observed intensity only influenced by the emissivity j_ν;
- in an optically thick case ($\tau \gg 1$), the absorption by the medium creates strong absorption features.

Scattering can also have an important impact on the change of intensity I_ν. It can be included in the radiative transfer equation by considering the scattering phase function $\Phi_\nu(\vec{n},\vec{n'},\vec{x})$, describing the probability that a photon initially propagating in the direction $\vec{n'}$ of being scattered at position $\vec{x}$ in the direction $\vec{n}$. By definition, the phase function satisfies:

$$\oint \Phi_\nu(\vec{n},\vec{n'},\vec{x})d\Omega' = 1 \tag{1.24}$$

Including scattering effects in the radiative transfer equation (eq. 1.21) leads to:

$$\frac{dI_\nu}{ds}(s,\vec{n}) = -\kappa_\nu^{tot}(s)\rho(s)I_\nu(s,\vec{n}) + j_\nu(s) + \kappa_\nu^{scat}(s)\rho(s)\oint \Phi_\nu(\vec{n},\vec{n'},\vec{x})I_\nu(s,\vec{n})d\Omega' \tag{1.25}$$

where $\kappa_\nu^{tot} = \kappa_\nu^{abs} + \kappa_\nu^{scat}$ is the total mass-weighted opacity. Analytical solutions are challenging to derive for an equation with this complexity. However, it is possible to numerically solve it. The code used in this thesis for this purpose, `RADMC3D`, is described in Chapter 2. Radiative transfer codes can be used to derive synthetic images of modeled protoplanetary discs and to compare them to observations.

Dust observations

When observing a planet-disc system, the short wavelengths are dominated by the accretion processes, creating a UV excess in the Spectral Energy Distribution (Hartmann et al., 1994; Calvet & Gullbring, 1998); the optical and Near-InfraRed (NIR) wavelengths are dominated by the stellar emission; and the longer wavelengths, from sub-millimeter to millimetre wavelengths, are dominated by the dust emission.

Millimeter and sub-millimeter observations are mostly sensitive to the thermal emission of the large grains (pebble size, $a \sim 1$ mm) and therefore probe the mid-plane structures of the discs (see section 1.1.2). Many surveys have looked at protoplanetary discs at these wavelengths and observed substructures in the dust distributions.

At the present time, the DSHARP survey is the largest survey which observed protoplanetary discs at millimeter wavelengths with very high angular resolution (Andrews et al., 2018). The gallery of images obtained is shown on the left panels of Fig.1.6. The majority of these discs present substructures: the most common ones are the rings and gaps, but spirals are also observed as in IM Lup or Elias 27, or clumps as in HT Lup. The origin for these substructures is still unclear, as I will discuss in the following section.

On the other hand, observations in the NIR ($\lambda \sim 1\mu$m) probe the light scattered by the small grains present in the upper layers of the discs (see Section 1.1.2). With the DARTTS-S survey, Avenhaus et al. (2018) observed the vertical structure of the discs. As shown on the right panels of Fig.1.6, some discs are clearly flared, with the upper layers enlightened by the central star (Dullemond & Dominik, 2004) and a dark mid-plane where the larger dust density blocks the radiation. Interestingly, some discs like IM Lup present substructures in the millimeter and in the micrometer wavelength. However, the substructures characteristics (size and position) often do not match when observed at the two different wavelengths. The link between these substructures is still challenging to explain. One way to improve our understanding of these substructures, is to gather constraints on the gas behavior in these discs.

Gas observations

As mentioned in section 1.1.3, the dust contributes the most to the emission of the disc due to their important continuum opacities. However, gas atoms and molecules also interact with the radiations received by the disc. Due to their discrete energy levels, an atom (or a molecule) receiving energy can jump from one energy level to the other. This process is ruled by the quantum mechanical properties of the atom. The atom can therefore interact with the radiation present in the disc by absorbing or emitting some photons, resulting in absorption or emission lines in the final spectrum. Observing these lines therefore gives an insight on the gas composition of the protoplanetary discs (for a review on chemistry in protoplanetary discs see, Öberg & Bergin, 2021).

Gas observations also holds information about the dynamic of the gas in the disc. For example, CO observations can trace the deviation in the gas velocity via Doppler shift (Disk Dynamics Collaboration et al., 2020). This technique is used to probe different structures in the gas, such as asymmetries induced by instabilities (Teague et al., 2016) or pressure bumps (Teague et al., 2018; Pinte et al., 2020). While they show in this last case that the pressure bumps can be induced by planets, the origin for these substructures is still under debate.

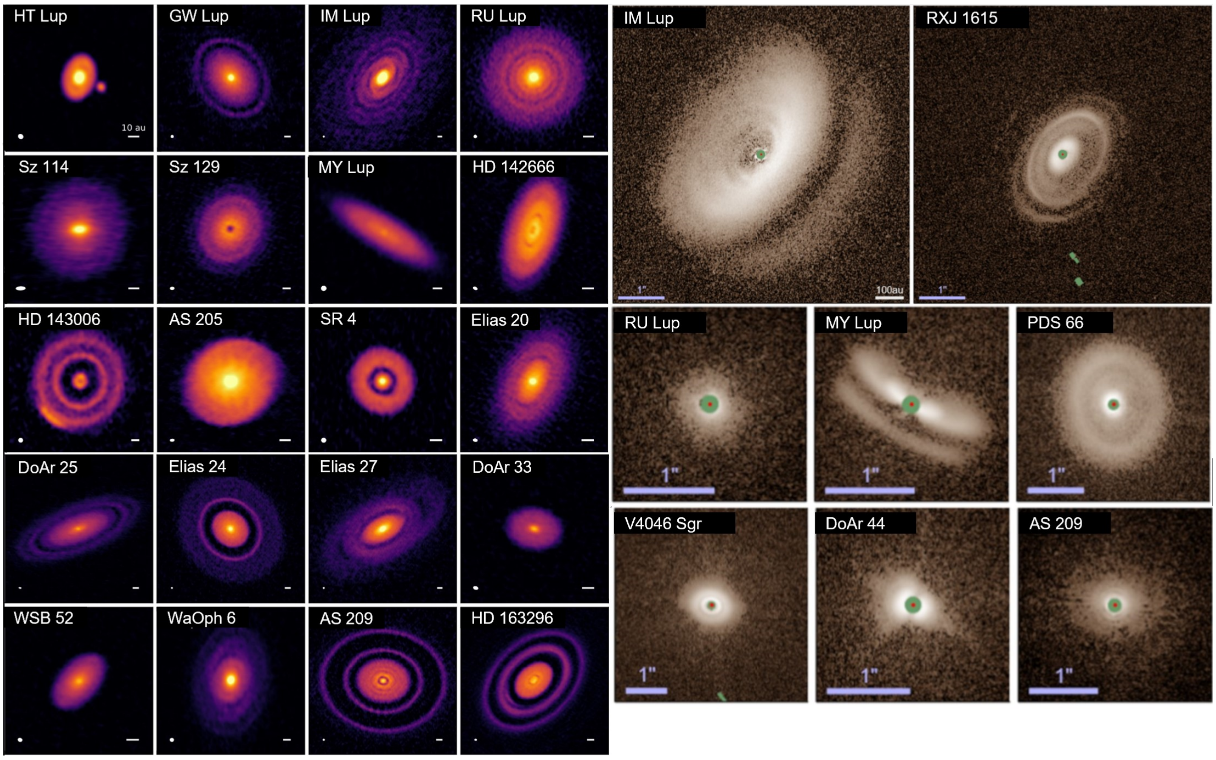

Figure 1.6: Adapted from Andrews et al. (2018) and Avenhaus et al. (2018): DSHARP (left panels) and SPHERE (right panels) images of protoplanetary discs at high resolution. On the left panels, the DSHARP survey observed discs with an beam resolution resolving the substructures smaller than 10 AU at $\lambda = 1.3$mm. On the right panels, the DARTTS-S survey observed discs at $\lambda = 1.6\mu$m (i.e., in band H). Millimeter observations probe the mid-plane structures while observation at micrometer wavelengths probe the surface layers of the discs.

Substructures origins

Many studies investigate the possible origins for these observed substructures. Most of the time, asymmetries like clumps are linked to the presence of vortices in the disc (e.g., Casassus et al., 2019). These vortices can be induced by instabilities like the Rossby Wave Instability (Lovelace et al., 1999), which requires a sharp gas density gradient. This gradient can originate from planet gaps (Pierens & Lin, 2018; Baruteau et al., 2021), but other mechanisms generating vortices exist, like the baroclinic instability (Klahr & Bodenheimer, 2003) or the zombie vortex instability (Marcus et al., 2015). Regarding the gaps and rings observed, different origins are possible, including: self-induced dust traps due to dust growth and backreaction on the gas (Gonzalez et al., 2017), dust growth at snow lines (Zhang et al., 2015), zonal flows (Flock et al., 2015), secular gravitational instabilities (Takahashi & Inutsuka, 2016; Tominaga et al., 2020), sintering-induced rings (Okuzumi et al., 2016), and gap opening of embedded planets (Pinilla et al., 2012). While it is suggested that planets can create such substructures, it is hard to observe the planets directly while they are embedded in their protoplanetary disc (Sanchis et al., 2020; Kloster & Flock, 2021; Asensio-Torres et al., 2021). At the present time, there is only one system with a clear detection of two embedded giant planets: PDS70b and c (Keppler et al., 2018; Haffert et al., 2019). The properties of the embedded planets have to be derived indirectly, via the analysis of the impact of the planet on their surrounding discs. Different techniques include the analysis of the gap size (Zhang et al., 2018) or the CO velocity perturbations (Teague et al., 2018; Pinte et al., 2020).

1.2 Planet-disc interactions

As planets form in discs, they influence their birth environment and vice-versa. Depending on their formation mechanism and their properties (mostly mass, semi-major axis), they will influence the disc structures in different ways. After presenting different planet formation models in section 1.2.1, I present two main planet-disc interactions, namely gap formation in section 1.2.2 and planet migration in section 1.2.3. These processes are inter-dependent as they all rely on the gas distribution in the vicinity of the planet while simultaneously interfering with this same distribution. I refer the reader to the summarizing figure 1.1 for a global view on their inter-dependence.

1.2.1 Planet formation models

Nowadays, there are two main competing scenarios to explain how planet can form. The most standard scenario is the core accretion model, where planets are built from the pile up of dust grains: they first aggregate into 100 km sized objects, which can then further accrete solids and then eventually gas to form gas giants. The other possible planet formation model relies on the gravitational instability of the disc from which gas collapses gravitationally to form giant planets directly. The two next sections present each formation model.

Gravitational instability

When a protoplanetary disc is really massive, it can become gravitationally unstable. This can be monitored with the Toomre parameter (Toomre, 1964):

$$Q = \frac{\kappa c_s}{\pi G \Sigma} \tag{1.26}$$

where κ is the epicyclic frequency, c_s is the sound speed, G is the gravitational constant and Σ is the surface density.

A disc is considered to be unstable when $Q < 1$, which requires a massive disc. Generally, only the outer part of the disc becomes unstable. If the cooling capacities of the disc allows it, then the disc fragments in clumps, forming giant planets by collapse (see Kratter & Lodato (2016) for a review on gravitational instability and Paardekooper & Johansen (2018) for a review on planet formation).

Planets formed by gravitational collapse are therefore very massive ($> 1\mathrm{M_j}$) and located in the outer part of the discs (Rafikov, 2005). While this formation scenario could explain the observations of very large giant planets far from their host star (Wang et al., 2018), it has difficulties reproducing less massive giant planets as in our Solar System. However, a recent work by Deng et al. (2021) shows that, in a magnetized disc (MHD simulation), the magnetic field is enhanced around clumps made by gravitational instability, isolating the protoplanet from the disc environment. This leads to the formation of planets that are an order of magnitude lower in mass than previously expected.

Gravitational instability might be able to explain part of the planet population observed, but another mechanism is needed to explain the formation of smaller planets close to their star.

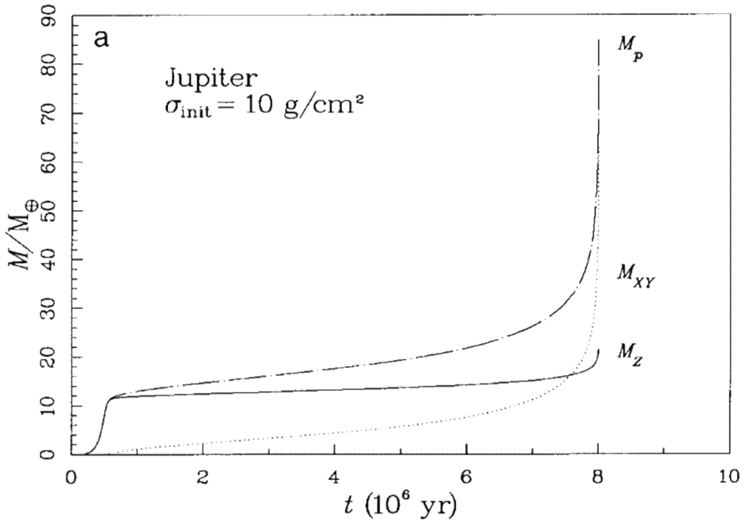

Figure 1.7: From Pollack et al. (1996): Evolution of the planetary mass in the core accretion planet formation scenario. The different lines represent the mass contained in the solids (solid line) and in the gas (dotted line). The total mass, which is the sum of the two, is represented by the dotted dashed line.

Core accretion model

In this thesis, planet formation is supposed to follow the standard formation model called the core accretion model. Here, the planets follow three different growing processes, as described by Pollack et al. (1996) and shown in Fig.1.7:

- during the first 0.5 Myr, dust, pebbles and planetesimals agglomerate until forming a planet core of $\sim 10\mathrm{M}_\oplus$, during a solid accretion phase;
- once it is massive enough, the planet core slowly starts to gravitationally attract gas and form a small gas envelope,
- if nothing alters its growth, the planet reaches a critical mass where the mass of the core is comparable to the mass of the envelope: then the atmosphere collapses on itself, allowing more gas to flow in. The planet enters the final phase of runaway accretion.

The first phase of the core accretion model corresponds to the formation of the solid core. As mentioned in section 1.1.2, the growth of dust grains is limited by different mechanisms such as the radial drift and the fragmentation. In order to overcome these limitations, a mechanism is needed to force the pile up of solids.

Different processes are studied in order to grow from dust to planetesimals. The current promising mechanism is called the streaming instability (Youdin & Goodman, 2005; Youdin & Johansen, 2007). This instability relies on the relative velocity of pebbles compared to the gas velocity. Above a certain solid concentration (dust-to-gas ratio $\gtrsim 0.015$ for St ≈ 0.1, Carrera et al. 2015), the exchange of angular momentum between the pebbles and the gas leads to an accumulation of the pebbles, resulting in a local collapse of the pebbles into planetesimals. The triggering of the streaming instability can be boosted in pressure bumps where the dust is already trapped (Johansen et al., 2006; Dittrich et al., 2013), resulting in the formation of planetesimals, with typical sizes oh $\sim 1 - 100$ km (e.g., Morbidelli et al., 2009).

Once the drift and fragmentation limits are overcome, the protoplanet can grow via two mechanisms: either by planetesimal collisions and agglomeration (e.g., Levison et al., 2010; Kobayashi et al., 2016) or via the accretion of the remaining pebbles (Johansen & Lacerda, 2010; Ormel & Klahr, 2010; Lambrechts & Johansen, 2012). Each growing mechanism has its limit: while growth by planetesimal collision results in long growing timescales due to the scattering of planetesimals via the gravitational interactions with the protoplanet (Tanaka & Ida, 1999), Visser & Ormel (2016) find that pebble accretion is efficient only when the protoplanet already reached a size of $\sim$ 100km. Therefore, it is probable that the core formation consists in a mixture of planetesimal and pebble accretion, depending on the disc properties.

When the protoplanet is large enough, it also slowly starts to accrete the surrounding gas. It is still under debate whether this first slow phase of gas accretion occurs at the same time as the protoplanet grows via planetesimal or pebble accretion (Brouwers & Ormel, 2020; Ormel et al., 2021) or not (Alibert 2017, and for a review on pebble accretion, see Johansen & Lambrechts 2017). During its growth, the protoplanet reaches a critical point where the gaseous envelope is comparable to the mass of the core: then, it collapses on itself and the planet enters a runaway phase of gas accretion. In the pebble accretion scenario, this characteristic mass is called the pebble isolation mass: it corresponds to the moment when the planet becomes massive enough to form a strong enough pressure bump outside of its orbit, blocking the flux of pebbles to the planet (Lambrechts et al., 2014; Bitsch et al., 2015).

The gas accretion process is a complex mechanism that has been studied in many different frameworks. From 2D simulations with and without migration (e.g., Kley, 1999; Crida & Bitsch, 2017) to full 3D simulations including different physics (D'Angelo et al., 2003; Tanigawa & Ikoma, 2007; Ayliffe & Bate, 2009; Machida et al., 2010; Tanigawa & Tanaka, 2016; Schulik et al., 2019), the gas accretion rate onto the planet can vary by multiple order of magnitudes. Lambrechts et al. (2019) even suggested a new definition for the gas accretion rate by differentiating the actual accretion rate from the flux of material that occurs in the Hill sphere of the embedded planet without being bound to it. The Hill sphere represents the region where an object originally orbiting the central star becomes mainly influenced by the gravitational field of the planet. It is written as:

$$r_H = r_p \left(\frac{M_p}{3M_*}\right)^{1/3} \tag{1.27}$$

where r_p is the location of the planet, M_p is its mass and M_* is the mass of the central star. I summarize in table 1.1 the different accretion rates obtained for the runaway phase by some of the cited studies. The resulting accretion rates varies over four orders of magnitudes. Including more physics in future simulations, with high resolution around the planet and the recent observations of accreting planets (like PDS70 b and c) will help constraining the gas accretion rates onto the planets.

Table 1.1: Different gas accretion rates from the literature.

Paper	$\dot{\mathrm{M}}_{\mathrm{runaway}}$ in $\mathrm{M_j/yr}$	Note
D'Angelo et al. (2003)	$\sim 10^{-4}$	
Tanigawa & Ikoma (2007)	$\sim 10^{-8}$	With photoevaporation included
Machida et al. (2010)	$\sim$ (2 to 6) $\times 10^{-5}$	Used in this thesis
Tanigawa & Tanaka (2016)	$\sim 10^{-8}$	
Schulik et al. (2019)	$\sim 10^{-4}$	
Lambrechts et al. (2019)	$\sim 10^{-5}$ to 10^{-6}	Atmospheric flux: $\dot{\mathrm{M}}_{\mathrm{atm.flux}} = 10^{-4}\mathrm{M_j/yr}$

1.2.2 Gap formation

Planets embedded in their disc exert a torque on the disc in their vicinity. As they are growing, this torque becomes more and more important, until it surpasses the disc torque originating from its viscosity. When this happens, the gas is pushed away from the planetary horseshoe orbit, creating a gap. The horseshoe orbit region corresponds to the ring where, in the reference frame of the planet, the gas does a "U-turn" at the planet location, orbiting in an horseshoe shape (see Fig.1.8). It is represented by the half-width of the horseshoe region x_s, written as (Masset et al., 2006b; Paardekooper & Papaloizou, 2009):

$$x_s = 1.16\, r_p \sqrt{\frac{q}{h}} \tag{1.28}$$

The shape and depth of the created gap therefore depends on the equilibrium between the torque exerted by the planets, repelling the gas, and the torque exerted by the disc viscosity $\nu(\alpha, h)$, trying to close the gap. Many different studies investigated gap formation, in particular the link between the gap depth and width, the planet mass and the disc parameters. For example, in Crida et al. (2006), they study the minimum planet mass needed to create a deep gap. They consider that a gap is opened when there is only 10% of the initial gas surface density remaining at the planet location, i.e. $\Sigma_{min}/\Sigma_0 = 0.1$. They find a gap-opening criterion depending on the aspect ratio and α-viscosity:

$$P = \frac{h}{q^{1/3}} + 50\frac{\alpha h^2}{q} \leqslant 1 \tag{1.29}$$

where $q = m_p/m_*$ is the planet to star mass ratio and a planet opens a gap when $P \leqslant 1$. It is clear that it requires less massive planets to open deep gaps when the α-viscosity or the aspect ratio h are small.

More recent studies investigate the evolution of the gap depth as a function of planetary mass and disc parameters. In Kanagawa et al. (2015), the depth of the gap is given as:

$$\frac{\Sigma_{\rm gap}}{\Sigma_0} = \frac{1}{1 + 0.04K} \tag{1.30}$$

where $K = q^2 h^{-5} \alpha^{-1}$ and $\Sigma_{\rm gap}$ is the minimal surface density in the gap region. This criterion is valid for $K \leqslant 10^4$. It is derived for a uniform disc, meaning that the initial

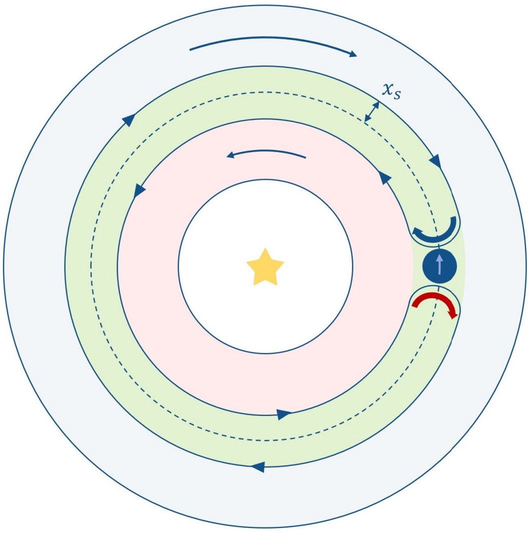

Figure 1.8: Sketch of the horseshoe region of a planet embedded in its protoplanetary disc. The planet is represented by the blue circle and is moving on a circular orbit marked by the dashed line, in the direction marked by the gray arrow. In the reference frame of the planet, the gas evolves in a horseshoe orbit, marked by the green area. The thick red (resp. blue) arrow shows the motion of the gas from the inner (resp. outer) to the outer (reps. inner) disc due to angular momentum exchanges.

surface density is constant in the radial direction. Gyeol Yun et al. (2019) add a correction to this work by studying gap opening in a non-uniform disc, having a power law initial surface density profile with an exponential cutoff. They found a very similar result as that found by Kanagawa et al. (2015), with $\Sigma_{\mathrm{gap}}/\Sigma_0 = 1/(1+0.046K)$.

Another study has been conducted by Fung et al. (2014). They also derive a gap depth description for planetary masses in the range of $10^{-4} \leqslant q \leqslant 5\times10^{-3}$, for $10^{-3} \leqslant \alpha \leqslant 10^{-1}$ and for $0.04 \leqslant h \leqslant 0.1$:

$$\frac{\Sigma_{\mathrm{gap}}}{\Sigma_0} = 0.14\left(\frac{q}{10^{-3}}\right)^{-2.16}\left(\frac{\alpha}{10^{-2}}\right)^{1.41}\left(\frac{h}{0.05}\right)^{6.61} \tag{1.31}$$

These two last criteria can be compared to the Crida et al. (2006) criterion by comparing the mass needed to open a gap where $\Sigma_{\mathrm{gap}}/\Sigma_0 = 0.1$ (see Chapter 3).

Even if it is complicated to determine exactly the shape of the formed gap depending on the planet and disc parameters, it is already clear that gap formation has an impact on the evolution of the planet. In Chapter 3, I present the impact of gas accretion on the gap opening and how it compares to the criteria listed above.

Gap formation is one example of interaction between the planet and its protoplanetary disc. However gap formation requires massive planet. Before opening a gap, the planet is subject to other planet-disc interactions which lead to planet migration.

1.2.3 Migration

When a planet is embedded in a differentially rotating gaseous disc, it excites spiral waves via the Lindblad resonances (Goldreich & Tremaine, 1979; Lin & Papaloizou, 1979). The overdensity resulting from these spiral waves corotates with the planet and exerts a torque on it. As the interior wave leads the planet, it exerts a positive torque on the planet, while the exterior wave trails the planet and exerts a negative torque. The balance between these two torques results in a total torque called the Lindblad torque. In a classic smooth disc profile (i.e., a power law surface density profile decreasing with the radius), the torque from the outer wave is dominating over the torque from the inner wave, leading to an inward migration of the planet.

Considering a disc where the surface density and the temperature can be written as power laws ($\Sigma \propto r^{\alpha_\Sigma}$ and $T \propto r^{\beta_T}$), the Lindblad torque can be expressed as a function of a normalizing torque $\Gamma_0 = (q/h)^2 \Sigma_p r_p^4 \Omega_p^2$:

$$\gamma \Gamma_{\mathrm{L}}/\Gamma_0 = -2.5 - 1.7\beta_T + 0.1\alpha_\Sigma \tag{1.32}$$

where γ is the adiabatic index, Σ_p is the surface density at the location of the planet, r_p is the distance star-planet, and Ω_p is the planet's angular velocity.

However, as mentioned in the previous section, the gas present in the corotation region of the planet evolves on a horseshoe orbit (green region of Fig.1.8). When the gas does the "U-turn" close to the planet, it exchanges angular momentum with the planet. Considering the material coming from the outer disc (blue arrow in Fig.1.8), the gas loses angular momentum to the planet and moves inward, bringing a colder and denser plume of gas in the inner region where the gas is hotter and denser. On the other hand, the material originating from the inner disc (red arrow in Fig.1.8) gains angular momentum and moves outwards, bringing a hotter and diluted plume of gas in the outer region of the disc where the gas is colder and less dens. This flow of material results in a complementary torque called the corotation torque.

The corotation torque has two different main components: the barotropic component Γ_{baro} originates from the change in density when the gas moves along the horseshoe orbit, and the entropic component Γ_{ent} arises from the change in entropy due to the change of temperature during the "U-turn". The importance of each component is not always linear and depends on the viscosity of the disc. If the viscosity is too low, then the material present in the horseshoe region does not have time to be replenished with new material via viscous spreading: the gas in the horseshoe region already lost its angular momentum and the torques vanishes. Therefore, the importance of the corotation torque depends on the libration timescale compared to the viscous timescale needed to cross the half-width of the horseshoe region x_s (see eq.1.28). Depending on which saturation state the planet-disc system stands, the corotation torque is considered to be a linear combination of the linear (Γ_{lin}) and non linear (Γ_{HS}) barotropic and entropic corotation torques, where the coefficients (based on F, G and K) of the linear combination depend on the saturation parameters p_ν and p_χ. The total torque Γ_{tot} felt by the planet is thus the sum of the Lindblad torque and the corotation torque. It is written as (Paardekooper et al., 2011):

$$\begin{aligned}\Gamma_{\mathrm{tot}} = \Gamma_{\mathrm{L}} &+ F(p_\nu)G(p_\nu)\Gamma_{\mathrm{HS,baro}} + (1-K(p_\nu))\Gamma_{\mathrm{lin,baro}} \\ &+ F(p_\nu)F(p_\chi)\sqrt{G(p_\nu)G(p_\chi)}\Gamma_{\mathrm{HS,ent}} \\ &+ \sqrt{(1-K(p_\nu))(1-K(p_\chi))}\Gamma_{\mathrm{lin,ent}}\end{aligned} \tag{1.33}$$

where $p_\nu = 2/3\sqrt{(r_p^2\Omega_p x_s^3)/(2\pi\nu_p)}$ is the viscous saturation parameter depending on the horseshoe half width x_s and the viscosity ν_p at the location of the planet r_p; and $p_\chi = 3p_\nu/2\sqrt{\nu_p/\chi_p}$ is the thermal saturation parameter depending on the thermal diffusion, χ_p, which depends on the opacities in the disc. $\Gamma_{\mathrm{HS,baro}}$, $\Gamma_{\mathrm{HS,ent}}$, $\Gamma_{\mathrm{lin,baro}}$ and $\Gamma_{\mathrm{lin,ent}}$ are the different components of the corotation torque and can be expressed as a function of Γ_0. Their detailed expression can be found in Paardekooper et al. (2011). The total torque formula has been compared to 3D radiation hydrodynamic simulations (Bitsch & Kley, 2011; Lega et al., 2015) and found to be a good match.

This total torque concerns only the planet of small mass: as soon as a gap starts to be opened, the impact of the spiral waves and the flow of gas in the corotation region are completely different. A gap opening planet is generally considered to be locked in the disc due to its gap, evolving with the viscous evolution of the disc. However, recent studies suggest that as there is still a significant flow of gas through the gap and the migration timescale of a planet in its gap is slightly different from the viscous timescale of the disc (Dürmann & Kley, 2015; Robert et al., 2018).

The first regime of migration where the planets are not massive enough to open a gap, described by equation 1.33, is called Type I migration. As soon as a deep gap is opened, the planet slows down in the Type II migration. An intermediate migration regime can arise, called type III migration, when the gap region is partially depleted (Masset & Papaloizou, 2003). In this case, the planet enters a phase of runaway migration.

Migration is therefore an important mechanism in the evolution of planets: depending on the disc parameters and on the planet mass, it dictates where the planet moves in the disc. This can have an impact on the gas accretion process (Crida & Bitsch, 2017) or on the observable substructures left in the dust distribution (e.g., Meru et al., 2019; Weber et al., 2019). Moreover, it is difficult to determine where the planets form, as their migration pushes them away from their birthplace. Analysing the structure of the observed planetary systems is one way to understand their migration history and to determine where they come from.

1.3 Planetary systems

While observations of protoplanetary discs give direct constraints on the birth environment of planets, some constraints can also be derived from the observations of the architecture of planetary systems. The easiest system to study is our own Solar system as we are part of it. The description of the Solar system and how formation constraints can be derived from its study is developed in section 1.3.1. On the other hand, since the discovery of the first exoplanet around a Sun-like star in 1995 (Mayor & Queloz, 1995), plenty of exoplanetary systems were observed. These new planetary architectures completely changed our view on planet formation (see section 1.3.2). Nowadays, planet formation theories try to explain both formation of these exosystems as well as our own Solar system.

1.3.1 Solar System

The Solar System is composed of a multitude of different bodies: the mass distribution ranges from giant planets like Jupiter and Saturn down to small dust grains. Each of these objects contain information about their formation history. However, this section focuses on some key observations that can help constrain the formation of giant planets.

The Minimum Mass Solar Nebula

The Solar system can be divided in four major parts. The inner region is mainly composed of the four terrestrial planets located between 0.3 and 2 AU, and of the asteroid belt, ranging from 2.3 to 3.3 AU (see bottom row of Fig.1.10). This belt marks the inner limit of the giant planet region, mostly composed of the two gas giants Jupiter and Saturn followed by the two icy giants Uranus and Neptune and their moons. The outer region is comprised of the Kuiper belt, where several of the small icy bodies are in resonance with Neptune and stops abruptly around 50 AU. Beyond 50 AU, the objects form the Oort cloud and, even though they are still dynamically bound to the Solar system, start to be non-negligibly influenced by the galactic tides (Dybczyński, 2006).

One difficulty of planet formation models is the lack of constraints on the initial surface density profile, which can have an important impact on the resulting system. Weidenschilling (1977) and later Hayashi (1981) suggested that it is possible to use the mass distribution of the present Solar System to derive the minimal surface density profile needed to reproduce the planets. By spreading locally the total solid mass of the different bodies, they reached the conclusion that this minimal surface density profile should follow:

$$\Sigma_r(r) = 7\ \mathrm{g/cm^2} \times \left(\frac{r}{1\mathrm{AU}}\right)^{-3/2} \qquad \text{for } 0.35\ \mathrm{AU} < r < 2.7\ \mathrm{AU} \tag{1.34}$$

$$\Sigma_{r+i}(r) = 30\ \mathrm{g/cm^2} \times \left(\frac{r}{1\mathrm{AU}}\right)^{-3/2} \qquad \text{for } 2.7\ \mathrm{AU} < r < 36\ \mathrm{AU} \tag{1.35}$$

$$\Sigma_g(r) = 1700\ \mathrm{g/cm^2} \times \left(\frac{r}{1\mathrm{AU}}\right)^{-3/2} \qquad \text{for } 0.35\ \mathrm{AU} < r < 36\ \mathrm{AU} \tag{1.36}$$

$$h_g(r) = 0.033 \times \left(\frac{r}{1\mathrm{AU}}\right)^{2/7} \qquad \text{for } 0.35\ \mathrm{AU} < r < 36\ \mathrm{AU} \tag{1.37}$$

where Σ_r is the rock surface density, Σ_{r+i} is the rock and ice surface density, Σ_g is the gas surface density and h is the gas aspect ratio profile. The discontinuity in the solid profiles originates from the ice-line, corresponding to the position at which the water condensates on the dust grains.

These profiles rely on different important assumptions. First, it assumes that the planets formed in situ, ignoring migration or dynamical interactions. Then it assumes the classical dust-to-gas ratio of 0.01. However, as discussed in the previous section 1.1.2, this ratio evolves with time and with the gas structure. Then, the position of the ice-line is also supposed to be fixed, while the temperature of the disc evolves with time. Finally, it is based on the estimated solid core masses of the giants at that time. Note that this is the minimum surface density profile needed, meaning that this requires a planet formation efficiency of 100% which is not realistic. The actual protoplanetary disc was more massive and probably larger than this profile (Kretke et al., 2012; Lenz et al., 2020).

These profiles give an insight on the potential global structure of the protoplanetary disc. Further constraints on the birth environment of the Solar System can be estimated by analysing the characteristics of the different bodies.

Giant planets composition

As shown at the bottom of Fig.1.10, the four giant planets are located in the outer part of our system. Jupiter and Saturn each have a massive gaseous atmosphere, mainly composed of hydrogen and helium. The similarity in composition with the composition of the gas during the protoplanetary disc phase sets a first constraint on their formation: they must have acquired their gas during the disc lifetime (i.e. in a few million years, see section 1.1.1). Their atmosphere is slightly enhanced in metals (elements heavier than hydrogen and helium): this can be used to time the moment when the solids are accreted (Valletta & Helled, 2020) or to measure the mass of the solid core (Lozovsky et al., 2017). Even if it is not clear wether the giants have a solid core or a more diluted one (Helled & Stevenson, 2017), the mass of the core can help quantify when the planet switched to the runaway gas accretion regime in the core accretion scenario (see section 1.2.1).

Asteroid belt and meteorites

The Solar system contains different reservoirs of small bodies. They hold important constraints on the formation of giant planets. The Asteroid belt, located between Mars and Jupiter (in green in Fig.1.10), is composed of asteroids which sizes range from 100m to a few hundreds of km. Some fragments of these asteroids are ejected towards the Earth allowing us to analyze directly their composition. These meteorites represent the primordial composition of the Solar system building blocks. The meteorites can be classified in two different categories: the carbonaceous meteorites, located mainly in the outer part of the Asteroid belt, and non-carbonaceous meteorites located preferably in the inner part of the belt. (e.g., DeMeo & Carry, 2014; Kruijer et al., 2017; Budde et al., 2019). This dichotomy suggests that there were two different solid reservoirs quite early in the evolution of the Solar system. With time, these two distinct reservoirs must have been mixed to end in the Asteroid belt region.

Formation scenarios

From the architecture and composition of our Solar System, we can derive two important constrains regarding the formation of giant planets: first, the giants must acquire their gaseous envelope during the disc lifetime and should explain the dichotomy observed in the composition of the bodies of the Asteroid belt. There exists different scenarios trying to conciliate these two constraints as well as trying to reproduce the current architecture of the Solar system. Raymond et al. (2020) summarized three of the most probable scenarios, as shown in Fig.1.9.

In the **Grand Tack scenario** (e.g., Walsh et al., 2011; Raymond et al., 2011; Pierens et al., 2014), the cores of Jupiter and Saturn form quickly, creating a pressure bump which separates the inner and outer discs in two different solid reservoirs. Both planets migrate inward until they get caught in resonance, making them migrate outward (Masset & Snellgrove, 2001). During their outward migration, they scatter the non carbonaceous solids present in the inner disc to the outer disc, mixing them with the carbonaceous bodies. At the end of the disc lifetime, the inner planets form by collisions and the remaining solids end up in the asteroid belt region. While this scenario can reproduce the mass distribution of both the inner planets and the asteroid belt (Walsh et al., 2011, 2012; Brasser et al., 2016), the conditions needed for the outward migration to be efficient are difficult to meet. As different studies show (Masset & Snellgrove, 2001; Pierens et al., 2014), outward migration can only occur if the mass ratio between Jupiter and Saturn is between 2 to 4 and, depending on the local properties of the disc such as the viscosity, if they get caught in the correct resonance. It is also unsure whether gas accretion onto the giants can alter the migration pattern of the planets.

Another possible scenario involves a **Low mass asteroid belt** (Hansen, 2009; Drążkowska et al., 2016; Raymond & Izidoro, 2017). In this model, it is suggested that the Asteroid belt region is originally depleted in solids. The bodies are located both in the outer region of the disc, where the cores of Jupiter and Saturn form, and in an inner narrow ring ranging from 0.7 to 1 AU. The terrestrial planets grow from the interactions between the planetesimals in the inner ring. The Asteroid belt region either starts with the right amount of non carbonaceous asteroids and is populated in carbonaceous bodies during the growth of Jupiter and Saturn, or the inner planets scatter the leftover of their formation in the Asteroid belt region that is originally completely depleted.

The Low mass asteroid belt model easily and accurately reproduces the inner disc distribution. However, it is still challenging to explain how such narrow ring can form at this location, together with the formation of Jupiter and Saturn's cores (Drążkowska et al., 2016; Carrera et al., 2017; Izidoro et al., 2021a). Furthermore, this model results in Earth and Mars being formed from the same reservoir, making difficult to explain their difference in composition.

Finally, in the **Early instability** model (Clement et al., 2018), the giant planets grow during the disc lifetime and scatter some carbonaceous meteorites in the inner regions of the disc. After the gas disc dispersal, the giant planets undergo an important dynamical instability. Clement et al. (2018) show that if this instability occurs within 10 Myrs after the gas disc dispersal, then it can excite the asteroid belt, depleting the regions in solids simultaneously with the formation of the terrestrial planets. This results in realistic Earth to Mass mass ratios and in a correct distribution of asteroids. Moreover, the inner disc is

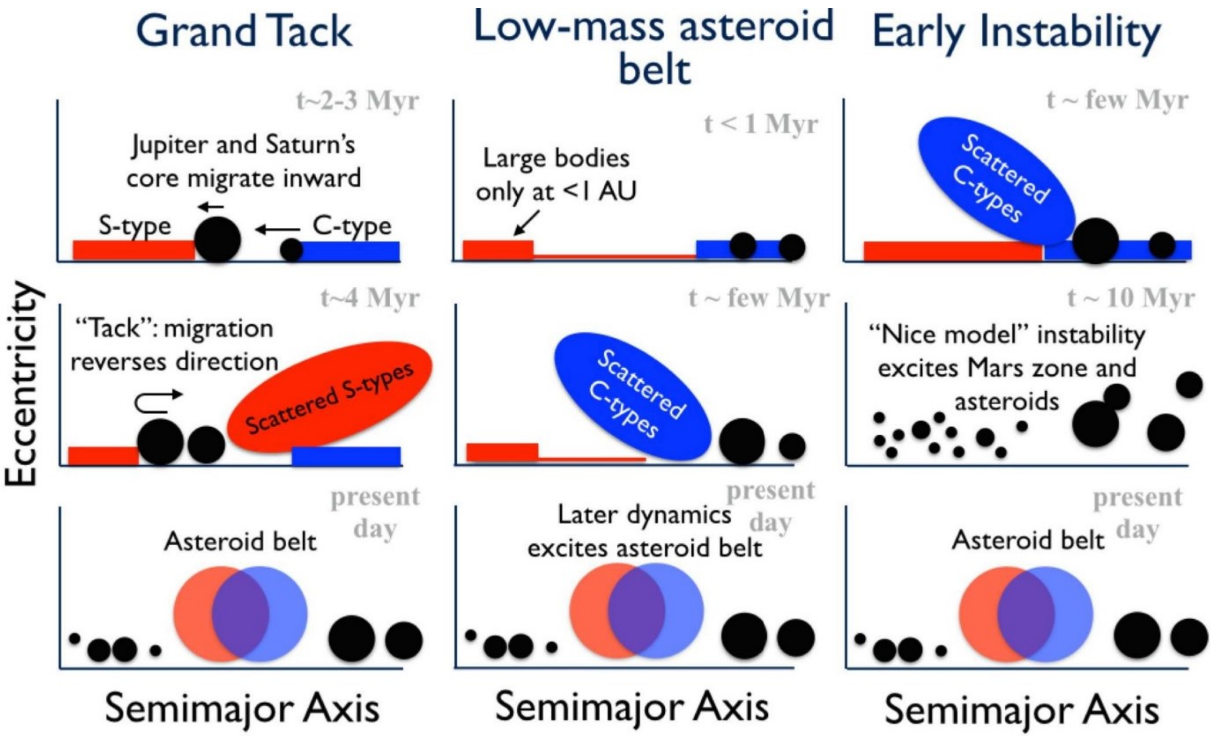

Figure 1.9: Possible Solar system formation scenarios, from Raymond et al. (2020). In the Grand Tack scenario, the inward then outward migration of Jupiter and Saturn distribute the solids in the inner disc. The Low-mass asteroid belt scenario relies on a originally depleted asteroid belt, populated in C-type solids by the growth of Jupiter and Saturn. In the Early Instability scenario, the inner region of the system is populated during the giant planet instability occurring quickly after the dispersal of the gas disc.

better reproduced when the outer giant planets match the current Solar system.

The difficulty encountered by this model is the importance of having this instability to occur early after the disc dispersal. As Raymond et al. (2020) explain, the Xenon signature of the Earth is inconsistent with an early giant planet instability due to its potential cometary origin. Moreover, Nesvorný (2015) shows that the inclination distribution of the Kuiper belt objects are consistent with a late giant planet instability.

Currently, it is still challenging to find a planet formation scenario that matches all the constrains derived from the studies of our own Solar system. Understanding the mechanisms regulating the formation of exoplanetary systems can be beneficial to understand the formation of our own system.

1.3.2 Exoplanets

As of the 20th of March 2022, the Nasa Exoplanets Archive counts more than 5000 observed exoplanets. This allows us to discover a variety of planetary architectures and therefore to statistically derive planet formation characteristics. After discussing the exoplanet multiplicity in a first section, constraints from the analysis of the different planetary architectures are presented in the last section.

Multiplicity

Among all the observed planetary systems, some only have a single planet detected while the others host multiple planets. The challenge of exoplanet observations is to deal with the bias resulting from these observations due to their limited range of sensitivity. Here, this impacts the occurrence rates of multiple planets: when a survey detects a single planet around a star, is it because it is indeed alone or is it due to a detection limit (e.g., non-transiting second planet or second planet with a very high inclination) which hides the other planets? While recent different methods aim to take into account the survey incompleteness to recover more realistic occurrence rates, these methods are still being improved and are not always applied to the surveys.

With this in mind, it is possible to investigate the fraction of multiple planetary systems compared to single ones in the recent surveys. Wright et al. (2009) observe a fraction of 28% of multiple planetary systems detected with the radial velocity method. Zhu (2022) finds a similar fraction with planets derived from transit observations. In general, recent studies tend to conclude that multiple planets are common (Wright et al., 2009; Lissauer et al., 2012; Fabrycky et al., 2014; Zhu, 2022), but their exact multiplicity is still under debate.

Architecture of the systems

Multi-planetary systems come with a variety of different architectures. This can be seen in Fig. 1.10, where all the documented planetary systems with more than two planets around Sun-like stars are shown as a function of their semi-major axis and orbital period. The data originates from the Nasa Exoplanets Archive on the 20th of March 2022. The selected planets orbit around single Sun-like stars, filtered by their effective temperature ($\mathrm{T_{eff}} \in [4700, 6500]K$) and the stellar surface gravity ($\log(g_*) > 4$) as in Zhu (2022). In order to avoid brown dwarfs, the maximum planet mass is limited to 10 $\mathrm{M_J}$. The marker size is proportional to $m_p^{1/3}$.

The Solar System is represented for comparison at the bottom of each column. The first interesting observation that can be made is that a multitude of systems harbor planets with orbits smaller than our Mercury. The presence of super close-in planets is an argument that can validate the importance of migration of planets but challenges our understanding of the formation of the Solar system.

On the other hand, planets within the same system tend to have similar characteristics such as the size, the mass or the spacing (Millholland et al., 2017; Weiss et al., 2018). This is an interesting constraint for planet formation scenarios: while they need to be able to reproduce a variety of different architectures, they should also produce systems with similar planets in them. Note that there is still a significant fraction of systems (as can be seen in Fig.1.10 and in our Solar system) that harbor planets with different masses. In Chapter 4, I will discuss in more details the impact of similarities in the mass for gaseous giant planets.

Another aspect that can be investigated is the distribution of period ratios. As Fabrycky et al. (2014) show, multi-planetary systems do not seem to privilege any particular resonance. As can be seen with the Grand tack scenario (see previous sections), the capture in resonance is a key process during the radial evolution of a migrating system. While resonant chains might be formed during the gaseous disc phase, mechanisms need to be involved after the disc dispersal to explain to break the resonant chains, as they are not common in planetary systems (Izidoro et al., 2021b).

Finally, one last important constraint originates from the coplanarity of the systems. Fang & Margot (2012) show that 85% of the multi-planetary systems observed with *Kepler* have mutual inclinations lower than 3 degrees. This suggests that the planets formed in the same protoplanetary disc and that instabilities between the planets after the gas disc phase should be rather mild to explain the low levels of inclination rather than very violent. It emphasises the point that planet formation studies should also take the phase after the gas disc dissipated into account.

1.4 Motivations of this thesis

As discussed in the last sections, even if planet formation theories have significantly improved thanks to better computation power and new observations techniques, they still are challenged by a variety of different constraints.

This thesis is mostly motivated by the last constraint discussed: planets form in the same protoplanetary disc. By focusing on the formation of giant planets, I numerically investigate, with the help of my collaborators, how the presence of other forming planets can influence their birth environment and their own growth. After presenting the numerical tools used in the different projects in the next chapter (Chapter 2), three different projects are presented in three different chapters:

Chapter 3 investigates the impact of gas accretion on the shape and depth of gaps in the protoplanetary disc. This study allows us to determine the impact of different accretion rates on the global structure of the protoplanetary disc and on the resulting gap opening mass. While the impact on the gap opening mass can be important for the derivation of the planet masses from disc observations, the understanding of the behavior of the competition between gas accretion and gap formation is primordial for the following chapter.

Chapter 4 presents the influence of simultaneous gas accretion of two giant planets on their own growth and on their natal protoplanetary disc. This study starts from the same set-up as in the previous chapter but adds a second planet accreting in the disc. We investigate the impact of the disc parameters on the resulting similarities between the two planets masses. This work is then compared to the distribution of exoplanetary systems as well as our own solar system, clarifying some aspects of simultaneous planet formation.

Chapter 5 addresses the question of the uniqueness of the Solar system with the help of synthetic ALMA images of its potential protoplanetary disc. By considering different birth environments in which the giants of our Solar system could have formed, we analyze the structures produced by the four giants in the gas and dusty discs. Thanks to a radiative transfer code, we generate synthetic ALMA images of the potential parental protoplanetary disc of our Solar system that can then be compared to the observed population of protoplanetary disc.

Finally, **Chapter 6** summarizes the conclusions of the different studies presented in this thesis before finishing on the potential future projects that can help improve our understanding of planet formation.

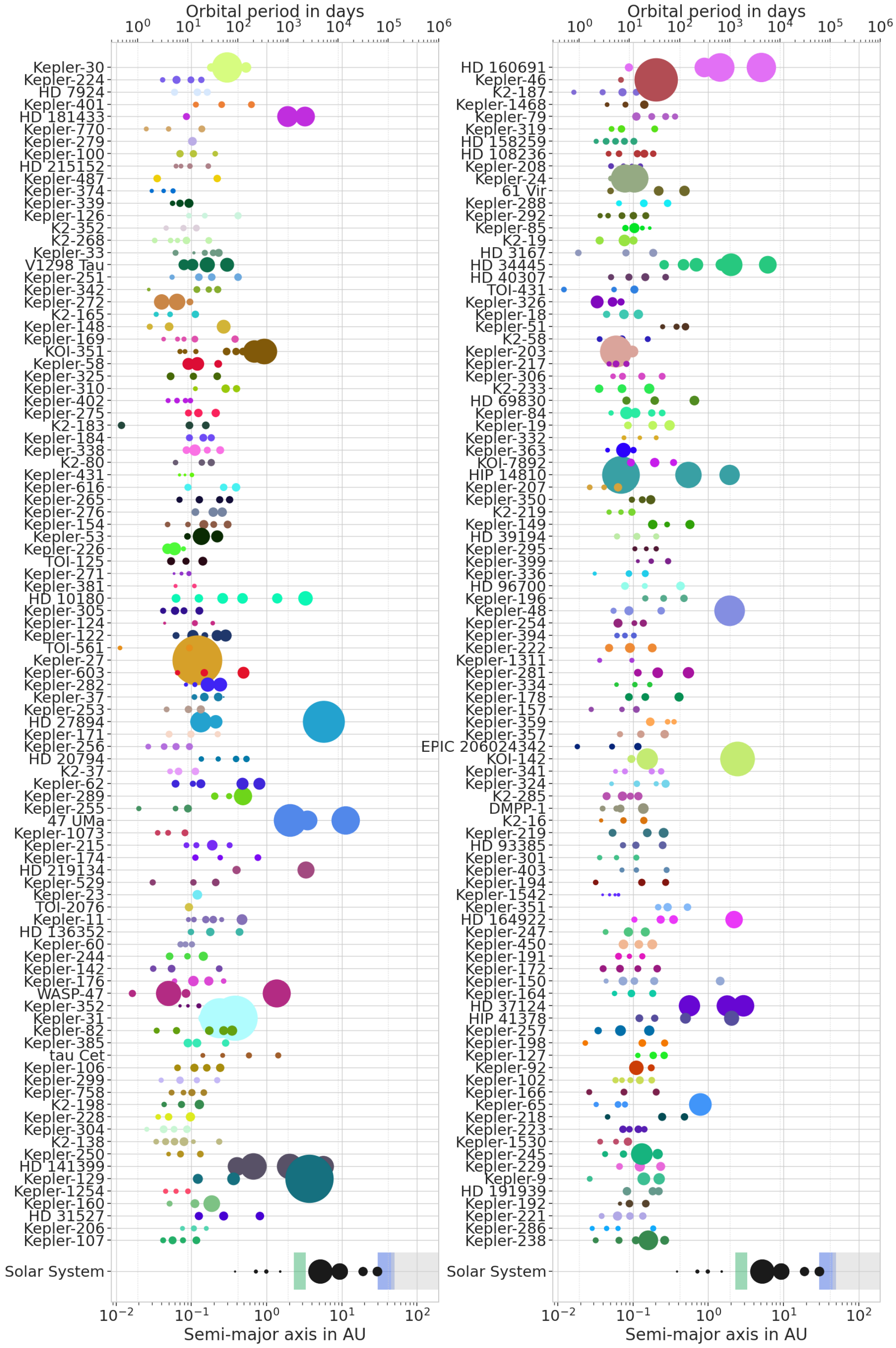

Figure 1.10: Exoplanetary system architectures of known systems with multiple planets around Sun-like stars as of the 20th of March 2022 compared to the Solar System. The data originates from the Nasa Exoplanets Archive. The systems are filtered to select only the systems orbiting single Sun-like stars (i.e. with $\mathrm{T_{eff}} \in [4700, 6500]K$ and $\log(g_*) > 4$), with a maximum planet mass of 10 $\mathrm{M_J}$, to avoid potential brown dwarfs, and where both the orbital period and the mass are known. This results in 654 planets spread over 192 planetary systems. The color only represents the planets from the same system and the marker size is proportional to $m_p^{1/3}$. The Solar system is represented at the bottom of each column: the Asteroid belt is shown in green, the Kuiper belt in blue and the Scattered disc in gray.

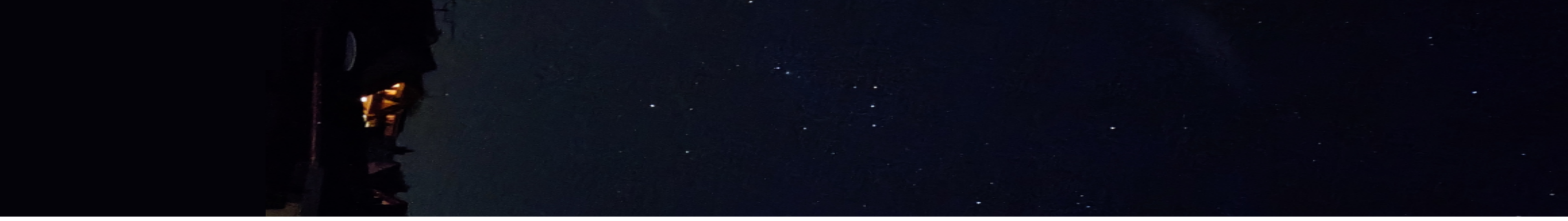

2

Numerical methods

This chapter is partially based on the papers published in Astronomy and Astrophysics: Bergez-Casalou et al. (2020) and Bergez-Casalou et al. (2022).

The goal of this thesis is to investigate the influence of multiple growing planets on the protoplanetary disc structure that surround them. For that purpose, a hydrodynamical code and a dust evolution model are used to simulate how the gas and the dust behave in presence of these planets. A comparison with observations is made with the help of synthetic images produced by a radiative transfer code.

In this chapter, I present the structure of the different codes used in the different chapters: the hydrodynamical code for gas evolution is described in section 2.1 and used in all the projects; the dust evolution code is presented in section 2.2 and the radiative transfer code is depicted in section 2.3. The last two codes are used in Chapter 5.

2.1 Simulating gas disc evolution: `FARGO-2D1D`

To simulate the gas behavior, I used a hydrodynamical code called `FARGO-2D1D`. After describing the features of such a code in section 2.1.1, our gas accretion routine is presented in section 2.1.2.

2.1.1 The `FARGO-2D1D` features

`FARGO-2D1D`[1] is a hydrodynamical code used to simulate the gas behavior of a disc in differential rotation around a central object, in presence or not of embedded objects. It is developed by Crida et al. (2007), based on the `FARGO` ("Fast Advection in Rotating Gaseous Objects") algorithm (Masset, 2000). It has the ability to solve the Navier-Stokes and continuity equations, as described in Sect. 1.1.1. `FARGO-2D1D` uses a locally isothermal equation of state, dictated by a given temperature (or sound speed) radial profile.

The algorithm operates on a 2D polar grid, centered on the central object. The particularity of the `FARGO-2D1D` code is the possibility to extend the 2D polar grid with two 1D grids in the inner and outer parts of the disc. Including these grids allows us to self-consistently simulate the whole viscous evolution of the disc at a reasonable computational cost, by assuming that the disc is axisymmetric when it is located far from the planets. It is important to have an accurate description of the viscous evolution of the gas as it dictates the amount of gas available for the planets to accrete. The configuration of the grids is presented in Fig. 2.1: the planets are located in the 2D polar grid, and the extent of the grids is chosen so that the 1D grids are far enough from the planets.

To ensure a smooth continuity between the different grids, additional ghost cells are present at the interface of the 2D and 1D grids, taking care of the mass and angular momentum conservation. The inner and outer boundaries of the 1D grids are set to be open, so that the gas can flow through them (i.e., accretion onto the star and viscous spreading).

For computational accuracy, the code uses dimensionless units. The masses are normalized by the mass of the central star, $M_0 = M_\odot$ and the lengths by the position of the inner planet, $r_0 = 5.2$ AU. The gravitational constant is set to be $G = 1$. This leads to a time normalized by the orbital time at r_0, $t_0 = (r_0^3/(GM_*))^{-1/2}$, meaning that the orbital period of the planet is $P = 2\pi t_0$.

`FARGO-2D1D` takes different input parameters to describe the initial disc profile. The vertical structure of the disc is represented by its aspect ratio (see Sect. 1.1.1), described by a power law:

$$h = h_0 \times \left(\frac{r}{5.2\mathrm{AU}}\right)^{f_l} \tag{2.1}$$

where h_0 is the value of the aspect ratio at $r = 1 = 5.2$ AU and f_l is the disc's flaring index. These values set the temperature profile of the disc. The disc is subject to an α-viscosity description (Shakura & Sunyaev, 1973). Together with the disc aspect ratio h, they describe the kinematic viscosity $\nu(\alpha, h)$ of the disc (see Sect. 1.1.1).

Similarly to the aspect ratio, the initial surface density profile is represented by a power law following:

$$\Sigma = \Sigma_0 \times \left(\frac{r}{5.2\mathrm{AU}}\right)^{-p} \tag{2.2}$$

---

[1] `http://fargo.in2p3.fr/-FARGO-2D1D-`

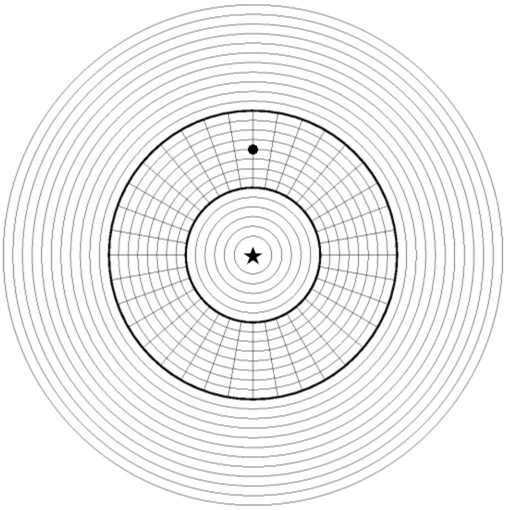

Figure 2.1: Sketch of the grid configuration in `FARGO-2D1D`. The 1D grids surround the 2D grid, allowing a self consistent simulation of the whole disc viscous evolution. The dot represents the location of the planet and the star represents the central star, in a case of a simulation with a single planet. The planet is considered far enough from the boundaries of the 2D grid for the disc to be considered axisymmetric.

where Σ_0 is the value of the surface density at $r= 1 = 5.2$ AU in numerical units and p is the surface density slope. In this thesis, the value of Σ_0 is always chosen such that the total mass of the disc is $0.1M_*$, corresponding to a heavy disc with a large radius (Baillié et al., 2019). However, the large radial extent of the discs, thanks to the presence of 1D grids, allows us to neglect self gravity and to consider our disc gravitationally stable.

Even if the radial extent of the grids varies from one project to the other, the resolution of the 2D grid is always based on the same quantity: in order to properly resolve the region around the planet, the resolution is based on the Hill radius of the planets (see eq.1.27): it is chosen such that there are five cells per Hill radius of the planet at t = 0. In a case of a growing planet, as the resolution is fixed in time, the Hill sphere will become more and more resolved as the planet grows.

The planets are represented as gravitational potential in the code, meaning that they are not spatially resolved (i.e., their radius is not computed). They are therefore defined by their mass and position in the disc. Each planet is introduced in the disc with a mass-taper function, making the planet grow from 0 to its initial mass in n_{orb} orbits. The mass taper function is written as:

$$m_{taper} = \sin^2\left(\frac{t_{orb}}{4n_{orb}}\right) \tag{2.3}$$

where t_{orb} is the time of the simulation in planetary orbits. This function allows a smooth introduction of the planet gravitational potential in the disc.

As described in section 1.2, the embedded planets interact with the disc, migrating and creating gaps in the gas surface density. `FARGO-2D1D` allows the user to chose if the planets feel the effect of the back reaction of the gas on themselves, leading to migration. While the disc will always feel the effect of the presence of the planets, creating gaps, migration is neglected in all the projects for the moment. This allows us to disentangle the structures created by the migration of the planet from the ones induced from their growth. Similarly, the code allows the user to turn off the interactions between the planets, ignoring the dynamics of the planets between themselves. Future projects will take into account the impact of migration and dynamical interactions between the planets on their growth and on the structure of the surrounding disc (see Chapter 6). In this thesis, all the planets are fixed on circular orbits and they do not dynamically feel each other.

2.1.2 Gas accretion routine

In Chapters 3 and 4, I investigate the behavior of gas accreting planets. Gas accretion is modeled using the Machida et al. (2010) and Kley (1999) principles, as in Crida & Bitsch (2017). The Kley (1999) principle is an arbitrary accretion rate, limited by how much gas is available within the Hill sphere of the planet (eq. 1.27). The Machida et al. (2010) accretion rate is based on 3D isothermal shearing box simulations and represents the accretion rate of the planet in the runaway gas accretion phase. The accretion rate is different than in the contraction phase, as predicted by the core accretion model (Piso & Youdin, 2014).

Crida & Bitsch (2017) used Machida's accretion rate without reducing the gas surface density from its initial value Σ_0 when computing the accretion rate. To make sure that they were limited to what the disc can provide, they limited the accretion rate to the minimum between Machida's and Kley's accretion rates. As planets create gaps, the surface density profile around the planet is reduced compared to the initial profile. Therefore, in this thesis, I used the local surface density, defined as the average of the surface density from the position of the planet to 0.9 r_H. The resulting accretion routine is written as follows:

$$\dot{M}_p = \min \begin{cases} \dot{M}_M = <\Sigma>_{0.9r_H}\ H^2\Omega \times \min\left[0.14; 0.83(r_H/H)^{9/2}\right] \\ \dot{M}_K = \iint_{S_{disc}} f_{red}(d)\ \Sigma(r,\phi,t)\ \pi d^2 f_{acc}\ dr\ d\phi \end{cases} \tag{2.4}$$

where S_{disc} is the disc surface, H the disc scale height, Ω the keplerian orbital period of the planet, d the distance from the planet, r_H is the Hill sphere of the planet, and f_{acc} is the inverse timescale upon which the accretion rate of Kley (1999) is occurring. Here, $f_{acc} = 1$ to determine which of the accretion rate is the smallest. f_{red} is a smooth reduction function used to predict what fraction of gas must be accreted on the planet as a function of the distance to the planet. It is defined as:

$$f_{red} = \begin{cases} 2/3 & \text{if } d < 0.45\ r_H \\ 2/3 \times \cos^4\left(\pi\left(\frac{d}{r_H} - 0.45\right)\right) & \text{if } 0.45\ r_H < d < 0.9\ r_H \end{cases}. \tag{2.5}$$

This function is based on Robert et al. (2018), where the authors assume that close to the planet gas accretion is 100% efficient ($f_{red} = 1$). However, it seems that 100% efficiency is not realistic. Schulik et al. (2019) showed that gas accretion does not start from the full Hill sphere but only from a fraction of it. The accreted mass fraction increases closer to the planet but it does not accrete 100% of the gas in the vicinity. Thus, I modified the accretion routine such as the planet accretes maximum 2/3 of the gas present close to it ($f_{red} = 2/3$).

As Machida's formula only provides information on the amount of mass that should be accreted, we remove the gas in this regime with the same formalism as for the Kley (1999) method. This means that if the planet is accreting in the Machida regime, the total amount of gas it accretes is given by eq.2.4 and the distribution stating from where the gas is removed in the disc is given by eq.2.5.

This way, the removal scheme of the gas is the same for both regimes, but the mass that can be accreted is either limited by the derived accretion rates of Machida et al. (2010) or by the maximum amount the disc can provide, given by the Kley (1999) method. Unless specified, the planets remain in the regime where $\dot{M}_M < \dot{M}_K$, meaning that they always accrete the amount of mass suggested in Machida et al. (2010).

2.1.3 Gas disc parameters

To summarize, the hydrodynamical simulations in this thesis involve a single or multiple planets embedded in their surrounding gaseous protoplanetary disc simulated by 2D and 1D grids. The planets can accrete gas or not following the routine presented in section 2.1.2 and could but do not migrate nor feel the dynamical interactions from other planets. Each simulation is represented by a set of parameters as presented in table 2.1. Each Chapter presents a similar table summarizing the initial parameters proper to the study.

Table 2.1: Global gas disc parameters.

Gas parameters	
Aspect ratio value at r_0	h_0
Aspect ratio flaring index	f_l
Alpha viscosity	α
Surface density value at r_0	Σ_0
Surface density slope profile	p
Planet parameters	
Planet initial mass	m_p
Planet initial position	r_p
Accretion time	$t_{start,acc}$
Planet migration	NO
Planet interactions	NO
Planet mass taper	n_{orb}
Planet eccentricity	0
Grids parameters	
Radial extent of 1D grid	$[R_{min,1D},R_{max,1D}]$
1D radial resolution	$N_{rad,1D}$
Radial extent of 2D grid	$[R_{min,2D},R_{max,2D}]$
2D radial resolution	$N_{rad,2D}$
2D azimuthal resolution	$N_{\phi,2D}$

2.2 Simulating dust evolution in a gas disc: `TWO-POP-PY`

In Chapter 5, we investigate the influence of the presence of multiple giants on the gas and the dust distributions in order to derive millimeter synthetic images. The dust distributions are derived with the help of a dust evolution code called `TWO-POP-PY` (Birnstiel et al., 2012, 2015).

2.2.1 Structure of `TWO-POP-PY`

`TWO-POP-PY`[2] is a 1D code computing the radial motion of growing grains from given initial dust and gas radial profiles by dividing the different grains into two groups. The two different populations depend on their coupling to the gas and therefore on their size (see section 1.1.2): the small grains are mostly subject to the gas drag while larger grains are mostly influenced by their drift. To precisely delimit each population, instead of using directly the Stokes number as explained with eq. 1.14, the code discriminates the two populations with their drift velocity compared to the gas drag velocity: any grain which drift velocity is larger than its gas drag velocity is considered to be a large grain, otherwise it is seen as a small grain. The motion of the grains are therefore based on the velocities of each population (see eq. 1.15), calculated as an average for each group and defined as in Birnstiel et al. (2012):

$$v_i = v_{\rm drag} + v_{\rm drift} \tag{2.6}$$

$$v_i = \frac{v_{r,\rm gas}}{1+{\rm St}_i^2} + \frac{|\gamma| c_s^2}{v_k({\rm St}_i + {\rm St}_i^{-1})} \tag{2.7}$$

where $i = \{0, 1\}$ represents each grain population, $v_{r,gas}$ is the radial velocity of the gas, $|\gamma| = d\ln(P)/d\ln(r)$ is the pressure profile of the gas disc, c_s is the sound speed and St is the Stokes number.

As mentioned in section 1.1.2, the growth of grains can be estimated by taking into account the dust-to-gas ratio as in eq. 1.20. Considering the growth, drift and fragmentation limits (equations 1.16, 1.18 and 1.20), the code computes the dust evolution as a function of time.

After the final time step, the full grain size distribution is reconstructed from the two different populations, determining the surface density as a function of orbital distance for each grain size (Birnstiel et al., 2015). The particle grid used by the reconstruction routine logarithmically ranges from the initial size a_0 to $6 \times a_{max}$, a_{max} being the maximum grain size reached at the end of the simulation, resolved with 300 cells.

2.2.2 Dust evolution parameters

To summarize, `TWO-POP-PY` starts with given dust and gas initial profiles and supplies the final grain radial distribution as a function of the grain sizes after a given time t_{max}. Note that `TWO-POP-PY` also has an integrated simple hydrodynamical routine to compute the time evolution of an unperturbed gas disc. The user has the opportunity to either fix the gas profile to the initial profile or to let it evolve with the dust.

In this thesis, the goal is to study the perturbations induced by multiple giant planets. Therefore the simple unperturbed hydrodynamical routine available in `TWO-POP-PY` cannot

---

[2] `http://birnstiel.github.io/two-pop-py/`

be applied here: the initial gas profile is always supposed to be fixed during the dust evolution model. As for `FARGO-2D1D`, the list of input parameters are summarized in table 2.2. Chapter 5 presents a similar table summarizing the initial parameters proper to this project.

Table 2.2: Global dust evolution parameters.

Initial profiles	
Initial gas profile	$\Sigma_{g,0}$
Initial gas radial velocity	$v_{r,\mathrm{gas},0}$
Gas alpha-viscosity	α
Gas evolution	NO
Initial dust profile	$\Sigma_{d,0}$
Dust characteristics	
Internal density of the grains	ρ_s
Fragmentation velocity	v_f
Sticking probability	e_s
Initial dust size	a_0
Grid parameters	
Radial extent of the grid	$[R_{min},R_{max}]$
Radial resolution	N_{rad}
Time of integration	t_{max}

2.3 Simulating dust emission to produce synthetic images: `RADMC-3D`

In Chapter 5, synthetic images of protoplanetary discs are derived. As mentioned in section 1.1.3, this can be done with the help of a radiative transfer solver such as `RADMC-3D` developed by Dullemond et al. (2012).

2.3.1 Structure of `RADMC-3D`

`RADMC-3D`[3] (RADiative Monte Carlo 3D) is a tool solving the radiative transfer equation (eq. 1.25) for a radiation field created by a star and crossing a dusty and/or gaseous astrophysical cloud. In this thesis, we focus on the radiative transfer modeling through a dusty continuum.

The challenge of radiative transfer in a dusty medium resides in the estimation of the dust temperature. As explained in section 1.1.3, a large part of the dust emission originates from its thermal emission. However, the dust temperature is influenced by the surrounding radiation field which means that it is both heated by the incoming radiation but also from the radiation heat emitted by the nearby grains. In order to correctly compute the resulting emission, `RADMC-3D` goes through two main steps: it starts by computing the dust temperature when heated by a given radiation field; then it computes the radiative transfer equation of the system. For each step, the code uses a Monte Carlo simulation, dividing the stellar irradiation in photon packages treated as actual photons.

---

[3] `https://www.ita.uni-heidelberg.de/~dullemond/software/radmc-3d/`

`RADMC-3D` does not have pre-built models: it relies entirely on input files and computes the Monte Carlo simulations depending on them. This means that the user has to provide their own grid and physical set-up as well as the physical properties of the grains, in particular their shape and opacities. While the grid and protoplanetary disc model set-ups are described in the corresponding Chapter, another tool called `OpTool` is used to derive the properties of the grains.

2.3.2 Opacities with `OpTool`

The optical properties of dust grains depend on their shape and composition. `OpTool`[4], developed by Dominik et al. (2021), derives the total mass-weighted opacity of the grains needed in the radiative transfer equation (see eq. 1.25), for a given set of wavelengths and for grains of a given size and composition. It uses Mie theory calculations and the optical properties of grains derived from laboratory experiments (mostly from the Jena Database of Optical Constants[5] and Aerosol Refractive Index Archive[6]). For simplicity, only spherical grains are considered in this thesis. Note that `OpTool` produces opacity files directly compatible with `RADMC-3D`.

2.3.3 Radiative transfer parameters

The combination of `RADMC-3D` and `OpTool` allows us to determine the dust emission from our modeled protoplanetary discs. Just as for the other two numerical tools, the input parameters needed for the radiative transfer calculations are summarized in table 2.3.

Table 2.3: Global radiative transfer parameters.

Physical set-up	
Dust density	ρ_d
Grid specifications	$[\vec{r}, \vec{\phi}, \vec{\theta}]$
Star characteristics	$[R_*, M_*, (r_*, \phi_*, \theta_*)]$
Wavelength grid	$[\lambda_{min}, \lambda_{max}]$
Number of photons packages	$N_{phot}, N_{phot,scat}$
Opacities parameters	
Dust size range	$[a_{min}, a_{max}]$
Composition	Elements mass fractions
Wavelength grid	$[\lambda_{min}, \lambda_{max}]$
Emission image parameters	
Observed emission wavelength	λ_{obs}
Position of the observer	$[\phi_{obs}, i_{obs}]$
Image size	$N_x \times N_y$ pixels

---

[4] https://github.com/cdominik/optool

[5] https://www.astro.uni-jena.de/Laboratory/Database/databases.html

[6] http://eodg.atm.ox.ac.uk/ARIA/

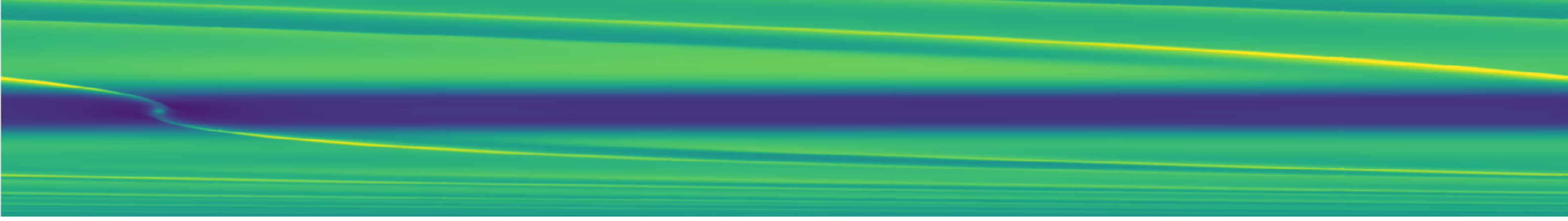

3

Single accreting planet: How is gas accretion impacting the gap depth ?

This chapter is based on the paper published in Astronomy and Astrophysics in November 2020, titled *Influence of planetary gas accretion on the shape and depth of gaps in protoplanetary discs* (Bergez-Casalou, Bitsch, Pierens, Crida, & Raymond, 2020). The published paper has been reformatted to match the structure of this thesis. The contribution to this paper was distributed as followed: I performed the hydrodynamical simulations with the help of Aurélien Crida regarding the structure of the code; the analysis was conducted by myself, Bertram Bitsch and Arnaud Pierens regarding the gas behavior and Sean Raymond helped me confirm the analysis of the migration maps. Finally, I wrote the text myself with suggestions from all coauthors.

Abstract

It is widely known that giant planets have the capacity to open deep gaps in their natal gaseous protoplanetary discs. It is unclear, however, how gas accretion onto growing planets influences the shape and depth of their growing gaps. We performed isothermal hydrodynamical simulations with the `FARGO-2D1D` code, which assumes planets accreting gas within full discs that range from 0.1 to 260 AU. The gas accretion routine uses a sink cell approach, in which different accretion rates are used to cope with the broad range of gas accretion rates cited in the literature. We find that the planetary gas accretion rate increases for larger disc aspect ratios and greater viscosities. Our main results show that gas accretion has an important impact on the gap-opening mass: we find that when the disc responds slowly to a change in planetary mass (i.e., at low viscosity), the gap-opening mass scales with the planetary accretion rate, with a higher gas accretion rate resulting in a larger gap-opening mass. On the other hand, if the disc response time is short (i.e., at high viscosity), then gas accretion helps the planet carve a deep gap. As a consequence, higher planetary gas accretion rates result in smaller gap-opening masses. Our results have important implications for the derivation of planet masses from disc observations: depending on the planetary gas accretion rate, the derived masses from ALMA observations might be off by up to a factor of two. We discuss the consequences of the change in the gap-opening mass on the evolution of planetary systems based on the example of the grand tack scenario. Planetary gas accretion also impacts stellar gas accretion, where the influence is minimal due to the presence of a gas-accreting planet.

3.1 Motivations

Recent ALMA observations have revealed protoplanetary discs with many diverse features in the gas (Teague et al., 2018; Pinte et al., 2020) or in the dust (Andrews et al., 2018). An important question considers whether these features can be explained by the presence of planets. Recent exoplanet statistics show that most stars host planets around them (Mayor et al., 2011; Howard et al., 2012; Suzuki et al., 2016; Mulders et al., 2018), but it can be difficult to observe them directly as they might be extinct in the disc itself (Sanchis et al., 2020). A viable recourse is to rely on the impact of the presence of these planets on the disc. A number of studies have shown that planets are capable of producing the features observed in these discs (Pinilla et al., 2012). For example, Zhang et al. (2018) shows that the gaps and rings seen in the DSHARP survey could be explained by the presence of gap-opening planets in the disc.

The formation of gaps by giant planets in protoplanetary discs in the dust (Paardekooper & Mellema, 2006) and in the gas (Lin & Papaloizou, 1986; Crida et al., 2006; Fung et al., 2014; Kanagawa et al., 2015) has been studied in the past via hydrodynamical simulations. Different criteria for the gap-opening mass (i.e., planetary mass needed to open a gap of a given depth) have been derived as a function of disc parameters. The main motivation for these studies has, in fact, been the migration of the giant planets that have the capacity to open these deep gaps. However, it is only recently that these migration studies have started to factor in planetary gas accretion (Dürmann & Kley, 2015; Crida & Bitsch, 2017; Robert et al., 2018).

Gas accretion is a complicated problem that requires 3D high resolution hydrodynamical simulations. The core accretion model (Pollack et al., 1996) suggests that after forming a solid core, a gaseous envelope is slowly accreted until the planet reaches a critical mass where the mass of the gas envelope is equal to the mass of the core. The planet then enters a runaway growth phase of gas accretion during which we can assume that only gas is accreted (Hubickyj et al., 2005; Lissauer et al., 2009). Previous studies have described how gas accretion can be modeled in different frameworks: in 2D with and without migration (Crida & Bitsch, 2017; Kley, 1999) or in 3D (Ayliffe & Bate, 2009; Machida et al., 2010; D'Angelo & Bodenheimer, 2013; Lambrechts et al., 2019; Schulik et al., 2019). These complex hydrodynamical simulations are needed to understand each phase of gas accretion. Due to their high computational cost, they are often integrated over short timescales. In fact, a lot of these recent simulations can only cover 100 planetary orbits (or less), making it impossible to study the long-term evolution of these systems within the 3D high resolution framework with the current computing systems.

As gas accretion requires a computationally expensive resolution, previous studies on gap-opening by giant planets neglected planetary gas accretion. Our goal in this study is to apply established gas accretion rates (Kley, 1999; Machida et al., 2010) in a 2D isothermal disc framework to study the long-term behavior of the growth of the planet and its influence on the shape and depth of the created gap.

This Chapter is structured as follows: the numerical set-up is described in Sect. 3.2; in Sect. 3.3, we study the difference between an accreting planet and non-accreting planets, the impact that different accretion rate can have on the gap shape and on the accretion onto the star. Different disc parameters are explored in Sect. 3.4, as well as the impact of gas accretion on the gap-opening mass and migration of other planets that could form in these discs. We summarize our findings with discussing the consequences for observation and planetary system structures in Sect. 3.5 and present our conclusions in Sect. 3.6.

3.2 Numerical setup

In this Chapter, we simulate an accreting planet on a fixed circular orbit embedded in a viscous disc with `FARGO-2D1D` (Crida et al., 2007). A detailed description of the code can be found in Sect. 2.1.

Here, the 1D inner disc spans from 0.1 AU to 0.78 AU. The 2D grid then ranges from 0.78 AU to 23.4 AU, with a 1D outer disc from 23.4 AU to 260 AU. The resulting 2D-1D grids are shown in Fig. 3.1: the dashed black lines represent the 2D-1D interfaces. For better readability the radial dimension is on a logarithmic scale. The color scale shows the perturbed surface density of the gas compared to the initial profile. The planet, sitting at 5.2 AU is far enough from the 2D-1D interfaces so the disc can be considered axisymmetric after 23.4 AU.

The resolution is such that there are five cells per Hill radius (eq. 1.27) of the planet at t=0, which leads to $N_{r,2D} = 802$ and $N_{\phi,2D} = 1158$ ($dr/r_0 \simeq d\phi \simeq 0.005$). Considering that the resolution is fixed in time, the Hill sphere region will become more and more resolved as the planet grows ($r_H \propto m_p^{1/3}$).

The disc has a constant aspect ratio $h = H/r$. We investigate three different values for this ratio in Sect. 3.4.1: $h = 0.03$, 0.05 and 0.07. The density profile is defined by $\Sigma(r) = \Sigma_0 \times (r/r_0)^{-1}$, where $\Sigma_0 = 3.10^{-4} = 93.6$ g/cm^2 at r_0. Its value is chosen such that the total mass of the disc is $0.1 M_*$, corresponding to a heavy disc with a large radius (Baillié et al., 2019). This large radial extent allows us to neglect self-gravity. The disc is subject to an α-viscosity as described by Shakura & Sunyaev (1973). We investigate the influence of the viscosity in Sect. 3.4.2 by taking different values for $\alpha = 2 \times 10^{-2}$, 10^{-2}, 10^{-3}, and 10^{-4}. Our fiducial setup is shown in bold in table 3.1, where we summarize the parameters of the different simulations investigated in this Chapter.

The accreting planet starts with a mass of $m_p = 20\ M_\oplus$ or $m_p = 10\ M_\oplus$, depending on the aspect ratio (see Sect. 3.4.1). With this initial mass, the planet is assumed to be directly in the runaway gas accretion regime (Pollack et al., 1996). The accreting planet is introduced into the disc with a mass-taper function (see eq. 2.3), making the planet grow from 0 to its initial mass in $n_{orb} = 3$ orbits.

In order to let the disc adapt to the planet, we wait until the initial mass creates a steady gap. We define the equilibrium by a change of gap depth of less than 1% within 100

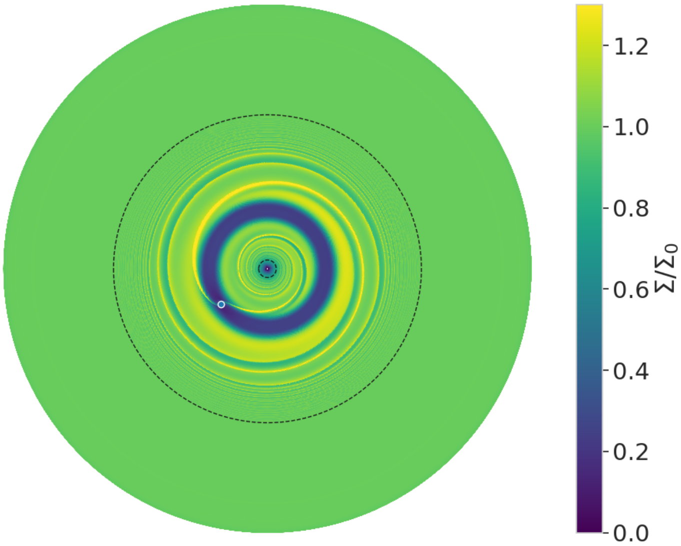

Figure 3.1: Grid configuration in `FARGO-2D1D`. The 1D-grid ranges from 0.02 to 50.0 and the 2D grid from 0.15 to 4.5 in code units. For better readability, the radial dimension is shown on a logarithmic scale. The color scale shows the perturbed surface density of the disc, normalized to the initial disc profile. The planet, represented by the blue dot and located at $r_p = 1 = 5.2$ AU, is considered far enough from the boundaries of the 2D-grid for the disc to be considered axisymmetric.

Table 3.1: Gas disc parameters.

Gas parameters	
Aspect ratio value at r_0	$h_0 = 0.03$, $\mathbf{0.05}$, 0.07
Aspect ratio flaring index	0
Alpha viscosity	$\alpha = 10^{-4}$, 10^{-3}, $\mathbf{10^{-2}}$, 2×10^{-2}
Surface density value at r_0	$\Sigma_0 = 3.10^{-4} = 93.6$ g/cm^2
Surface density slope profile	$p = 1$
Planet parameters	
Planet initial mass	$m_p = 10$ M$_\oplus$, $\mathbf{20}$ $\mathbf{M_\oplus}$
Planet initial position	$r_p = 1 = 5.2$ AU
Accretion time	$t_{start,acc}(\alpha, h)$ (see table 3.2)
Planet migration	NO
Planet interactions	NO
Planet mass taper	$n_{orb} = 3$
Planet eccentricity	0
Grids parameters	
Radial extent of 1D grid	[0.1 AU, 260 AU]
1D radial resolution	$N_{rad,1D} = 9214$
Radial extent of 2D grid	[0.78 AU, 23.4 AU]
2D radial resolution	$N_{rad,2D} = 802$
2D azimuthal resolution	$N_{\phi,2D} = 1158$

orbits. The times needed to reach the steady state and steady gap depth are summarized in table 3.2 as a function of the disc parameters. In principle, the introduction of the planet in the simulation can change the resulting structure of the disc depending on the length of the ramp-up time (Hammer et al., 2017). However, this applies mostly for giant planets and low viscosities. For our initially small planets, we found no significant difference if we let gas accretion onto the planet start after a longer wait time.

3.3 Influence of gas accretion

In this section, we first investigate the difference in gap shape between accreting and non-accreting planets. Then we focus on the influence of different gas accretion rates to explore the variety of gas accretion rates found in the literature. We conclude this section by studying the influence of planetary accretion on stellar accretion.

3.3.1 Accretion versus non-accretion

In this section, we investigate the effect of gas accretion on the gap shape and the pressure bumps generated by the planet exterior to its orbit. We compare three different simulations: (i) a planet accreting gas following the recipe presented in Sect. 2.1.2, where the mass is removed from the disc and added to the planet (solid gray line in the following plots); (ii) a mass-tapered planet where the mass of the planet is changed via the mass-taper function given by eq. 2.3 and no mass is removed from the disc (dashed blue line); and (iii) a planet with its mass fixed to the value where the comparison is made (dotted dashed red line). Each simulation is compared at the moment when the planets reach

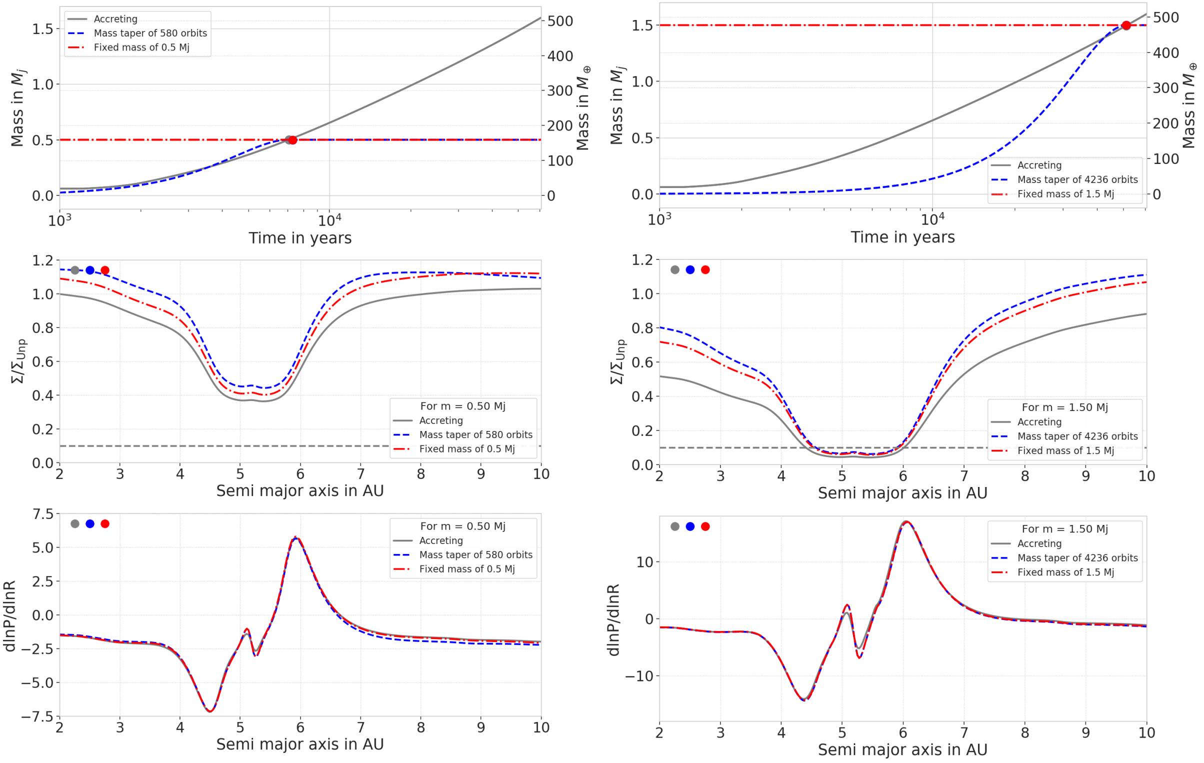

Figure 3.2: Influence of gas accretion on the gap shape for a planet of m = 0.5 M_J, below the nominal gap-opening mass (left column), and of m = 1.5 M_J, above the nominal gap-opening mass (right column) for $h = 0.05$ and $\alpha = 10^{-2}$. *Top row:* Time evolution of the planetary mass in the three different cases: accreting planet (solid gray), mass-tapered planet (dashed blue), and fixed planet mass (dashed red). Mass is removed from the disc only for the accreting example. We plot the mass evolutions after gas accretion is allowed (after t = 100 planetary orbits $\simeq 1.2 \times 10^3$ yrs) *Middle row:* Perturbed surface density at the time when masses reached the comparison masses (dots in the top panel). The horizontal gray dashed line marks the gap-opening criterion defined by Crida et al. (2006). An accreting planet creates a deeper gap than a non-accreting one. *Bottom row:* Pressure gradient in the three different cases. Similar pressure gradients imply that gas accretion does not have a major influence on the pressure structure in the protoplanetary disc. This implies that particles are trapped at a similar position and we cannot distinguish between accreting and non-accreting planets via the shape of dust traps in this case.

the same mass $m_{\rm comp}$. For the mass-tapered planet, n_{orb} is chosen so that the planet grows from 0 to $m_{\rm comp}$ over the same number of orbits that the accreting planet needs to reach this mass. We chose to make the comparison before and after reaching the gap-opening mass for $\alpha = 10^{-2}$ and $h = 0.05$, where the gap-opening mass is the mass needed to open a gap of a depth of $\Sigma/\Sigma_{\rm unp} = 0.1$, as in Crida et al. (2006). We compare the structure of the disc for planets of masses equal to 0.5 M_J (left column of Fig. 3.2) and 1.5 M_J (right column of Fig. 3.2). Within these parameters, n_{orb} is equal to 580 orbits for $m_{\rm comp} = 0.5\ M_J$ and to 4236 orbits for $m_{\rm comp} = 1.5\ M_J$.

On the top left panel of Fig. 3.2, we show the time evolution of the planetary masses in the three different cases for $m_p = 0.5\ M_J$. The mass evolution of the planet growing via the mass taper is very similar to that of the accreting planet. The dots show the mass and time given for the comparison. In the second left panel, we show the gap profiles at the time when the accreting planet reaches 0.5 M_J (marked by the dots in Fig. 3.2).

The surface density profile has been normalized to the surface density of a disc without a planet at the same time (Σ_{unp}) in order to get rid of the effect of natural viscous evolution of the disc. Our simulations show that the accreting planet generates a slightly deeper gap than the planet with a fixed mass, which is in line with the results of Dürmann & Kley (2015).

To create a gap, a planet needs to have a strong enough gravitational torque to overcome the pressure torque and viscous spreading that tend to close the gap (Crida et al., 2006). The accreting planet presents a deeper gap as material is removed from the disc as compared to the other two simulations. The difference in surface density at the bottom of the gap is very similar to the difference in surface density in the inner disc due to the fact that mass is removed partially from the inner disc. This will impact the stellar accretion, as we discuss in Sect. 3.3.3. For these disc parameters ($\alpha = 10^{-2},\ h = 0.05$), Dürmann & Kley (2015) found the same behavior (their Fig. 2). Therefore, relative to the edges of the gap, the gaps have similar depths, but when compared to a disc without a planet, the accreting planet produces a deeper gap, as the non-accreting planets only push material away from their orbit, enhancing the surface density in the inner disc while the accreting planet is removing material. On the other hand, the fixed mass planet is opening a deeper gap than the mass-tapered planet, because the fixed-mass planet exerts a stronger torque on the disc material due to its larger mass up until the time of comparison. At later time, when the mass taper fixes the mass of the planet to 0.5 M_J and the disc has time to adjust to this planetary mass, the shape of the gaps of the fixed-mass and mass-tapered planets is the same.

At later time, when the planet becomes heavier ($m_p = 1.5\ M_J$), we can also see on the middle right panel of Fig. 3.2 that the inner disc is more depleted for the accreting planet. Gas accretion plays, therefore, an important role in the depletion of the inner disc. One of the consequences of this behavior is discussed in Sect. 3.3.3. The gap depth is only slightly influenced by gas accretion in this case.

The difference in the gap depth can lead to a difference in the torques acting on the planet and, thus, impacting its migration behavior. Kanagawa et al. (2018) found that when the planet creates a deep-enough gap ($\Sigma_{\mathrm{min}}/\Sigma_{\mathrm{unp}} < 0.6$), then the total torque felt by the planet is proportional to the gap depth. Thus, the difference in gap depth between the accreting and the planet with fixed mass should lead to an equivalent difference in total torque. The difference in gap depth for $m_p = 0.5\ M_J$ is of about 24% while the difference in the total torques measured in our simulations is $\sim$ 17%. Using the approach by Kanagawa et al. (2018) regarding the migration behavior and comparing it to our simulations indicate a deviation of 25% between the torques actually measured and the difference that should occur because of the difference in gap depth. This deviation might lie within the errorbars of the fit derived by Kanagawa et al. (2018). On the other hand, for the more massive case plotted in Fig. 3.2, the difference in gap depth is 38% and the difference in the total measured torques is $\sim$ 37%. Here, the differences match and our simulations confirm the results from Kanagawa et al. (2018). Additional simulations with 1 M_J planets confirm this trend. Therefore, the differences in torques between an accreting planet and a planet with fixed mass can be explained by their difference in gap depth, as long as the gap is deep enough.

The difference in gap depth and shape will have an influence on the drift of dust particles in the disc. Observations (Teague et al., 2018; Andrews et al., 2018) often show rings and gaps in the dust profile of discs, which could be explained by the presence of planets (Pinilla et al., 2012; Zhang et al., 2018) that generate pressure bumps exterior to their orbits where dust can accumulate (Paardekooper & Mellema, 2006). We show in the lower panels of Fig. 3.2 the pressure gradients obtained in the three different cases. As expected from the surface density profiles, the pressure gradients are too similar to display the differences seen through observation.

In the following sections, we investigate different levels of gas accretion strength and other disc parameters that influence the depth and shape of gaps.

3.3.2 Influence of different gas accretion rates

As discussed in Sect.1.2.1, gas accretion rates onto planets are not very precisely constrained. In the runaway gas-accretion phase, rates range from $\dot{M}_p \simeq 10^{-7}\ M_J/yr \simeq 3 \times 10^{-5}\ M_\oplus/yr$ to $\dot{M}_p \simeq 10^{-4}\ M_J/yr \simeq 3 \times 10^{-2}\ M_\oplus/yr$ (D'Angelo et al., 2003; Ayliffe & Bate, 2009; Machida et al., 2010; Schulik et al., 2019). Recent studies claim that the accretion rates could be even smaller; Lambrechts et al. (2019) found that the mass flux through the envelope is different from the gas accretion rate, therefore, even if the mass flux is on the order of $10^{-5}\ M_J/yr$, the gas accretion rate is actually 10 to 100 times smaller. Tanigawa & Tanaka (2016) derived an even smaller accretion rate when accounting for the gap-opening ($\dot{M}_p \simeq 10^{-8}\ M_J/yr \simeq 3 \times 10^{-6}\ M_\oplus/yr$). In order to reflect this discrepancy, we investigate different accretion rates in this subsection by scaling our nominal Machida accretion rates (eq. 2.4) by a factor of between 0.1 to 10.

In the top left panel of Fig. 3.3, we show the seven different accretion rates obtained when we scale the Machida accretion rate by a factor of 0.1, 0.2, 0.5, 1, 2, 5, and 10. The darker color represents a higher accretion rate. The maximum of the accretion rate is shifted to later time if the accretion rate is reduced. This maximum is reached when the accretion rate (eq. 2.4) switches from a regime dominated by the Hill sphere to a regime proportional to 0.14. The critical mass that is needed for this switch in accretion rate is reached at later times for reduced accretion rates.

As gas accretion is limited by what the disc can provide, the accretion rates in the case of an enhancement by 5 and 10 are the same at the beginning of the simulation: they start in the Kley accretion regime (eq. 2.4). Both simulations switch to the Machida accretion regime and become different after a certain time. This indicates that most of the time the planet is accreting less than what the disc can provide. The values of the accretion rates range from $\sim 6 \times 10^{-6}\ M_J/yr$ to $\sim 2 \times 10^{-4}\ M_J/yr$, corresponding to the different values reported in the literature (D'Angelo et al., 2003; Ayliffe & Bate, 2009; Machida et al., 2010; Tanigawa & Tanaka, 2016; Schulik et al., 2019; Lambrechts et al., 2019). We note, however, that the accretion rates are reduced over time, where at later stages, our measured accretion rates are below $2 \times 10^{-5}\ M_J/yr$. This indicates that the gap-opening process of planets plays a role in setting the accretion rate.

In the bottom left panel of Fig. 3.3, we show the time evolution of the planetary mass in the seven different cases. The biggest planet formed after 6×10^4 years is slightly less than 3 M_J, obviously, this is the case of the highest accretion rate. In addition to the assumptions of our simulation setup, time evolution plays a crucial role. A longer integration time would lead to a larger planetary mass. In reality, a planet would also migrate to the inner disc, where the gas surface density is larger and thus the accretion rate could be higher, even if the Hill sphere of the planet shrinks while getting closer to the central star, depending on the surface density profile slope (Crida & Bitsch, 2017).

In the panels on the right of Fig. 3.3, we show the azimuthally averaged surface density profiles. We normalized the profiles to the profile of a disc without a planet as explained

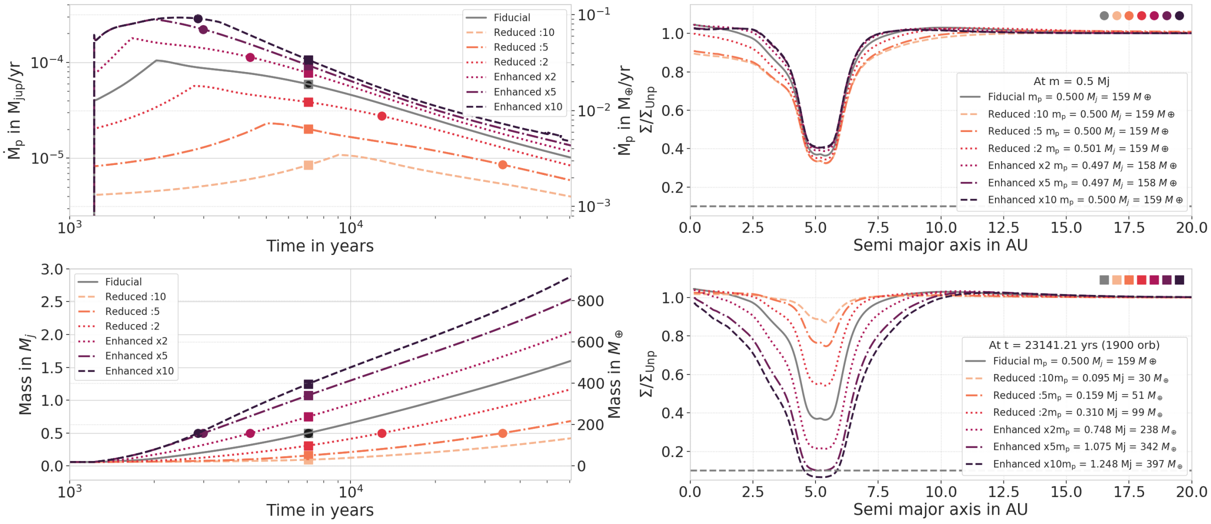

Figure 3.3: Influence of different accretion rates. *Top left:* Time evolution of the different accretion rates. The fiducial setup is represented in solid gray line. The dashed, dotted, and dotted-dashed lines represent the different accretion rates applied here, where the Machida part was divided and multiplied by 10, 5, and 2. The enhanced by 10 and 5 simulations show a similar rate at the beginning of the simulation as they are limited to the maximum accretion the disc can provide. *Bottom left:* Time evolution of the planetary mass in the seven different accretion regimes. The dots represent the time at which the mass is 0.5 M_J and the squares represent the different masses at the same time. *Top right:* Perturbed surface density at the time where m = 0.5 M_J (dots in previous panels). The surface density is normalized to a disc without a planet. *Bottom right:* Perturbed surface density at the same time t = 580 orbits (squares in previous panels). The horizontal gray dashed line marks the gap-opening criterion as defined by Crida et al. (2006): $\Sigma/\Sigma_{\text{unp}} = 0.1$.

in Sect. 3.3.1. This way we compare the actual shape of the gap. For this viscosity and aspect ratio, $\alpha = 10^{-2}$ and $h = 0.05$, gas accretion seems to have only a small effect on the gap shape, resulting in a slightly deeper gap for the most reduced accretion rate. The difference in gap depth is due to the depletion of the inner disc: for the reduced accretion rate, the planet reaches 0.5 M_J at a later time, giving time to the inner disc to be depleted via viscous spreading towards the star. We discuss this in more detail in the next section. As the gap shapes are only slightly influenced by gas accretion, one can expect the pressure bumps to be similar, which is shown in Fig. 3.4. The difference in the disc pressure profiles for planets with different accretion rates are very small, making it indistinguishable via observation, in contrast to migrating planets (Meru et al., 2019; Weber et al., 2019). However, in the next section, we investigate the influence of planetary gas accretion on another observable: gas accretion onto the star.

3.3.3 Influence on the stellar accretion rate

Gas accretion onto the star is an observable feature that can be measured via the UV excess in a star SED (Hartmann et al., 1994; Calvet & Gullbring, 1998). Here, we study the influence that a gas-accreting planet has on stellar gas accretion compared to a disc without a planet. We define the stellar gas accretion rate as the mass flux through the inner boundary of the disc: $\dot{M}_* = -2\pi\, r_{in} v_{r,in} \Sigma_{in}$, where $r_{in} = 0.2$ AU and $v_{r,in}$ and Σ_{in} are the radial velocity and surface density at r_{in}, respectively. We compare in Fig. 3.5,

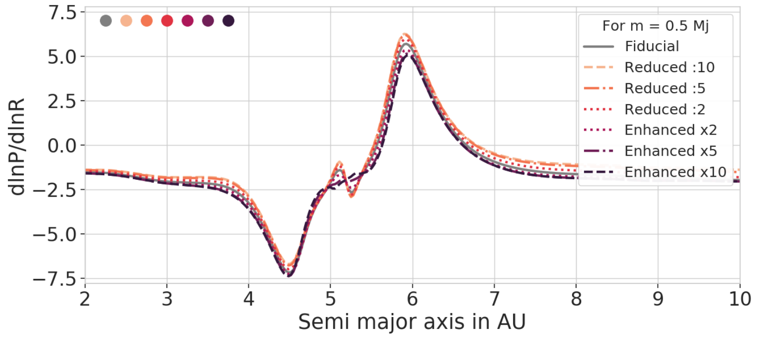

Figure 3.4: Pressure gradient in different gas accretion models for m = 0.5 M_J. Even though the different models present different inner disc structures at the same planetary mass, the difference in the pressure gradients is too small to be observationally resolved. The bump located at the planet position is due to the material around the planet location. It vanishes with higher accretion rates as the planet accretes all the material at this location.

the stellar gas accretion of a disc with an accreting planet (solid gray line), a fixed-mass planet (dotted dashed red), a mass-tapered planet (dashed blue), and a disc without a planet (bold dashed black). The two non-accreting planets have a mass of $m_p = 1.5\ M_J$, as in Fig. 3.2, leading to a mass taper of $n_{orb} = 4236$ orbits $\simeq 51600$ yrs.

At the start of the simulations, only the fixed-mass planet shows a significantly higher stellar accretion rate than the others. This is due to the fact that a massive planet of 1.5 M_J was introduced into the disc in only three orbits. Therefore, the disc is highly perturbed and the planet pushes a significant quantity of material in the inner disc. As $\dot{M}_* \propto \Sigma$, the stellar gas accretion is then enhanced. At the same time, the mass-tapered and accreting planets are slowly growing into the disc, pushing less material to the inner disc at the beginning of the simulation.

Even though Rafikov (2016) showed that spiral arms can drive accretion via depositing angular momentum, these spiral arms are too weak at this location to make a difference. They also showed that such accretion may occur at the end of the lifetime of the disc, as it corresponds to very short accretion timescales. In consequence, the stellar accretion rates for the mass-tapered planet, the fixed-mass planet, and the disc without a planet are all similar.

On the other hand, we see that after $\sim 10^4$ years, the accretion rate differs from one simulation to another. First, the fixed-mass planet shows an accretion rate that is slightly lower than the disc without a planet. Even though the gap might prevent some material from reaching the inner disc, there is still a large flow of material through the gap to keep the inner disc from becoming significantly depleted. This can be seen in the right panel of Fig. 3.2, where the surface density in the inner disc of the fixed mass case is only slightly affected by the presence of the planet. This is due to the high viscosity of this simulations ($\alpha = 10^{-2}$). Before the end of the simulation, the stellar accretion rate in the case of the mass-tapered planet becomes slightly higher than the accretion of the disc without a planet. In the top left panel of Fig. 3.2, we see that the mass taper function makes the planet grow rapidly after $\sim 10^4$ years, resulting in the same effect as for the fixed-mass planet: as the planet grows rapidly, it pushes a large quantity of material into the inner disc, enhancing the stellar accretion rate, and as the gap profile tends to reach an equilibrium at this stage, it will reach the same flow through the gap as the fixed mass planet.

On the other hand, the presence of the accreting planet decreases the stellar accretion

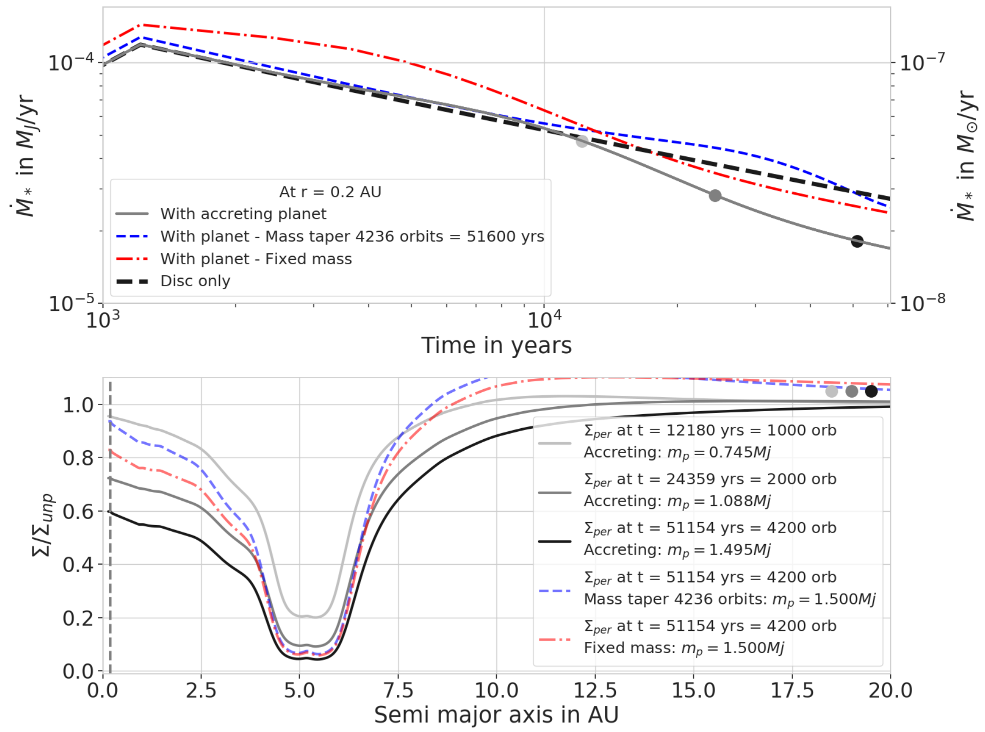

Figure 3.5: Influence of planetary gas accretion on the stellar gas accretion for our fiducial disc parameters ($h = 0.05,\ \alpha = 10^{-2}$). *Top:* Time evolution of the stellar gas accretion rates at the inner disc (0.2 AU). The different lines represent different simulations: with an accreting planet (solid gray), with a mass-tapered planet (dashed blue), with a fixed-mass planet (red dotted dashed). and without a planet (bold black dashed). We can see here that an accreting planet decreases the stellar accretion rate. *Bottom panel:* Perturbed surface density at three different times for the accreting case and after 4200 orbits in the mass tapered and fixed mass cases. The dashed vertical line is located at 0.2 AU, where we measure the stellar accretion rate. The three different times correspond to the dots in the upper panel. The time evolution of the perturbed gas surface density shows how the inner disc is slowly depleted by the viscous stellar accretion but also by the accreting planet. In comparison, the mass tapered and fixed mass cases present a less depleted inner disc, due to the absence of planetary gas accretion (see also Fig. 3.2).

rate. This is due to the fact that the planet, besides accreting material from the outer disc and therefore preventing a large amount of gas to flow through the disc, accretes gas from the inner disc as well. This helps deplete the inner disc quicker than through the viscous accretion naturally present in the disc. The depletion of the inner disc by planetary gas accretion can be seen in the lower panel of Fig. 3.5, with the surface density profiles of the accreting planet shown at different times: $\Sigma/\Sigma_{\text{unp}} < 1$, as Σ_{unp} is defined to be the surface density of the empty disc. As in Fig. 3.2 (middle row), we also see that the depletion is enhanced by the accretion onto the planet compared to the two non-accreting planets.

However, we notice that the accretion rate onto the planet can be higher than the stellar accretion rate (top panels of Figs. 3.3 and 3.6). The planet can accrete more than what the disc can supply only at the very beginning of the simulation as it is emptying its horseshoe region. Then it accretes material from the inner and outer parts of its orbit: this is where planetary accretion is limited to what the disc can provide. The reason the stellar gas accretion rate is smaller than the planetary accretion rate after a longer time is that the stellar accretion rate is measured at the inner edge of the disc (mass flux at r = 0.2 AU), whereas the planet is accreting material from the inner and the outer disc

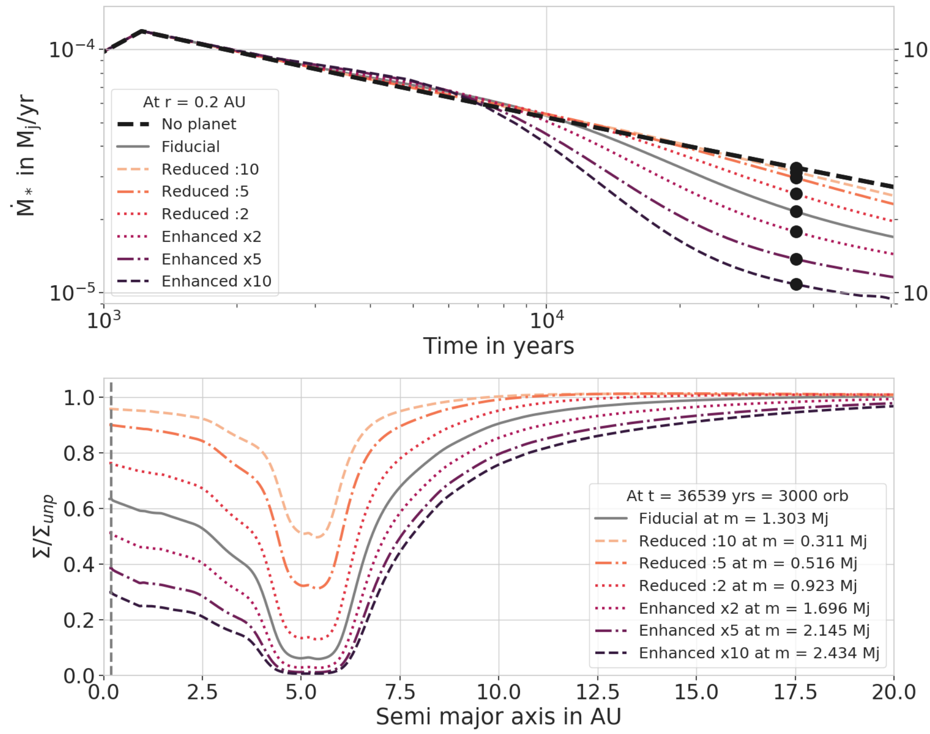

Figure 3.6: Influence of different planetary gas accretion rates on the stellar gas accretion for the fiducial disc parameters ($h = 0.05$, $\alpha = 10^{-2}$). *Top:* Time evolution of the accretion rates onto the star at the inner disc (0.2 AU) for eight different cases: the seven different planetary accretions rates (enhanced, fiducial, and reduced) and a disc without a planet (bold black dashed line). A more efficiently accreting planet decreases the stellar accretion rate more efficiently. This is due to the depletion of the inner disc induced by the planetary accretion. The black dots mark the time at which the surface density profiles are plotted. *Bottom panel:* Perturbed surface density at time t = 3000 orbits = 36 539 years for the seven different cases. The vertical gray dashed line lies at 0.2 AU which is the location of the inner disc, where the stellar accretion is measured.

(inside and outside r = 5.2 AU). We compared the stellar flux at a radius located beside the planet (i.e., at 7.5 AU while the planets is located at 5.2 AU) and we observed that the planet's accretion rate becomes limited by the mass flux at this location after a certain time: the time needed to empty its horseshoe region and a large part of the inner disc. In conclusion, planetary accretion is limited to what the outer disc can provide as the inner disc is depleted by the planet and the viscous accretion towards the star.

To investigate the influence of planetary gas accretion into the depletion of the inner disc, we show in Fig. 3.6, the stellar accretion rate for all our enhanced and reduced planetary accretion rates. The top panel shows that larger planetary accretion rates result in lower stellar accretion rates. As the planet accretes more gas, it depletes the inner disc faster, reducing the stellar accretion rate. At $t = 36500\ yrs = 3000$ orbits, the time shown with the black dots on the top panel, the lowest stellar accretion rate is roughly three times lower than the highest rate. However, the corresponding planetary accretion rates differ by a factor of four (Fig. 3.3). This means that the stellar accretion does not directly scale with the planetary accretion. This is due to the fact that the depletion of the inner disc also highly depends on the viscosity of the disc. Here, the viscosity is high: with $\alpha = 10^{-2}$, planetary gas accretion and viscous spreading through the gap act together to deplete the inner disc. Therefore, if the planetary gas accretion rate is not high enough, then the inner disc is replenished by viscously spreading gas, whereas when the planetary accretion rate is high, the inner disc does not have time to be replenished by viscous spreading. In Sect. 3.4.2, we study the influence of the viscosity on the stellar accretion and discuss its consequences in Sect. 3.5.1.

In conclusion, at high viscosity, the planetary gas accretion rate has a strong influence on stellar accretion. In the following section, we investigate the influence of two disc parameters: the aspect ratio and the viscosity, which can have an influence on the accretion onto the planet and onto the star.

3.4 Influence of disc parameters

Disc parameters have a strong impact on how a planet carves a gap (Lin & Papaloizou, 1986; Crida et al., 2006; Fung et al., 2014; Kanagawa et al., 2015). Therefore, we can expect them to have a strong influence on gas accretion as well. Here, we study the influence of the aspect ratio and the viscosity on the planetary gas accretion rate before studying the influence on the gap-opening mass. Finally, as migration depends on the disc parameters too, we investigate how planetary gas accretion can alter the migration of outer planets in the disc by studying migration maps.

3.4.1 Different aspect ratios

The aspect ratio of the disc impacts accretion in two ways. The first is related to gas accretion (eq. 2.4), which is, to some extent, proportional to $(r_H/H)^{9/2}$. At the beginning of the simulation, the planet remains in this regime until the Hill sphere reaches 2/3 of the disc scale height and then switches to the regime where $\dot{M} \propto 0.14$. In Machida et al. (2010), the different regimes are explained by the switch from a regime regulated by Bondi accretion to a regime governed by Hill accretion. This switch is visible in our work in the time evolution of the gas accretion rates in Figs. 3.3, 3.5, 3.7, and 3.8. The aspect ratio has a direct influence on the mass at which the switch occurs. In panels on the left of Fig. 3.7, we show the resulting planetary accretion rates for different aspect ratios, with $h = 0.03, 0.05$ and 0.07. As the aspect ratio increases, the switch occurs at higher masses and therefore at later time. For $h = 0.03$, the simulation directly starts in the regime $\propto 0.14$ (eq. 2.4) as the mass at which $r_H \simeq 2H/3$ is smaller than our initial mass of 20 $M_\oplus$ ($m_{switch} = 7.8\ M_\oplus$).

We show in the lower right panel of Fig. 3.7, the perturbed gas surface density profiles for the different aspect ratios and compare accreting planets with planets that have a fixed planetary mass of 0.5 M_J. Gas accretion has a different impact on the gas surface density profile depending on the aspect ratio. For $h = 0.07$, the gap is deeper with accretion than without accretion. For $h = 0.05$, we find back the same result from Sect. 3.3.1, where gas accretion has only a slight impact on the gap depth. Finally, for $h = 0.03$, the planet has reached its gap-opening mass, which shows a similar-looking for both the accreting and non-accreting cases. Comparing a planet with a fixed mass of 0.2 M_J for $h = 0.03$ (below the gap opening mass defined by Crida et al. 2006) with an accreting planet of the same mass (not shown) reveals a deeper gap in the case of the fixed mass planet. Our results show three different behaviors depending on the aspect ratio: 1) gas accretion helps creating a deeper gap (large h); 2) it has almost no impact ($h = 0.05$); or 3) it prevents the creation of a deeper gap (low h). These three behaviors are explained

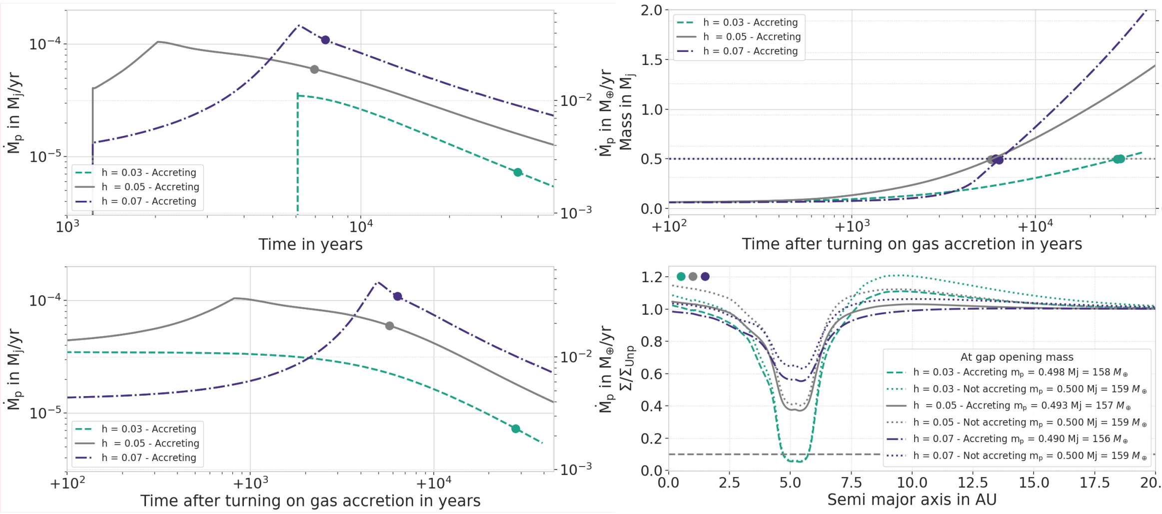

Figure 3.7: Influence of different aspect ratios with $\alpha = 10^{-2}$ and $m_{\rm init} = 20\ M_\oplus$. *Top left:* Time evolution of the planetary accretion rate. The flip in the accretion rate occurs at different moment (i.e., different planet mass) due to the dependence on h of the Machida accretion rate (eq. 2.4). As the time needed for the initial mass to reach an equilibrium is higher for lower aspect ratios, gas accretion starts later for $h = 0.03$ (see table 3.2). *Bottom left:* Evolution of the accretion rates as a function of the time after gas accretion is turned on. *Top right:* Time evolution of the planetary mass. Lower aspect ratios result in more massive planets. *Bottom right:* Perturbed surface density at the time where $m_p = 0.5\ M_J$ (dots on previous panels). The two effects added up here make the gap shapes really different, namely, the influence of the aspect ratio on the shape of the gap and the time at which the planet reaches $0.5\ M_J$. We compare the gap shapes of accreting planets with gaps created by fixed mass planets: depending on the aspect ratio, gas accretion has a different influence. The horizontal gray dashed line marks the gap-opening criterion as defined by Crida et al. (2006).

in Sect. 3.4.3, where we explore the impact of gas accretion on the gap-opening mass. In the case of a low aspect ratio, one should note that a 20 $M_\oplus$ mass planet already creates a deep gap at low viscosities. We chose to keep this initial mass in this section in order to compare it with the higher aspect ratios as the comparison is made at high viscosity. However, we reduce the initial mass down to 10 $M_\oplus$ in Sect. 3.4.3 to study the impact on the gap-opening mass as a function of the disc parameters.

As the accretion rates are very different from one aspect ratio to the other, the planet masses are diverse as well. The top right panel of Fig. 3.7 shows that a later switch in accretion rates results in more massive planets. As a result, our simulations indicate that planetary gas accretion is more efficient in hotter discs. As it is harder to create a deep gap in hotter discs, the surface density at the location of the planet is larger (lower panel of figure 3.7) and allows for a more efficient planetary gas accretion. On the other hand, if the disc is hotter, it is harder for a planet to reach the pebble isolation mass (Lambrechts et al., 2014; Bitsch et al., 2018; Ataiee et al., 2018), where the planet generates a small pressure bump exterior to its orbit preventing solid accretion. In addition, if the disc is hotter, it is more difficult to accrete pebbles efficiently because they are less concentrated in the disc's midplane (Youdin & Lithwick, 2007), resulting in a less efficient formation of planetary cores (Ndugu et al., 2018). Therefore, it is easier to form giant planets via runaway gas accretion when their core is already formed but it is harder to initially form these cores in hotter discs.

Parameters	α	$\Sigma/\Sigma_{\mathrm{unp}}$	$t_{\mathrm{gap,init}}$ in orbits
$h = 0.03$ $m_{\mathrm{init}} = 20\ M_\oplus$	10^{-2}	0.7414	500
$h = 0.05$ $m_{\mathrm{init}} = 20\ M_\oplus$	2×10^{-2}	0.9823	100
	10^{-2}	0.9678	100
	10^{-3}	0.7317	900
	10^{-4}	0.2949	3300
$h = 0.07$ $m_{\mathrm{init}} = 20\ M_\oplus$	10^{-2}	0.9953	100
	5×10^{-3}	0.9923	100
	10^{-3}	0.9644	300
	10^{-4}	0.7795	1700
$h = 0.03$ $m_{\mathrm{init}} = 10\ M_\oplus$	10^{-2}	0.8912	300
	10^{-3}	0.4859	1300
	5×10^{-4}	0.3408	1900

Table 3.2: Depth of the initial gap and time needed to reach the equilibrium as a function of the disc parameters. Lower viscosities ($\nu = \alpha h R c_s$) imply deeper initial gap and larger gap opening times. For $h = 0.03$, we used two different initial masses: $m_{\mathrm{init}} = 20\ M_\oplus$ in Sect. 3.4.1 to compare with higher aspect ratios but $m_{\mathrm{init}} = 10\ M_\oplus$ in Sect. 3.4.3 as a $20 M_\oplus$ already opens a deep gap at low viscosities.

3.4.2 Different viscosities

Another important disc parameter is the viscosity of the disc, which determines how a planet opens a gap (Crida et al., 2006; Fung et al., 2014; Kanagawa et al., 2015) and dictates how gas flows in the vicinity of the planet. Both have a strong impact on gas accretion. In order to determine the influence of viscosity, we run five different simulations with the following alpha parameters: $\alpha = 2 \times 10^{-2}$, 10^{-2}, 10^{-3} and 10^{-4} (table 3.1). As mentioned in Sect. 3.2, we need to wait until the initial mass of 20 $M_\oplus$ creates a steady gap, defined as a change of less than 1% of the gap depth within 100 planetary orbits. This waiting time is dependent on the disc parameters and is summarized in Table 3.2.

We can expect the planetary accretion rate to decrease with decreasing viscosity because viscosity dictates how fast gas removed by accretion can be replenished from the viscously spreading disc. This behavior can be seen on the top panels of Fig 3.8: in the first panel, the gas accretion rates are plotted as a function of time. We can see that at lower viscosities, the initial mass needs a longer time to reach a steady gap. This means that at lower viscosity, gas accretion starts later. In the second panel the accretion rates are shifted so that they are plotted as a function of the time after gas accretion is turned on. The accretion rates plotted here show that a lower viscosity results in a lower planetary accretion rate.

At low viscosity, instabilities in the disc are generated (Klahr & Bodenheimer, 2003; Fu et al., 2014), resulting in a threshold value for the gas surface density in the vicinity of the planet. If this threshold exists, we would expect a limit of the planetary accretion rate as well. However, in order to resolve these instabilities adequately, high-resolution simulations are needed, which are computationally very expensive. Thus we limit our study to $\alpha \geq 10^{-4}$.

For $\alpha \lesssim 10^{-4}$, Rossby wave instability is triggered (Lovelace et al., 1999; Li et al., 2001). This instability generates vortices at the location of steep density gradients. Such steep gradients are induced by planetary gaps formed at low viscosity (Hammer et al.,

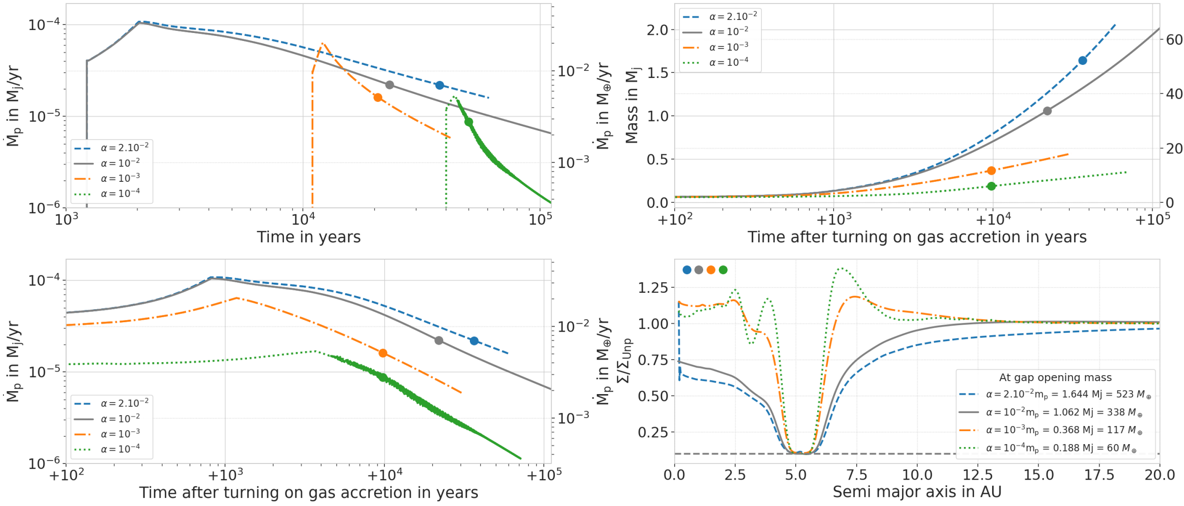

Figure 3.8: Influence of different viscosities for $h = 0.05$. *Top left:* Time evolution of the accretion rate onto the planet. As the time needed for the initial mass to reach an equilibrium is highly dependent on the viscosity, gas accretion starts later for lower viscosities. *Bottom left:* Evolution of the accretion rates as a function of the time after gas accretion is turned on. As the viscosity is lowered, the Rossby Wave Instability is triggered: for $\alpha \lesssim 10^{-4}$, vortices are formed and influence the planetary gas accretion rates, explaining the oscillations in the accretion rate curves. *Top right:* Evolution of the planetary mass as a function of the time after gas accretion is turned on. The dots represent the time at which the gap-opening mass is reached. *Bottom right:* Perturbed surface density at the time where gap-opening mass is reached (dot on the other panels). The gap-opening mass is defined by the mass needed to reach $\Sigma/\Sigma_{\rm unp} = 0.1$ (Crida et al., 2006). It is represented here by the horizontal gray dashed line.

2017; Pierens et al., 2019), as we can see on the radial density profiles in the lower panel of Fig. 3.8. Vortices will modify the flow of material into the gap, changing the amount of gas available for accretion by the planet. Such impact can be seen in the accretion rates. In the top panel of Fig. 3.8, for $\alpha = 10^{-4}$, the accretion rate is oscillating due to the presence of a vortex at the outer edge of the gap. We show in Fig. 3.9, the 2D (r, ϕ) surface densities at three different times. The fiducial case is plotted in the middle row. The asymmetrical overdensity (in yellow) located at the outer edge of the gap is characteristic of the presence of the vortex. At later times, the vortex vanishes. In the fiducial case, it completely vanishes after $t \gtrsim 8.1 \times 10^4$ years, inhibiting the oscillations in the accretion rate (top panel of Fig. 3.8).

As the presence of vortices is linked to the steepness of the density gradient, the characteristics of the created vortices depend on how fast the planet grows and creates its gap. Hammer et al. (2017) find that a slowly growing planet will create a weak vortex at the outer edge of the planet gap. We find a similar result when we apply our different accretion rates to simulations with $\alpha = 10^{-4}$. In Fig. 3.9 we show the 2D surface density snapshots for three different accretion rates (from top to bottom: reduced by 10, fiducial, and enhanced by 10) at three different times. The overdensity characteristic of the vortex evolves differently whether the planet is accreting quickly or not. We can see that the created vortex at the outer edge of the gap is stronger when the planet features a higher gas accretion rate. As stated previously, we expect to see oscillations in the gas accretion rate, with higher oscillations for the enhanced case as the vortex that is created is stronger.

In the top panel of Fig. 3.10, we show the planetary accretion rates reached with the enhanced and reduced accretion rates presented in Sect. 3.3.2 for $\alpha = 10^{-4}$. As

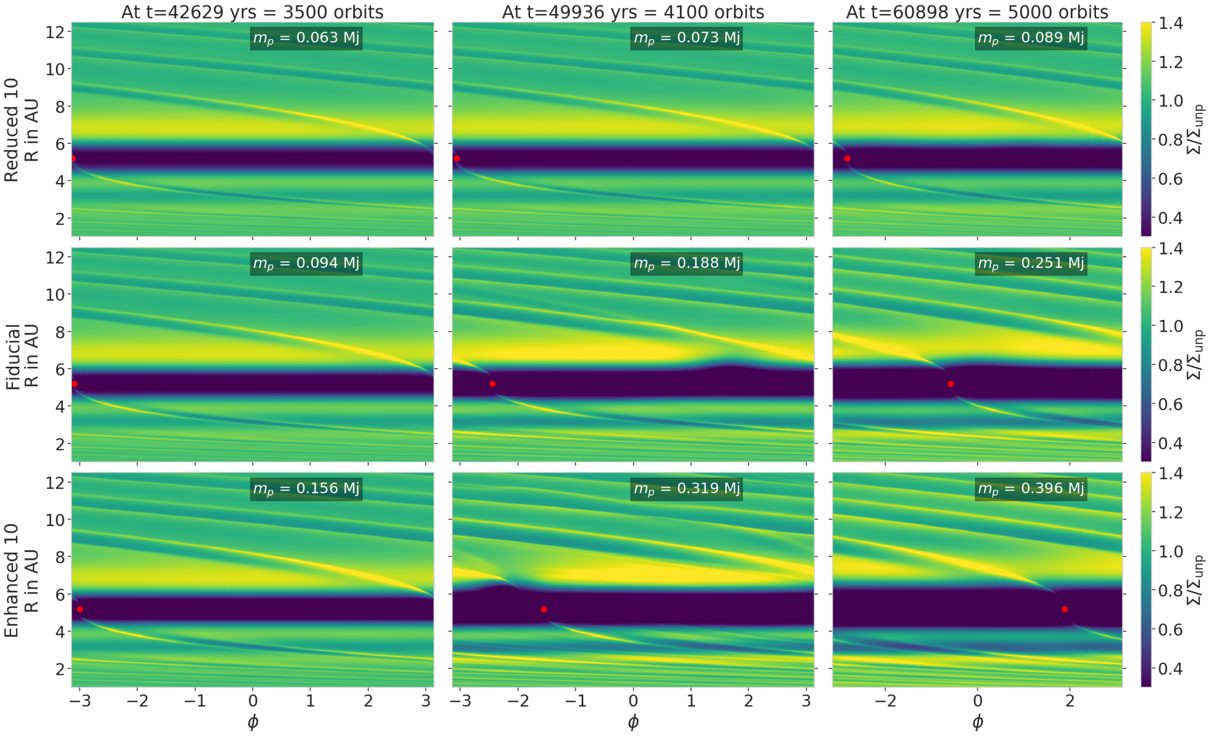

Figure 3.9: Perturbed surface density at three different time (from left to right) for three planetary accretion rates, with 0.1 (top), 1 (middle) and 10 (bottom) times the nominal accretion rate, in discs with $\alpha = 10^{-4}$, $h = 0.05$. Red dots show the position of the planet. *First row:* density snapshots for the reduced by 10 accretion rate. As the planet is growing really slowly, the gap edges are not very steep, creating a very weak vortex. *Second row:* density snapshots for the fiducial accretion rate. The edges of the created gap are steep enough to trigger the RWI, creating a vortex. The vortex vanishes after $\sim 8.1 \times 10^4$ years. *Third row:* density snapshots for the enhanced by 10 accretion rate. The planet is growing so fast that the edges of the created gap are steep, triggering the formation of a vortex stronger than in the previous cases. The vortex vanishes after $\sim 5.3 \times 10^4$ years.

in the fiducial case, all accretion rates show oscillations, with different amplitudes and duration times. As expected, larger accretion rates result in stronger oscillations. The small increase that can be seen on the time evolution of the enhanced accretion rates from $t \simeq 4.1 \times 10^4$ years to $\sim 5.1 \times 10^4$ years, is also due to the presence of vortices. It corresponds to the moment when the vortices are the strongest. Once they vanish after $\sim 5.3 \times 10^4$ years, the oscillations in the accretion rates vanish too. Our results are, therefore, in agreement with Hammer et al. (2017), with the vortices pushing material into the vicinity of the planet and their presence demonstrating a link to an enhancement in the gas accretion rate.

The presence of these vortices has a strong impact on the density profiles of the disc. The large viscous timescale at low viscosity results in a long period of time for the disc to adjust to the presence of the planet, resulting in an highly perturbed disc structure. The perturbed density profiles are shown in the lower panel of Fig. 3.10. Perturbations are particularly high in the inner disc. This has a strong influence on the stellar accretion, shown on the middle panel of Fig. 3.10. Compared to what we describe in Sect. 3.3.3, the scaling of the stellar accretion with the planetary accretion is reversed here: a more efficiently accreting planet results in a larger stellar accretion rate. We expect this effect to flip at later time, when the inner disc gets depleted by the viscosity: the viscous time

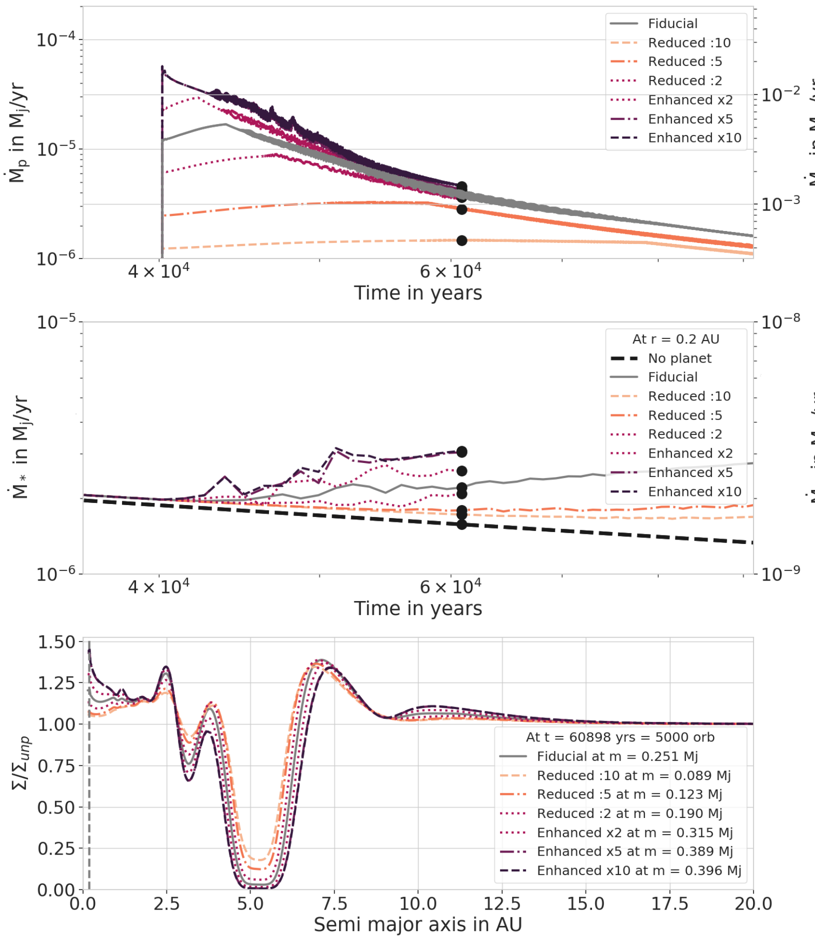

Figure 3.10: Influence of different accretion rates on stellar gas accretion for $\alpha = 10^{-4}$ and $h = 0.05$. *Top:* Planetary gas accretion rate for the seven reduced, enhanced, and fiducial accretion rates. The presences of vortices create oscillations in the accretion rate: the larger the vortex, the larger the oscillations. *Middle:* Stellar gas accretion at the inner edge of the disc (0.2 AU). At this low viscosity, the trend is flipped compared to the high viscosity case: a more efficiently accreting planet will lead to an enhanced accretion onto the star. This is due to the fact that at low viscosity, the inner disc is mostly perturbed by the presence of the planet and the viscosity is too low to compensate for it. *Bottom:* Perturbed surface density at time t = 4000 orbits = 48 718 yrs. The vertical line shows the location at which the stellar accretion rates are measured (0.2 AU).

at $\alpha = 10^{-4}$ is 100 times longer than for $\alpha = 10^{-2}$, requiring $t_\nu = 8$ Myrs for material to move from the position of the planet to the inner disc, which is too long for computational integration. Therefore, the depletion of the inner disc is less affected by smaller viscosities: instead the inner disc is mostly influenced by the presence of the growing planet. Larger planets induce larger perturbations: the enhancement [1] created by the planet in the inner disc, at $r < 1$ AU as shown in the lower panel of Fig. 3.10, is larger for the largest planet, that is, in the case of enhancement by 10. The presence of this enhancement at the inner disc is the reason the stellar accretion is higher compared to the disc without a planet. As soon as the disc starts to deplete its inner disc via viscous spreading, the accretion

---

[1] We note that we plot the perturbed surface density, therefore the "bump" shown here is not present in the actual gas surface density profile. This enhancement in density is caused by the growing planet that pushes material from its orbit.

rate onto the star behaves as displayed in Fig. 3.6, where we observe a higher decrease in stellar accretion rate with quickly accreting planets. This behavior was confirmed by investigating the evolution of the stellar accretion rate for an intermediate viscosity: for $\alpha = 10^{-3}$ (not shown), the stellar accretion rate is larger compared to a disc without a planet at the beginning of the simulation, but it then becomes smaller when the inner disc starts to deplete via viscous spreading.

Viscosity has an impact on how the planet will open a gap, as can be seen on the lower panel of Fig. 3.8: depending on the viscosity, a gap is opened at a different mass and the gap has a different shape. In the next section, we investigate the impact of gas accretion on the gap-opening mass.

3.4.3 Gap-opening mass

As mentioned in Sect. 1.2.2, the criterion for gap-opening mass has been derived in several previous studies. Here, we compare in Fig. 3.11 different gap opening criteria to the gap-opening masses of our accreting planets. We consider the criterion derived by Crida et al. (2006) (see eq. 1.29, for which we focus on the mass needed to satisfy $P = 1$) as well as the criteria derived by Kanagawa et al. (2015) (eq. 1.30) and by Fung et al. (2014) (eq. 1.31).

In Fig. 3.11, we see that Fung and Kanagawa's criteria show a linear evolution for the gap-opening mass as a function of the viscosity, unlike Crida's criterion that levels off at low viscosity. This leveling off is caused by the fact that even when the viscosity vanishes, the planet is still in competition with the pressure of the disc to create a gap, creating a lower threshold for the gap-opening mass. Moreover, there should be a threshold at low viscosity as the presence of vortices generates a certain background level of turbulence, independently of the prescribed alpha viscosity.

In order to determine the influence of planetary gas accretion on the gap-opening mass within our simulations, we investigated the gap-opening masses of fixed mass planets in our simulations (squares in Fig. 3.11). Our planets with fixed mass seem to be opening gaps following Fung's criterion for $h = 0.05$ and high viscosity only. For the other aspect ratios, all gap-opening criteria seem to be failing. We suspect that our simulations do not match any criteria directly as they are all derived from fits to simulations and, a a result, inducing errors. Using the gap-opening masses derived from the Crida et al. (2006) criterion (eq. 1.29) we actually find deeper gaps than $0.1\ \Sigma_{\rm unp}$. It is also important to note that we are investigating gap-opening mass in non-equilibrium discs: the mass accretion rate onto the star is evolving over time as material is accreted onto the planet and the star. Earlier studies (Crida et al., 2006; Fung et al., 2014; Kanagawa et al., 2015) were made on the basis of equilibrium discs, meaning that the stellar accretion rate is constant over time. Having a viscously evolving disc may change the gap-opening mass because the accretion onto the star leads to depletion in the inner disc, influencing the material around the planet and therefore influencing how the gap is opened (especially at high viscosities). To maintain consistency, we therefore compare gap-opening masses within our simulations.

At this point in the study, we can identify three behaviors depending on the level of viscosity: 1) at low viscosity (e.g., at $\alpha = 10^{-4}$ for $h = 0.05$), the gap-opening mass is highly dependent on the gas accretion rate. Simulations with faster accreting planets result in larger gap-opening masses, while simulations with slower accreting planets result in smaller gap-opening masses; 2) at high viscosity (for example at $\alpha = 2 \times 10^{-2}$ for

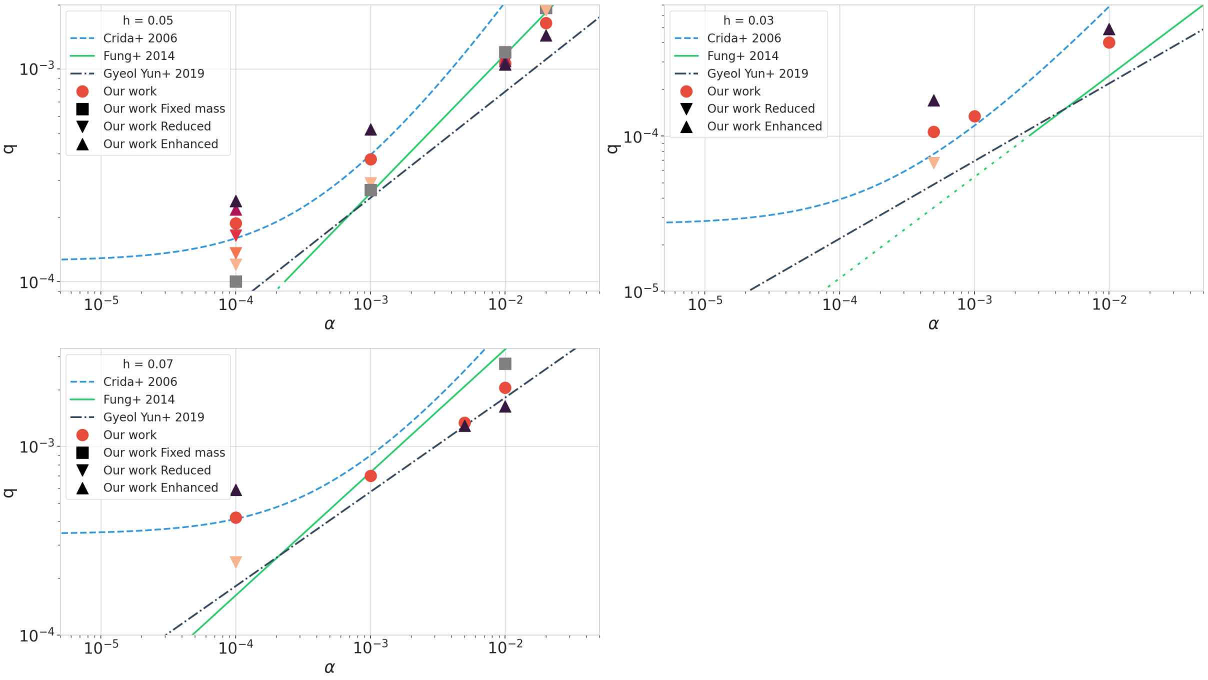

Figure 3.11: Gap-opening mass as a function of the viscosity for different criteria and our simulations. The lines represent the different gap-opening criteria from the literature: Fung et al. (2014) in solid green, Crida et al. (2006) in dashed blue, and Gyeol Yun et al. (2019) in dashed-dotted black. The dotted green line represents the mass limit of the Fung et al. (2014) study. None of these works include planetary gas accretion. Red dots represent our fiducial simulations. Results from the different accretion rates are represented by upward triangles for the enhanced accretion rates and downward triangles for the reduced accretion rates. The color coding is the same as in Fig. 3.3: darker colors represent larger accretion rates. The two panels on the left are for the two high aspect ratios: $h = 0.05$ (top) and 0.07 (bottom) where the initial mass of the planet is $20M_\oplus$. The panel on the right is for $h = 0.03$ where the initial mass of the planet is of 10 $M_\oplus$, changing the gas accretion rate and, therefore, the gap-opening mass compared to the left panels. Gas accretion has different impact as a function of disc parameters. This discrepancy can be explained by the time needed to the disc to react to a change of planetary mass.

$h = 0.05$), we find the opposite behavior. A simulation with a high accretion rate will open a gap at a smaller mass than a slowly accreting planet; 3) as the behavior flips between high and low viscosity, a peculiar viscosity exists, for example at $\alpha = 10^{-2}$ for $h = 0.05$, for which the gap-opening mass is insensitive to the different gas accretion rates. For the seven simulations, the gap opening mass is nearly the same: $m_{\rm gap} \simeq 1.06\ M_J$.

In order to explain these behaviors, we investigate the time needed for a fixed mass planet to open a gap as a function of its mass, at low and high viscosities. Our results are shown in Fig. 3.12 for low ($\alpha = 10^{-4}$) and high ($\alpha = 2 \times 10^{-2}$) viscosities. The crosses represent the time needed for fixed-mass planets of different masses to open a gap. To be consistent with regard to the comparison, in this case, the fixed-mass planets are introduced in exactly the same way as the accreting planets: after the $20M_\oplus$ core is introduced and its initial gap has been created, the mass of the planet is switched to the final mass of interest. The time needed to open a gap corresponds then to the time needed to reach the $\Sigma/\Sigma_{\rm unp} = 0.1$ threshold after the planet mass is switched to its final mass.

As expected, we see that more massive planets open gaps more rapidly than low-mass

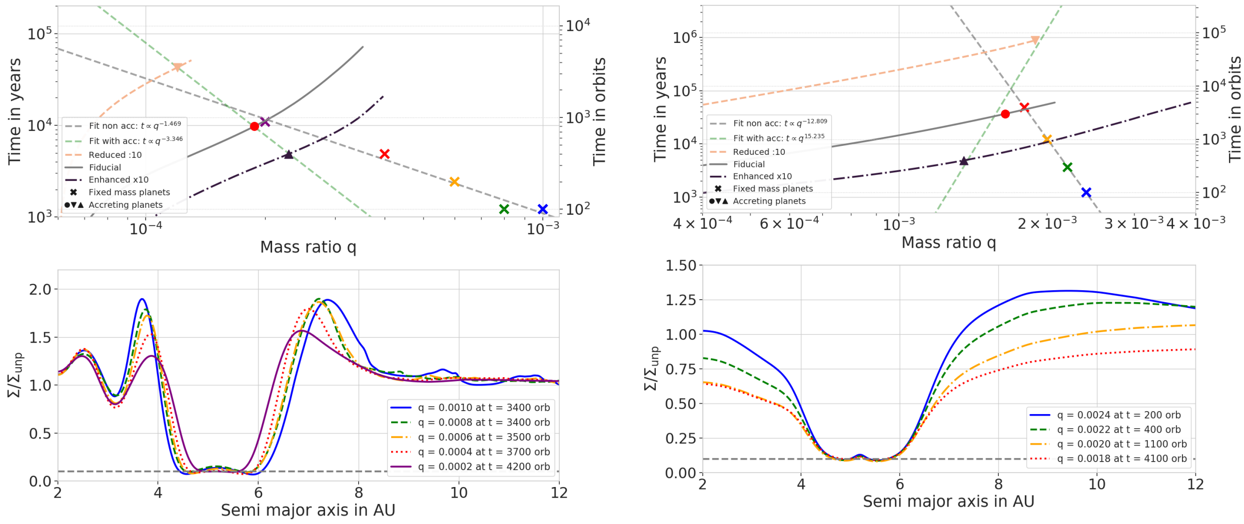

Figure 3.12: Time needed for gap opening as a function of the planetary mass for $\alpha = 10^{-4}$ and $h = 0.05$ in the left panel and $\alpha = 2\times10^{-2}$ and $h = 0.05$ in the right panel. The gap opening time is defined as the time needed to reach the $\Sigma/\Sigma_{\rm unp} = 0.1$ threshold by gas accretion, therefore, we removed the time needed to reach the initial gap, $t_{\rm gap,init}$ (see table 3.2). *Top row:* Gap opening time as a function of the planetary mass. Fixed-mass planets are represented by crosses and linearly fitted by the dashed gray line. For comparison, the time evolution of the planetary masses for the accretion rate enhanced by 10, fiducial accretion rate, and that reduced by 10 are represented by the dashed-dotted dark, solid gray, and dashed light lines, respectively. Their gap-opening masses are represented with the same symbol as in Fig. 3.11. At low viscosity (left panel), the gap-opening mass and time of the accreting planet follow the predictions of the fixed-mass planets. The disc response time is therefore the dominant phenomenon for gap opening. On the other hand, at high viscosity (right panel), the gap-opening mass and time of the accreting planets do not follow predictions for the fixed-mass planets. Gas accretion is, therefore, the dominant phenomenon for gap formation. *Bottom row:* Perturbed surface densities of the fixed-mass planets at gap opening time. Gap-opening mass and time are defined by the moment at which the surface density is $\Sigma = 0.1\Sigma_{\rm unp}$.

planets (Lin & Papaloizou, 1986). In consequence, the way the planet is introduced in the disc has a strong influence on the gap-opening mass (more precisely, on the time at which the 0.1 $\Sigma_{\rm unp}$ threshold is reached). To make a comparison with accreting planets, we show, using the same figures, the time evolution of the masses of the accreting planets. The dots and triangles represent the time and mass at which each accreting planet is observed to open a gap (same dots and triangles of Fig. 3.11). In the lower panels of Fig. 3.12, we show the surface density profiles of the non-accreting planets at the time and mass used for the gap definition. We observe two different behaviors at low and high viscosities that can explain the gap-opening masses of our accreting planets (Fig. 3.11). First, at low viscosity (left panel of Fig. 3.12), the gap-opening masses of the accreting planets and the one of the fixed-mass planets are both inversely proportional to the planet mass ($t \propto q^{-X}$). In this case, the gap-opening phenomenon is governed by the disc response to the change in the mass of the planet. Gas accretion only changes the value of the slope compared to the fixed-mass planets ($X \simeq -1.47$ for the fixed-mass planets and $X \simeq -3.35$ for the accreting planets). This means that the process of gas accretion is dominated by the disc response time, that is, the time needed for the disc to react to a change of planetary mass. In this case, when the planet is slowly introduced in the disc, it opens a gap at a lower mass than a planet that is rapidly introduced. This explains the behavior seen in Fig. 3.12 at low viscosity: slowly accreting planets are slowly changing in mass, resulting in smaller gap-opening masses. On the other hand, at high viscosity (right panel of Fig. 3.12), the behavior is completely different. The gap-opening masses of the fixed-mass planets is still inversely proportional to the planet mass ($t \propto q^{-X}$) but the gap-opening mass of the accreting planets is proportional to q ($t \propto q^{+X}$). In this case, the disc response is quick enough for planetary gas accretion to help carve a deeper gap. Gap opening is, therefore, dominated by gas accretion and not by the disc response time.

The key parameter here is the disc response time to a change of planetary mass. A formula for the gap opening time in an inviscid disc was derived by Lin & Papaloizou (1986). They found that $\tau_{\text{gap}} \propto q^{-2}$. As plotted in Fig. 3.12, we find $\tau_{\text{gap}} \propto q^{-1.47}$ for $\alpha = 10^{-4}$ and $\tau_{\text{gap}} \propto q^{-12.81}$ for $\alpha = 2 \times 10^{-2}$, meaning that at higher viscosity, the gap opening time is more dependent on the planetary mass. It is important to mention that the discrepancy between our result and that of Lin & Papaloizou (1986) comes from the importance of viscosity in the gap-opening process and the definition for the gap opening time. Indeed, we define the gap-opening mass as the mass needed to create a gap of a certain depth ($\Sigma/\Sigma_{\text{unp}} = 0.1$), whereas they define it on the basis of when the forces applied by the planet on the disc are equilibrated and vice versa.

In conclusion, gas accretion has a different impact on the gap-opening mass depending on the disc response time. It is a dominating phenomenon at high viscosities. These differences in gap-opening mass can have an important impact on the transition to type II migration, which is investigated in the next section.

3.4.4 Migration maps

Planets embedded in discs interact with the gas by exchanging angular momentum, which results in planet migration (see Sect. 1.2.3). Migration is a robust phenomenon and a central ingredient in global models of planet formation that attempt to reproduce known exoplanet systems as well as our own Solar System (for a review, see Raymond et al. (2020)). In order to study the type I migration of planets that could be present in the same disc as our gas-accreting planets, we employ the formulae from Paardekooper et al. (2011) to estimate the torque acting on the smaller bodies (see eq. 1.33), assuming Bell & Lin (1994) opacities.

A negative torque would result in an inward migration, towards the star. On the other hand, a positive torque reflects outward migration, toward the outer parts of the disc. Inward migration is mostly due to the Lindblad component of the torque. In order to have outward migration in our locally isothermal case, where the temperature gradients are quite shallow, sharp positive radial gradients in the surface density are needed Masset et al. (2006a). These gradients appear at the outer edge of the gap created by the accreting planet.

In Figs. 3.13 and 3.14, we show the migration maps for different viscosities and different aspect ratios when the accreting planet has reached its gap-opening mass. Regions of inward (blue) and outward (red) migration are represented as well as the potential equilibrium position of the low mass migrating planet: the zero-torque position (black line) and the resonances (dashed white vertical lines) with the accreting giant planet, whose position is marked by the dashed blue line.

An outer lower mass planet would stop migrating either at the zero-torque location or if it is trapped in resonance with the inner planet, depending on its migration speed

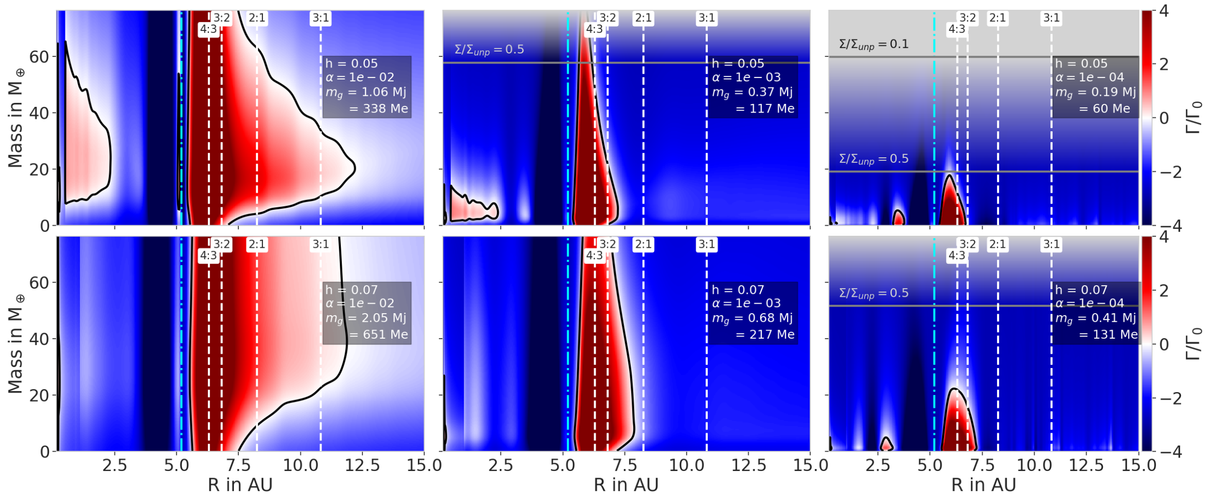

Figure 3.13: Migration maps for low-mass planets orbiting near our accreting planets. The accreting planet has reached gap-opening mass. The different panels represent different disc parameters: the viscosity decreases from left to right ($\alpha = 10^{-2}, 10^{-3}, 10^{-4}$) and the aspect ratio increases from top to bottom ($h = 0.05, 0.07$). Positive (red) torques indicate outward migration while negative (blue) torques represent inward migration. The black solid line represents the zero torque line, a position where the second planet would stop migrating. The two gray horizontal lines represent the masses at which $\Sigma/\Sigma_{\rm unp} = 0.5$ and 0.1. We consider that the planet will smoothly switch from type I to type II migration between these two masses. The vertical white dashed lines locate the positions of the resonances with the accreting planet situated at 5.2 AU (vertical blue dotted dashed line).

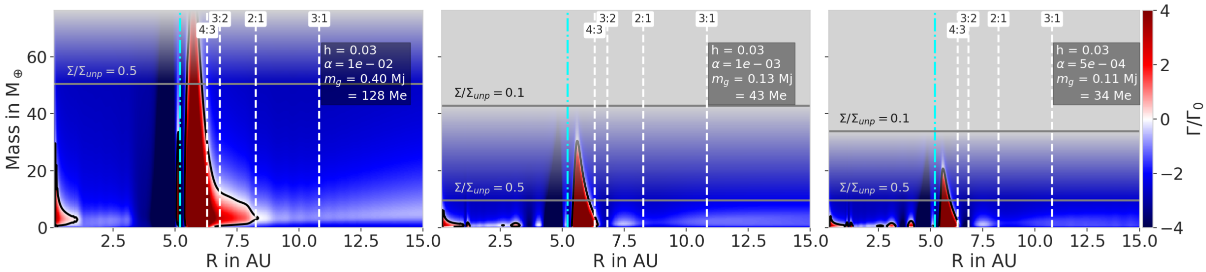

Figure 3.14: Same as Fig. 3.13 but for $h = 0.03$. Here, $m_{\rm init} = 10\ M_\oplus$ and $\alpha = 10^{-2}, 10^{-3}$, and 5×10^{-4}.

(Thommes, 2005; Pierens & Nelson, 2008). In our simulations, if an inward migrating planet can jump the 2:1 resonance and continue to migrate further in, it would reach the position of the 3:2 resonance for the lowest viscosities, when the torques saturate. At high viscosity, for all aspect ratios, the outward migration zone is wide enough to overlap over the 3:2 resonances positions and the 2:1 resonances positions if the mass of the second planet is small enough. It these cases, the migrating planet is prevented to be locked in 3:2 resonance by the zero torque line, specifically for low-mass planets. When the planet mass is small enough, the 2:1 resonance is also unreachable due to the extend of the outward migration zone. Depending on the shape of the gap created and the migration speed of the low-mass planet, the capture in certain resonances might therefore be avoided. The capture in resonance is important for the grand tack scenario (Walsh et al., 2011), where Jupiter and Saturn get locked in 3:2 or 2:1 resonance and start migrating outward (Masset & Snellgrove, 2001; Morbidelli & Crida, 2007; Pierens & Nelson, 2008; Raymond et al., 2011; Pierens et al., 2014; Chametla et al., 2020). We discuss, in Sect. 3.5.3, the impact

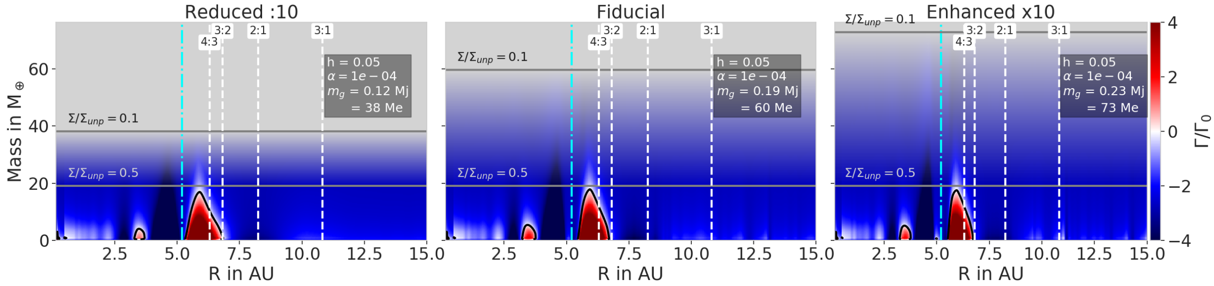

Figure 3.15: Migration maps for $\alpha = 10^{-4}$ and $h = 0.05$ for low-mass planets orbiting near our accreting planets. The accreting planet has reached the gap-opening mass. The three panels represent different accretion rates: the reduced by 10 (left), fiducial (middle), and enhanced by 10 (right). The plotted information is the same as in Fig. 3.13. As gas accretion has an influence on the gap-opening mass, the migration maps look different due to the switch from type I to type II migration when a gap is opened. Here, the $\Sigma/\Sigma_{\rm unp} = 0.5$ is at the same mass for all the different accretion rates as the initial depth for these discs parameters is smaller than 0.5 (see table 3.2).

of resonance capture on the structure of our Solar System.

Pierens et al. (2014) investigate which disc parameters (Σ_0 and α) and capture in resonance are needed to allow outward migration of Jupiter and Saturn. For h=0.05 (middle row in Fig. 3.13) and our surface density $(\Sigma/\Sigma_{MMSN} = 1.5)$[2] with $\alpha = 10^{-3}$, outward migration for the Jupiter-Saturn pair would happen in the 3:2 resonance. Still, according to Pierens et al. (2014), the Jupiter-Saturn system would show divergent migration for $\alpha = 10^{-2}$ and be captured in the stable 2:1 configuration for $\alpha = 10^{-4}$. In Fig. 3.13, we see that the capture in the 3:2 resonance is possible for $\alpha = 10^{-3}$ and $h = 0.05$; for these disc parameters, Saturn would not open a deep gap ($m_S = 95 M_\oplus < m_{\rm gap} = 117 M_\oplus$). Therefore, our migration maps agree with the results found in (Pierens et al., 2014), assuming that Saturn's migration speed allows it to be locked in the 3:2 resonance. In addition, our results show that N-body simulations of growing planets should take the disc profile into account to correctly assess the migration behavior of the planets.

As a planet grows and carves a deep gap, it is transitioning from type I to type II migration. In Fig. 3.15, we show the migration maps for $h = 0.05$ and $\alpha = 10^{-4}$ for the fiducial, the enhanced, and the reduced by 10 rates for planetary gas accretion. If the planet accretes slowly, a gap is opened at a smaller mass than when the planet accretes quickly for these disc parameters (see Sect. 3.4.3). The mass at which the planet is expected switch from type I to type II migration (depicted by the gray area in Figs. 3.13, 3.14, and 3.15) is, therefore, dependent on the planetary accretion rate, assuming that the second potential planet in the system accretes at the same rate and would thus have the same gap-opening mass. At these disc parameters, the difference in gap-opening mass does not have an impact on the capture in resonance: the region of outward migration is small and does not overlap with resonances for planets more massive than 15 $M_\oplus$. The dynamics of multiple planetary systems can be highly impacted by planetary gas accretion via the influence on the migration type and on the potential trapping in resonance.

---

[2] Note that their surface density profile is different from our setup: $\Sigma \propto r^{-3/2}$ as opposed to $\Sigma \propto r^{-1}$ in this work. Therefore the outcome of planet migration in our case might be different from their results.

3.5 Discussion

3.5.1 Accretion onto the star

In this work, we study the influence of planetary gas accretion on the stellar accretion (Sects. 3.3.3 and 3.4.2). We show that the stellar accretion is reduced with increasing planetary accretion rates. Even though, at low viscosity, our results show an enhancement of the stellar gas accretion rate, we expect this trend to flip and follow the high viscosity case after reaching the viscous time needed for material to reach the inner disc from the planet position.

In both previous cases, the stellar accretion was only decreased or increased by a factor of up to three compared to the case of a disc without any planet. These results are quite different from what Manara et al. (2019) find. In their models, they find that stellar gas accretion rate can be reduced by over two orders of magnitude due to the presence of giant planets. In our simulations, these large spreads of stellar accretions could only be achieved by changing the disc viscosity over orders of magnitude, however, this parameter is fixed in the simulations used in Manara et al. (2019). The difference might come from the difference in gas flow between a 2D and a 1D disc: indeed, in the approach of Manara et al. (2019), gas accretion onto the star is derived from the viscous spreading of a 1D disc containing a giant planet. As Lubow & D'Angelo (2006) conclude in their work, in a 2D disc, mass can flow through the gap even in the presence of a giant planet. Moreover, in Manara et al. (2019), the planetary gas accretion rates are higher than ours as theirs are proportional to the unperturbed surface density in their accretion routine (Mordasini et al., 2012). Therefore, the 1D model from Manara et al. (2019) might be overestimating the efficiency of the planet in blocking material from the inner disc.

In addition, Lubow & D'Angelo (2006) showed that the modeling of the inner disc and the process whereby gas is accreted onto the planet is of crucial importance for calculating the stellar accretion rate. Our simulations indicate that planetary gas accretion might have a smaller impact than expected on the stellar gas accretion rates.

3.5.2 Implications for observations

Observations of protoplanetary discs have revealed structures in the dust distribution (Pinilla et al., 2012; Andrews et al., 2018; Zhang et al., 2018). However, these dust structures are ultimately caused by the drifting dust grains trapped at pressure bumps in the gas discs. Therefore, as mentioned in previous sections, looking at the pressure bumps created by planets in the gas can give us an insight into how the dust is trapped and how gas accreting planets might influence the interpretation of the observations. When we compared the pressure bumps in Sects. 3.3.1 and 3.3.2 for our simulations with the fiducial parameters, we found that the pressure bumps were too similar to show distinguishable features. This result is expected, as in Sect. 3.4.3 we showed that for these disc parameters, gas accretion has almost no influence on the gap depth. On the other hand, at low viscosity the gap-opening mass changed dramatically with the planetary accretion rate.

In Fig. 3.16 we show the surface density profiles of discs containing accreting planets at gap-opening mass and the corresponding pressure bumps for $\alpha = 10^{-4}$ and $h = 0.05$ and for the different planetary accretion rates studied. Profiles plotted in the top panel show similar gap width for the same gap depth. The pressure bumps created here are,

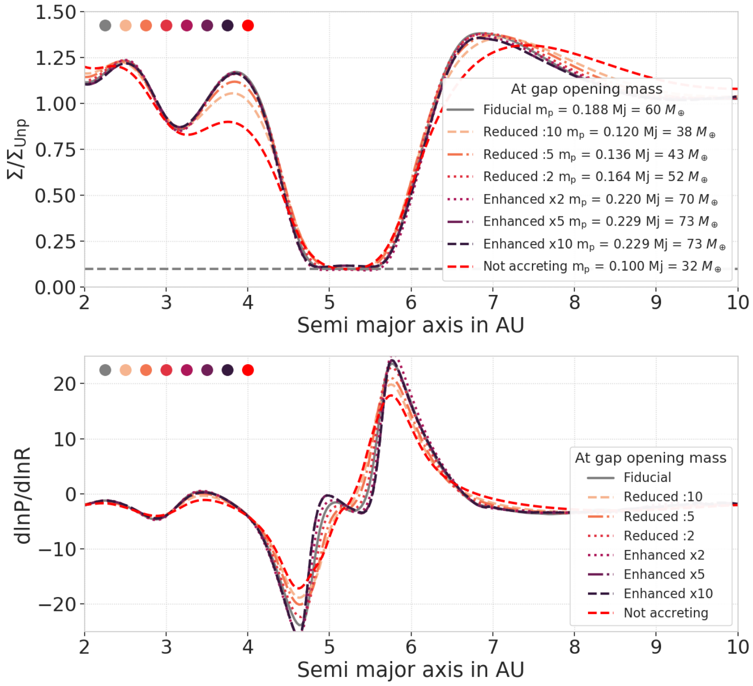

Figure 3.16: Influence of gas accretion on the disc structure at the gap-opening mass for $\alpha = 10^{-4}$ and $h = 0.05$. *Top:* Perturbed surface density profiles at gap-opening mass in the seven different gas accretion cases and in the fixed-mass case. For these disc parameters, the gap-opening mass is highly influenced by gas accretion, making the planet open a gap at a higher mass when the planetary gas accretion rate is enhanced. However, the resulting gap shape at gap-opening mass is independent on the gas accretion rate. The accreting planets show some differences when compared with the planet of a fixed mass. *Bottom:* Pressure bumps at the gap-opening mass in the seven gas accretion cases and in the fixed-mass case. As the gap shapes are similar, the difference in the created pressure bumps is too small to be observable.

thus, very similar. Even if the difference in planetary mass is of almost a factor of two, the created gaps are too similar to show features that can be distinguished by observations. Our simulations thus indicate that for the same gap depth, gas accretion has a negligible impact on the gap width. However, it does have an impact on the mass creating such a gap: depending on the gas accretion rate, a very similar gap can be created by planets of different masses, as we can see in Fig. 3.16. This implies that the planetary masses derived from 2D simulations designed to match the observations might be off by up to a factor of two for $\alpha = 10^{-4}$ and $h = 0.05$. This factor is dependent on the viscosity, ν, and is larger for lower viscosities, as we can see in the right panel of Fig. 3.11, where $h = 0.03$.

Recent studies (Teague et al., 2018; Pinte et al., 2020) have shown that CO velocity field observations can be used to observe planets in discs. As gas accretion has an impact on how the gap is formed, it also has an impact on the velocity field of the gas around the planet. In Teague et al. (2018), hydrosimulations with non-accreting planets were run in 2D. The planetary masses were derived by comparing the deviation to the rotational velocity in the simulations and the observations. Their derived masses can be altered by gas accretion if the disc parameters make the gap formation sensitive to gas accretion.

3.5.3 Implications for the grand tack scenario

The gap-opening mass is an important parameter for the structure of planetary systems. When multiple planets are taken into account, as in the grand tack scenario with Jupiter and Saturn (Walsh et al., 2011) or in recent N-body planet formation simulations (Bitsch et al., 2019), the timescales for gas accretion and migration become important. Indeed, if Saturn is accreting rapidly in a disc where $h = 0.05$ and $\alpha = 10^{-3}$, then it will reach a high mass before opening a gap. In our case, the gap-opening mass is $\sim 0.5 M_J$ with the highest gas accretion rate. It means that if there is a mechanism that stops planetary gas accretion (like photoevaporation (Rosotti et al., 2015)), then Saturn ($m_S = 0.3\ M_J$) would not open a gap and it would thus migrate through type I migration towards Jupiter and be captured in resonance or at a zero-torque location. As type I migration is fast, we can imagine that some resonances might be jumped and Saturn and Jupiter would end up in close relative final positions. On the other hand, if Saturn would be accreting very slowly, then it would switch to type II migration when reaching a gap-opening mass of $m_{\rm gap} = 0.29\ M_J$. The growing body of Saturn would then slowly arrive towards Jupiter and would be less likely to jump into the first resonance positions encountered. Therefore, depending on the gas accretion rate, the migration speed will be different, leading to different configurations for the relative positions of Jupiter and Saturn.

As discussed in Sect. 3.4.4, the capture in resonance, as well as the order of the resonance if the capture occurs, would then trigger (or not) the outward migration of Jupiter and Saturn that is needed to explain the formation of our solar system within this scenario. We plan on studying this impact in more details in a future project. The influence of relative migration speed on the capture in resonance was investigated by Kanagawa & Szuszkiewicz (2020). They found that because of gap formation, a planet pair can break the resonant configuration they had been locked in. It confirms the assumption that gap formation is a key process in understanding planetary systems structures and that the impact of gas accretion on gap formation is an important parameter that should be taken into account.

3.6 Conclusions

With this project, we study the influence of gas accretion on a planet embedded in its gaseous protoplanetary disc. Our main results are as follows:

1. Planetary gas accretion has a non-negligible impact on stellar gas accretion. The depletion of the inner disc by planetary accretion and the creation of a gap effectively reduces the stellar accretion. Even though our study is focused on extreme cases of planetary gas accretion, we find that stellar accretion is impacted by less than one order of magnitude compared to discs evolving purely through viscous spreading, which stands in contrast to earlier results derived from 1D disc evolution models (Manara et al., 2019). We attribute this difference in part to the higher planetary gas accretion rates in Manara et al. (2019), which are up to one order of magnitude higher than in our simulations[3].

---

[3] We believe these high accretion rates are caused by the usage of the unperturbed gas surface density to calculate the planetary gas accretion rates in the work of Mordasini et al. (2012), used in Manara et al. (2019)

2. Disc parameters have a strong impact on planetary gas accretion. The aspect ratio changes the accretion rate evolution as the gas accretion rate formula depends on h directly and on Σ: as it is more difficult for planets to create gaps in discs with larger aspect ratios, the gas surface density in the gap is larger, resulting in larger accretion rates. On the other hand, the viscosity is a key parameter as it dictates how much gas is refilled around the planet: lower viscosities imply lower planetary gas accretion rates.

3. Planetary gas accretion has a strong impact on the gap-opening mass, depending on the disc parameters and assuming that the gap-opening mass is defined by the mass needed to reach $\Sigma/\Sigma_{\rm unp} = 0.1$. The impact will be stronger when the disc response time is large (low viscosity), as it does not have time to adapt to a change in planetary mass. It results in higher gap-opening masses for the planets that quickly change their mass (i.e., for the quickly accreting planets described here). On the other hand, gas accretion becomes a dominant phenomenon when the disc time response is small (high viscosity): planetary gas accretion can help carve a deeper gap in this case, resulting in smaller gap-opening masses when the accretion rate is larger.

In addition we discuss the implications of our results on the planetary interpretation of observed rings and gaps. Indeed, similar pressure bumps are produced by planets of different masses depending on the gas accretion rate used, meaning that we should also take gas accretion into account in order to be able to constrain the mass of a planet that is in the process of creating a gap in the observed disc.

The gap-opening mass is also an important parameter for the study of the formation of multiple planets in discs. We discuss the impact of gas accretion on migration, concluding that a major impact is linked to the gap-opening mass as it dictates when the planet is expected to switch its migration type (from type I to type II). This switch in migration type then changes the migration speed of the planets, which determines the possibility of capture in resonances. The structure of such systems can, therefore, be highly impacted by planetary gas accretion. Even though our results rely on assumptions based on disc evolution and gas accretion rates, we identify important trends for planet formation simulations. In particular, the change of the gap-opening mass for accreting planets at low viscosity has important implications for simulations of planet population synthesis. In addition, our results are important when investigating the growth and migration of multiple planets in the same disc, as required by the grand tack scenario. Our study supports the fact that gas accretion is an important factor not only for planetary growth, but also for the migration behavior of other planets and the gap shape. Thus, it should be taken into account in future simulations and interpretations with regard to observations of protoplanetary discs where planets are suspected.

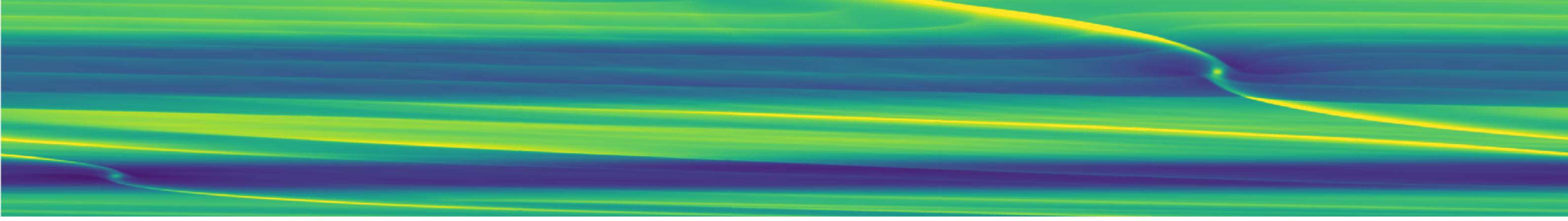

4

Two accreting planets: How is gas distributed between the planets ?

This chapter is based on the paper in preparation *Bergez-Casalou et al., in prep.*

Abstract

Our Solar system, together with several observed exoplanetary systems, is known to host multiple giant planets. They are thought to have formed in the same gaseous protoplanetary disc. While many different studies investigate their formation, it is unclear how the simultaneous formation of giant planets can influence their own growth. Following the study developed in the previous Chapter, I perform 2D isothermal hydrodynamical simulations with the `FARGO-2D1D` code considering two planets accreting from the same gaseous disc. The evolution of the planet masses is integrated for around 0.5 Myrs, which is longer than the majority of hydrodynamical simulations investigating gas accreting planets, allowing us to investigate their long term evolution. We find that the evolution of the planets mass ratio depends on the gap formation timescale compared to the accretion time scale: whether gas accretion helps gap formation or not (see Chapter 3) determines the moment when the inner planet accretes more than the outer one. When the planets accrete simultaneously, they end up with very similar masses ($0.9 < m_{out}/m_{in} < 1.1$ after 0.5 Myrs). Delaying the accretion between the planets helps reaching more extreme mass ratios at the beginning of the simulations but the planets quickly converge towards similar masses ($0.8 < m_{out}/m_{in} < 2$ in 10^5 yrs). When compared to the observed exoplanet population, we find that to reproduce the mass distribution in the observed systems, the planets must start accreting at different times *and* their accretion must be stopped quickly after the beginning of runaway gas accretion (less than 0.5 Myrs), by disc dispersal for example. The evolution of the planet mass ratio can have an important impact on the dynamics of the system and can help further constraining the formation history of Jupiter and Saturn.

4.1 Motivations

When we observe our own Solar system, multiple giant planets are observed. Recent surveys also tend to show that planetary systems hosting multiple giants are common (e.g., Lissauer et al., 2012; Fabrycky et al., 2014; Zhu, 2022). These planets are believed to have formed in the same parental protoplanetary disc, where they acquired their massive gaseous atmospheres. Previous hydrodynamical studies investigate either the growth of single planets in the disc (e.g., Ayliffe & Bate, 2009; D'Angelo & Bodenheimer, 2013; Crida & Bitsch, 2017; Schulik et al., 2019) or the evolution of already formed multiple planets (e.g., Baruteau & Papaloizou, 2013; Lega et al., 2013; Pierens et al., 2014; Morbidelli et al., 2018). This dichotomy originates from the difficulty to accurately model each evolution process.

Gas accretion requires 3D high resolution hydrodynamical simulations. Some studies have described how gas accretion can be approximated in 2D, considering or not planet migration (Kley, 1999; Crida & Bitsch, 2017). Other studies used complex 3D simulations to take into account the various fluid and thermal processes governing gas accretion of an embedded planet (e.g., Ayliffe & Bate, 2009; Machida et al., 2010; D'Angelo & Bodenheimer, 2013; Szulágyi & Mordasini, 2017; Lambrechts et al., 2019; Schulik et al., 2019). Due to their high computational cost, they are often integrated over short timescales, covering around 100 planetary orbits, making it impossible to investigate the long-term growth of single accreting planets with the current computing facilities.

Moreover, the gas distribution around embedded giant planets is impacted by gap formation. The formation of these gaps has been observed both in the dust (e.g., ALMA Partnership et al., 2015; Andrews et al., 2018; Benisty et al., 2021) and in the gas (e.g., Huang et al., 2018b; Smirnov-Pinchukov et al., 2020). Several studies investigate the characteristics of the gap (such as its depth and width) as a function of the planet and disc characteristics (Lin & Papaloizou, 1986; Crida et al., 2006; Fung et al., 2014; Kanagawa et al., 2015). However, due to computational limitations, these studies neglected gas accretion. Recent works show that gap formation and gas accretion are highly dependent on each other through the viscosity of the disc (Bergez-Casalou et al., 2020; Rosenthal et al., 2020).

As gap formation has a non negligible impact on the gas structure, the growth of giant planets must be impacted by the presence a second accreting planet in the same disc. The goal of this study is to quantify this impact as a function of the disc parameters and planet characteristics (i.e., their radial separation and delay in accretion). We perform 2D isothermal hydrodynamical simulations similar to Bergez-Casalou et al. (2020) (see Chapter 3) to monitor the growth of two planets accreting in the runaway accretion regime from the same disc. Our 2D isothermal set-up allows us to integrate the evolution of the planet masses for around 0.5 Myrs, which is longer than the majority of the studies investigating gas accretion onto planets with hydrodynamical simulations.

This Chapter is structured as follows: the numerical set-up is described in Sect. 4.2. In Sect. 4.3 we investigate the impact of different disc viscosities on the growth of each planet. A comparison with single accreting planets is developed in Sect. 4.4. Different planet separations are investigated in Sect. 4.5. In Sect. 4.6, we show the mass evolution of planets accreting at different times. Our findings are discussed in Sect. 4.7, where we develop the impact on the stellar gas accretion and on the planetary dynamic evolution of the systems. A comparison with the exoplanets population is discussed as well before we summarize and conclude in Sect. 4.8.

4.2 Numerical setup

In this Chapter, we simulate two accreting planets on fixed circular orbits embedded in their gaseous disc. As in Chapter 3, the hydrodynamical simulations are derived with `FARGO-2D1D` (Crida et al., 2007). Compared to Chapter 3, a second planet is added in the disc. In order to focus on the impact of gas accretion, dynamical interactions between the planets and planet migration are neglected. This choice is discussed in Sect. 4.7.2. The planets are fixed on circular orbits, at key positions corresponding to different period ratios. We privilege the term "period ratio" instead of "resonance", as they are not dynamically locked in resonance but are forced by the code to stay at their position. Four period ratios are investigated: 2:1, 3:1, 4:1 and 5:1. These positions were chosen such as the planets are far enough from each other to be considered dynamically stable during their growth (Chambers et al., 1996; Raymond et al., 2009b). In order to compare to a single planet case, we also simulate the growth of single planets located at positions corresponding to the investigated period ratios. The planets configurations are summarized in table 4.1.

Table 4.1: Semi-major axis of the different planet configurations considered in this Chapter.

Configuration	Inner planet r_p	Outer planet r_p
2 planets 2:1	5.2 AU	8.22 AU
2 planets 3:1	5.2 AU	10.82 AU
2 planets 4:1	5.2 AU	13.42 AU
2 planets 5:1	5.2 AU	15.18 AU
1 planet inner	5.2 AU	-
1 planet outer 2:1	-	8.22 AU
1 planet outer 3:1	-	10.82 AU
1 planet outer 4:1	-	13.42 AU
1 planet outer 5:1	-	15.18 AU

Each planet starts with an initial mass of 20 $M_\oplus$, allowing them to directly accrete in the runaway gas accretion regime (see Sect. 1.2.1). The planets are introduced in the disc with the mass-taper function described in section 2.1.1, making the planet grow from 0 to its initial mass in $n_{orb} = 3$ orbits of the inner planet.

Unlike in Chapter 3, the planets do not wait for their gap to reach equilibrium before accreting as we do not investigate their gap opening mass. Except for section 4.6 where the accreting times are specified, all planets start accreting simultaneously after 100 orbits of the inner planet.

Regarding the grid settings, they are the same as in Chapter 3: the 1D inner disc ranges from 0.1 AU to 0.78 AU, with the 2D grid ranging from 0.78 AU to 23.4 AU. The outer 1D disc spans from 23.4 AU to 260 AU. The resolution is such that there are five cells per Hill radius of the inner planet before it starts growing, which leads to $N_r = 802$ and $N_\phi = 1158$. Both 2D and 1D grids are shown in Fig. 4.1, where the perturbed surface density is shown on a logarithmic radial scale. The 2D-1D boundaries are represented by the black dashed circles, while the planets positions are represented by the blue and orange dots. In this example the planets are in the 3:1 period ratio.

As we enhance the planet separation, we need to adjust the 2D-1D boundary located at the outer edge of the 2D grid in order to properly take into account the perturbations of the furthest planet. Therefore, in the 4:1 and 5:1 case, this boundary is moved to 36.4

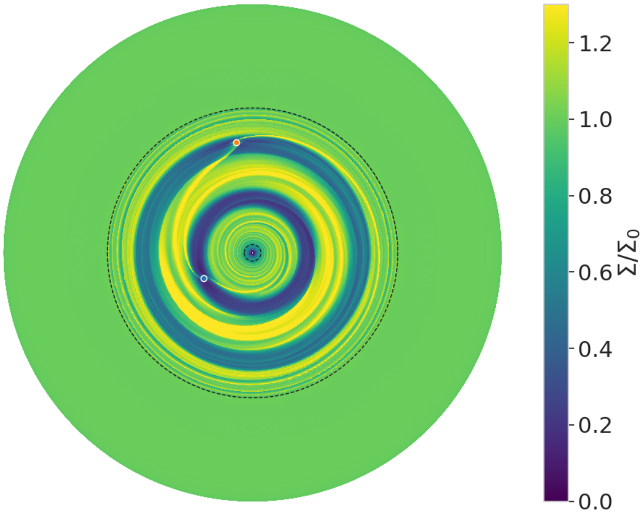

Figure 4.1: Grid configuration in `FARGO-2D1D`: the 1D-grid ranges from 0.1 AU to 260 AU and the 2D grid from 0.78 to either 23.6 AU in the 2:1 and 3:1 cases (shown here) or 36.4 AU in the 4:1 and 5:1 cases. The dots represent the location of the planets. The color scale shows the gas perturbed surface density. The planets are considered far enough from the boundaries of the 2D-grid for the disc to be considered axisymmetric.

AU, enhancing the radial number of cells of the 2D grid to $N_r = 1262$. The azimuthal number of cells remains unchanged.

As in Chapter 3, the surface density profile is chosen such that the total mass of the disc is $M_d = 0.1M_*$, leading to $\Sigma_0(r_0) = 93.6$ g/cm^2 with $r_0 = 5.2$ AU. Even if this can be considered as a heavy disc (Baillié et al., 2019), its large radial extent allows us to neglect self-gravity. The aspect ratio of the disc is constant. In the following section, different gas kinematic viscosities are investigated by varying the aspect ratio as well as the α-viscosity parameter. The investigated values are the same as in Chapter 3 and are summarized in table 4.2. Our fiducial parameters are shown in bold.

Table 4.2: Gas disc parameters used in this study.

Gas parameters	
Aspect ratio value at r = 1	$h_0 = 0.03, \mathbf{0.05}, 0.07$
Aspect ratio flaring index	$f_l = 0$
Alpha viscosity	$\alpha = 10^{-4}, \mathbf{10^{-3}}, 10^{-2}$
Surface density value at r = 1	$\Sigma_0 = 3.10^{-4} = 93.6$ g/cm^2
Surface density slope profile	$p = 1$
Planet parameters	
Planet initial mass	$m_p = 20M_\oplus$
Planet initial position	r_p = [5.2, 8.22, **10.82**, 13.42, 15.18] AU
Accretion time	$t_{start,acc} = 100$ orb.
Planet migration	NO
Planet interactions	NO
Planet mass taper	$n_{orb} = 3$
Planet eccentricity	0
Grids parameters	
Radial extent of 1D grid	[0.1 AU, 260 AU]
1D radial resolution	$N_{rad,1D} = 9214$
Radial extent of 2D grid	**[0.78 AU, 23.4 AU]**,[0.78 AU, 36.4 AU]
2D radial resolution	$N_{rad,2D}$ = **802**, 1262
2D azimuthal resolution	$N_{\phi,2D} = 1158$

4.3 Influence of the disc viscosity

The flow of gas in the disc is dictated by the kinematic viscosity, $\nu = \alpha h^2 r^2 \Omega_K$, which depends on the α-viscosity parameter in one hand and on the aspect ratio h of the disc on the other hand. In this section, we investigate the influence of the disc viscosity on the accretion behavior of two planets fixed in a 3:1 period ratio. We start by changing the α-viscosity parameter in section 4.3.1, then the influence of different aspect ratios is studied in section 4.3.2. We focus on the influence of the viscosity on the planet mass-ratio in a last section (Sect. 4.3.3).

4.3.1 Influence of the turbulent viscosity

As mentioned in previous sections, the turbulent viscosity is parametrized by the α-viscosity parameter. Disc turbulence increases with increasing α, leading to faster evolving discs (see Sect. 1.1.1 and 3.4.3). We show in Fig. 4.2 the planetary accretion rates (top row) and the resulting masses (bottom row) for planets in discs with different α parameters. From left to right, α increases from 10^{-4} to 10^{-2}. The behavior of the accretion rates is the same as in Chapter 3: reducing the viscosity induces a slightly lower planetary accretion due to a slower flow of gas in the vicinity of the planet (see Sec. 3.4.2).

The difference in accretion rates between the inner and the outer planet slightly evolves as a function of time and viscosity (top row of Fig. 4.2). At the beginning, the planets accrete in the first Machida et al. (2010) accretion regime (dominated by Bondi accretion), leading to a larger inner planet (see eq. 2.4). The flip in accretion rate is due to the switch of accretion regime, from a Bondi to a Hill dominated accretion scheme (see Section 3.4.2). While the inner planet accretes slightly more in the first regime of accretion, the accretion rates become more similar when the planets accrete in the second accretion regime.

This similarity in accretion rates results in planets of similar masses (bottom row of Fig. 4.2). Even if the planets are more massive in the high viscosity case than in low viscosity discs, the differences between the inner and outer planet masses does not seem to be highly influenced by the change of α-viscosity. This can be expected as the Machida accretion recipe does not directly depend on this parameter (see eq. 2.4). The influence of the α-viscosity is indirect, as it influences the gas flow around the planet, changing the surface density $< \Sigma >_{0.9 r_H}$ from which the planets accrete their gas.

As observed in Sect. 3.4.2 with single planets, instabilities are triggered at low viscosity (Klahr & Bodenheimer, 2003; Fu et al., 2014). The Rossby Wave Instability (RWI, Lovelace et al., 1999; Li et al., 2001) produces vortices at the locations of steep pressure gradients, such as produced by the gap of massive planets. The presence of vortices modify the flow of gas in the vicinity of the planets, creating the oscillations observed on the top left panel of Fig. 4.2. In the case of two accreting planets, vortices are produced at three different locations: at the outer edge of the outer gap, in between the planets and even at the inner edge of the inner gap. We show in Appendix A.1 the 2D (r, ϕ) surface density maps of the disc containing the planets in the 3:1 period ratio at low viscosity ($\alpha = 10^{-4}$ and $h = 0.05$) at three different times. The strength of these vortices depend on the growing timescale of the planets (Hammer et al., 2017, 2021). However here, due to the presence of the second planet, the vortex present in between the planets quickly vanishes (in less than 4×10^4 years). The strongest vortex is the one located at the outer edge of the gap of the outer planet and takes about 10^5 years to vanish.

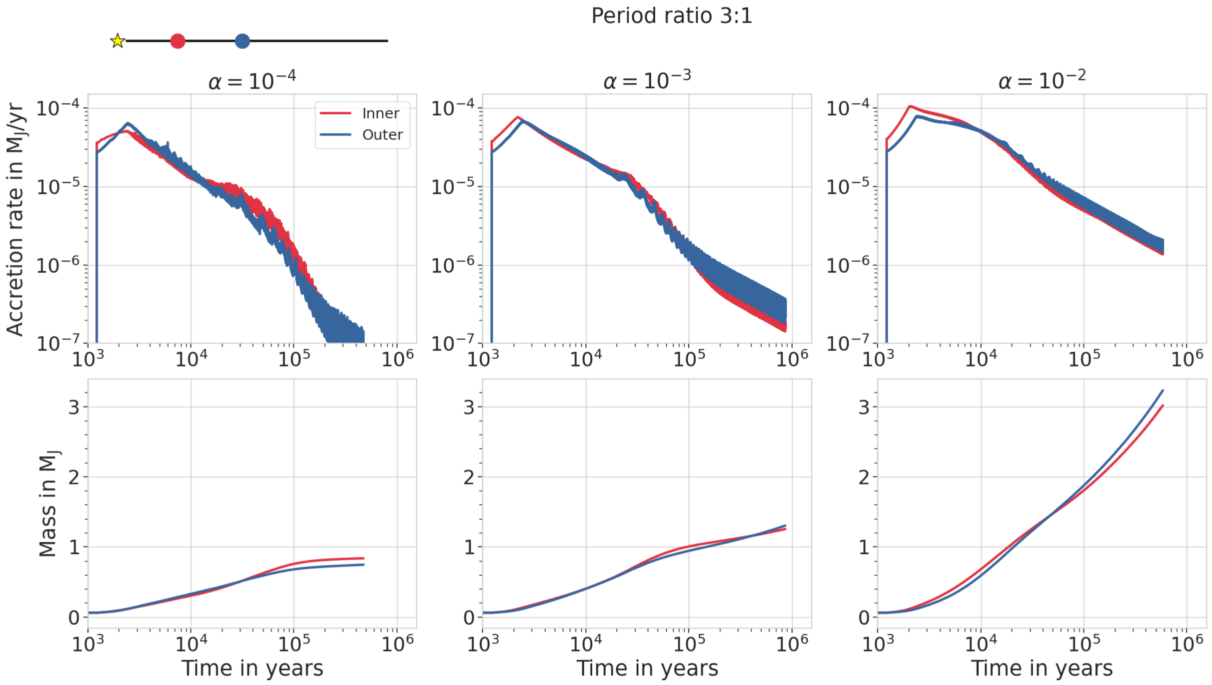

Figure 4.2: Planetary accretion rates (top row) and masses (bottom row) as a function of time for different α-viscosities. Here the planets are fixed in a 3:1 period ratio. As in Bergez-Casalou et al. (2020), the accretion rates are slightly increasing with increasing viscosity. The oscillations in the accretion rate at low viscosities are due to the presence of vortices. The inner and outer planets display similar accretion rates, leading to similar planet masses.

4.3.2 Influence of the aspect ratio

Another way to study the impact of the disc viscosity is to modify the disc's aspect ratio. We show the impact of this parameter in Fig. 4.3. Here, α is fixed to 10^{-3} and h varies from 0.03 (left panel) to 0.07 (right panel). The fiducial value of 0.05 is shown in the middle panel for reference. Note that changing the constant aspect ratio from 0.03 to 0.05 accounts for a reduction of viscosity ν of a factor 2.8 while enhancing the aspect ratio from 0.05 to 0.07 increases the disc viscosity of a factor 2.0.

Even if the change in the disc kinematic viscosity is weaker than when the α-viscosity is varied in the previous section (change of a factor ten), the accretion rates behavior are significantly different depending on the aspect ratio. This arises from the direct dependence of the accretion rate recipe on the aspect ratio, while it is indirectly dependent on α. When the gas disc scale height H increases, it requires a larger Hill sphere radius for a planet to switch from the Bondi regulated accretion regime to the Hill regulated one (see eq. 2.4 and Sect. 3.4.1). This can be seen on the top row of Fig. 4.3: the flip in accretion rates occurs at later times for higher aspect ratios. As in Chapter 3, at low aspect ratio (left panel), the planets initial mass is large enough to start accreting immediately in the second regime. In this case, the accretion rates always decrease in time, proportionally to the local surface density.

The timing of the accretion switch between the Bondi and Hill regimes has an important influence on the evolution of the planet masses and their difference. As the inner planet accretes significantly more than the outer one when they are limited to the Bondi accretion regime, a later switch results in more diverse planetary masses. Therefore, the difference between the inner and outer planets increases with an increasing aspect ratio.

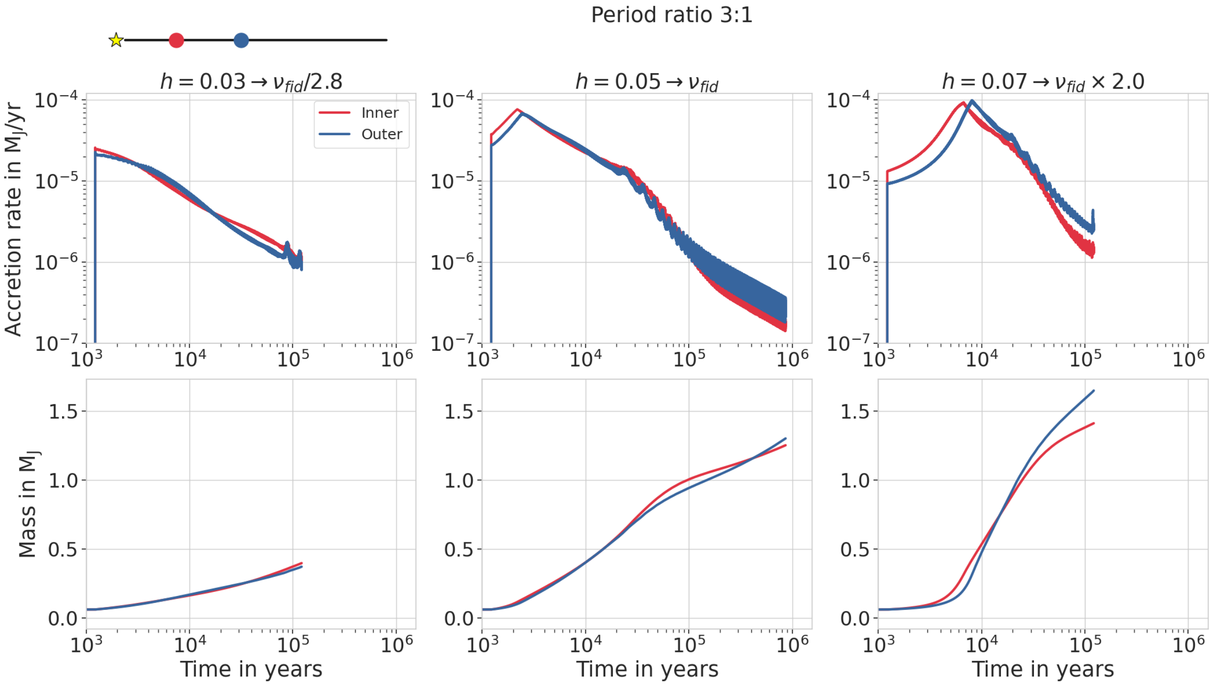

Figure 4.3: Same as Fig. 4.2 but for different aspect ratios, increasing from left to right, with $\alpha = 10^{-3}$. We note on the top of each row also the difference in kinematic viscosity caused by the change in the disc's aspect ratio ($\nu = \alpha h^2 r^2 \Omega_K$). The differences in the planetary accretion rates originate from the structure of the accretion itself (see eq. 2.4). At low aspect ratio ($h = 0.03$, left panel), the accretion starts immediately in the second Machida regime. On the other hand, for $h = 0.07$, the accretion takes more time before switching regimes, leading to a very different planet mass evolution.

4.3.3 Impact on the planets mass ratio

In order to better understand the differences in planetary mass, we analyse in Fig. 4.4 and Fig. 4.5 the ratios of the planetary masses. We focus first in Fig. 4.4 on the impact of the α-parameter on these ratios. The top row represents the mass ratio as a function of time. We arbitrarily decided to show the ratio of the outer planet mass divided by the inner planet mass: this means that when the ratio is decreasing, the inner planet accretes more than the outer one and vice-versa. Depending on the viscosity, we see that the ratio shows different flips. A first flip ① occurs at each viscosity around 2.5×10^3 years. This flip originates from the accretion rate switch discussed in the previous paragraphs: the planets become massive enough to change their accretion regime, resulting in a higher accretion rate for the outer planet (increasing mass ratio).

A second flip ② is observed around 10^4 years, at all viscosity except for $\alpha = 10^{-2}$ (right panel, which is discussed below). This flip is linked to the formation of deep planetary gaps. In the bottom panels of Fig. 4.4, we show the perturbed surface densities at the different times marked by the vertical lines in the top panel. The perturbed surface density is defined as in Chapter 3: it is the surface density of the disc in presence of the planets normalized to the surface density of a disc without planets at the same time ($\Sigma_{perturbed}(t) = \Sigma_{planet}(t)/\Sigma_{disc}(t)$). These perturbed surface density profiles are used to determine when a gap is opened. As in Sect. 3.4.3, we use the definition suggested by Crida et al. (2006): a gap is considered opened when the gas surface density is depleted by 90% compared to a disc without planets. This threshold is represented by the horizontal

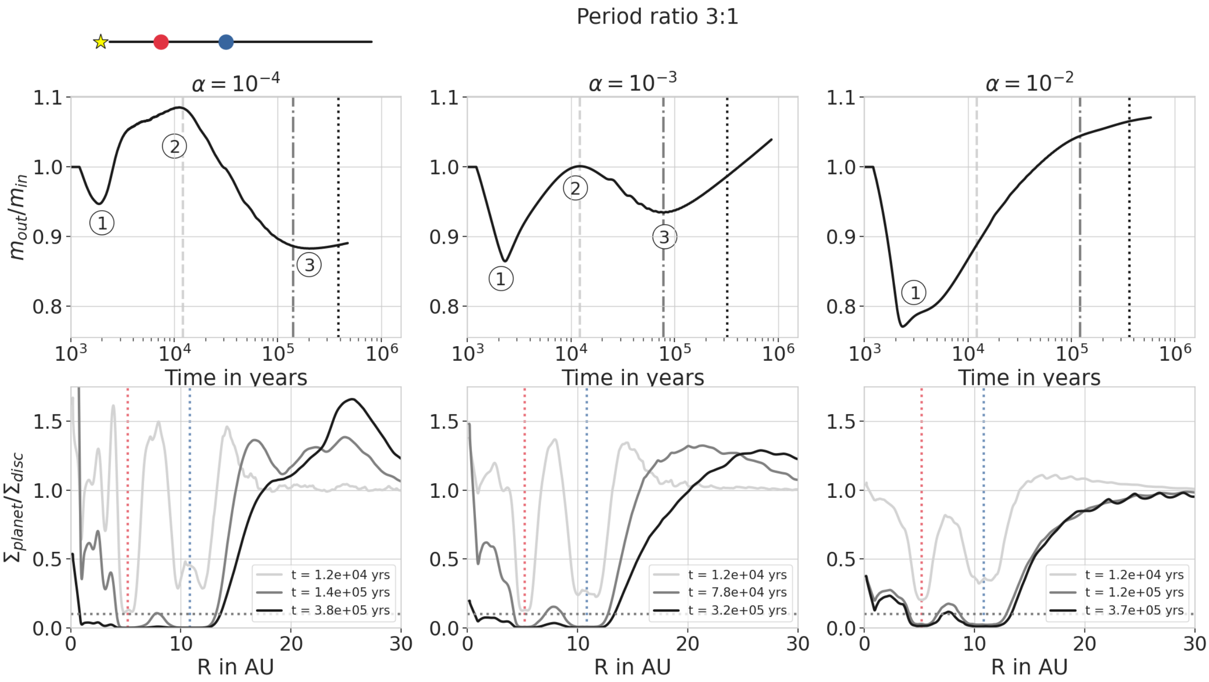

Figure 4.4: Mass ratio (top row) and perturbed density profiles (bottom row) as a function of time for different α-viscosities. As in Fig. 4.2 the planets are fixed at the 3:1 period ratio positions, represented by the 2 vertical dotted lines in the bottom row. The horizontal dotted lines in the bottom panels mark the $\Sigma_{planet}/\Sigma_{disc} = 0.1$ threshold where we consider that a gap is opened (Crida et al., 2006). In the top panels, a decreasing (resp. increasing) mass ratio indicates that the inner (resp. outer) planet is accreting more than the other planet. Different flips are observed in the evolution of the mass ratios. The first one ① is common to all the viscosities and originates from the choice of accretion recipe (see eq. 2.4). At low viscosities, a second flip ② is observed and originates from the enhancement of planetary gas accretion due to the consequent amount of material pushed in each planet feeding zone by the formation of the gap of the neighbouring planet. A last flip ③ is occurring when the inner planet is starved by the outer planet as the disc becomes depleted in gas. The color of the surface density profiles shown in the bottom row corresponds to the color of the different vertical lines in the top row, representing different times. The last snapshot of the perturbed surface density is taken 2.4×10^4 years (2000 orbits of the inner planet) after the last mass ratio flip, shown by the vertical black dotted line. This density profile shows the depletion of the inner disc ($r < r_{p,out}$). At high viscosity (right panel), we observe only a single mass ratio flip ①. Here, the viscosity is large enough to dissipate the impact of gap formation on the mass ratio of the planet masses.

gray dotted line at $\Sigma_{planet}/\Sigma_{disc} = 0.1$. The second flip ② in the mass ratio occurs when the inner planet reaches this threshold: when the inner planet opens a deep gap, it starts to accrete more than the outer planet.

This link between the gap opening of the inner planet and the decrease of the mass ratio can be explained by the impact of gas accretion on gap opening described in Chapter 3. At low viscosity, gas accretion does not help to carve a gap because the disc reaction time is long. The gas is therefore dominantly pushed away from the planets orbit by gap formation, enhancing the surface density in between the planets as well as in the inner and outer regions of the disc. This results in a perturbed surface density larger than one (light-gray line in the bottom panels of Fig. 4.4). When the gap is opened, the planetary gas accretion becomes the dominant process influencing the gas distribution. As the inner planet opens its gap first, it starts by depleting the material present in between the planets

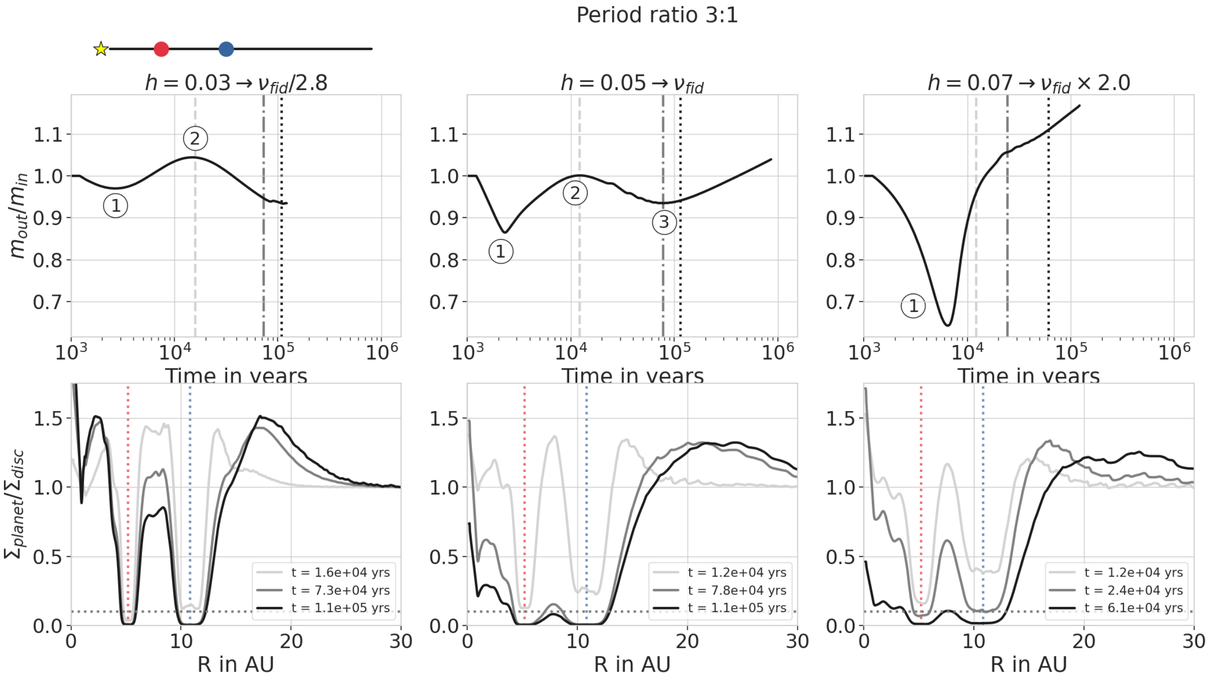

Figure 4.5: Same as Fig. 4.4 but for different aspect ratios, with $\alpha = 10^{-3}$. As in Fig. 4.3, we note on the top of each row also the difference in kinematic viscosity caused by the change in the disc's aspect ratio. Here the mass ratio evolutions differ in amplitude, but they present the same behavior as in Fig. 4.4. The difference in amplitude comes from the dependence of the accretion routine (eq. 2.4) on the aspect ratio, and not on the α-viscosity.

and in the inner region of the disc, leading to an inner planet with a higher accretion rate than the outer one. Then, the outer planet also opens a deep gap, helping the inner planet to deplete the material located in between them. At this stage, the amount of gas present around the inner planet (at $r < r_{p,out}$) is dictated by three different processes. Gas is removed from this region of the disc by i) the accretion onto the planets and ii) the accretion onto the star, and is replenished by iii) the viscous diffusion of the gas from the outer part of the disc through the planet gaps. As here the viscosity is low, only a small amount of gas manages to diffuse through the gaps of both planets. This results in a depletion in gas of the inner disc, resulting in the starvation of the inner planet.

The accretion rate of the inner planet is reduced because the planet is starved. The third flip ③ in the mass ratio, shown in the top panels of Fig. 4.4, corresponds to the moment when the outer planet starts accreting more than the starved inner planet, as it is supplied in gas by the outer region of the disc. The depletion of the inner disc can be seen in the corresponding perturbed surface density profiles of the bottom row of Fig. 4.4: the gray line shows a depleted region in between the planets and in the inner disc. We additionally show the surface density profiles 2 000 inner planetary orbits ($\simeq 2.4 \times 10^5$ yrs) after the last mass ratio flip ③: after this time, the inner disc is almost completely emptied in gas, with a perturbed surface density of less than 0.1 within 12 AU. It is clear that after this time, the outer planet will accrete more than the inner one, until it becomes the most massive planet of the system. The only differences between the $\alpha = 10^{-4}$ (left panel) and $\alpha = 10^{-3}$ (middle panel) cases are the delay in time of the flips due to different viscous timescales and the presence of vortices at $\alpha = 10^{-4}$, influencing the accretion rates of both planets, as mentioned earlier.

The behavior of the mass ratio in a high viscosity disc (right panel) is slightly different than at lower viscosities. As explained in Chapter 3, at high viscosity, gas accretion helps gap formation. Therefore, the material located in between the planets and the inner disc is immediately depleted by gas accretion and viscous stellar accretion. As these two regions are not enhanced in gas by gap formation, the inner planet accretion rate slowly reduces as the inner disc is immediately depleted in gas, meaning that no additional mass ratio flip is observed except for the very first one originating from the accretion recipe. At this viscosity, the gas manages to diffuse efficiently through the gaps of both planets, avoiding a complete depletion of the inner region: this can be seen by comparing the surface density profiles at two different times towards the end of the simulation (marked by the gray and black lines on the right panels). Indeed, the difference in the profiles after 2 000 orbits of the inner planet is small, meaning that the disc gas flow is high enough to prevent the total depletion of the inner region, unlike at lower viscosities (middle and left panels). However, in this configuration, even if the material around the inner planet is replenished by viscous evolution, the amount of gas diffused through both gaps is not high enough to allow the inner planet to accrete more than the outer planet.

These behaviors at high and low viscosity are also observed when we vary the disc aspect ratio. In Fig. 4.5, we show the evolution of the mass ratios as a function of time (top row) as well as the perturbed surface density profiles at given times (bottom row) for the different aspect ratios presented in Fig. 4.3. As the behaviors described in the previous paragraphs are only dependent on the gas kinematic viscosity ν, we recover the same behaviors when we change the aspect ratio: at low viscosity, the mass ratios are highly influenced by gap formation whereas at high viscosity, the mass ratio does not present more than one flip. However, due to the dependence of the accretion recipe on the aspect ratio, the amplitudes of the mass ratios are highly dependent on h. While the mass ratios reached values between 0.8 and 1.1 for the different α parameters (Fig. 4.4), here the planets show a larger spread in mass ratio at the beginning of the simulations in discs with larger aspect ratios. However, once the gaps are formed in all cases and the inner disc is depleted, all the mass ratios result in planets with similar masses, with an outer planet less than 1.2 times larger than the inner planet.

As a conclusion, the mass ratio between the planets is highly and mainly dependent on the disc kinematic viscosity ν. The resulting mass ratios are close to 1 even after 0.5 Myrs of evolution, leading to planets with rather similar masses. In all the explored cases, we expect the outer planet to become the most massive planet of the system.

4.4 Single accreting planet compared to two accreting planets

The presence of the second planet highly influences the growth of the inner planet. In order to quantify the effect of the presence of the second planet, we compare the growth of the two planets to two separate simulations where the planets are alone in their disc.

4.4.1 Accretion rates and masses comparison

It has been shown in Sect. 4.3.3 that the outer planet has the capacity to starve the inner planet once the gaps are formed and the inner disc is depleted. Consequently, the differences between two accreting planets and single accreting planets should increase with time. We show in Fig. 4.6 the comparison between three different simulations: the first

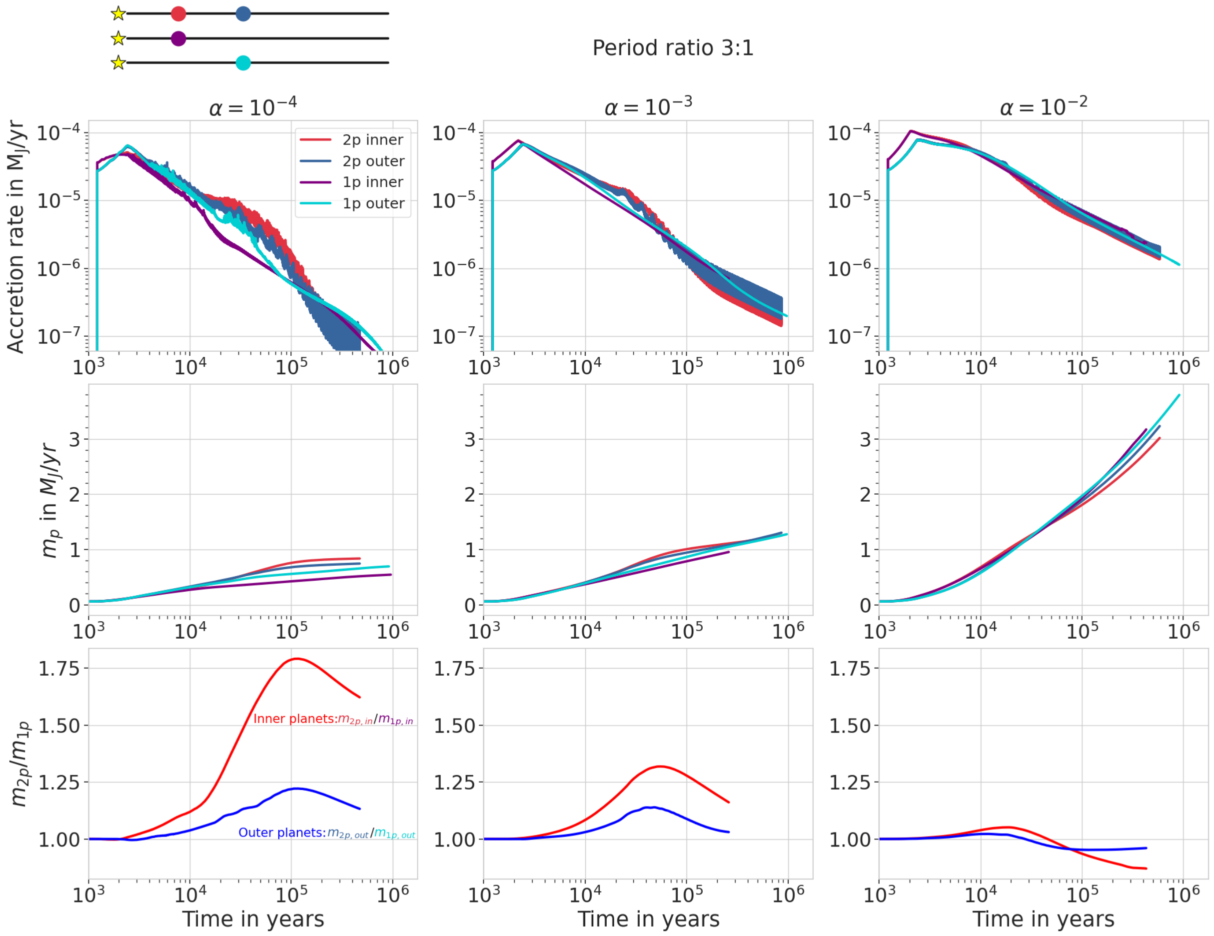

Figure 4.6: Comparison between single accreting planets and two simultaneously accreting planets. The planets are fixed at positions corresponding to the 3:1 period ratio. As in Fig. 4.2 and 4.3, the top row presents the accretion rates as a function of time and the middle row, the planet masses. On the bottom row, we show the ratio of the masses in the single and two planets case: the red line represent the ratio of the inner planets ($m_{2p,in}/m_{1p,in}$) and the blue line represent the outer planets ratio ($m_{2p,out}/m_{1p,out}$). At low viscosity (left panels), the differences with the single planet case originates from the additional formation of vortices in between the planets, enhancing the accretion rates during the vortices lifetime. At high viscosity (right panel), while the outer planet is slightly impacted by the presence of the inner planet, we observe the starvation of the inner planet. We expect to see similar behavior at lower viscosities but delayed in time, due to longer viscosity timescales.

one, represented by the blue and red colors, considers the simultaneous accretion of two planets in the 3:1 period ratio as in the previous section; in the second simulation, the disc hosts only a single planet located at the position of the inner planet (purple line); in the third simulation, the disc hosts also a single planet located this time at the position of the outer planet (cyan line). Each planet configuration is represented in the top left corner of the figure. Like in Sect. 4.3.1, different α are shown in the different columns, increasing from left to right.

The different planetary gas accretion rates are shown in the top row of Fig. 4.6. At high viscosity, in the right panel, the accretion rate between the single planets and the two planets are very similar. As expected, only the accretion rate of the inner planet is significantly impacted by the presence of the second planet: after 2×10^4 yrs, the accretion rate of the inner planet in the two planet case (red line) starts to be reduced compared to the single planet case (purple line). This is particularly visible in the bottom right panel of Fig. 4.6, where we compare the masses in the two planets case to the single planet case: the red line represents the mass ratio of the inner planets ($m_{2p,in}/m_{1p,in}$) while the blue line represents the mass ratio of the outer planets ($m_{2p,out}/m_{1p,out}$). After 2×10^4 yrs, the red line continuously decreases, meaning that the planet at the inner position has a reduced accretion rate in the two planets case compared to the single planet. This is due to its starvation, as discussed in the previous section.

At high viscosity, the outer planet is only slightly impacted by the presence of the inner planet. While their accretion rate seems very similar (blue and cyan line in the top right panel), the mass ratio shows a slight reduction of the mass in the two planets case (blue line slightly below one in the bottom right panel). This originates also from the depletion of the inner disc: the gas accretion rate of the outer planet only relies on the material located outside the planet's orbit in the two planets case, while the single planet accretes material from both the outer and inner disc.

At lower viscosities, the impact of the presence of the second planet occurs earlier and is more important. Focusing on the intermediate viscosity ($\alpha = 10^{-3}$, in the middle column), we see that the accretion rates (top panel) in the two planets case are enhanced after $\sim 10^4$ years for both the inner and the outer planet compared to the single planets. This enhancement, absent at high viscosity, originates from the gap formation process: as mentioned in Sect. 4.3.3, at this viscosity, gap formation pushes material away from the vicinity of each planet, enhancing the surface density around them. In this case, the planets are close enough to each other to push material in the feeding zone of the neighbouring planet. Therefore, the inner planet pushes material towards the outer planet and vice-versa. Each accretion rate is enhanced until the depletion of the inner disc ($r < r_{p,out}$), resulting in lower accretion rates than in the single planet cases. This enhancement can also be seen in the evolution of the planet masses (bottom and middle panels of Fig. 4.6 for $\alpha = 10^{-3}$). In the long term, the evolution of the mass ratios between the two planets and single planets case are expected to behave like at high viscosity: the inner planet will be starved in gas, leading to a smaller inner planet in the two planets case compared to the single planet case. As for the outer planet, once the inner disc is depleted, it is fed only by the outer disc in the two planets case whereas the single outer planet accretes also from the inner disc, leading to a decreasing outer planet mass ratio $m_{2p,out}/m_{1p,out}$.

Regarding the lowest viscosity case ($\alpha = 10^{-4}$, in the left column of Fig. 4.6), the presence of additional vortices located in between the planets significantly alters the accretion rates of the two accreting planets compared to the single planets. Even if the single planets also produce vortices, leading to the oscillations observed in their accretion rate too, the additional vortex present in between the planets quickly enhances the accretion of both planets. Except from this non negligible influence, the overall evolution of the planet masses follows the trend observed at higher viscosities, where we expect the different flips to occur at latter times due to the larger viscous time scale.

Finally, we also compare the masses of the outer planets with the inner planets, as in Sect. 4.3.3. In Fig. 4.7, the solid line represents the ratio of the outer planet mass to the inner planet mass in the case of the two planets configuration (same as Fig. 4.4), whereas the dashed line represents the ratio of the mass of the single planet located at the outer location to the mass of the single planet located at the inner location. Again, a schematic representing the different configurations is shown in the top left corner of the figure. At intermediate viscosity ($\alpha = 10^3$, middle panel of Fig. 4.7), the mass ratio in the

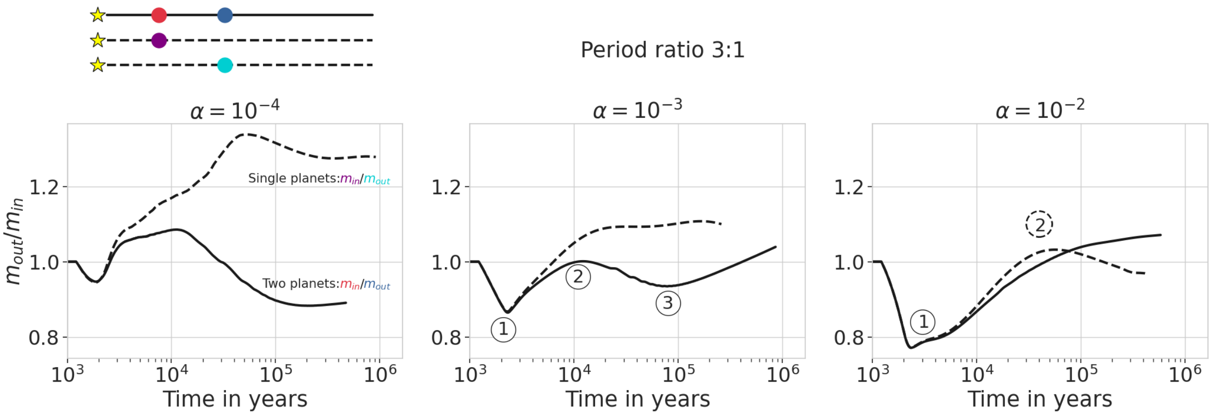

Figure 4.7: Comparison of the mass ratios in the single planet and two accreting planets cases as a function of time and for different viscosities. Again, the planets are fixed at the 3:1 period ratio positions. In solid lines we show the mass ratios of the outer over the inner planet in the two planets case, whereas the dashed lines represent the mass ratio of the single planets. We observe different behaviors when a second planet is added: at high viscosity, the inner planet in the disc with two planets is quickly starved by the outer one, resulting in a single flip ①. The mass ratio in the single planets case present a second flip ② because the flow of gas through a single planetary gap is high enough to maintain a higher accretion of the inner planet compared to the single outer planet. In the two planets case, the gas flow to the inner disc is too reduced by the presence of the two planets, resulting in a larger outer planet (increasing mass ratio). At lower viscosities, the single planet case does not present the flips ② and ③ originating from the material pushed by gap formation of the neighbouring planet and depletion of inner disc ($r < r_{p,out}$) respectively.

single planets case (dashed line) features only one flip ① before reaching a plateau after $\sim 2 \times 10^4$ yrs. As before, the first flip ① is due to the accretion recipe, and it occurs at the same time in the two planets case as in the single planets case. The second flip ② in the case of the two planets in the same disc, due to gap formation, is absent in the single planets case. It is expected because it is the presence of the second planet creating a gap that enhances the accretion of the inner planet, which is not the case in the single planet simulations. With our disc profile (a surface density power law of -1 and constant aspect ratio), the single planet located at the outer position accretes naturally more than the inner planet, leading to an increasing mass ratio. The plateau observed after $\sim 2 \times 10^4$ corresponds to the moment when the single planets open a deep gap: then, the accretion of each planet is mainly governed by the flow of gas originating from the outer region of the disc. With our disc profile and due to the proximity of the planets, the gas flow from outside of the inner planet position is similar to the flow from outside of the outer planet position, leading to similar accretion rates. The same behavior is observed at low viscosity ($\alpha = 10^{-4}$, in the left panel of Fig. 4.7), considering the perturbations and enhancement produced by the vortices.

At high viscosity ($\alpha = 10^{-2}$, right panel of Fig. 4.7), the behavior of the single planet simulations is again different compared to the simulations with two planets. The absence of additional flips after 2×10^3 yrs in the two planets case is explained by the absence of impact of gap formation at this high viscosity (see Sect. 4.3.3): the viscosity is high enough to cause the immediate depletion of the inner disc via both viscous accretion towards the star and the accretion of the inner planet, immediately leading to its starvation. However, in the mass ratio of the single planets, we observe another flip ② around 4×10^4 yrs.

After this time, the inner planet accretes more than the outer one. This originates from the flow of gas reaching the inner disc once each gap is opened: at this viscosity, the gas can significantly flow through the gaps of the planets. However, it is easier to flow through the gap of the single planet located in the inner region as it is less wide than the gap of the single planet located in the outer region. This results in a inner disc that is more depleted in the case of the outer single planet than in the case of the inner single planet, leading to the reduction of the accretion rate onto the outer single planet.

4.4.2 Impact on the accretion onto the star

The presence of a single gap opening planet can alter the gas accretion onto the central star (e.g., see Sect. 3.3.3 and 3.5.1). Here, we investigate the impact of the presence of a second planet on the evolution of the stellar gas accretion. As in Sect. 3.3.3, the stellar gas accretion rate is defined by the flow of mass through the inner edge of the disc: $\dot{M}_* = -2\pi\ r_{in} v_{r,in} \Sigma_{in}$, where $v_{r,in}$ and Σ_{in} are the radial velocity and surface density at the inner boundary located at $r_{in} = 0.2$ AU. In Fig. 4.8, we compare the stellar accretion rates of discs containing either two accreting planets in the 3:1 period ratio (solid black line), or single planets located at the inner (purple dashed line) and outer (cyan dotted dashed line) positions of the two planets simulation, or hosting no planets at all (gray dotted dashed line). Again, the α-viscosity increases from left to right. Independently on the viscosity, the stellar accretion rate in the presence of two planets features oscillations: they originate from the periodic overlap of the planets spiral density arms, locally enhancing the surface density of the gas.

At intermediate viscosity ($\alpha = 10^{-3}$, middle panel of Fig. 4.8), the presence of the planets has two distinct impacts. Before 10^4 yrs, the planets are not large enough to influence the accretion onto the star. Between 10^4 and 10^5 yrs, the discs hosting planets harbor an enhanced stellar accretion rate compared to the disc without planets. This originates from gap formation: material is pushed to the inner region, feeding the star. After 10^5 yrs, planetary gas accretion and gaps prevent part of the gas to reach the inner region, leading to the decrease of the stellar accretion rate. It takes more time for the disc hosting the single planet located at the outer position to reduce the stellar accretion rate due to the larger inner disc present in this configuration. After a given time (here after 2×10^5), the flow of gas through the gaps reach a quasi equilibrium state, leading to a linear evolution of the stellar accretion rate, with a similar slope compared to the slope of the stellar accretion rate of the disc without planets. At this stage, the stellar accretion rate is reduced by a factor between 4 and 5 when the disc hosts two accreting planets compared to the disc without planets.

The enhancement produced by the two accreting planets is slightly more pronounced than in the single planets case as it relies on the material pushed by both planets. As one could expect, the decrease of the stellar accretion rate in the two planets case occurs at the same time as in the disc hosting the single planet located at the inner position. However, at this viscosity, the reduction of the stellar accretion rate is only slightly influenced by the presence of the second planet, resulting in a decrease of only $\sim 30\%$ compared to the single inner planet case. This means that the flow of gas reaching the inner disc is mostly governed by the influence of the inner planet.

At high viscosity, the viscous spreading of the gas prevents the enhancement of the stellar accretion rate: the material pushed to the inner regions by the gap opening planets is both less important than at lower viscosity and quickly diffused towards the star by

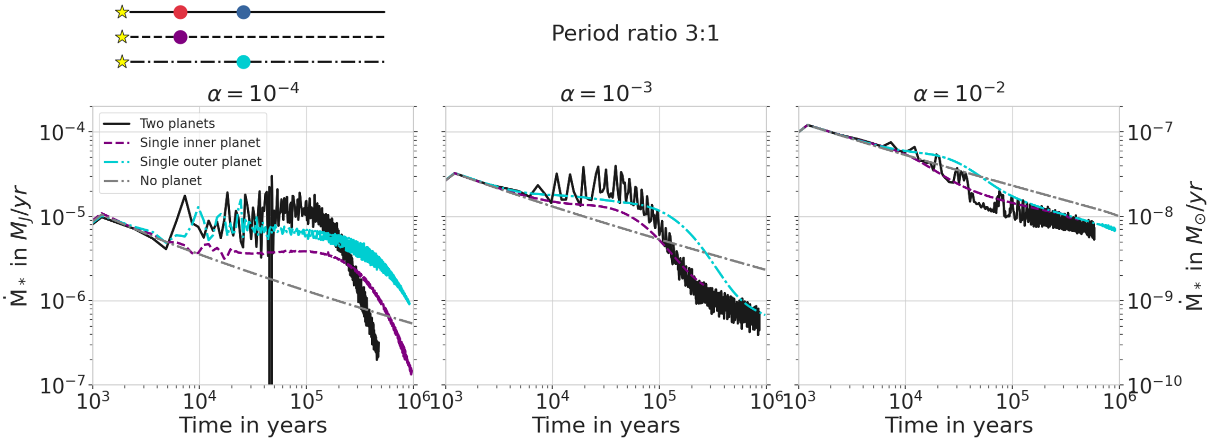

Figure 4.8: Influence of a second accreting planet on the stellar accretion rate at the inner edge of the disc (0.2 AU). As in Fig.4.6 and 4.7, the planets are located in the 3:1 period ratio positions, with an increasing α-viscosity from left to right. The comparison is made between the two planets case (solid black line), the single planet cases (purple dashed line for the single inner planet and cyan dotted dashed line for the single outer planet) and a disc without planets (gray dotted dashed line). The oscillations present in the case of the two accreting planets are due to the overlap of their spiral arms, coupled with the presence of vortices at low viscosity. At high viscosity (right panel), the accretion onto the star in presence of two accreting giant planets is only slightly reduced compared to the single planet case: the viscosity is high enough to flow through both gaps and maintain a certain flow in the inner region. On the other hand, at lower viscosities (middle and left panels), the planets push material by gap formation to the inner regions of the disc, enhancing the accretion compared to a disc with no planet, then they deplete this same region by accretion. This effect was also observed in Bergez-Casalou et al. (2020). Compared to a disc with no planet, the accretion onto the star is only reduced by up to a factor of 3 in presence of multiple giant planets, similar to the scenario with a single planet.

viscous spreading. This results in a reduction of the stellar accretion rate after 10^4 yrs only. The gas is efficiently diffused through the planet gaps, maintaining a high stellar accretion rate, even in presence of multiple accreting planets. Here, the stellar accretion rate is only reduced by up to a factor of 2.5 compared to the accretion in a disc without planets. Moreover, the presence of the second planet only influences the stellar accretion rate by less than 20% compared to the cases with single planets. Focusing on the single planets case, we see that the stellar accretion reaches a similar equilibrium in both cases, independently on the planet location. As expected, with this high viscosity, the presence of accreting planets barely influences the gas disc evolution.

The opposite behavior is observed at low viscosity ($\alpha = 10^{-4}$, left panel of Fig. 4.8). Here, the stellar accretion rate is highly influenced by the vortices and by the gaps formed by the planets. Material is efficiently pushed in the inner regions, enhancing the stellar accretion rate by up to a factor of 10 in the disc hosting two planets compared to the accretion of a disc without planets. The reduction of the accretion occurs at later time than at higher viscosity, which is expected because the planets grow slower and that gap opening takes more time (see Sect. 3.4.3). However, the presence of the second planet in the disc highly influences the stellar accretion rate, because its viscosity is not high enough to diffuse gas through both gaps. Due to the long viscous timescale, we are not able to determine the final reduction factor compared to the higher viscosity cases. At the end of the simulation containing the two planets, the stellar accretion rate is reduced by a factor of 3 compared to the disc without planets, giving a lower estimation of the reduction factor. In Sect. 4.7.1, we discuss the impact that this reduction factor can have on observations and compare it to other studies.

4.5 Influence of the planet separation

Our study focused so far on planets placed at positions corresponding to the 3:1 period ratio. However, the separation between forming planets is not fixed in time as they can dynamically interact with the disc and with each other (e.g., Baruteau et al., 2014; Crida & Bitsch, 2017). While we will investigate the impact of the radial evolution of the planets on their growth in a future study, we study in the following section the impact of the planet separation in their growth by placing the planets at different period ratios.

4.5.1 Impact on the mass ratio

As shown in Sect. 4.3.3, the planet mass ratio evolution is well representative of the accretion history of the planets. We show in Fig. 4.9 the mass ratio evolutions of two simultaneously accreting planets located at different period ratios, ranging from 2:1 up to 5:1. These period ratios, represented to scale in the top left corner of the figure, were chosen such as the planets can be considered dynamically stable during their growth, as we neglect their dynamical interactions. As in Fig. 4.4, the mass ratio presented is the ratio of the outer planet mass divided by the inner planet mass and each panel represents an α-viscosity, increasing from left to right. A darker line depicts a larger planet separation.

Independently on the viscosity, we first observe that the first mass ratio flip ①, originating from the switch of accretion regime in our accretion recipe (see eq. 2.4), is delayed in time when the planets are further away from each other. Indeed, with our disc profile, a planet located further away in the disc has a slightly lower gas accretion rate, meaning that it will need more time to reach the mass needed to switch from the Bondi to the Hill accretion regime. This delay affects the similarities between the planets: the further the planets are from each other, the more extreme are their mass ratios at the beginning of the simulations (i.e., the deeper the first mass ratio flip ① is).

Focusing on the high viscosity behavior ($\alpha = 10^{-2}$, right panel of Fig. 4.9), we observe the same behavior as described in Sect. 4.3.3 except for the 2:1 period ratio. While the other period ratios feature only the first flip ① due to the rapid depletion of the inner disc via viscous stellar accretion, a second flip ② is observed at around 10^5 yrs in the mass ratio of the 2:1 period ratio case. In this disc, the planets are close enough from each other to facilitate the diffusion of gas through both gaps compared to the other period ratios, as they quickly form a common gap. As the flow of gas to the inner disc is higher, more material is present around the inner planet. In this case, the amount of gas diffusing through both gaps, is high enough to prevent the starvation of the inner planet, leading to a decreasing mass ratio.

The behavior of the mass ratio at $\alpha = 10^{-3}$ (middle panel of Fig. 4.9) is also the same for each period ratio. The second mass ratio flip ②, occurring at around 10^4 yrs, is always due to the formation of the planetary gaps. The delay in the flip originates from the time needed for the outer planet to also significantly enhance the surface density in between the planets via gap formation. The amplitude of the mass ratio between the second ② and third flip ③ (i.e., the difference between the local maximum ② and the local minimum ③) is decreasing with decreasing planet separation. As this moment corresponds to the

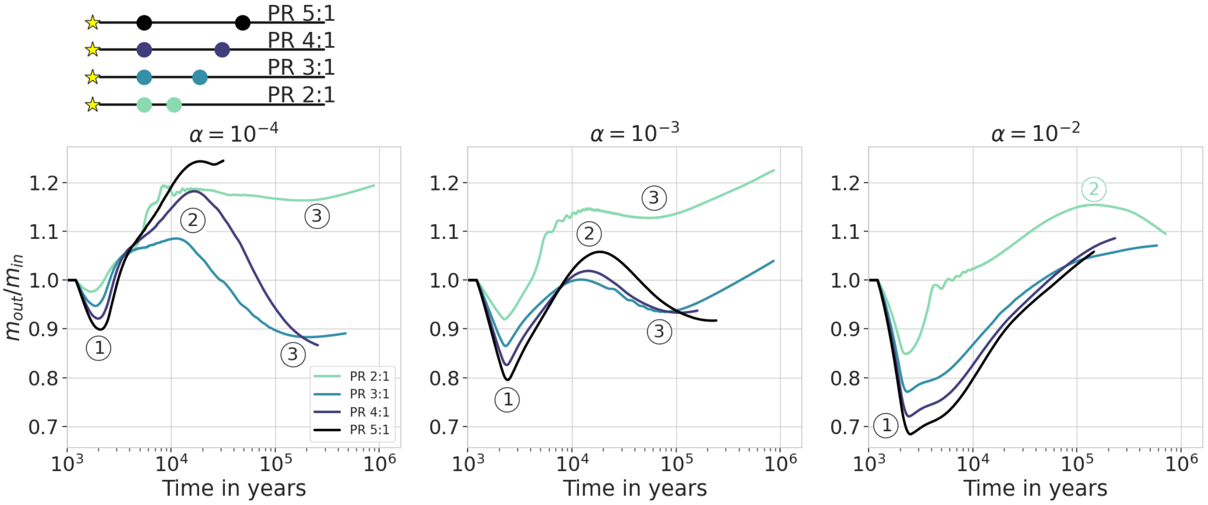

Figure 4.9: Mass ratio as a function of time for different α-viscosities and different period ratios. The darker the line, the further away the planets are located from each other. The separation between the planets has a small impact on the similarities between the planets, meaning that planets which start accreting at the same time will lead to planets with similar masses. The behavior of the mass ratio evolution is not impacted by the planet separation: at all viscosities the mass ratio flips are due to the same reasons described in Fig. 4.4. The exception is for the 2:1 period ratio at high viscosity (right panel): here the planets are close enough and the viscosity is sufficiently high to maintain a significant flow toward the inner disc through the gaps, preventing the inner planet to be starved. This results in an addition mass ratio flip ②, similar to the high viscosity single planets case of Fig. 4.7.

moment when the inner planet is accreting more thanks to the enhancement of material in between the planets and in the inner disc after gaps are formed, closer planets have less material in between them by construction, leading to a smaller mass ratio amplitude. Note that it also takes more time for planets located further away from each other to empty the material located between the planets, meaning that the inner planet accretes more than the outer planet for a longer time compared to planets closer to each other. Therefore, the inner planet is starved more easily the closer the planets are.

At low viscosity ($\alpha = 10^{-4}$, left panel of Fig. 4.9), the planet separation has an additional impact on the formation of vortices. In the 2:1 period ratio simulation, the planets quickly create a common gap, preventing the formation of a strong vortex in between them. As we mentioned in Sect. 4.3.1, as vortices push material towards the planets, it means that the gas accretion of the planets in the 2:1 period ratio are less impacted by the presence of vortices compared to planets located further away from each other. In the 5:1 period ratio case, the planet gaps are clearly distinct from each other. Each planet therefore create sharp density gradients at the inner and outer edge of their gaps, resulting in the formation of four vortices. Even though the vortices located in the inner disc (i.e., inner to the outer planet) dissipate quickly, they influence the evolution of the planet masses. Except from the formation of vortices, the global behavior of the mass ratio is due to the same processes as at intermediate viscosity.

Overall, independently on the planet separation or disc viscosity, the mass ratios stay close to one ($0.7 < m_{out}/m_{in} < 1.25$). We discuss in Sect. 4.7.4 how does this compare to the observed planetary systems.

4.5.2 Impact on the gap opening mass

The gap opening mass is an important parameter used both in theoretical models to approximate when a planet switches from the fast type I migration to the slow type II migration (e.g., Ndugu et al., 2018; Bitsch et al., 2019; Miguel et al., 2020; Ndugu et al., 2021) and in observations to indirectly derive the masses of embedded planets from the observed characteristics of gaps (e.g., Zhang et al., 2018; Asensio-Torres et al., 2021). As we showed in Sect. 3.4.3, gas accretion has a non negligible impact on the gap opening mass. In this section, we investigate the influence of the presence of a second accreting planet on the gap opening mass of each planet.

As in Sect. 3.4.3, we compare in Fig. 4.10 the gap opening mass of our accreting planets to different gap opening criteria derived in previous studies (Crida et al., 2006; Fung et al., 2014; Gyeol Yun et al., 2019). The gap opening masses of the inner planets are shown on the left panel of the figure while the outer planets are shown on the right panel[1]. As in the previous section, the color represents the different period ratios, as can be seen on the schematics of the disc configurations represented in the top of the figure. Triangles represent the gap opening masses of the planets located in a two planets disc and single planet gap opening masses are shown with circles. The gray circles correspond to the gap opening masses of the single planets located at the inner location (they correspond to the gap opening masses presented in Sect. 3.4.3 for the fiducial gas accretion rate). The different lines represent the different gap opening criteria compared in this study: the blue dashed line shows Crida et al. (2006)'s criterion (see eq. 1.29), the solid orange line represents the work done by Fung et al. (2014) (see eq. 1.31) and the dotted dashed red line shows the criterion derived by Gyeol Yun et al. (2019) based on the study by Kanagawa et al. (2015) (see eq. 1.30). In the right panel, the viscosity is divided in discrete intervals for each of the studied viscosity ($\alpha = 10^{-4}, 10^{-3}, 10^{-2}$) to help visualising the different configurations.

In Sect. 3.4.3, we conclude that gas accretion has a different impact on the gap opening mass depending on the disc viscosity: at high viscosity, gas accretion helps carving deeper gaps resulting in a lower gap opening mass for an accreting planet while at low viscosity, gap formation is not helped by gas accretion, resulting in a higher gap opening mass for an accreting planet. When a second planet is added in the disc, the accretion of each planet is impacted by the gap formation of the neighbouring planet, as shown in Sect. 4.4. However, this impact depends on the viscosity.

At high viscosity, gas accretion helps carving a deeper gap. Here, with $\alpha = 10^{-2}$ and $h = 0.05$, the disc is at the intersection between the high viscosity regime and low viscosity described in Sect. 3.4.3, meaning that the gas accretion has no important impact on the gap opening mass. The gap opening masses are therefore solely dependent on the amount of gas diffusing through the gaps. As the gas diffuses efficiently in this case, gap formation is not impacted by the presence of a second planet. Indeed, the inner disc is more depleted by viscous accretion than by the accretion of both planets, meaning that the material pushed away by the gap forming planets is dissipated via viscous spreading. This can be seen in Fig. 4.10, where the gap opening masses are the same in the single or two planets case, for both the inner and outer planets.

At lower viscosities, gas accretion does not help gap formation. Therefore the gap opening mass depends on the accretion rate of the planet. As presented in Sect. 4.4.1,

---

[1] Note that the simulation did not reach gap opening mass yet in the case of the outer planet of the 5:1 period ratio at low viscosity. However, we clearly see the expected trend.

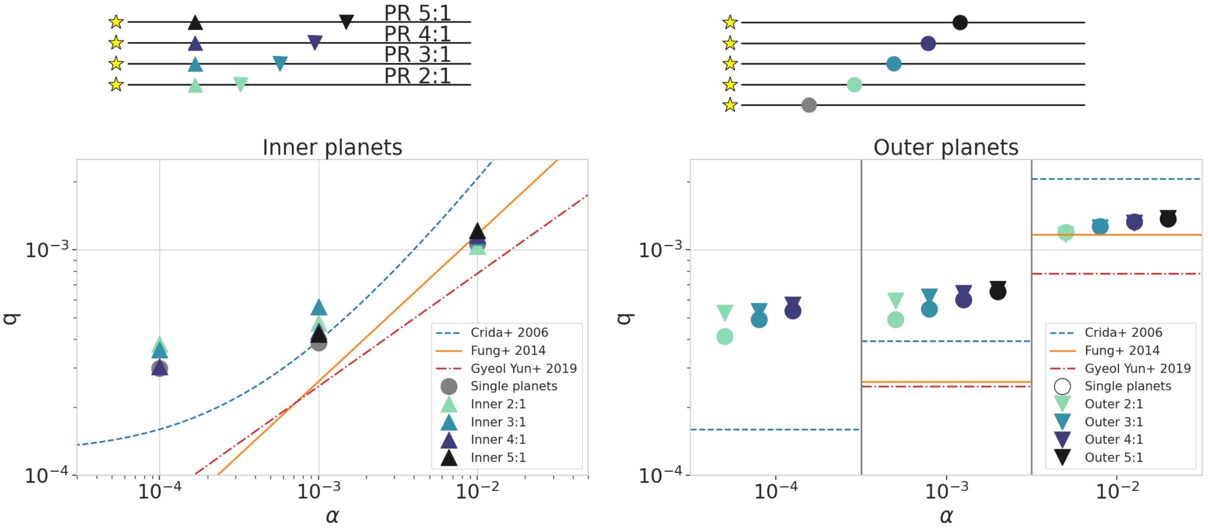

Figure 4.10: Gap-opening mass as a function of the viscosity for different criteria and our simulations as in Bergez-Casalou et al. (2020). In the left panel, I show the gap opening masses of the inner planets in the two planets case compared to the single planet cases located at the inner position. The outer planet cases are shown in the right panel. In each panel, the lines represent the different gap-opening criteria from the literature: Crida et al. (2006) in dashed blue, Fung et al. (2014) in solid orange and Gyeol Yun et al. (2019) in dashed-dotted red. As shown with the cartoons above the panels, the two planets case are represented by triangles (upward for the inner planets and downward for the outer planets) and the single planets are represented by circles. The inner single planet case is shown in gray while the colored circles correspond to the colors of the outer positions in each configuration. For clarity, in the right panel, the viscosity is divided in discrete intervals, allowing us to compare the gap opening mass at one given viscosity in the different configurations. The gap opening masses of the inner planet are barely impacted by the presence of a second outer planet. On the other hand, at low viscosity, the closer the planets are from each other, the higher the gap opening mass is compared to the single planet case.

the accretion rates of the two accreting planets are slightly enhanced compared to the single planets due to the formation of the planets gaps pushing material in the feeding zones of the neighbouring planet. This slight enhancement of the accretion rate of the planets leads to slightly higher gap opening masses. This impacts both the inner and the outer planets, as shown in Fig. 4.10. As the gap opening mass then relies on the amount of material pushed towards the neighbouring planet, planets that are close enough from each other enhances their gap opening mass more. Intuitively, when the planets are further from each other, they tend to behave as if they are isolated and have gap opening masses closer to the single planets simulations.

Overall, the gap opening masses are barely impacted by the presence of a second planet in the disc. The small differences originate from the differences in accretion rates as the planets push material towards each other. Considering the conclusions of Chapter 3, it seems that the gas accretion rate on the planet itself has a stronger impact on the gap opening mass than the presence of a simultaneously accreting companion.

4.6 Influence of delayed accretion

Giant planet formation models have very few constraints on the timing at which runaway gas accretion occurs (see Sect. 1.2.1). So far, we only considered the simultaneous accretion of both giants. However, depending on the disc local properties and on the formation mechanism, giant planets located in the same disc could start accreting at different times. We investigate here the influence of the delayed accretion on the evolution of the planetary growth. Different time delays are considered, on the outer and on the inner planet. We base our delays on the mass of the neighbouring planet: the accretion on the second planet is allowed when the other planet reaches 0.3 M_J, 0.5 M_J and 1 M_J. We choose to investigate the impact of the accretion delay on the 2:1 period ratio configuration at high and intermediate viscosities as they reach these masses in a reasonable computational time.

All the resulting mass ratios are shown in Fig. 4.11. The mass ratio of planets simultaneously accreting is shown in black, and corresponds to the 2:1 mass ratio presented in Fig. 4.9. Note the difference in the mass ratio scale: while before the mass ratios are shown on a linear scale, here the scale is logarithmic for readability. The colors represent the different delays: darker colors represent shorter delays; the purple lines show the mass ratio when the inner planet accretion is delayed whereas the green lines represent the mass ratio when the outer planet accretion is delayed. We mark by a dot the moment when both planets have masses larger than 0.3 M_J and can be considered as gas giant planets after this time. The large spread in mass ratio is induced by our initial choice for the different delays. Indeed, as we wait for the neighbouring planet to reach a given mass before accreting, this sets the maximal and minimal mass ratio reached by the planets. We therefore expect the planets to reach a final mass ratio located in between these initial values.

The evolution of the different mass ratios is very different from the simultaneously accreting planets. When the outer planet accretion is delayed (green lines in Fig. 4.11), it allows the inner planet to accrete slightly more gas before being starved by the growth of the outer planet. At high viscosity, the gas diffuses efficiently through the planet gaps. This diffusion efficiently depletes the disc in gas, leading to a high stellar accretion rate (see Sect. 4.4.2). Therefore, a longer delay results in accretion in a more depleted disc. As a consequence, the mass ratio is lower for longer delays.

At lower viscosity, the effect of viscous spreading as described above can be perturbed by the formation of the inner planet gap. However, the gap opening mass at this kinematic viscosity is around 0.5 M_J at the location of the inner planet. For a delay of 400 orbits, corresponding to an inner planet mass of 0.3 MJ, the outer planets starts accreting while the inner planet did not create a deep gap yet. This leads to a very similar final mass ratio evolution as in the simultaneous case. However, we know from Sect. 4.3.3 that when the inner planet creates its gap, it starts to deplete the material located in the inner disc and in between the planets. Therefore, when the outer planet starts accreting even later (e.g. when the inner planet has reached its gap opening mass), the inner planet already depleted part of the material in between them, leading to a lower gas accretion rate of the outer planet compared to the simultaneous case. This results in lower mass ratios for longer delays.

The delayed accretion of the inner planet (purple lines of Fig. 4.11) highly depends on the depth of the gap of the outer planet and on the viscosity of the disc. Indeed, at low viscosity, if the inner planet starts accreting before the formation of the gap of the

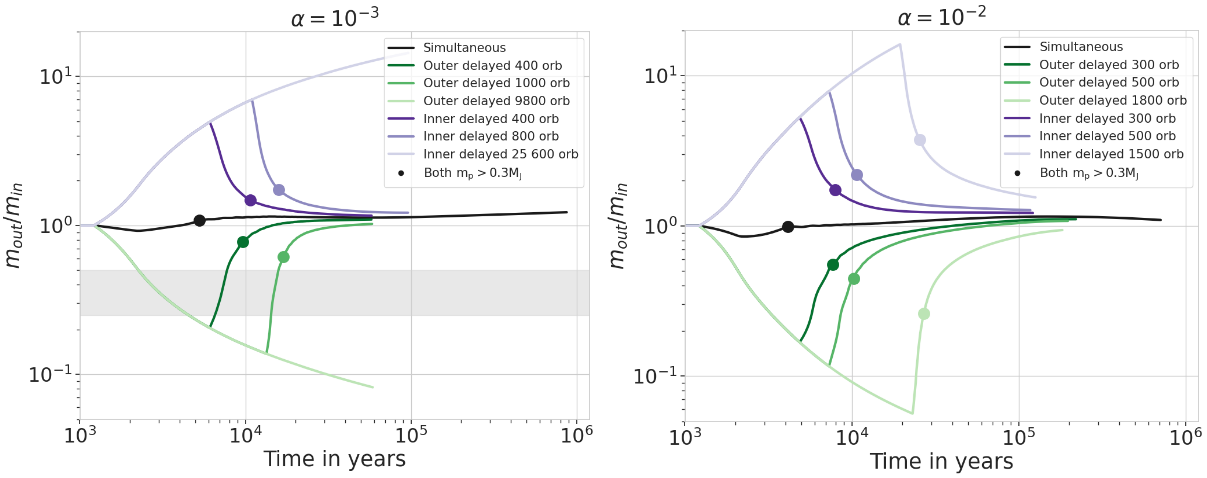

Figure 4.11: Mass ratio as a function of time for different delay of accretion on the inner (purple lines) or the outer planet (green lines). The planets are located in the 2:1 period ratio configuration. The two panels represent two different viscosities: $\alpha = 10^{-3}$ in the left panel and $\alpha = 10^{-2}$ in the right. Darker lines represent shorter delays. Note that this time the mass ratio is displayed on a logarithmic scale compared to previous plots which are on a linear scale, due to the extreme mass ratios induced by our initial setup here. The dots mark the moment when both planets have reached at least 0.3 M_J and can be considered as gas giant planets. The gray rectangle represents the region where the mass ratio lies between 0.25 and 0.5 and shows the region where the planets meet the required conditions to enter outward migration (needing $\alpha \lesssim 10^{-3}$). Independently on the viscosity, all the mass ratios quickly tend towards the $m_{out}/m_{in} = 1$ line, leading to similar planet masses in either case ($0.8 < m_{out}/m_{in} < 2$ after 10^5 yrs).

outer planet, then the inner region is not depleted in gas yet. The behavior of the mass ratio then quickly tends to be the same as in the simultaneous case. However, if the outer planet already opened its gap, then a longer delay of accretion results in a more depleted inner disc. The inner planet has therefore less material to accrete, leading to higher mass ratios. At high viscosity, the same behavior occurs, with the inner disc being efficiently depleted by stellar accretion.

Even if different mechanisms influence the mass ratio in the case of delayed accretion, the giant planets always end up with rather similar masses: $0.8 < m_{out}/m_{in} < 2$ after 10^5 yrs. We discuss in Sect. 4.7.4 how does this compare to the observed mass distributions in the exoplanet population and what kind of constrains on planet formation can be derived.

4.7 Discussion

4.7.1 Accretion onto the star

In Sect. 4.4.2, we investigate the influence of the presence of multiple gas accreting planets on the stellar accretion at different viscosities. The results are compared to the stellar accretion in discs hosting single planets and in discs without any planet. We find that the presence of the second planet only has a significant effect when the viscosity of the disc is low ($\alpha \lesssim 10^{-4}$). For higher viscosities, the presence of the second planet only influences the stellar accretion rate by up to 30% compared to the case with single planets.

We can compare our results with two planets to the different stellar accretion rates obtained with different planetary accretion rate in the previous Chapter (Sect. 3.3.3). At high viscosity, the presence of the second planet has less impact on the stellar accretion rate compared to a significant enhancement of the planet accretion rates. Due to the uncertainties in gas accretion rates (see Sect. 1.2.1), it is impossible to use the stellar accretion rates to determine if the protoplanetary disc hosts a single fast accreting planet or multiple planets accreting at a lower rate.

As discussed in Sect. 3.5.1, our results are quite different from the study derived by Manara et al. (2019). In their models, they find that the stellar gas accretion rates can be reduced by over two orders of magnitude when the disc is hosting accreting giant planets. While we showed in the previous Chapter that these large spreads of stellar accretion rates could only be reached by widely changing the disc viscosity (over several orders of magnitude), we show here that the presence of a second accreting companion cannot explain such large reduction of the stellar accretion rate neither. Indeed, while reducing the disc viscosity to $\alpha = 10^{-4}$ enhanced the impact of the two accreting planets on the stellar accretion rate, we expect the reduction to be of a factor of 10 at most compared to a disc without planets. These discrepancies between our study and the work done by Manara et al. (2019) are the same as mentioned in Sect. 3.5.1. Their model simulates a 1D gas disc while our study is performed in 2D, allowing us to better accurately determine the flow of gas through the gaps of the planets Lubow & D'Angelo (2006). Moreover, their planetary gas accretion rates might be overestimated as they rely on the unperturbed surface density (Mordasini et al., 2012), while we showed here that the depletion of the inner disc leads to the starvation of the inner planet and consequently a reduction of its accretion rate.

As in the previous chapter, our simulations indicate that planetary gas accretion might have a smaller impact than expected on the stellar gas accretion rates, even in the presence of multiple accreting planets.

4.7.2 Impact of planet dynamics

In order to determine the impact of the gas accretion on two planets embedded in the same disc, we neglected both the dynamical interactions between the planets and their migration. Regarding migration, different studies investigate how it impacts gas accretion (e.g., Dürmann & Kley, 2015; Crida & Bitsch, 2017; Dürmann & Kley, 2017). The main results of these studies are that the evolution of the planet characteristics (i.e., mass and semi-major axis) highly depends on the timescales of each process: a fast migrating planet tends to accrete more gas as it quickly moves towards regions with high surface densities. However, as we showed in Bergez-Casalou et al. (2020) (Chapter 3), gas accretion has an impact also on the gap opening mass, influencing the migration speed of the planet as it transitions from a fast type I to a slow type II migration. This effect was observed in Crida & Bitsch (2017), where their accreting planet slowed down its migration speed earlier compared to a non accreting planet. Therefore, the resulting planetary systems highly depend on the timescales of migration, gap formation and gas accretion.

Another dynamical effect can play an important role in the evolution of the planets. Previous hydrodynamical studies show that multiple planets can be captured in resonant chains during the gas phase of the disc (e.g., Baruteau & Papaloizou, 2013; Pierens et al., 2014; Kanagawa & Szuszkiewicz, 2020). The capture in resonance can have an important impact on the migration behavior of the planets. For example, in the Grand Tack scenario (see Sect. 1.3.1), Jupiter and Saturn are believed to migrate inward and then outward due do their capture in resonance. This outward migration is occurring for precise disc parameters and mass ratios, as shown in Pierens et al. (2014). As migration can be altered by the capture in resonance, gas accretion and gap formation will also be indirectly altered by the planet radial motion.

We plan on implementing the impact of both migration and capture in resonance on the growth of our two planets in follow-up studies. We expect that, if the planets start accreting simultaneously, then the structure of the resulting system highly depends on the timing at which gap formation will occur because it will slow down the migration of the planets and determine their accretion behavior. A potential outward migration can delay the depletion of the inner disc, altering the mass ratio behavior discussed in Sect. 4.3.3. However, due to the high interdependence of each mechanism, it is difficult to precisely predict how the planets will behave.

4.7.3 Implications for the Grand Tack scenario

In the Grand Tack scenario, if Jupiter and Saturn have a mass ratio between 0.25 and 0.5, then they can migrate outwards to their current locations (Masset & Snellgrove, 2001; Crida et al., 2009; Pierens et al., 2014). In Sect. 4.5.1, we show that if the planets start accreting simultaneously, they reach mass ratios that are between 0.7 and 1.3. Therefore, in order to trigger outward migration, the planets have to start accreting with a delay. It also requires that the inner planet is more massive than the outer planet, otherwise the torques arising from the outer disc are too large, leading to inward migration. Pierens et al. (2014) find that outward migration depends also on both the period ratio of the planets and the disc parameters. In order to trigger outward migration in a low mass disc, a capture in a 2:1 resonance is needed. If the disc is more massive, then the planets need to reach the 3:2 resonance. Both scenarios require a relatively low α-viscosity ($\alpha \lesssim 10^{-3}$).

Within our current parameter study, we only investigated the impact of delayed accretion in the 2:1 period ratio configuration. At low viscosity (left panel of Fig. 4.11), the conditions are barely met for the outward migration to occur: for the two shorter delays (dark and normal green lines), the mass ratios quickly evolve in the disc, making the planets barely stay in the needed mass ratio range (marked by the gray area). Therefore with our current results, it seems that outward migration of the two giant planets is very challenging to reach. However, we plan to expand our parameter space study in the near future, allowing us to better analyse if and how a planetary system like Jupiter and Saturn could have formed via the Grand Tack scenario. In the mean time, we discuss in the following section how our current mass ratios compare to the observed exoplanetary systems and what kind of constrains can be derived.

4.7.4 Comparison to exoplanets

Considering our current parameter space study, planets accreting from the same disc end up with very similar planet masses. Delaying the accretion of the respective planets allowed us to broaden slightly the mass ratio range reached, however in 10^5 years, the final mass ratio obtained still are lying between 0.8 and 2. These mass ratios are quite different from the mass ratios observed in different planetary systems. In Fig. 4.12, we compare the evolution of our mass ratios to different exoplanetary systems. The data originates from the NASA exoplanet archive[2]. We selected the planetary systems as follows: first of all, we are interested in systems containing exactly two giant planets (i.e., with $m_p > 0.3\ M_J$) as we investigate the accretion of two planets in the runaway gas accretion phase. Our simulation considers planet formation in a disc orbiting the Sun, therefore the selected planetary systems orbit Sun-like stars ($4700K < \mathrm{T_{eff}} < 6500K$ and $\log(g_*) > 4$). Each panel represents the ratio of the outer planet mass divided by the mass of the inner planet like in previous figures as a function of the planet period ratio. Vertical dashed lines represent the investigated period ratios. The colorbar shows the sum of the planet masses in M_J.

From the top panel the figure, it is clear that the planetary systems observed hosting two giant planets have a broad range of mass and period ratios. We highlight the systems hosting at least one hot Jupiter (i.e., planets with periods shorter than 10 days) with a thick black contour. These planets might be formed after a very efficient inward migration, leaving them very close to their host star. This results in a system where the period ratio of the planet is very large. As we do not implement migration in this study, we focus on the planets located closer to each other. Interestingly, it appears that planets located closer to each other seem to have more similar masses (except for 3 systems with mass ratios higher than 8). For better readability and comparison with our simulation, a zoom on the planets placed in the gray rectangle is shown in the lower panel of the figure.

Due to computational constraints, we could not investigate the evolution of the mass ratio until the end of the disc lifetime. Therefore, in order to make the comparison with fully formed planets as the one observed in the different planet surveys, we show the maximal and minimal mass ratios obtained by our simultaneously accreting planets with the pink, red and purple vertical lines. As we selected the observed systems by considering planets with $m_p > 0.3\ M_J$, we show the mass ratio spread once both planets reached 0.3 M_J. The ratios obtained for different viscosities are slightly offset from the exact period ratio for visibility. At low viscosity and small period ratios, the mass ratio range was too small to be represented by a line, therefore the final mass ratio is shown with a square. Over the 45 observed planetary systems (including Jupiter and Saturn and hot Jupiters), 5 have a mass ratio lower than 0.7, 11 systems have a mass ratio lying between 0.7 and 1.3 and 29 systems have a mass ratio higher than 1.3. The majority of the systems cannot be explained by the simultaneous accretion of the planets. We also note that very few systems (only 5 here) feature a mass ratio as seen in our Solar system with Jupiter and Saturn. While this might be explained by the difficulty of our current facilities to see low mass planets, it also raises the question of the peculiarity of the Solar system among other systems: is our planetary system common or singular ?

In this study, such a large spread in mass ratio was only reached when the planets are accreting in the runaway gas accretion phase with different delays. This accretion delay can be justified by the dependence of the beginning of the runaway gas accretion phase on the disc characteristics. Here, we followed the classical original core accretion model, where it is assumed that runaway gas accretion is triggered when the planetary core reaches a mass of 20 $M_\oplus$, with a solid core of 10 $M_\oplus$ surrounded by a first gaseous atmosphere of 10 $M_\oplus$ (see Sect. 1.2.1). However, more recent studies show that the initial total mass of the core can vary depending on the local properties of the disc. In Piso & Youdin (2014), they show that runaway gas accretion can be triggered at different core masses depending on the local disc temperature and opacity (Bitsch & Savvidou, 2021). Moreover, in the pebble accretion scenario, the pebble isolation mass corresponds to the

---

[2] https://exoplanetarchive.ipac.caltech.edu/docs/data.html

mass at which the core is shielded from the pebble flux by the pressure bump created by its own gap. Then, the atmosphere of the planetary core is not heated anymore by the accretion of solids and cools down, entering the runaway gas accretion phase. The pebble isolation mass depends on the disc's aspect ratio, α-viscosity, pressure profile and turbulent diffusion of the particles (Bitsch et al., 2018). Therefore, the delay of accretion time between two giants highly depends on the local properties of the disc. Protoplanetary discs can be flared, featuring large aspect ratio variations, and different hydrodynamical properties can lead to important radial variations of α (e.g., Flock et al., 2011; Dullemond & Penzlin, 2018; Delage et al., 2022). The disc properties can lead to the delay of either the inner or the outer planet.

Even when we applied different accretion delays, the long term trends could only reproduce mass ratios lying between 0.8 and 2. With these parameters, the only remaining way to reach large (or small) mass ratios, is to stop the accretion at a given mass ratio. The timing of the dissipation of the gas disc can be crucial here. For example, photoevaporation can dissipate the gas disc from inside-out by creating a inner hole separating the inner disc ($r < 1$ AU) from the outer disc and quickly depleting it (for a review, see Ercolano & Pascucci, 2017). Such depletion of the disc might have the capacity to starve the giant planets, influencing the evolution of their mass ratio.

To summarize, the simultaneous runaway gas accretion of planets cannot explain the distribution of mass observed in discs as it leads to planets with very similar masses. To increase the difference in planet masses, the accretion between the planets have to be delayed and efficient disc dispersal mechanisms are required to end the growth of the planets at given mass ratios. These two last points highly depends on the disc local properties of the gas.

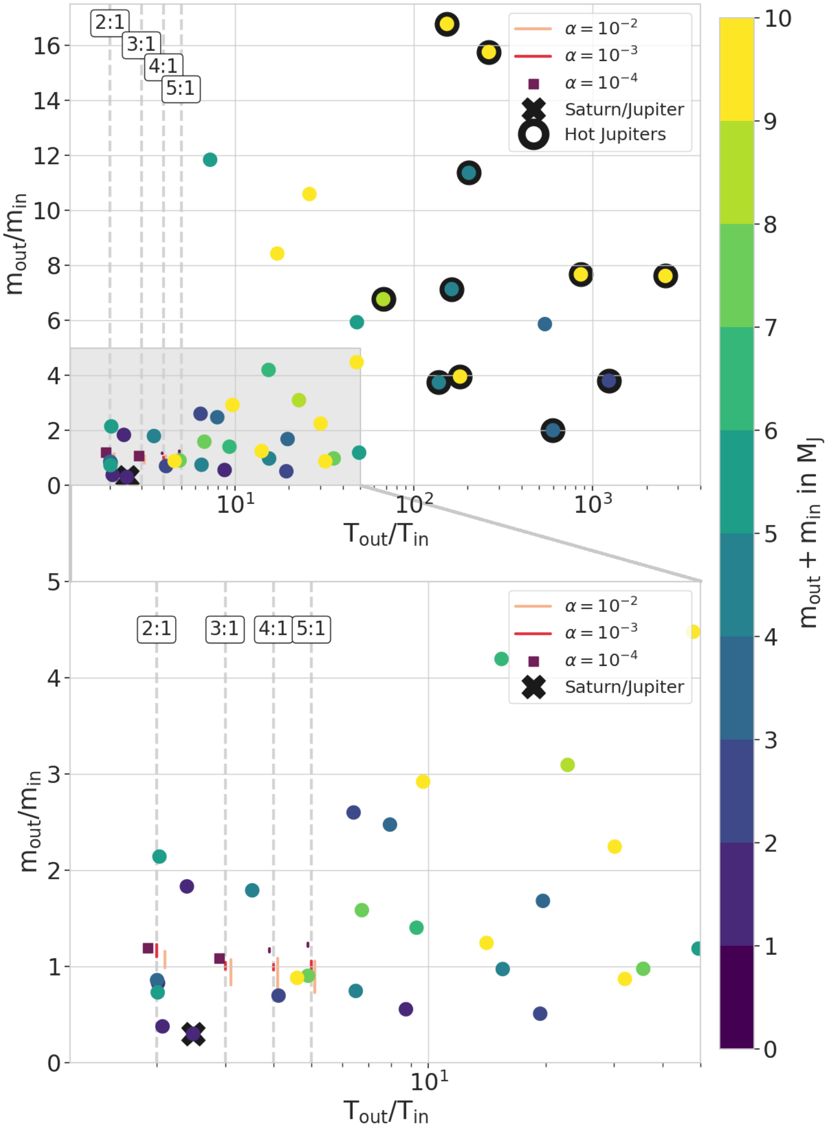

Figure 4.12: Mass ratio evolution of the two accreting planets as a function of their period ratio compared to exoplanetary systems. The data comes from the NASA exoplanet archive, for which we selected the systems as follows: the system contains exactly 2 detected planets, both of them larger than 0.3 M_J. They orbit a single Sun-like star ($4700K < T_{\rm eff} < 6500K$ and $\log(g_*) > 4$). The color of the dots represent the sum of the planet masses in Jupiter masses, without error bars. A black contour surround the planets considered as hot Jupiters (i.e. with a period of less than 10 days). The investigated period ratios from our simulations are marked by vertical gray dashed lines. As we expect their formation to be highly influenced by the dynamics of the system which we do not model here, we focus the comparison to the exoplanets on the planets marked by the gray area. A zoom on this region is shown on the second panel. The vertical red and pink lines represent the maximum and minimum mass ratio reached in each of our simulation once both planet reach 0.3 M_J. Darker colors represent lower viscosities. For visibility, the lines corresponding to the different α-viscosities are slightly offset from the period ratio line. The extent of the $\alpha = 10^{-4}$ was so small at low period ratio that we represent it with squares. The cross marks the Jupiter and Saturn couple. Simultaneously accreting planets lead to planets that are very similar in mass compared to the exoplanet population. Some systems seem to be consistent with simultaneous accretion, however another mechanism is needed to explain the existence of the other systems. Delayed accretion as shown in Fig. 4.11 coupled with different disc lifetimes could explain the difference in planetary masses.

4.8 Conclusions

In this chapter, we investigate the mass distribution of two accreting planets located in the same disc. Using 2D hydrodynamical simulations, we monitor the evolution of the planetary mass ratio for different disc viscosities, different planet configurations and different accretion timings. Our main conclusions can be summarized as:

1. The evolution of multiple accreting planets is mainly governed by the viscosity of the disc. The mass ratio evolution of simultaneously accreting planets depends on the balance between gas accretion and gap formation timescales. As Bergez-Casalou et al. (2020) shows (see Chapter 3), at high viscosity, when gas accretion acts in favor of gap formation, the inner planet is rapidly starved by the viscous accretion onto the star and the outer planet accretes more until becoming the more massive than the inner planet.

   However, at lower viscosities, when gap formation is only dependent on the disc reaction time (i.e., when gas accretion does not help gap formation), the evolution of the mass ratio of the planets follows a different behavior: the outer planet accretes more gas until the inner planet forms its gap. Then, the inner planet starts depleting the inner disc and the material present in between the planets, resulting in a higher accretion rate for the inner planet than for the outer one. When the amount of material located in these two regions is significantly depleted, the inner planet becomes starved by the outer planet.

2. Simultaneously accreting planets always end up with similar masses. In order to reach more extreme mass ratios, we simulated a delayed accretion of the inner or outer planet in one configuration at high and intermediate viscosities. While the initial mass ratios are large by construction, the planets quickly tend towards similar mass ratios ($0.8 < m_{out}/m_{in} < 2$ in 10^5 years).

3. By comparing to the observed exoplanet population, we concluded that gas accretion occurring at the same time can explain the characteristics of only a few planetary systems. Delaying the accretion coupled with different disc lifetimes leads to mass ratios that are more consistent with the observations. While core formation timescales and different disc dissipation mechanisms can explain the possibility of a delayed accretion and depletion of gas, our study shows that the majority of the observed systems of multiple gas giant planets starts accreting at different times.

Understanding how material is distributed between multiple planets is crucial to better understand the dynamical evolution of the forming system. As discussed in Sect. 4.7.2 and in Fig. 1.1, the radial evolution of multiple planets is governed by the migration and capture in resonance of the planets, themselves dependent on the gas distribution in the disc which is governed by gap formation and by planetary and stellar gas accretion. Future studies investigating the growth of multiple giant planets should both consider that the gas accretion of the planets is impacted by the presence of neighbours planets and provide mechanisms explaining the spread in mass ratios observed in distant exoplanetary systems as well as our own Solar system.

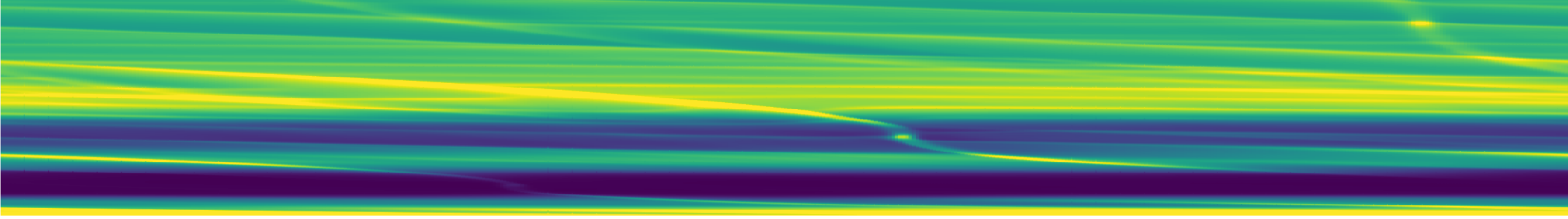

5

Four fixed planets: How would the Solar System natal protoplanetary disc be observed with ALMA ?

This chapter is based on the paper published in Astronomy and Astrophysics in March 2022, titled *Constraining giant planet formation with synthetic ALMA images of the Solar System's natal protoplanetary disk* (Bergez-Casalou, Bitsch, Kurtovic, & Pinilla, 2022). The published paper has been reformatted to match the structure of this thesis. The contribution to this paper was distributed as followed: we discussed the initial setups for each step with Bertram Bitsch and Paola Pinilla; I performed all the hydrodynamical, dust evolution and radiative transfer simulations; I conducted the analysis supported by the advice of Bertram Bitsch; Nicolas Kurtovic and Paola Pinilla helped me producing realistic ALMA synthetic images; Nicolas Kurtovic provided the list of existing discs to which the comparison can be made. Finally, I wrote the text myself with suggestions from all coauthors.

Abstract

New ALMA observations of protoplanetary discs allow us to probe planet formation in other planetary systems, giving us new constraints on planet formation processes. Meanwhile, studies of our own Solar System rely on constraints derived in a completely different way. However, it is still unclear what features the Solar System protoplanetary disc could have produced during its gas phase. By running 2D isothermal hydro-simulations used as inputs for a dust evolution model, we derive synthetic images at millimeter wavelengths using the radiative transfer code `RADMC3D`. We find that the embedded multiple giant planets strongly perturb the radial gas velocities of the disc. These velocity perturbations create traffic jams in the dust, producing over-densities different from the ones created by pressure traps and located away from the planets' positions in the disc. By deriving the images at $\lambda = 1.3mm$ from these dust distributions, we show that very high resolution observations are needed to distinguish the most important features expected in the inner part (< 15AU) of the disc. The traffic jams, observable with a high resolution, further blur the link between the number of gaps and rings in discs and the number of embedded planets. We additionally show that a system capable of producing eccentric planets by scattering events that match the eccentricity distributions in observed exoplanets does not automatically produce bright outer rings at large radii in the disc. This means that

high resolution observations of discs of various sizes are needed to distinguish between different giant planet formation scenarios during the disc phase, where the giants form either in the outer regions of the discs or in the inner regions. In the second scenario, the discs do not present planet-related features at large radii. Finally, we find that, even when the dust temperature is determined self-consistently, the dust masses derived observationally might be off by up to a factor of ten compared to the dust contained in our simulations due to the creation of optically thick regions. Our study clearly shows that in addition to the constraints from exoplanets and the Solar System, ALMA has the power to constrain different stages of planet formation already during the first few million years, which corresponds to the gas disc phase.

5.1 Motivations

Recent observations with the Atacama Large Millimeter/Submillimeter Array (ALMA) and the Spectro-Polarimetric High-contrast Exoplanet REsearch (SPHERE) instruments show protoplanetary discs that present different kinds of substructures (rings, gaps, cavities, and asymmetries) present in the gas (e.g., Teague et al., 2018; Pinte et al., 2020) and in the dust (e.g., ALMA Partnership et al., 2015; Avenhaus et al., 2018; Andrews et al., 2018). These substructures may have different possible origins, including: self-induced dust traps due to dust growth and dust backreaction on the gas (Gonzalez et al., 2017), dust growth in snow lines (Zhang et al., 2015), zonal flows (Flock et al., 2015), secular gravitational instabilities (Takahashi & Inutsuka, 2016; Tominaga et al., 2020), sintering-induced rings (Okuzumi et al., 2016), and gap opening embedded planets (Pinilla et al., 2012).

Focusing on the features created by planets, it is hard to observe the planets directly while they are embedded in their protoplanetary disc (Sanchis et al., 2020; Kloster & Flock, 2021; Asensio-Torres et al., 2021). Therefore, analyzing the dust gap size (Zhang et al., 2018) or the CO velocity perturbations (Teague et al., 2018; Pinte et al., 2020) are ways to indirectly derive the properties of potentially embedded planets. Assuming that these features are indeed caused by planets, we are able to probe forming planets that are not observable directly and that will continue to evolve by accretion and migration in discs. These objects can then be used to derive or confirm some constraints on planet formation processes.

On the other hand, our own Solar System has some characteristics representative of its birth environment. For example, meteorites are solid remains of the protoplanetary solid disc. Kruijer et al. (2017) showed that their chemical composition in the Solar System can be used to constrain the time at which Jupiter's core formed, as it is supposed to separate the reservoirs of carbonaceous and non-carbonaceous chondrites by blocking the pebbles flowing through the disc. Using solid mass estimates from the asteroid and Kuiper belts, Lenz et al. (2020) tried to reproduce the possible gas and solid distributions of our natal protoplanetary disc.

Different models investigate how different parts of the Solar System could have formed. For example, the classical model (Wetherill, 1994; Raymond et al., 2009c) attempts to reproduce the inner Solar System via impacts and the accretion of planet embryos and planetesimals; in the Nice model (Gomes et al., 2005; Nesvorný, 2011; Morbidelli et al., 2018) the dissipation of the gas disc triggers a dynamical instability, spreading the solids in the system; and in the Grand Tack scenario (Walsh et al., 2011; Pierens et al., 2014), Jupiter and Saturn migrate inward during the gas phase until their capture in resonance, inducing an outward migration of the two giants. According to all these models, different noticeable features would be created in the protoplanetary disc as the models require different giant planet configurations, which influence the dust distributions in the disc. The goal of this study is to determine what kinds of features a Solar System embedded in its natal gaseous and dusty disc could produce and how they would be observed by today's instruments. By comparing the resulting images to current observations, we are able to situate the Solar System protoplanetary disc in the wide spectrum of planet-forming discs.

In order to derive these synthetic images, we divided our study into four different steps: we start by simulating the gaseous disc containing the different giant planets using 2D isothermal hydro-simulations with the `FARGO-2D1D` code (Crida et al., 2007). These simulations allow us to derive a detailed radial gas profile that is used as input for a dust evolution model, derived in the `TWO-POP-PY` code (Birnstiel et al., 2012). This radial dust model takes growth, fragmentation, and drift into account. The resulting dust size distributions are then extended in three dimensions and used in a radiative transfer code, `RADMC-3D` (Dullemond et al., 2012), to derive the synthetic images at different wavelengths; these images are finally convolved with different beam sizes in order to represent more realistic observations.

This Chapter is structured as follows. First, in Sect. 5.2 we outline the different numerical setups of the steps listed above. We present the results of the dust evolution model in Sect. 5.3, and then the derived images, convolved with beams, are shown in Sect. 5.4. The derived images are discussed in Sect. 5.5, and we summarize and conclude our results in Sect. 5.6.

5.2 Numerical setups

In this study, we want to simulate how the dust would be distributed in a protoplanetary disc where multiple fully formed giant planets are embedded. We therefore proceed in four steps: i) first, hydrodynamical simulations are run with `FARGO-2D1D` (see Sect. 2.1) in order to determine the gas distribution in the disc, considering different planet configurations, described in Sect. 5.2.1 and exploring different disc parameters; ii) using the time and azimuthally averaged gas distribution from the hydrodynamical simulations, we investigate how dust behaves in such discs using the `TWO-POP-PY` dust evolution code (see Sect. 2.2), giving us the dust surface density distributions as a function of radius and grain size; iii) we derive the synthetic images from a 3D extension of the dust distributions using the radiative transfer code `RADMC-3D` (see Sect. 2.3), which outputs can then be convolved with different beams in step iv), giving us realistic images of the discs.

In this section we present the different setups for each step, starting by presenting the different planet configurations explored. In Sects. 5.2.2 and 5.2.3, we present the numerical setups we used for the hydrodynamical and dust evolution simulations. The radiative transfer code as well as the beam convolutions are presented in Sect. 5.2.4.

5.2.1 Planet configurations

As we simulate planetary systems that are still embedded in their gas discs, we consider two possible formation scenarios. Assuming that the four giant planets in the Solar System are already formed (i.e., their mass are fixed to their present value), they are

Table 5.1: Semi-major axis and masses of the three different configurations considered here (Compact, Spread, and Three Giants).

Config	Jupiter	Saturn	Uranus	Neptune
Compact r_p	5.45 AU	8.18 AU	11.5 AU	14.2 AU
Spread r_p	6.76 AU	12.4 AU	24.9 AU	39 AU
Masses	1 M_J	0.3 M_J	0.044 M_J	0.051 M_J

Config	Giant 1	Giant 2	Giant 3
3 Giants r_p	5.2 AU	8.11 AU	12.69
Masses	1 M_J	1 M_J	1 M_J

placed in either a Compact or a Spread configuration (see table 5.1). In the Compact configuration the planets are located in a tight configuration corresponding to the initial configuration needed by the Nice instability to occur (Gomes et al., 2005); whereas in the Spread configuration, the planets semi-major axis are increased by 30% compared to their nowadays positions. This aims to take into account migration, assuming that after they formed they migrated inward from further away orbits toward their current configuration (Bitsch et al., 2015; Sotiriadis et al., 2017; Pirani et al., 2019; Öberg & Wordsworth, 2019).

To investigate planet formation in a global scale, we also chose a third configuration representing an exoplanetary system. This system is studied to help the comparison between the resulting images and the observations. It is composed of three giant planets of 1 M_J located at $\sim 5\ R_{H,mut}$ (Chambers et al., 1996) from each other in the inner region of the disc. This configuration represents a possible intermediate step of N-body simulations aimed to study giant planet formation (Bitsch et al., 2020), but serves also as initial conditions for N-body simulations aimed to explain the eccentricity distribution of giant planets via scattering (Jurić & Tremaine, 2008; Raymond et al., 2009a).

As our goal is to constrain giant planet formation, we also investigate the impact of the planet masses on the discs. By changing the planet masses, we probe different stages in the formation process. We study this effect for two of our configurations, the Spread and the Three Giants, with reduced planet masses corresponding to one-half or one-third of their current mass. In return, we enhance the disc gas masses by 1% and 2%, respectively, as the discs harboring the less massive planets represent an earlier evolution step. Only one set of disc parameters is used in this case ($\alpha = 10^{-4}$ and $h = 0.025 \times r_{\rm AU}^{2/7}$; see next subsection).

5.2.2 Hydro-dynamical setup

In order to derive the gas disc profile in presence of four giant planets, we run hydrodynamical simulations with the `FARGO-2D1D` code (Crida et al., 2007). In this project, the 2D grid spans from 1 AU to 52 AU and is prolonged by the inner 1D grid from 0.1 to 1 AU and by the outer 1D grid from 52 to 160 AU, except when otherwise specified. As in the other projects, the interfaces between the 2D and 1D grids are chosen to be far enough from the planets so that we can consider the disc axisymmetric (see Fig. 5.1).

We investigate the influence of viscosity by taking three different values for $\alpha = 10^{-4}$, 10^{-3}, 10^{-2}. For the aspect ratio, we use the minimum mass solar nebula (MMSN) profile (see Sect. 1.3.1), derived by Weidenschilling (1977); Hayashi (1981): $h = 0.033 \times r_{\rm AU}^{2/7}$. We also investigate the impact of the aspect ratio by taking a lower value: $h = 0.025 \times r_{\rm AU}^{2/7}$. For simplicity, in this study, the first aspect ratio will be called the "MMSN-

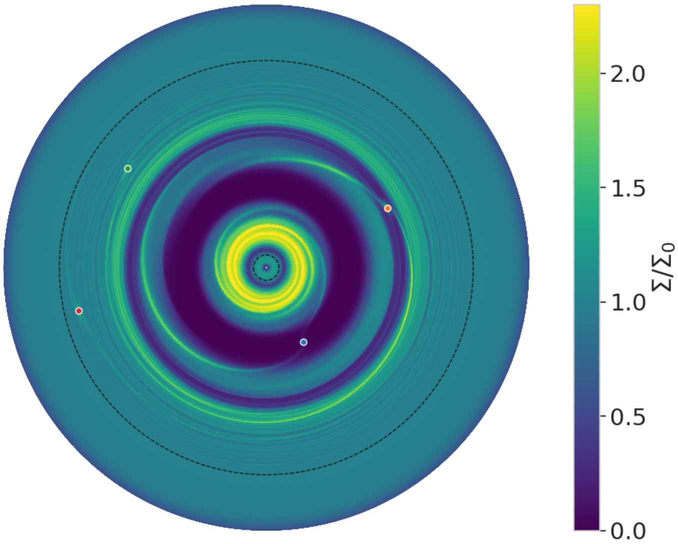

Figure 5.1: Grid configuration in `FARGO-2D1D`. The 1D-grid ranges from 0.02 to 30.77 and the 2D grid from 0.2 to 10.0 in code units. For better readability, the radial dimension is shown on a logarithmic scale. The color scale shows the perturbed surface density of the disc, normalized to the initial disc profile. The planets, represented by the dots and positioned in the Spread configuration (see table 5.1), are considered far enough from the boundaries of the 2D-grid for the disc to be considered axisymmetric.

like" aspect ratio whereas the second one is referred as the "small" aspect ratio. In each case, the snow line (i.e., the location at which water vapor freezes in the disc, T = 160K) is located at 3.3 AU in the MMSN-like case and at 0.9 AU in the small aspect ratio one. Even if the snow lines are located within the simulation domain, we neglect any physical changes that can occur around this location.

The radial extent of our gaseous initial disc (from 0.1 to 160 AU) is consistent with Lenz et al. (2020) and Kretke et al. (2012), where they derived the possible properties of the Solar System protoplanetary disc taking into account different available constraints. We also chose a gas surface density profile in agreement with Lenz et al. (2020): $\Sigma(r) = \Sigma_{\text{init}} \times (r/r_{\text{AU}})^{-1}$, where $\Sigma_{\text{init}} = 836.1$ g/cm^2 at $r = 1$ AU. This value was chosen so that the total mass of the disc is $0.1 M_\odot$. Even if this is considered a heavy initial disc, its large radial extent allows us to neglect self-gravity. Furthermore, as `FARGO-2D1D` features open inner and outer boundaries, the mass of the disc will decrease with viscous evolution. The disc parameters are summarized in table 5.2, where the fiducial parameters are written in bold and the values are given at $r_0 = 5.2$ AU.

The resolution is such that the innermost planet (i.e., the planet located at $r_p = r_0 = 5.2$ AU) is resolved by five grid cells within its Hill radius (eq. 1.27). This leads, for the 2D grid, to a radial resolution of $N_{rad,2D} = 707$ cells with an azimuthal resolution of $N_{\phi,2D} = 454$ cells. This corresponds to a radial resolution of $N_{rad,1D} = 2218$ when considering the whole disc (i.e., the two 1D grids combined with the 2D grid). As at low viscosity some instabilities can be triggered (Klahr & Bodenheimer, 2003; Fu et al., 2014), we enhanced the resolution for $\alpha = 10^{-4}$: $N_{rad,2D} = 1414$ and $N_{\phi,2D} = 906$ leading to $N_{rad,1D} = 4436$. In one particular case, the 2D-1D boundary was too close to the outer planet, creating unrealistic features. Therefore, in the Spread configuration case with low alpha ($\alpha = 10^{-4}$) and small aspect ratio, the 2D-1D outer boundary was moved from 52 to 78 AU. The radial resolution was adapted in the 2D part to match the radial resolution of the other simulations at low viscosity: here, $N_{rad,2D} = 2135$.

The planets are introduced into the disc with a mass-taper function (2.3) making the planets grow from 0 to m_p in $n_{orb} = 10$ orbits. The disc is integrated for 12 500 orbits at 5.2 AU ($\sim 1.5 \times 10^5$ years) until it adjusts to the perturbations induced by the giant planets. The 2D density profiles after 12 500 orbits can be seen in Appendix B.1 for each configuration and disc parameter. The discs are then evolved for another 2 500 orbits at

5.2 AU ($\sim 3.0 \times 10^4$ years). These gas density profiles are used as an input for the dust evolution setup.

Table 5.2: Gas disc parameters.

Gas parameters	
Aspect ratio value at r_0	$h_0 = 0.0528$ (MMSN), 0.04 (small)
Aspect ratio flaring index	2/7
Alpha viscosity	$\alpha = 10^{-4}$, $\mathbf{10^{-3}}$, 10^{-2}
Surface density value at r_0	$\Sigma_0 = 5.2.10^{-4} = 161.1$ g/cm^2
Surface density slope profile	$p = 1$
Planet parameters	
Planet initial mass	see table 5.1
Planet initial position	see table 5.1
Accretion time	$t_{start,acc}$ = OFF
Planet migration	NO
Planet interactions	NO
Planet mass taper	$n_{orb} = 10$
Planet eccentricity	0
Grids parameters	
Radial extent of 1D grid	[0.1 AU, 160 AU]
1D radial resolution	$N_{rad,1D}$ = **2218**, 4436
Radial extent of 2D grid	**[1 AU, 52 AU]**; [1 AU, 78 AU]
2D radial resolution	$N_{rad,2D}$ =**707**, 1414
2D azimuthal resolution	$N_{\phi,2D}$ = **454**, 906

5.2.3 Dust evolution setup

To derive the dust distributions in the discs, we use the dust evolution code `TWO-POP-PY` (Birnstiel et al., 2012, 2015). `TWO-POP-PY` (see Sect. 2.2) computes the radial motion of grains as well as their growth from an initial dust and gas radial profile. These initial profiles are derived from the hydrodynamical setup presented above. The same radial resolution is used as in the hydro-simulations ($N_{rad,1D} = 2218$ for the highest viscosities and $N_{rad,1D} = 4436$ for $\alpha = 10^{-4}$).

The initial gas profile corresponds to the azimuthally averaged gas density and velocity profiles averaged in time over 2 500 orbits at 5.2 AU (average taken between t= 12 500 and 15 000 orbits). This time average will smooth the highly perturbed disc, which is a necessary step as we do not simulate the gas and dust evolution simultaneously in 2D, as in more sophisticated simulations (Drążkowska et al., 2019). We discuss this choice in Sect. 5.5.4. The used radial gas density profiles can be found in Appendix B.1 while the radial gas velocities are shown in Appendix B.1.

The initial dust profile is derived from the gas profile by assuming a dust-to-gas ratio of 0.01. As we consider that all the planets already fully formed in the disc, we need to take into consideration that some planets already reached the pebble isolation mass and therefore are able to block the pebble flux from the outer regions of the disc (Morbidelli & Nesvorny, 2012; Lambrechts et al., 2014; Ataiee et al., 2018; Bitsch et al., 2018). The pebble isolation mass can be estimated from the aspect ratio h of the disc:

$$M_{iso} \simeq 20 \left(\frac{h}{0.05}\right)^3 M_{Earth} \tag{5.1}$$

For our different configurations and each disc scale height profile, Jupiter and Saturn are always above the pebble isolation mass. In the Three-Giants configuration, each planet is above the pebble isolation mass. As some of the giants gaps are able to block the pebble flux from the outer disc, we assume that the dust located between the inner edge of the disc and the outer gap edge of the furthest planet that has reached the pebble isolation mass had time to drift inward during planet formation, making the inner disc depleted in dust. Therefore, our initial dust profile can be written as

$$\Sigma_d = \begin{cases} 0 & \text{if } r \leq r_{p,trunc} + 2H_{p,trunc} \\ 0.01 \times \Sigma_g & \text{if } r > r_{p,trunc} + 2H_{p,trunc} \end{cases} \tag{5.2}$$

where $r_{p,trunc}$ is the semi-major axis of the planet considered to block the dust flux (Saturn in the Solar System cases, the third giant in the Three-Giants case) and $H_{p,trunc}$ is the disc gas scale height at the location of the planet, used to estimate the position of the outer edge of the planet gap (Paardekooper & Mellema, 2006). The capacity of the giant planets to block the small dust flux is dependent on the dust diffusion and on the gap depth, which in turn depends on the disc viscosity. We show in Sect. 5.3 that if the viscosity is high, the gaps are actually not strong enough and dust diffusion is important, allowing dust from the outer disc to flow in and fill the inner disc (de Juan Ovelar et al., 2016). Therefore, the inner disc will remain empty only if the viscosity is low enough to block the dust flux from the outer disc.

We note that studies have showed that filtering of dust to the inner parts depend on the Stokes number of the dust and the gas properties (Weber et al., 2018; Haugbølle et al., 2019). As `TWO-POP-PY` only considers two populations of dust (see Sect. 2.2) representing only two different categories of Stokes numbers, this code gives us a first approximation only of how dust is filtered to the inner parts of the discs.

The model is evolved for 1 Myr, during which we consider that the gas disc does not evolve significantly (i.e., the gas profile is fixed). The impact of time evolution is discussed in Sect. 5.5.4. During these 1 Myr, the grains grow, fragment and drift. The maximal grain size depends on each limiting mechanism: $a_{\rm max} = \min(a_{\rm frag}, a_{\rm drift}, a_{\rm growth})$ (see Sects. 1.1.2 and 2.2). These limiting mechanisms depend on the physical properties of the grains (summarized in table 5.3). We assume a sticking probability $e_s = 1$ and the internal density of the grains is taken to be $\rho_s = 1.675$ g/cm^3, matching the disc Substructures at High Angular Resolution (DSHARP) survey's composition of grains (Birnstiel et al., 2018).

As mentioned in Sect. 1.1.2, fragmentation velocities are challenging: laboratory experiments inferred low velocities ($\sim$ 1 m/s) when considering the physical conditions of protoplanetary discs (Musiolik & Wurm, 2019; Schneider et al., 2019) while numerical simulations show that large fragmentation velocities ($\sim$ 10 m/s) are required to form large planetesimals (Drążkowska et al., 2016; Lenz et al., 2019). From eq. 1.18, it is clear that a lower fragmentation velocity will yield small grain sizes in the fragmentation limit, if the disc's viscosity is large. In order to reach at least millimeter particles observable with ALMA, we thus use larger fragmentation velocities (1, 3, and 10 m/s) for higher alpha values ($10^{-4}, 10^{-3}$, and 10^{-2}) in order to have a similar fragmentation limit for all simulations.

After 1 Myr of evolution, we reconstruct the full grain size distribution, determining the surface density of each grain size as a function of orbital distance (Birnstiel et al., 2015). The particle grid used by the reconstruction routine logarithmically ranges from $a_0 = 2.5 \times 10^{-6}$ cm to $6 \times a_{\max}$, $a_{\max}$ being the maximum grain size reached after 1 Myr of evolution, resolved with 300 cells. This dust size-density distribution, presented for each disc in Sect. 5.3, is the final 1D output used to produce the images.

Table 5.3: Dust evolution parameters.

Initial profiles	
Initial gas profile	Averaged `FARGO-2D1D` Σ_g
Initial gas radial velocity	Averaged `FARGO-2D1D` $v_{r,\mathrm{gas}}$
Gas alpha-viscosity	$\alpha = 10^{-4}$, $\mathbf{10^{-3}}$, 10^{-2}
Gas evolution	NO
Initial dust profile	$\Sigma_{d,0} = 0.01 \times \Sigma_g$
Dust characteristics	
Internal density of the grains	$\rho_s = 1.675$ g/cm^3
Fragmentation velocity	$v_f(\alpha)$ =(1, 3, 10 m/s)
Sticking probability	$e_s = 1$
Initial dust size	$a_0 = 2.5 \times 10^{-6}$ cm
Grid parameters	
Radial extent of the grid	[0.1 AU, 160 AU]
Radial resolution	N_{rad} = **2218**, 4436
Time of integration	$t_{max} = 1$ Myr

5.2.4 Synthetic image setup

The images are derived using the radiative transfer code `RADMC-3D` (Dullemond et al., 2012). Using the radial dust size-density distribution from `TWO-POP-PY`, we extrapolate the 3D distribution of the grains in the disc. We assume a volume density following:

$$\rho_d(r, \phi, z, \mathrm{St}) = \frac{\Sigma_d(r, \mathrm{St})}{\sqrt{2\pi}\, H_d(r, \mathrm{St})} \times \exp\left(- \frac{z^2}{2H_d(r, \mathrm{St})^2} \right) \tag{5.3}$$

where $z = r \cos\theta$ (θ being the polar angle) and H_d is the dust scale height. H_d is derived from the gas scale height as described in Sect. 1.1.2, taking into account vertical settling of grains (eq. 1.17).

The hydrodynamical and dust simulations are run with a very high radial resolution, specially at low viscosity. In order to add two dimensions to our discs, we need to reduce the overall resolution due to computational limitations. To do so, we interpolated the dust distributions radially, reducing the resolution by a factor of two (four at low viscosity). The new radial resolution, used to derive the images, is therefore of $N_{rad} = 1109$ cells. By applying the same method to the grain size grid, we reduce the number of dust grains by 2. The images are derived considering a disc containing 150 grain size bins. This procedure resulted in no major differences compared to simulations with the full resolution. Thanks to this reduced resolution distributions, the disc can be extended over 320 cells in colatitude ($N_\theta = 320$). Such resolution is needed to correctly derive the temperature of the dust settled to the mid-plane. Finally, we used an azimuthal resolution of $N_\phi = 4$ cells, as our discs are considered axisymmetric after the hydro-simulations step.

As mentioned in the previous section, the grains are taken to be spherical grains with the DSHARP composition (Birnstiel et al., 2018), detailed in the summarizing parameter table 5.4. Their opacities are derived using `OpTool` (Dominik et al., 2021). This library derives the opacity for each grain size using the Mie calculation (see Sect. 2.3.2). `OpTool` computes the full scattering matrices needed by `RADMC-3D` to include the full treatment of anisotropic polarized scattering.

After computing the temperature profiles of each grain size, `RADMC-3D` derives the images at $\lambda = 1.3$ mm, corresponding to band 6 of ALMA. We assume face-on discs at a distance of 140 pc, which is the typical distance of observed protoplanetary discs, such as in the Taurus, Lupus, and Ophiuchus regions (Gaia Collaboration et al., 2018). We investigate the influence of the inclination of the disc in Sect. 5.4.3 by showing how an inclination i of 30, 45 or 60 degrees influences our results.

In our configuration, `RADMC-3D` uses 10^7 photon packages and 5×10^6 scattering photon packages to derive the raw images. These images are then convolved with a Gaussian beam of FWHM = 0.04" × 0.04". In Sect. 5.4.4, we investigate different beam sizes that are coherent with different ALMA configurations. At a distance of 140 pc, the 0.04" × 0.04" beam size corresponds to a spatial resolution of 5.6 AU × 5.6 AU, which corresponds approximately to the semi-major axis of the inner giant in our different configurations.

Table 5.4: Radiative transfer parameters.

Physical set-up	
Dust density	ρ_d as in eq. 5.3
Grid specifications	$[\vec{r}, \vec{\phi}, \vec{\theta}]$
Star characteristics	$[R_\odot, M_\odot, (0,0,0)]$
Wavelength grid	$[0.1, 10^4]\mu$m
Number of photons packages	$N_{phot} = 10^7$, $N_{phot,scat} = 5 \times 10^6$
Opacities parameters	
Dust size range	$[2.5 \times 10^{-2}, a_{max}]\mu$m
Composition (mass fractions from Birnstiel et al. (2018))	Refractory organics = 0.3966
	Astronomical silicates = 0.3291
	Water ice = 0.2
	Troilite = 0.0743
Wavelength grid	$[0.1, 10^4]\mu$m
Emission image parameters	
Observed emission wavelength	λ_{obs} =1.3 mm
Position of the observer	$[\phi_{obs} = 0$, $i_{obs} = \mathbf{0}$, 30, 45, 60]
Image size	800 × 800 pixels

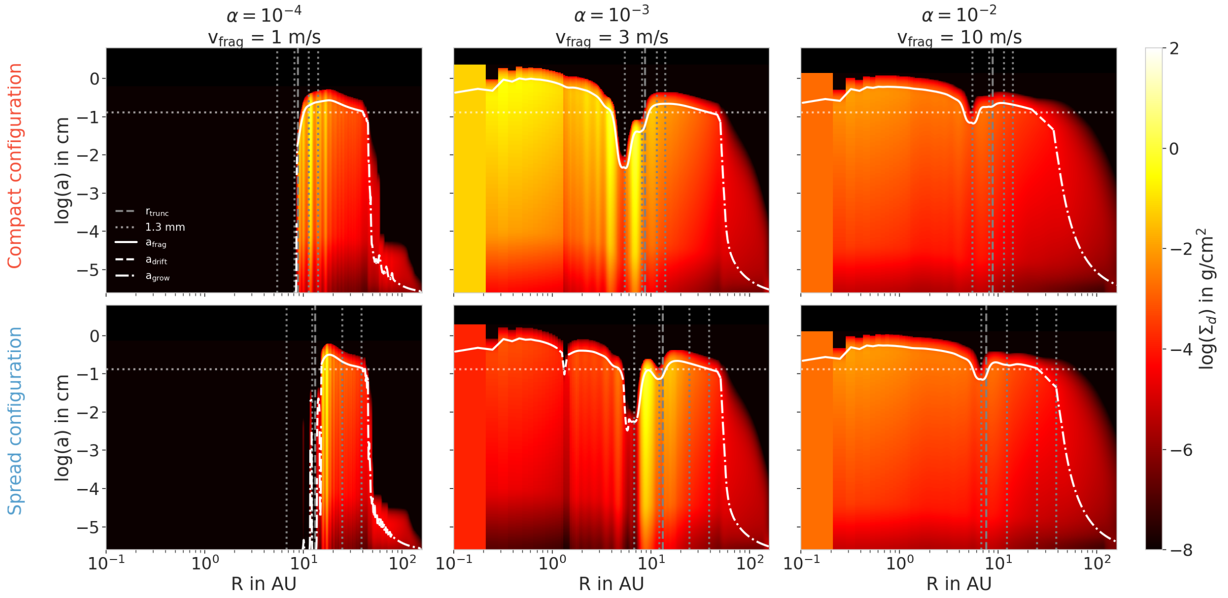

Figure 5.2: Dust densities distributions for the MMSN-like aspect ratio. Each line represents a Solar System configuration (Compact on the first row and Spread on the second row; cf. table 5.1) and each column represents a set of α viscosity and fragmentation speed (increasing from left to right). The vertical dotted lines represent the positions of each planet. The vertical dashed line shows the truncation radius (eq. 5.2). The white lines represent the maximum size reached by the grains, and each line style represents a limiting mechanism: solid line for the fragmentation limit, dashed line for the drift limit, and dotted dashed line for the growth limit size. At high viscosities, dust from the outer regions flows through Jupiter and Saturn's gap and replenishes the inner disc, which is not the case at low viscosity. At low viscosity, the perturbations induced by the planets in the gas velocity profiles produce dust over-densities (traffic jams), creating substructures not directly related to the positions of the planets.

5.3 Dust size distributions from `TWO-POP-PY`

5.3.1 Solar System configurations

In this section we present the radial dust size distributions from `TWO-POP-PY` after 1 Myr of evolution. In Fig. 5.2 we show the distributions in the different Solar System configurations (rows) at different α viscosities and fragmentation speeds (columns) for the MMSN-like aspect ratio. The distributions with a smaller aspect ratio are presented in Fig. 5.3. In both figures, the white lines represent the maximal size reached by the grains: the solid line shows the part of the disc where the grains are limited by fragmentation, the dashed one corresponds to the drift limit and the dotted dashed line represents the growth limit. We see that these lines are in general above the dotted horizontal line that marks the 1.3mm size. Vertical dotted lines represent the positions of each planet, and the vertical dashed line shows the location where the dust disc is initially truncated (see eq. 5.2).

We see that depending on the viscosity, some dust could flow through Jupiter and Saturn's gaps: as expected, at low viscosity $\alpha = 10^{-4}$, the gaps are too deep for the dust from the outer disc to replenish the inner region; however, at high viscosity $\alpha = 10^{-2}$, the dust diffused through the whole disc, leaving no strong substructures. At an intermediate viscosity ($\alpha = 10^{-3}$), we see that depending on the planet configurations, some dust

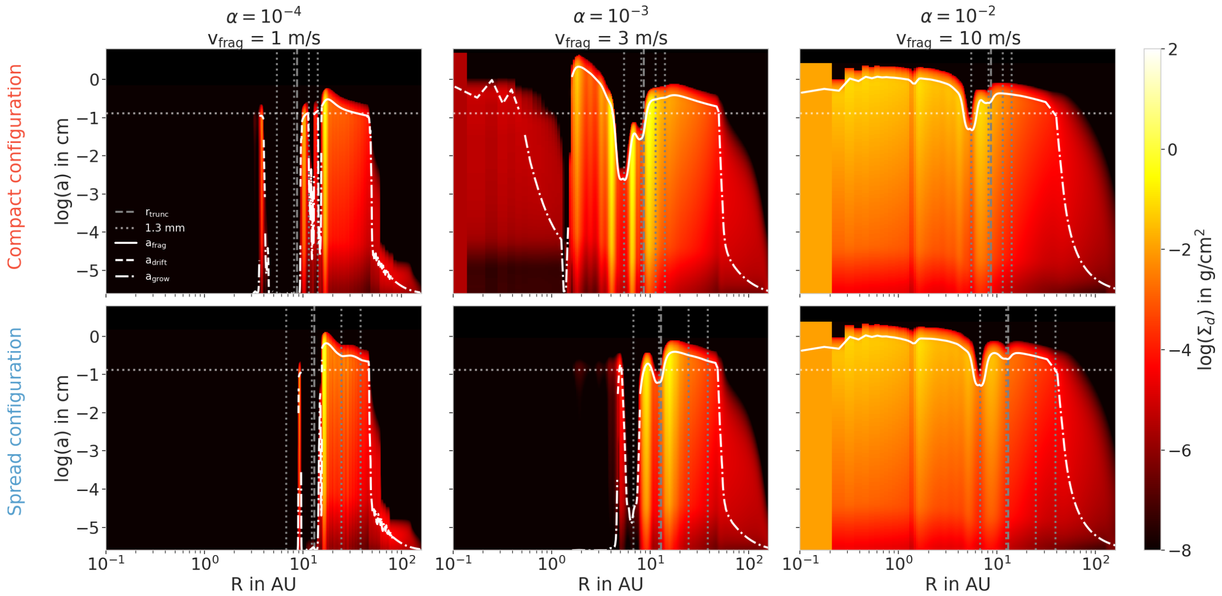

Figure 5.3: Same as Fig. 5.2 but for the smaller aspect ratio. A smaller aspect ratio induces deeper planet-induced gaps in the gas discs, creating stronger features in the dust compared to Fig. 5.2. In the Compact configuration, at $\alpha = 10^{-3}$, a small amount of small dust flows through the gaps of the giants. This produces a low dust-to-gas ratio in the inner region of the disc, resulting in grain sizes limited by growth and drift rather than fragmentation (see eq.1.20).

could accumulate around the giant planets locations: in the Compact configuration with an MMSN-like aspect ratio (Fig. 5.2, first row, second panel), dust flows from the outer disc and accumulated between Jupiter and Saturn as well as at the inner edge of Jupiter's gap, creating two over-densities. A similar behavior happened when considering a lower aspect ratio (Fig. 5.3, first row, second panel). However, as a lower aspect ratio implies deeper gaps, Saturn's gap becomes deep enough to accumulate dust at the outer edge of its gap. In this case, the inner disc is more depleted because it is harder for the dust to diffuse through.

The depletion of dust at low viscosity creates inner cavities. These cavities are observed in several discs (Espaillat et al., 2014; van der Marel et al., 2018) and are described as wide regions in discs where there is no emission observed and therefore possibly no dust present. These cavities can be explained by the presence of planets: either one giant planet is large enough to block the dust flux from the outer disc and the inner disc empties by radial drift; or multiple planets are present and large enough to create a wide common gap. In our simulations, the cavities are created by either mechanism, or a combination of them, depending on the configuration. Either way, the position of the cavity is linked to the position of Jupiter and Saturn, which are both located within 15 AU. In the next section (Sect. 5.4) we investigate if the resolution of ALMA is sufficient to see the cavities in our cases.

Comparing the Compact and Spread configurations distributions at $\alpha = 10^{-3}$ for each aspect ratio, we see that there is less dust flowing to the inner disc in the Spread configuration than in the Compact one. This can be explained by the quasi-common gap created by Jupiter and Saturn in the Compact configuration: as Saturn is located further in, the dust has to diffuse through one gap while it has to diffuse through two distinct gaps in the Spread configuration. Haugbølle et al. (2019) found a similar behavior: the presence of a common gap containing Jupiter and Saturn makes filtering less efficient.

Focusing on the Compact configuration with a small aspect ratio for a medium viscosity (Fig. 5.3, first row, second panel), the inner disc is not completely depleted in dust and limited by growth and drift. Reducing the aspect ratio influences the dust behavior in two ways: first, the planet gaps are deeper (Crida et al., 2006) and therefore filter dust more efficiently. Moreover, diffusion is reduced as the viscosity is lower for lower aspect ratios. It is therefore harder for the dust to flow through Jupiter and Saturn's gaps. As only some part of the small dust manage to reach the inner part of the disc, the dust-to-gas ratio is very low. As a result, the growing dust particles are limited by growth in the inner region before they drift away, in contrast to the simulations where a lot of dust can reach the inner disc, resulting in grain sizes limited by fragmentation. The capacity of the planet gaps to filter out larger dust can therefore produce an inner cavity with very low surface densities in dust, without being directly linked to the positions of the planets in the disc.

In each panel of both figures, the white lines show that all the discs are roughly fragmentation-limited at radii $r < 50$ AU and are growth-limited at larger radii. This is due to the fact that the timescales are longer at larger radii (differential rotation). This growth limit sets the size of the discs in the millimeter dust to be $\sim$ 50 AU. This size is dependent on the time length of the dust simulation: the millimeter dust disc starts by increasing in size until radial drift reduces the millimeter dust disc significantly. We discuss the impact of time evolution later in Sect. 5.5.4.

At the connection between the growth limit and fragmentation limit ($\sim$ 50AU), in each case, we observe a depletion of small dust ($a \lesssim 10^{-4}$ cm). This depletion is due to a narrow region where the dust is actually drift-limited, between the growth and fragmentation limits. We clearly see this regions at high viscosity (dashed line around 30 AU). This drift-limited region makes the largest grains drift inward, before becoming fragmentation-limited. This induces a depletion in small dust as there is no mechanism to replenish this region after the growth of the small dust. This phenomenon was studied by Birnstiel et al. (2015) and creates a gap in the small dust that is not linked to planets at all, but rather to grain growth and drift.

In the Compact configuration at low viscosity and MMSN-like aspect ratio (Fig. 5.2, first row, first panel), we clearly see over-densities that are not linked directly to the gaps caused by planets. These over-densities, not linked to pressure bumps in the gas disc, are due to the highly perturbed gas velocities. As the gas is highly perturbed by the presence of multiple planets (see Appendix B.1), the small dust coupled to the gas undergoes "traffic jams": the change of velocity creates over-densities as the dust is slowed down. In these cases, the dust is not trapped and continues to flow after staying in the traffic jam. However, this dust caught in a lower velocity region has time to grow, creating over-densities over a wide range of different sizes. These over-densities are therefore indirectly linked to the presence of the planets and can be observed depending on the resolution of the instruments (see Sects. 5.4 and 5.4.4).

5.3.2 Influence of planet mass and Three-Giants configuration

As presented in Sect. 5.2.1, we also investigate the impact of different planetary masses on the dust distributions in the Spread and in the Three-Giants configurations. In the first row of Fig. 5.4 we show the dust distributions in the Spread configuration case, at low viscosity and small aspect ratio, where the masses are reduced by a factor of two-thirds (left panel) and one-half (middle panel). We can compare them to the total mass

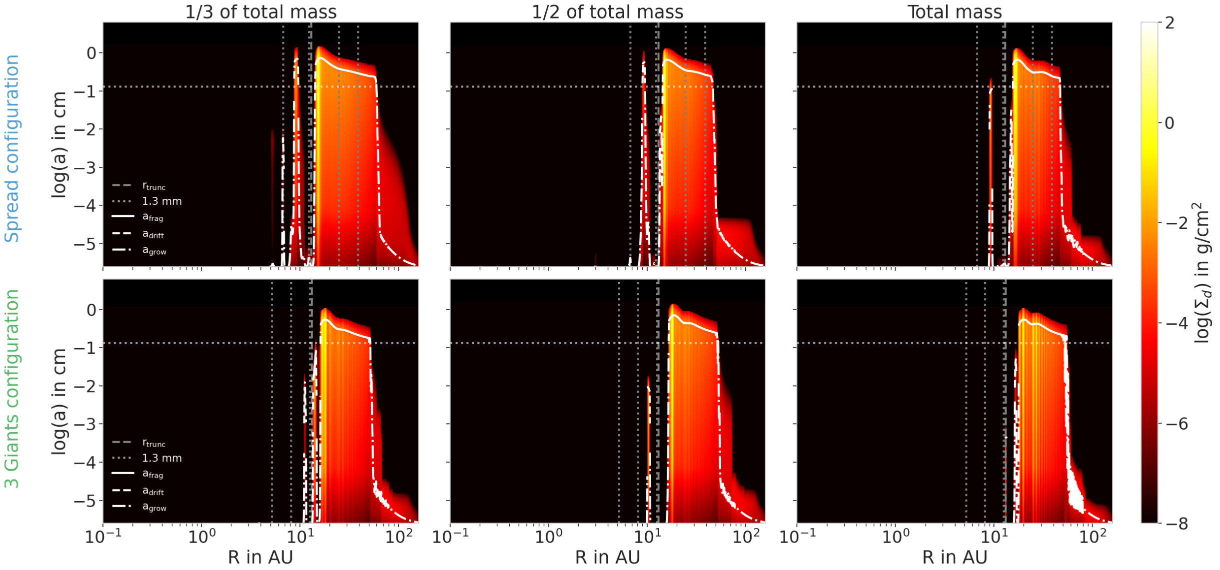

Figure 5.4: Dust densities distributions with the planet masses reduced by one-half and two-thirds in the Spread configuration (top row) and in the Three-Giants configuration (bottom row). In these simulations, the disc has the smaller aspect ratio and $\alpha = 10^{-4}$ with $v_{\text{frag}} = 1$ m/s. The masses of the planets mainly change the gap shapes, allowing more or less dust to flow to the inner regions. In the Three-Giants configuration, we also see that more massive planets create more traffic jams in the disc and therefore present more substructures.

case, presented on the right panel. On the second row, we present the distributions of the Three-Giants case, with the different masses as mentioned above.

Changing the mass of the planets will have two large impacts. The first comes from the initial gas distribution: with increasing planetary mass, the gas is pushed away from the planet more efficiently, depleting the gas disc (Bergez-Casalou et al., 2020). Our simulations start with lower disc masses for more massive planets to depict the effect of disc evolution during planetary growth. Consequently, as the initial dust content is derived from the gas profile (dust-to-gas ratio of 0.01), the dust disc in the case of full planetary masses is less massive than in the other two cases. As consequence, the maximal grain size reduces for the simulations with increasing planetary mass. Having a more massive dust disc also has an impact on the size of the dust disc in millimeter grains, as it allows faster growth in the outer regions of the discs.

Furthermore, the less massive planets cause shallower gaps. As the gaps are less deep, more dust can flow through the different gaps. For the Spread configuration, the planetary masses results in narrower gap in the dust profile at Saturn's location, while Jupiter is still massive enough to prevent efficient dust diffusion. Regarding the Three-Giants case, reducing the planet masses does not alter the formation of an inner cavity. Even if some dust diffuses through the gap of the third planet in the case of smallest planetary mass, the presence of the other giants is sufficient to keep an inner cavity. Therefore, as expected, bigger planets will create bigger cavities.

On the other hand, planets of different masses will perturb the gas disc differently. More massive planets will induce more perturbations in the gas and create more traffic jams (see the velocity profiles in Appendix B.1). This is particularly clear in the Three-Giants case, where we see on the lower panels of Fig. 5.4 that the outer disc presents different over-densities depending on the planet masses.

These dust distributions show that each configuration harbors different substructures, mostly at low viscosity. In the next sections we show that some of these features are observable with ALMA.

5.4 Synthetic images - `RADMC-3D` outputs convolved with Gaussian beams

The dust distributions studied in the previous section present different features, unique to each configuration. In this subsection we present the images and their the radial profiles derived following the setup presented in Sect. 5.2.4. First, we focus on the radial profiles at $\lambda = 1.3$ mm for the Solar System configurations at each aspect ratio (Sect. 5.4.1). The corresponding images can be found in Appendix B.3.1. Then we present the images and profiles in the Three-Giants and Spread configurations with the different planetary masses (Sect. 5.4.2). Different disc inclinations are investigated in Sect. 5.4.3 before studying the influence of the beam size on the observable features in Sect. 5.4.4.

5.4.1 Radial profiles in the Solar System configurations at $\lambda = 1.3$ mm

In order to determine which features are observable, we show in Fig. 5.5 the radial profiles of the normalized intensities (intensity of the image normalized to the peak intensity along one radius of the disc) for images with unconvolved (dashed) beams and for images with a 0.04" × 0.04" Gaussian beam convolution (solid). The corresponding images can be found in Appendix B.3.1. In the images, we assumed that the minimum flux that can be received due to noise is $F_{\rm min} = 10\ \mu$Jy/beam (Andrews et al., 2018). This minimum flux is represented in the radial profiles by the blue regions: in each profile, this minimum flux is normalized to the peak intensity and emission present in this region can be assumed to be lost in the noise of the images. The value of $F_{\rm min}/F_{\rm peak}$ is different for each panel as $F_{\rm peak}$ is unique to each image, whereas $F_{\rm min}$ is fixed.

As in the previous figures, each row represents a planet configuration and each column represents an α-viscosity. It should be noted that for a better comparison with the images, we present the profiles on a linear radial scale, whereas in the previous section the dust distributions are presented along a logarithmic radial scale.

Regarding the high viscosity cases ($\alpha = 10^{-2}$), as expected from the dust distributions, the discs show almost no noticeable feature. In the unconvolved images, we can distinguish the gap created by Jupiter. However, the gap is too close to the star and too small to avoid being smeared out by the beam. Therefore, if the viscosity is too high, then a Solar-System-like planetary structure would be completely invisible in the dust disc. This is consistent with the work of de Juan Ovelar et al. (2016), where they show that a high viscosity disc does not present strong substructures. It is also consistent with Zhang et al. (2018) where they show in their Section 5.1 that a Solar System protoplanetary disc featuring our giant planets in nowadays configuration would not present strong substructures if the viscosity is too high.

The images at $\alpha = 10^{-3}$ show a similar pattern: the features are mostly either too small or too close to the star to be distinguishable with this resolution. Although, in the Spread configuration case, the inner disc starts to be depleted in dust (see Figs. 5.2 and 5.3), resulting in a decrease in the normalized intensity in the inner regions of the images.

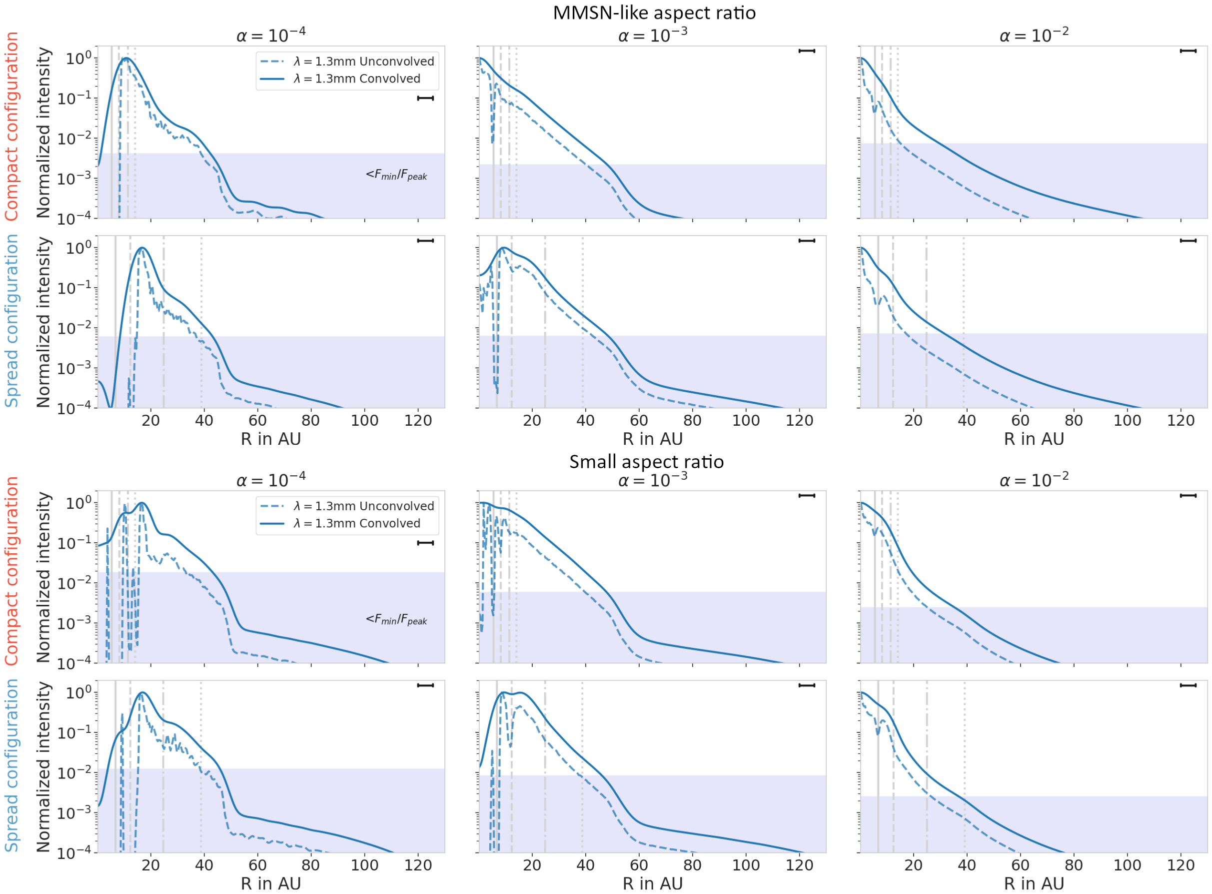

Figure 5.5: Radial profile of convolved and unconvolved images at $\lambda = 1.3$ mm with the MMSN-like aspect ratio in the two first rows and the small aspect ratio in the two last rows. Each row represents a Solar System configuration, and each column represents an α viscosity. The solid lines show the radial intensity of the images normalized to the peak intensity after convolution with a beam of FWHM $= 0.04" \times 0.04" = 5.6$ AU×5.6 AU. The beam is represented with a black horizontal line in the upper-right corner of each panel. The dashed lines represent the normalized intensity of the unconvolved image. Vertical lines show the positions of the planets in each configuration. The light blue area shows the region where the normalized intensity is smaller than $F_{\rm min}/F_{\rm peak}$, where $F_{\rm min} = 10\mu$Jy is the minimal flux considered to be observable. The value of $F_{\rm min}/F_{\rm peak}$ is different from each panel as $F_{\rm pea}$ is unique to each image, whereas $F_{\rm min}$ is fixed. Comparing the profiles in the case of the convolved and unconvolved images shows us how many features can be missed due to a too low resolution. Regarding the Compact configuration, all substructures are smeared out in the beam. On the other hand, with the small aspect ratio, some features become observable, as the dust distributions show more intense substructures,

These small inner cavities are located at a radius within Jupiter's orbit: the giant planets are therefore outside the cavity in this case. In this same configuration, Saturn's gap start to be large enough to induce a small dip in the intensity profile, slightly noticeable in the convolved images.

At low viscosity ($\alpha = 10^{-4}$), the dust distributions showed strong inner cavities and several substructures. The convolution with a beam of this size kept the inner cavities in all configurations, even if they are deeper in the Spread configuration than in the Compact one. In all the configurations, the intensity profiles decrease rapidly around 50 AU, which is caused by the growth limit of the grains discussed in the previous section. As the millimeter size dust is the dust that contributes the most to the 1.3 mm emission, the growth limit sets the size of the disc in the images (as can be seen in Appendix B.3.1). In the Spread configuration, depending on the sensitivity of the instrument, Neptune can be located close to the edge of the disc but only the growth limit sets the location of the drop of intensity.

As discussed in the previous section, the multiple planets can create some substructures in the disc not directly linked to the positions of the planets. Even if these over-densities can be seen in the unconvolved images, the beam smeared out the majority of them. However, in the Compact case, low viscosity, low aspect ratio (first top panel of small aspect ratio in Fig. 5.5), we see several dips in the intensity profile. The first one is linked to the inner cavity (r $<$ 10 AU). The second one is located at Uranus and Neptune orbits and originates from the small gaps that the two icy giants create in the gas and dust disc. However, the two gaps are indistinguishable here due to the beam size, reducing the emission of the dust located between the two planets. Similarly, as some dust piled up at the outer edge of Neptune's gap and due to the shape of the fragmentation limit in this case, a small part of the disc is shadowed outside of Neptune's orbit, creating a third dip in the intensity profile.

Focusing on the Spread configuration at low viscosity ($\alpha = 10^{-4}$) at each aspect ratio, Fig. 5.5 shows a bump in the intensity between the orbits of Saturn and Uranus. This bump originates from the pileup of dust that is blocked at Saturn's outer gap edge. This bump creates a bright ring separating the inner giants and the icy giants, located around 15 AU. This configuration and viscosity is the only setup that presents a bright clear ring at this resolution. We discuss this peculiarity in Sect. 5.5.1, where we compare our discs to known observed discs with similar resolutions.

In summary, the Solar System configurations do not present a lot of substructures in general at this resolution. At low viscosity, the Compact and Spread configurations are presenting very different features, with the Spread configuration showing a clear bright ring between Saturn and Uranus, whereas the Compact configuration presents features that are not directly linked to the positions of the planets. Therefore, the detectability of substructures is highly dependent on the disc viscosity and planet configuration.

5.4.2 Influence of the different masses on the 1.3 mm images

As discussed previously, the planet masses have a lot of impact on the dust distributions, creating different features in the discs. We show in Fig. 5.6 the radial normalized intensity profiles in the simulations with different planetary masses, for the Spread and the Three-Giants configurations. Due to the different masses of the dust disc, they have different sizes: in the Spread configuration (top row), we see that the drop in intensity due to dust growth is located at different radii. This effect is even more noticeable in Fig. 5.7, where we show the discs as they would be observed. This effect is less present in the Three-Giants case because the planets are located in the very inner region, therefore not having a strong impact on the gas distribution in the outer regions of the disc (see Appendix B.1).

As noticed in the previous section, having planets of different mass influence the amount of dust that can flow through the gaps of the giants. This has a very small impact here as the beam is too large to resolve the small amount of dust present between Saturn's gap (or the third giant's gap in the Three-Giants case) and the inner cavity. The only case where enough dust managed to flow to the inner regions is in the reduced

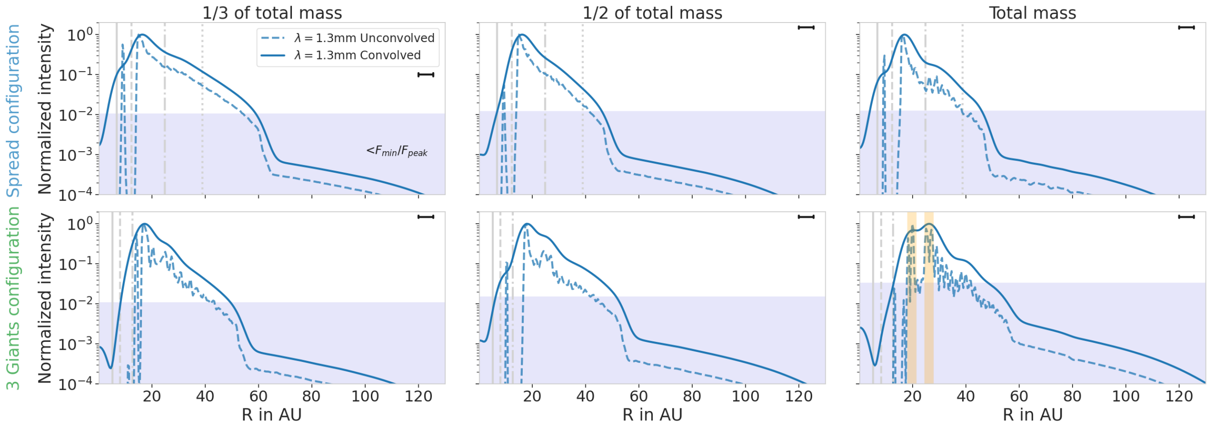

Figure 5.6: Radial profile of convolved and unconvolved images at $\lambda = 1.3$ mm with the planet masses reduced by $1/2$ and $2/3$ in the Spread configuration (top row) and in the Three-Giants configuration (bottom row). In these simulations, the disc has the smaller aspect ratio and $\alpha = 10^{-4}$. The intensity profiles are presented as in Fig. 5.5. The convolved profiles are convolved with a beam of 0.04"×0.04" = 5.6 AU×5.6 AU, represented with a black horizontal line in the upper-right corner of each panel. The similarities between each convolved profile makes it difficult to disentangle between each evolutionary stage and configuration. In the Three-Giants configuration, we highlight in orange the substructures outside of the giants' region, originating in the traffic jams discussed in Sect. 5.3.

by two-thirds case in the Spread configuration, as Saturn is only slightly above pebble isolation mass. Here, the amount of dust is large enough to slightly enhance the intensity between Jupiter and Saturn's orbit. This slight enhancement is particularly visible in the image in Fig. 5.7 (first top panel). On the other hand, as more massive planets block dust most efficiently, it accumulates more at the outer edge of Saturn's orbit. This results in a brighter and clearer ring separating the inner giants from the icy giants.

Regarding the features created by the different traffic jams, most of them are not strong enough to be noticed in the Spread configuration. However, in the Three-Giants case, the traffic jams create rings of different intensities. Expectedly, strongest over-densities create brighter rings. As the strength of the traffic jams are dependent on the planet masses, the most massive case present the strongest features. In the end, these two consecutive rings are due to the gas radial velocity profile and are not directly linked to the presence of planets close to the bright rings.

As already mentioned, changing the planet mass allows us to probe different stages of planet formation (i.e., different times in the formation process). One can notice that the differences between the Spread configuration with half its mass is quite similar to the reduced planet masses in the Three-Giants configuration (Figs. 5.7 and 5.6, middle panel of first row compared to the first and second panels of the second row). Therefore, in order to really disentangle planet formation processes, better resolution is needed. We discuss this in Sect. 5.4.4.

5.4.3 Influence of the disc inclinations

Many of the observed discs are actually inclined compared to our line of sight (ALMA Partnership et al., 2015; Andrews et al., 2018). In this section we explore how the inclination of these discs can have an impact on the visible substructures discussed in the previous sections. In order to do so, as in the previous section where we explored the

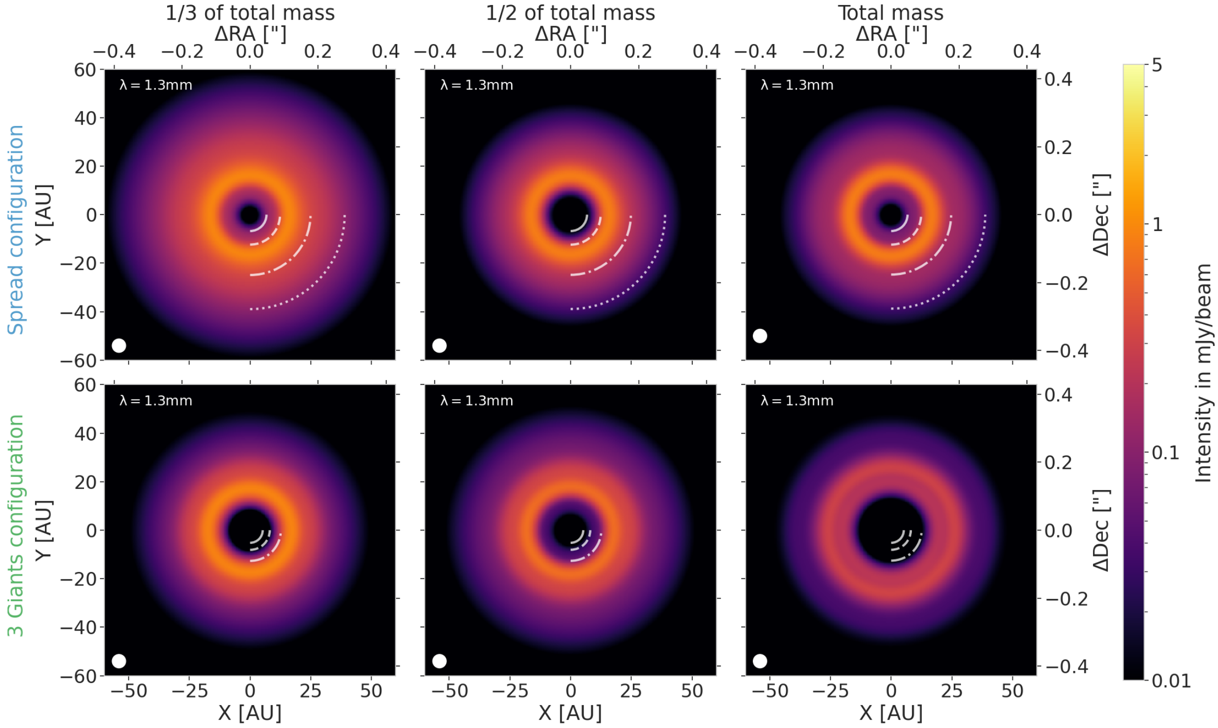

Figure 5.7: Images in total intensity at $\lambda = 1.3$ mm corresponding to the radial profiles presented in Fig. 5.6. The positions of the different planets are represented by the different white arcs. The beam size (0.04" × 0.04") is represented in the lower-left corner of each image by the white ellipse. In the Spread configuration, the size of the discs depends on the masses of the planets. In the Three-Giants configuration, one can notice the substructures outside of the giants' region corresponding to the orange regions of the profiles in Fig. 5.6 and originating from the traffic jams observed in Sect. 5.3; these traffic jams were created by the perturbed velocity profile of the disc (see Fig. B.7).

impact of the beam size, we derive the images in the Spread configuration at low aspect ratio and viscosity and in the Three-Giants configuration and infer three different inclinations to the discs: $i = 30, 45, 60°$. The images at different inclinations can be found in Appendix B.3.2.

In Fig. 5.8 we present the radial profiles of the normalized intensity with different inclinations. The radial profiles are taken to be a section of the image along the semi-major axis of the inclined image. No deprojection procedure was applied, as the discs are axisymmetric by construction. By taking the profile along the semi-major axis, we look at the section of the disc that is situated at the same distance from the observer, independently of the inclination. As in the previous profiles, we show the unconvolved profiles with dashed lines and convolved profiles with solid lines.

The profiles are very similar, presenting the same features in each case. The main difference resides in the inner cavities: a more inclined disc will hide the depth of the inner cavity as the dust present closer to the observer (lower part of our images) will hide the cavity. However, the cavities are wide enough to be visible: if the cavity is too small, the dust from the closer part of the disc will completely hide the cavity to the observer. On the other hand, larger cavities will be less impacted by the disc inclination. This can be seen with our configurations: in the Spread configuration, the inner cavity is smaller than in the Three-Giants one (see Figs. 5.4 and 5.7) and the inclination of the disc has a stronger effect on the inner cavity in the Spread configuration.

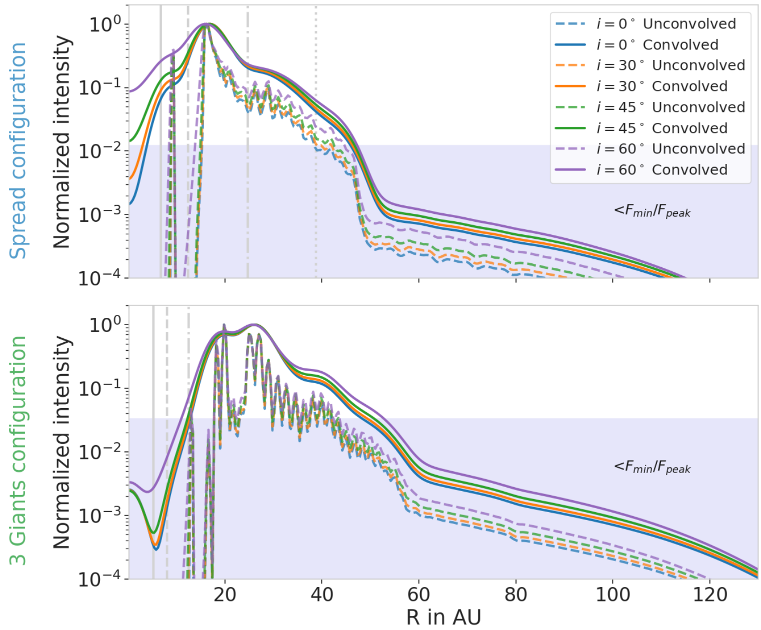

Figure 5.8: Radial profile of convolved and unconvolved images at $\lambda = 1.3$ mm with different inclinations in the Spread configuration (top row) and in the Three-Giants configuration (bottom row). Here, the discs have the smaller aspect ratio and $\alpha = 10^{-4}$ with $v_{\mathrm{frag}} = 1$ m/s. The convolved images present a beam of 0.04” × 0.04”. The profiles are derived from images that have inclinations ranging from $i = 0°$ to $i = 60°$. The light blue area shows the region where the normalized intensity is smaller than $F_{\mathrm{min}}/F_{\mathrm{peak}}$ (see Fig. 5.5). The only highly impacted region is the inner cavity: more inclined discs hide the inner regions more efficiently, influencing the depth of the observed cavities.

As disc millimeter emissions are geometrically flat (Birnstiel et al., 2010; Pinilla et al., 2021), we show here that the inclination of the disc does not have a strong effect on the observed profiles. This means that the inclination of the disc does not hide or create features that could originate from giant planets, important to derive constraints for planet formation.

5.4.4 Influence of the beam size

ALMA can reach different resolutions depending on the observed wavelength and configuration. As we derived the images at $\lambda = 1.3$ mm, we are interested in the Band 6 observations. With the different configurations available, the most common resolutions reached are therefore equivalent to beams of three different size: the most resolved one has a beam of 0.02” × 0.02” (as in Benisty et al., 2021), the most common one has a high resolution with a beam of 0.04” × 0.04” (as in Andrews et al., 2018) (used in the previous sections) and the last configuration gives a beam of 0.1” × 0.1” (as in Long et al., 2018; Kurtovic et al., 2021). In Fig. 5.9 we present the radial profiles of the normalized intensity in the Spread and Three-Giants configurations, with a small aspect ratio and low viscosity. The corresponding images are shown in Fig. 5.10. As we present the images in intensity per beam, the sensitivity are different for each resolution: the colorbars range from F_{min} to different maxima depending on the resolution.

In the Spread configuration, we noticed in the previous section that the dust situated between the inner giants and the icy giants creates a bright ring when the resolution is

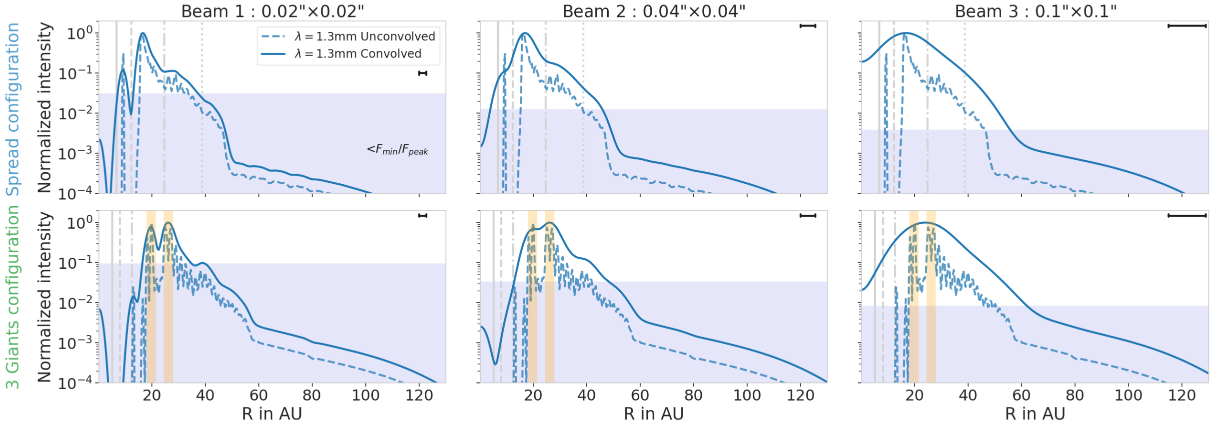

Figure 5.9: Radial profile of convolved and unconvolved images at $\lambda = 1.3$ mm with different beam sizes in the Spread configuration (top row) and in the Three-Giants configuration (bottom row). In these simulations, the disc has the smaller aspect ratio and $\alpha = 10^{-4}$ with $v_{\mathrm{frag}} = 1$ m/s. The different beams investigated range from 0.02" × 0.02" = 2.8 AU×2.8 AU (left) to 0.1" × 0.1" = 14 AU × 14 AU (right). We present the fiducial resolution (0.04" × 0.04" = 5.6 AU × 5.6 AU) in the middle panel for comparison. Each beam is represented by a horizontal line in the upper-right corner of each panel. Orange regions represent the substructures produced by traffic jams, clearly visible in the Three-Giants configuration. The different profiles show that the highest resolution is really needed to start to correctly represent the features of the dust disc.

0.04" × 0.04". When the resolution is lower (right panels), the emission is spread over Jupiter and Saturn's orbit, completely hiding Saturn's gap. However, the inner truncated disc is still noticeable, with a small decrease in the intensity. On the other hand, when we compare the high resolution case (at 0.04") with the highest resolution (at 0.02"), we see that the ring is clearly located at the outer edge of Saturn's gap. The resolution is even high enough to start distinguishing Uranus's gap and the small over-density of dust located between Jupiter and Saturn. On the other hand, with a minimum flux situated at 10μJy/beam, Neptune is completely missed and lost in the noise.

Regarding the Three-Giants configuration, we see a similar behavior: with a beam of 0.1" × 0.1" (right panels), the substructures created by the perturbations by the giants are completely washed out and the only feature remaining is the inner cavity. In both configurations, one can notice that the cavity is shifted compared to the planets orbits: the giants are located in the decrease in intensity, not at the minimum. As we noticed in the previous section, a resolution of 0.04" × 0.04" is sufficient to start to distinguish the over-densities of dust located at the outer edge of the further giant gap. The highest resolution is needed to really resolve the main over-densities that are due to the perturbations of the gas velocity by the multiple giants. With this very high resolution, two rings are observed, corresponding to the two brightest set of over-densities seen in the dust distributions (bottom left panel of Fig. 5.4).

Changing the resolution has an impact on the observable features, but has also an impact on the observed size of the disc. As the beam spread the intensity in the disc, this enhances the value of F_{peak}, reducing the value of $F_{\mathrm{min}}/F_{\mathrm{peak}}$, as we assume a fixed F_{min} value. Therefore, as the intensity decreases with the radius, the observed size of the disc will depend on the resolution used, presenting a larger disc at lower resolutions. As the disc size can change depending on the image resolution, alternative methods such as uv-modeling (Hendler et al., 2020) should be considered to retrieve such a quantity.

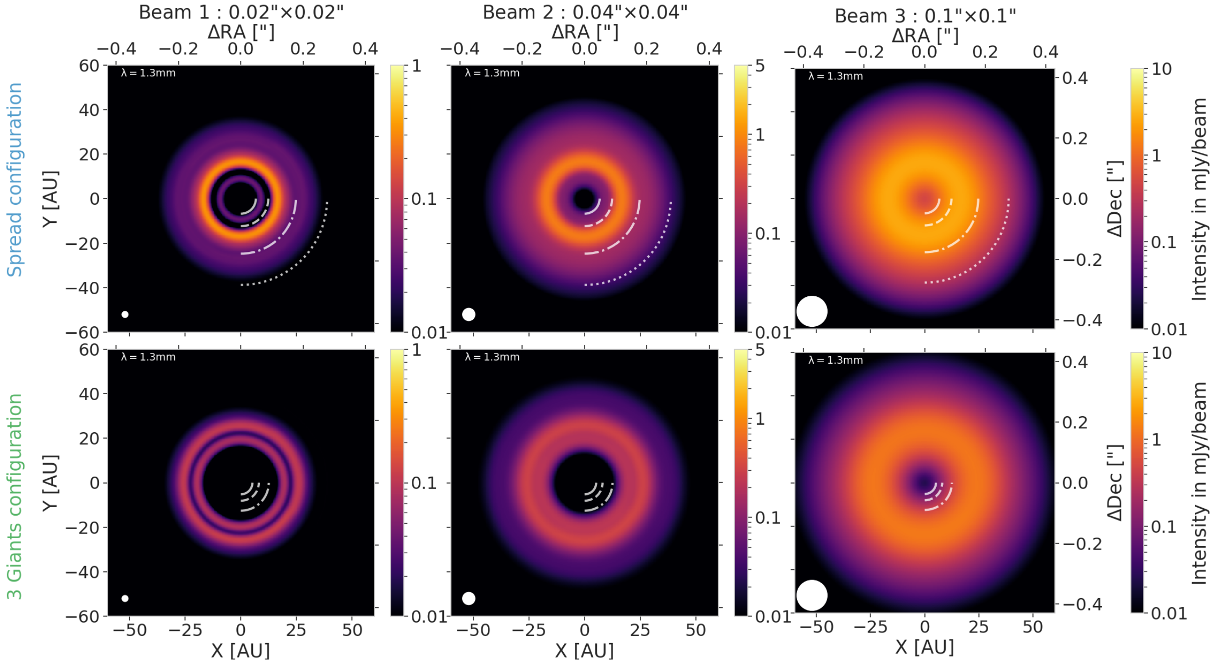

Figure 5.10: Images in total intensity at $\lambda = 1.3mm$ corresponding to the radial profiles presented in Fig. 5.9. The positions of the different planets are represented by the different white arcs. The different beams investigated range from 0.02" × 0.02" (left) to 0.1" × 0.1" (right) and are represented in the lower-left corner of each image by the white ellipses. We show the fiducial resolution (0.04" × 0.04") in the middle panel for comparison. The colorbars are adjusted for each resolution as they have different sensitivities. These images show the importance of resolution: the substructures start to be well represented at very high resolution.

5.5 Discussion

5.5.1 Comparisons to known observed discs

The DSHARP survey (Andrews et al., 2018) studied several bright massive discs around stars located in the vicinity of the Sun with a beam size of ~ 0.035". These discs present several features, such as gaps, rings, spirals and asymmetries. The most axisymmetric discs show several configurations of gaps and rings (Huang et al., 2018a). Some of the discs present bright rings located at large radii (r $>$ 50 AU), such as AS209 and HD163296. Our synthetic images never showed features at such large radii, even in the Spread configuration where Neptune is located at 39 AU. This can be explained by the sizes of the discs: our gas disc is small (160 AU in radius) whereas HD163296 is thought to be wider than 500 AU in radius (Isella et al., 2007; Muro-Arena et al., 2018) with a potential outer planet located at 260 AU (Pinte et al., 2018).

One of the explanations for the existence of structures at large radii is the presence of planets carving gaps and creating rings. Lodato et al. (2019) show that with giant planets migrating fast enough, it is possible to produce gaps and rings at large radii and still reproduce the distribution of eccentric giant planets observed in radial velocity. However, such migration speeds require a too high viscosity (Ndugu et al., 2019) compared to the viscosity needed to allow the formation of planets that could explain the observed substructures. On the other hand, it is also very unclear how planets can form that far in discs with the core accretion model (Morbidelli, 2020). Moreover, our images with the Three-Giants configuration do not present features in the outer disc because the planets are located in the inner disc. It is possible that this configuration will lead afterward to some scattering events that will produce systems with giant eccentric planets (Bitsch et al., 2020). We show here that planets forming in the inner disc do not result in features (rings or gaps) in the outer disc region as observed in the DSHARP survey. It is clear these two different giant planet formation channels result in different observable disc structures.

Another important point is linked to the substructures induced by the planets but not directly linked to their orbit and gap. For example, Zhang et al. (2018) analyze the rings and gaps structures present in the DSHARP discs and derive which possible planet mass could produce such substructures. Even if they take into account the fact that some planets can create multiple gaps at low viscosity (Dong et al., 2018; Bae & Zhu, 2018), as in AS 209, we found that the gas radial velocity structure can also create rings, blurring even more the link between the number of planets and the number of gaps present in the disc. We discuss in Sect. 5.5.3 how this problem could be addressed.

However, the disc surveys are biased toward the brightest discs. The differences in the images between the massive DSHARP discs and our study confirm that planet formation happening in the inner regions of the disc results in different features in observed discs. However, these surveys contain some bright discs that are similar in size and show comparable features as the discs studied here. In the Ophiuchus DIsc Survey Employing ALMA (ODISEA) (Cieza et al., 2019; Williams et al., 2019), DoAr44 presents a bright inner ring and a dimmer one exterior to it, resembling the image of the Spread configuration disc at low viscosity and low aspect ratio with a resolution of 0.02" (see Fig.5.10, first top panel). Similarly, Facchini et al. (2020) observed two discs, LkCa15 and J1610 showing features similar to our Three-Giants configuration disc with a resolution of 0.04" (see Fig. 5.10, middle panel of second row). Observations of the V4046 Sgr circumbinary disc by Martinez-Brunner et al. (2022) present features that are very similar to the Spread Solar System observed with a similar resolution (in Fig.5.10, top left panel), around a binary, unlike our configuration. This images prove that ALMA is capable of reaching such high resolution. Observations of such discs can therefore give us some insights on how planet formation can occur in the inner regions of the discs, compared to the DSHARP observations giving insights on how it occurs in the outer regions of the discs. Moreover, the constrains derived from the local study of the Solar System could help understand planet formation in discs such as DoAr44 that present similar features as our Solar System discs.

5.5.2 Comparing to exoplanet populations

In Sect. 5.4.4 we show that with the highest resolution, it is possible to observe features originating from the ice giants if they are in the very outer regions of the disc and far away from the inner gas giants. Microlensing surveys, such as that presented in Suzuki et al. (2016), claim that the most common type of planets observed are ice giants located at a few AU from their star. Our study shows that it is possible to observe, with the highest resolution that ALMA can reach, features caused by such planets if they are at a few tens of AU. These observations could therefore help to constrain the formation pathways of the ice giants found in microlensing surveys, under the assumption that these ice giants do not turn into gas giants. We should note here that microlensing surveys mostly observe dwarf stars, which should have less massive discs in the first place, making observations unfortunately very difficult.

Constraining planet formation during the disc phase is important to improve our understanding of different formation scenarios. Indeed, the gas disc phase contains information about the initial conditions of planet formation and the initial structure that could lead to dynamical instabilities after the disc phase. The final structure of the planetary system depends highly on the processes happening during the gas disc phase.

Currently, the formation of giant planets is still unclear. In one hand, observations of large discs, such as in the DSHARP survey, motivate the idea that giant planets must form in the outer part of the discs and then migrate inward, explaining the presence of bright outer rings and the planet distributions observed by different surveys (Lodato et al., 2019). However, this scenario requires a rather high viscosity in order to have an efficient migration of the giant planets. Ndugu et al. (2019) shows that if the viscosity of the disc is lower, as disc observations seem to suggest (Dullemond et al., 2018; Flaherty et al., 2018), then these giant planets do not have time to migrate to semi-major axis corresponding to distances within the reach of radial velocity surveys (e.g., Fulton et al., 2021).

Another possible giant planet formation scenario is to have giant planets forming in the inner regions of the discs, where the orbital timescales favor planet formation and where a slower migration of the planets can still explain the observed giant distributions (Bitsch et al., 2020). Our study shows that giant planets forming in the inner part of the discs do not produce bright features as observed in the DSHARP survey.

Higher resolution observations of discs can therefore help us distinguish between the formation of planets in the outer disc or in the inner regions of protoplanetary discs. This can give constraints on the initial conditions needed for planet formation to occur and improve the link between the different observed planet populations and the theoretical models studying different planet formation scenarios.

5.5.3 Features created by traffic jams

In Sect. 5.3 we present the dust distributions in each configuration. Some of the distributions show multiple narrow dust over-densities, specially at low viscosity. The configuration showing the clearest over-densities is the Three-Giants configuration (Fig. 5.4). These dust rings are created by traffic jams, as shown in Appendix B.2. As these traffic jams originate from the highly perturbed gas radial velocities and not from a pressure bump present in the gas, the dust is not trapped and will flow to the inner parts of the disc.

The presence of these traffic jams has several impacts on our understanding of planet formation. First, as they create features observable by ALMA, it blurs further the link between the number of planets present in discs and the number of gaps and rings created. Considering that a single planet can create multiple gaps in low viscosity discs (Dong et al., 2018; Bae & Zhu, 2018), having features created by velocity perturbations on top of the one created by pressure perturbations complicates our estimations of planet masses needed to create observed features.

However, in order to trigger the formation of these traffic jams, the disc needs to be highly perturbed in velocity. In our simulations, it requires the presence of multiple giant planets. In systems where only one or two giant planets are embedded, the velocity perturbations do not create strong traffic jams (Pinilla et al., 2015). The presence of traffic jams is therefore linked to the presence of the ice giants in our simulations, meaning that their impact is non-negligible on the dust substructures. Depending on the masses of these planets, many of the discs observed might therefore present features originating in some traffic jam effect rather than from dust trapped in pressure bumps. This effect has

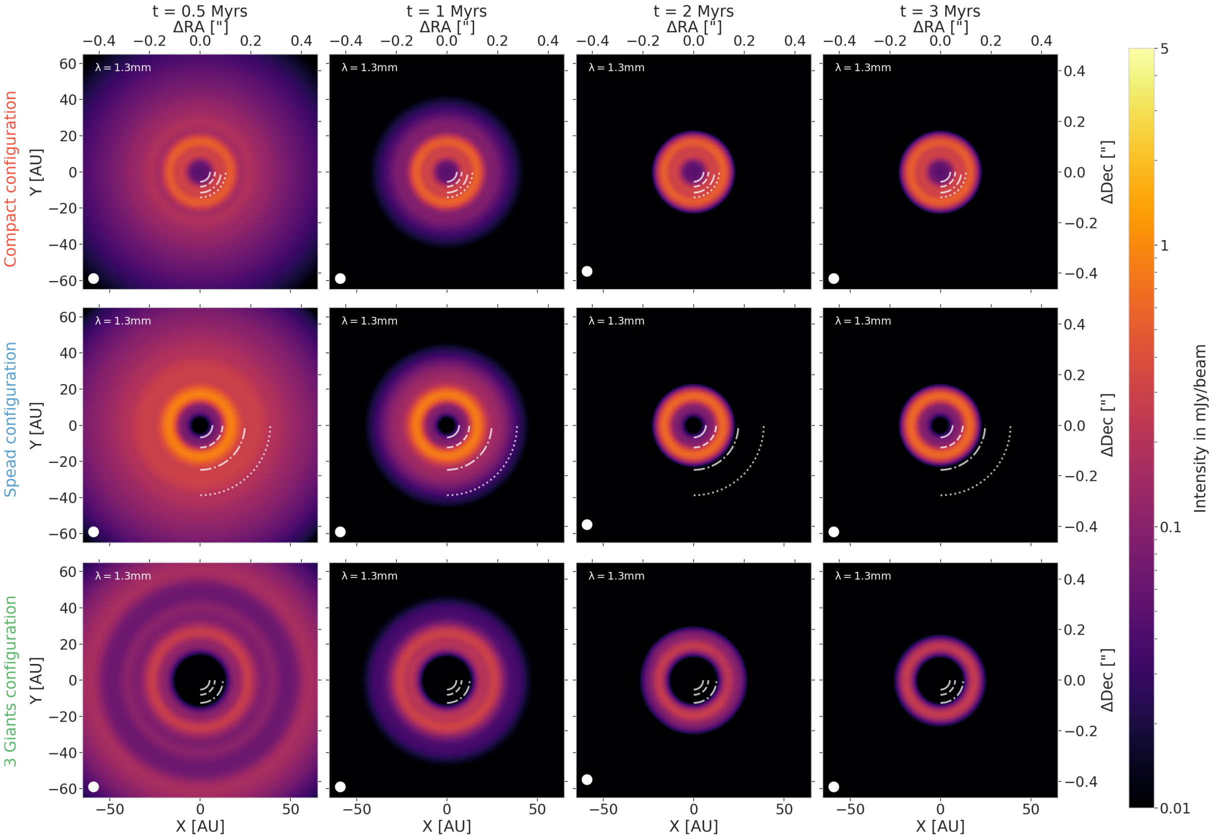

Figure 5.11: Images at λ =1.3mm of the different configurations, at low viscosity and low aspect ratio, at different times: 0.5 Myrs, 1 Myr, 2 Myrs, and 3 Myrs, from left to right. The white lines represent the positions of the different planets in each configuration. We assume that the sensitivity of the instrument is limited to fluxes larger than 10 μJy/beam. As time evolves, the sizes of the discs shrink due to inward drift, leaving stable rings in the inner discs after 1 Myr.

been encountered in the past (e.g., Rosotti et al., 2016) and some studies show that it is possible to disentangle between an over-density of dust caused by a pressure trap or by a traffic jam (Pinilla et al., 2017a,b; Dullemond et al., 2018). Observations at multiple wavelengths is a possible way to distinguish between each mechanism and can therefore help to unveil the number of planets contained in the observed discs.

Another method that can be used to determine if an observed ring is coming from a pressure trap or a traffic jam is to study the CO velocity perturbations (Teague et al., 2018; Pinte et al., 2018, 2020). In these studies, the presence of a pressure gradient in the disc can be linked to a change of rotational velocity. Traffic jams, originating from a perturbation of the radial gas velocity, would not influence the rotational velocity profile of the disc. The presence of this "kink" in the CO rotational velocity perturbations could be used to distinguish between a traffic jam or a pressure bump (Izquierdo et al., 2021).

5.5.4 Impact of time evolution

With this project, we made the choice to implement dust growth with `TWO-POP-PY` at the expense of a 2D or 3D evolution model, allowing us to study the time evolution of dust growth. As Drążkowska et al. (2019) show in their 2D study, including dust coagulation has a non-negligible impact on the dust distribution. In our case, we implemented dust growth by assuming that the gas is fixed during dust growth (here evolved for 1 Myr). This

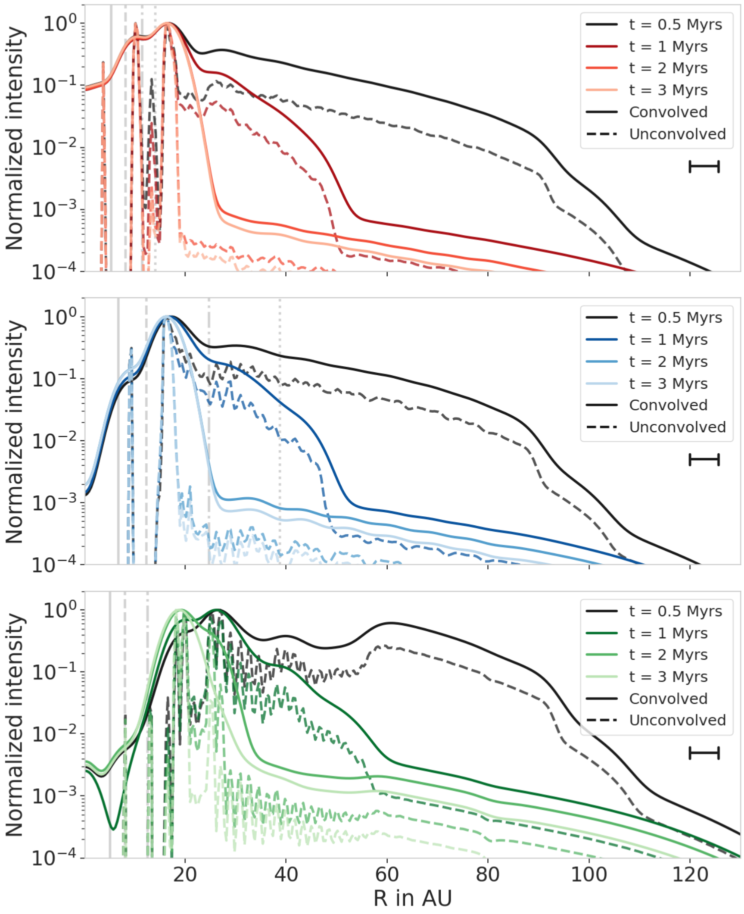

Figure 5.12: Radial intensity profiles after 0.5 Myr, 1 Myr, 2Myrs, and 3 Myrs of evolution in each configuration with low viscosity and a low aspect ratio. The total size of the disc depends on the time evolution, which determines the dust distribution.

assumption makes a good approximation at low viscosity for two reasons: the first one is that the viscous timescale is way larger than 1 Myr, meaning that the disc would remain almost static during this time; on the other hand, migration is slow at this viscosity (Baruteau et al., 2014), meaning that the dynamics of the planets would not strongly influence the gas disc structure. Even if instabilities can be triggered at low viscosities creating azimuthal asymmetries (as in Zhang et al. (2018), Section 5.1 with a low viscosity Solar System disc), we assume that these asymmetries vanished by the time the planets are fully formed, as supported also by other hydrodynamical simulations (e.g., Hammer et al., 2017; Bergez-Casalou et al., 2020) and shown in Appendix B.1.

However, at high viscosity, gas evolution and planet-disc interactions over 1 Myrs start to be non-negligible: the gas is accreted toward the star and planets migrate faster. Migration of planets can alter the dust distributions in the disc (e.g., Meru et al., 2019; Weber et al., 2019), but, as mentioned in Sect. 5.3, the substructures in the gas (e.g., pressure bumps) are not strong enough to block the inward diffusing dust, preventing the creation of notable features in the disc. Therefore, our setup is a good approximation to estimate how dust is distributed and further studies would be needed to detail the impact of gas evolution.

As mentioned, in this chapter, we chose to evolve the dust for 1 Myr during which the gas profile is considered constant. However, as eqs. 1.16 and 1.20 show, the millimeter dust disc size will expand with time as dust will grow further and further out in the disc, until drift will deplete the outer regions of the disc and reduce the millimeter disc size. In Figs. 5.11 and 5.12 we present the images and their radial intensity profiles at different times: after 0.5 Myrs, 1 Myr (as in Sect. 5.3), 2 Myrs, and 3 Myrs. After 0.5 Myrs, the dust disc is large as drift only starts to deplete the outer region of the disc, showing more substructures than at later times. In the Spread configuration, the gaps created by Uranus and Neptune are slightly distinguishable before being washed away by drift. In the Three-Giants case, the velocity perturbations induced by the planets create numerous gaps and rings in the outer regions, before being washed at later times by drift as for the other configurations. The presence of numerous substructures in young discs matches the observations of the disc around IRS 63, supposedly younger than 0.5 Myr Segura-Cox et al. (2020).

After 2 Myrs, the majority of the dust located in the outer disc had time to grow and drift to the inner regions. The only dust remaining is the dust trapped in the pressure bump located at Saturn's gap or at the outer giant gap. Long et al. (2020) also investigated the impact of time evolution of the dust size of the disc: they show that without any dust traps, the millimeter dust size of the disc increases until drift reduces the disc; on the other, in presence of a pressure bump created by a planet and acting like a dust trap, the size of the disc is first dominated by growth and then by the position of the dust trap.

Furthermore, at low viscosity, some asymmetries in the gas can arise due to instabilities (e.g., Rossby wave instability Lovelace et al., 1999; Li et al., 2001): to study these asymmetries, a 2D (at least) analysis has to be done. Future simulations, with sufficient computational power, should then consider both dust growth in multidimensional grids (Drążkowska et al., 2019). In our study, we avoided these asymmetries by simulating the gas disc for sufficient time, letting the possible instabilities dissipate in the disc (Hammer et al., 2017).

Time evolution also has an impact on the characteristics of the planets. Indeed, we assume that the planets already have their final mass and do not migrate. Bergez-Casalou et al. (2020) showed that gas accretion can have an impact on the gap depth, specially at low viscosities. This would influence the pressure profile of the discs and therefore the dust distributions and the created substructures. Computing the evolution of gas, planet mass and semi-major axis with dust growth and evolution simultaneously would be ideal but too computationally expensive. In order to investigate what the effect of the planet mass can have on the results, we showed in Sect. 5.4.2 how the images could be different at different stages of planet evolution. The similarities between the images showed us that it is more important to improve the resolution of our observations, as a resolution of 0.02" or better is needed to disentangle between different planetary systems.

5.5.5 Disc dust mass

One of the challenges of planet formation is to overcome the too large radial drift speed of dust. Cosmochemical studies show that planetesimal formation happened at all times during the Solar System disc age (e.g., Connelly et al., 2012). Therefore, if the dust drifts too rapidly during the disc lifetime, then there is not enough material to to ensure a continuous planetesimal formation as in the Solar System. One way to prevent fast inward drift that empties the disc is to trap the dust (Pinilla et al., 2012), as showed in Sect. 5.3. We investigate here how much dust is actually remaining in our discs as a function of disc parameters and planet configurations. In Fig.5.13 we show the total dust

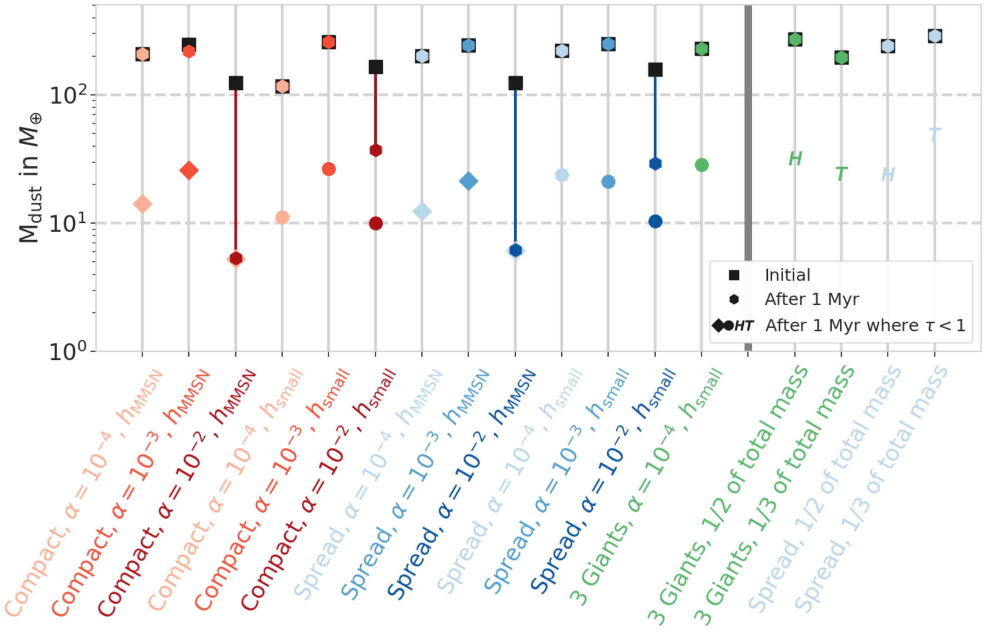

Figure 5.13: Masses of the dust discs for each configuration and each disc parameter derived from the dust evolution model. The squares correspond to the initial amount of dust mass, and the circles show how much of this mass is left after 1 Myr of dust evolution. The differences in initial dust masses for all discs originate from the assumption that the dust-to-gas ratio is initially 0.01 and the inner disc is depleted in dust by the giant planets (see Sect. 5.3). In most cases, all the dust is trapped in the discs, except at high viscosity because the planet gaps are not strong enough to prevent the dust from flowing toward the star. To compare to observed dust masses as in Fig. 5.14, we also derive the dust contained in the optically thin regions (represented by the markers corresponding to Fig. 5.14). We see here that the majority of the mass is hidden in the optically thick regions.

mass contained in each of our discs at two different times: initially and after 1 Myr of evolution.

As expected from Sect. 5.3, the high viscosity discs ($\alpha = 10^{-2}$) do not present strong dust traps and the high diffusion allows the dust to drift toward the star. Therefore, after 1 Myr, they lost a significant amount of dust. On the other hand, all the discs with lower viscosities ($\alpha = 10^{-3}$ and 10^{-4}) trap the dust efficiently. Even if the dust is distributed differently as a function of time (see Figs. 5.11 and 5.12 from the previous section), the amount of trapped dust available to form the small bodies of our Solar System stays constant (from the time the giant planets form and assuming that the inner disc is already depleted in dust).

In all the discs with efficient dust trapping, the total amount of dust is above 100 $M_\oplus$. This can be compared to the solid masses needed to form the small bodies of the Solar System. The solid budget needed to trigger the Nice instability is of at least 20 $M_\oplus$ (Nesvorný & Morbidelli, 2012; Nesvorný et al., 2013). As the mass contained in the asteroid belt is negligible ($5 \times 10^{-4} M_\oplus$, Kresak (1977)), our dust discs have enough material to form the small bodies of the Solar System even if the formation of planetesimal from pebbles is not 100% efficient. Moreover, having the majority of the dust located in the outer disc (i.e., outside Saturn's location) is in agreement with Izidoro et al. (2021a) where the authors show that the inner Solar System, after formation of some planetesimals, should be depleted in pebbles to explain the formation of the current terrestrial planets. This also clearly indicates that the viscosity of the gas in the protoplanetary disc must have been low, because at high viscosity even Jupiter is not able to block inward drifting pebbles, which is required by cosmo-chemical studies (e.g., Kruijer et al., 2017; Weber et al., 2018).

On the other hand, dust masses derived by observations are on the order of a few Earth masses to a few tens of Earth masses (Andrews et al., 2013; Ansdell et al., 2016). In order to understand the origin of this discrepancy between the dust masses in our simulations and the one derived by observations, we derive the dust masses from our disc images using the same methods as in the observations and compare them to the actual dust mass of our simulations. Assuming an optically thin disc, the observed dust mass $M_{d,obs}$ is given by (Hildebrand, 1983):

$$M_{d,obs} = \frac{F_\nu \, d^2}{\kappa_\nu^{abs} B_\nu(T_d)} \tag{5.4}$$

where F_ν is the total integrated flux density of the disc, d the disc's distance, κ_ν^{abs} the absorption opacity at the observed wavelength (here $\lambda = 1.3$ mm) and $B_\nu(T_d)$ the Planck function at temperature T_d.

In general, observers use the assumptions made by Andrews et al. (2013) regarding the opacity and dust temperature. The opacity is assumed to be $\kappa_\nu^{abs} = 2.3$ cm^2/g, following Beckwith et al. (1990). The averaged temperature is taken as $T_d = 20$ K. This value was derived from the observations of Taurus discs by Andrews & Williams (2005), using eq. 5.4: the authors assumed a simple disc model in order to determine the disc dust mass and derived the disc average temperature assuming the same opacity as mentioned above. To be consistent with our simulations, we derive the observed masses using the absorption opacity and average temperature from the `RADMC-3D` outputs and compare the resulting masses to the ones obtained by following Andrews et al. (2013). Assuming that mostly millimeter grains contribute to the opacity at this wavelength (Dullemond et al., 2018), we use the absorption opacity derived from `OpTool` following the assumptions made in Sect. 5.2.3, resulting in $\kappa_\nu^{abs} = 2.04$ cm^2/g for a grain size of $a = 0.1$ cm at $\lambda = 1.3$ mm. The dust disc temperatures and masses can be found in table 5.5.

The relation represented by eq. 5.4 relies on the assumption that the disc is optically thin. However, from the dust evolution models in Sect. 5.3, we know that the dust is trapped in relatively dense rings that can become optically thick. As some significant amount of mass can be hidden in optically thick regions, we compare the observed dust mass $M_{d,obs}$ to the dust mass contained in the optically thin regions. In order to do so, assuming $\tau_\nu(r) = \Sigma_d(r) \times \kappa_\nu^{abs}$, the comparison is made with the amount of dust contained in the regions where $\tau < 1$.

By comparing the total amount of dust to the mass contained in the optically thin regions (Cols. 3 and 5 or circles and diamonds in Fig. 5.13), we show that the majority of the mass is hidden in the optically thick regions. This results in masses $M_{d,\tau_\nu<1}$ that can be more than ten times lower than the actual total mass. Therefore, the presence of optically thick rings in disc images can hide a large amount of dust.

We show in Fig. 5.14 the difference between the masses derived from eq. 5.4, $M_{d,obs}^{\lambda=1.3\text{ mm}}$ and the masses contained in the optically thin regions of our discs, $M_{d,\tau_\nu<1}^{tot}$. The diamonds and hexagons represent the different disc parameters where the colors match the planet configuration (table 5.1). Markers surrounded by a black outline are the masses assuming the Andrews et al. (2013) setup. We clearly see that the masses are under-estimated when using the actual dust temperature average, whereas a colder temperature (as in Andrews et al. (2013)) tends to over-estimate it.

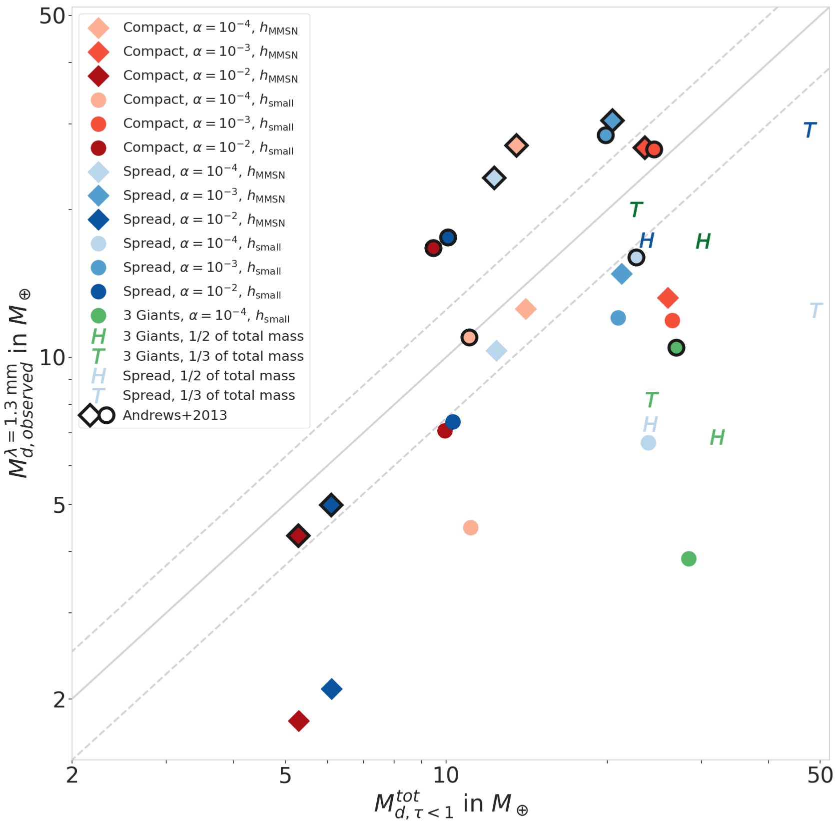

Figure 5.14: Observed dust masses for each configuration (colors) and each disc parameter (markers). A black outline surrounds the masses derived using the Andrews et al. (2013) assumptions for the disc's opacity and temperature. $M^{tot}_{d,\tau_\nu<1}$ corresponds to Cols. 5 and 7 (see also Fig.5.13) and $M^{\lambda=1.3\text{ mm}}_{d,obs}$ to Cols. 6 and 8 in table 5.5. The solid gray line represents the masses for which the observations match the masses from the simulations. The top (bottom) dashed line shows the discs for which the observations overestimate (underestimate) the actual mass contained in the optically thin part by 25%.

The underestimation of the observed dust mass derived with eq.5.4 with self-consistent opacities and disc temperatures originates from the calculation of $M^{tot}_{d,\tau_\nu<1}$. As this mass comes from our simulations, it contains all grain sizes present in the disc. However, as $M^{\lambda=1.3}_{d,obs}$ mm is based on F_ν (eq. 5.4), it represents only the grains emitting consequently at the observed wavelength. In our case, the image at $\lambda = 1.3$ mm is dominated by millimeter grains, meaning that the mass contained in the smaller grains is not probed here, leading to a less massive dust disc. As this mass underestimation is therefore expected, this shows that the $T_d = 20$ K assumption is leading to an unrealistic overestimation of the optically thin dust masses from observations. From our study, an average temperature of 45 K (see Table 5.5) might give more reasonable results; however, further complete studies can help in improving the estimation of T_d.

In conclusion, observations might completely under-estimate the total amount of dust mass contained in discs due to optically thick regions, as it was shown in other studies (Dullemond et al., 2018). Improving our understanding on opacities and discs temperatures are crucial to unveil the mystery around the amount of material available for planet formation.

Table 5.5: Dust masses calculated from the total integrated flux as in eq. 5.4.

			This study			Andrews et al. (2013) setup	
(1) Configuration	(2) F_ν (mJy)	(3) $M_{d,tot}$ ($M_\oplus$)	(4) T_d (K)	(5) $M_{d,\tau<1}^{tot}$ ($M_\oplus$)	(6) $M_{d,obs}^{\lambda=1.3\text{ mm}}$ ($M_\oplus$)	(7) $M_{d,\tau<1}^{tot}$ ($M_\oplus$)	(8) $M_{d,obs}^{\lambda=1.3\text{ mm}}$ ($M_\oplus$)
Compact, $\alpha = 10^{-4}$, MMSN h	48.9	206.8	41.8	14.1	12.6	13.1	27.1
Compact, $\alpha = 10^{-3}$, MMSN h	48.3	216.7	39.6	26.0	13.2	23.5	26.8
Compact, $\alpha = 10^{-2}$, MMSN h	7.8	5.33	45.8	5.3	1.8	5.3	4.3
Compact, $\alpha = 10^{-4}$, low h	19.8	115.9	46.8	11.0	4.5	11.0	11.0
Compact, $\alpha = 10^{-3}$, low h	48.0	258.9	43.2	26.4	11.9	24.4	26.6
Compact, $\alpha = 10^{-2}$, low h	30.1	37.1	45.4	9.9	7.1	9.5	16.7
Spread, $\alpha = 10^{-4}$, MMSN h	41.9	199.4	43.5	12.4	10.3	12.3	23.3
Spread, $\alpha = 10^{-3}$, MMSN h	54.9	243.3	40.1	21.2	14.8	20.5	30.5
Spread, $\alpha = 10^{-2}$, MMSN h	8.9	6.1	45.6	6.1	2.1	6.1	5.0
Spread, $\alpha = 10^{-4}$, low h	28.8	220.7	45.8	23.8	6.7	22.7	16.0
Spread, $\alpha = 10^{-3}$, low h	51.2	248.7	45.2	21.0	12.1	19.9	28.4
Spread, $\alpha = 10^{-2}$, low h	31.6	29.0	45.6	10.3	7.4	10.1	17.6
3 Giants, $\alpha = 10^{-4}$, low h	18.8	229.2	51.0	28.4	3.9	26.9	10.5
3 Giants, 1/2 of total planet mass	31.1	269.5	47.9	32.1	6.9	30.2	17.3
3 Giants, 1/3 of total planet mass	36.1	196.6	46.8	24.2	8.2	22.6	20.1
Spread , 1/2 of total planet mass	31.3	240.2	45.6	24.0	7.3	23.7	17.4
Spread , 1/3 of total planet mass	52.5	288.6	44.9	49.1	12.5	47.8	29.2

Columns are: (1) Planet and disc configuration. (2) Total integrated flux density in mJy. (3) Total dust mass from the dust evolution model after 1 Myr of evolution. (4) Average temperature from the RADMC3D outputs. (5) Actual mass contained in the optically thin region, assuming $\tau_\nu(r) = \Sigma(r) \times \kappa_\nu^{abs}$. (6) Mass derived from observations at $\lambda = 1.3$ mm, derived by eq. 5.4. (7) Actual mass contained in the optically thin region, assuming $\kappa_\nu^{abs} = 2.3$ cm^2/g as in Andrews et al. (2013). (8) Mass derived from observations at $\lambda = 1.3$ mm, derived by eq. 5.4 assuming $T_d = 20$ K as in Andrews et al. (2013). On average, our disc temperature is around 45 K, which is more than twice the usual dust disc temperature used in observational studies. Comparing the total mass (3) to the mass contained in the optically thin regions (5), we show that the majority of the mass is hidden in optically thick regions, like, for example, our dust rings.

5.6 Conclusions

In this chapter we derived images at $\lambda = 1.3$ mm of different planetary system configurations representing the potential Solar System protoplanetary disc. We also derived the images of a giant system composed of three planets of 1 Jupiter mass each, representing a potential initial state for scattering events to happen and produce eccentric planets that match the radial velocity observations (Jurić & Tremaine, 2008; Raymond et al., 2009a; Sotiriadis et al., 2017; Bitsch et al., 2020). Using 2D hydrodynamical simulations we determined the gas disc profile in the presence of four (or three) giant planets. This profile was then used as an input for a dust evolution model. After 1 Myr of dust evolution, the resulting dust distributions were used to compute synthetic images of these different discs. Our main conclusions are:

1. The dust distributions show that the perturbations created by multiple planets in one disc can lead to substructures that are not directly linked to the positions of the planets. These features are created by traffic jams in the disc, revealing the importance of the gas radial motion in the case of multiple giant planets. Consid-

ering that a single planet can also create multiple gaps and rings in a low viscosity disc by perturbing the gas surface density (Dong et al., 2018; Bae & Zhu, 2018), this complicates the relation between the number of features created by single or multiple planets and the actual number of perturbers. Our study thus highlights that not all individual gaps and rings are caused by individual planets perturbing the pressure profile of the discs, complicating the link between protoplanetary disc observations and exoplanets.

2. By comparing the synthetic images obtained to known observed discs, we showed that the disc phase can be used to derive robust constraints on planet formation scenarios. The presence of bright substructures located at large radii in the DSHARP survey can be explained by the large size, mass, and brightness of these discs. Here, we show that planet formation occurring in smaller discs can easily be missed at low resolutions in the observations (i.e., with a beam larger than 0.04" × 0.04"). One way to improve our understanding of planet formation is thus to observe small protoplanetary discs (i.e., of a few tens of AU) at high resolution to probe the formation environments of different planetary populations.

3. The Three-Giants configuration, representing a future system that could experience scattering events after the disc phase, only presents substructures within 40 AU. While Lodato et al. (2019) speculate that the bright rings observed by DSHARP can be explained by the presence of fast migrating giant planets matching the radial distribution of eccentric planets observed by radial velocity, Ndugu et al. (2019) show that this requires a migration at high viscosity, which is contrary to the recent derivation of disc viscosity. Our study here shows that a giant planet system that is susceptible to scatter later during its formation would not produce bright rings in the outer regions during its gas disc phase.

4. At high viscosity, too much dust diffuses through the gaps generated by Jupiter and Saturn, inconsistent with terrestrial planet formation (e.g., Izidoro et al., 2021a) and cosmo-chemical evidence (e.g., Kruijer et al., 2017). At low viscosity, dust can be retained in a pressure trap exterior to the giant planets, generating large optically thick dust pileups. Self-consistently constraining the dust mass of the discs observationally revealed that the observationally inferred dust mass can be a factor of ten below the real dust mass in optically thick rings in our simulations. Moreover, improving dust temperature estimates can highly improve the estimation of dust from the observations.

This study shows the importance of resolution in observations for our understanding of planet formation. For example, in the Compact configuration (Figs. 5.5, B.9, and B.10), the features created by the four giant planets were smeared out by the beam of the instrument, making it impossible to determine how many planets are located in this disc. If future surveys focus on very high resolution observations of smaller protoplanetary discs, then it will be possible to distinguish the conditions needed for giant planets to form in the outer or inner regions of the disc. As discussed in Sect. 5.5.1, an interferometer such as ALMA already has the power to produce images with a high enough resolution. Such observations should be combined with further studies that model the disc structures in the presence of multiple planets. Finally, in order to improve our understanding of the origin of the dust substructures (traffic jams or pressure bumps as discussed in Sect. 5.5.3), multi-wavelength imaging will help us determine how many planets are trapped in discs, as well as help us determine the optical properties of the dust. This last point is important for deriving how much mass is available in discs for planet formation.

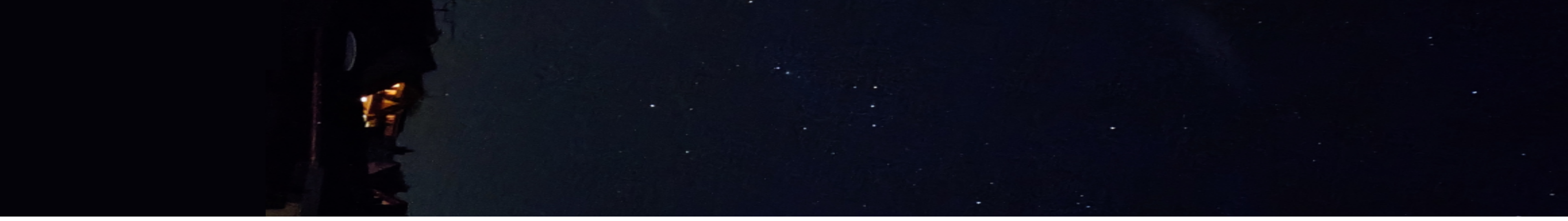

6

Summary and outlook

Planetary systems hosting multiple giant planets, such as our own Solar system, are observed and might be quite common (Wright et al., 2009; Fabrycky et al., 2014; Zhu, 2022). These giant planets are thought to have formed in the same parental protoplanetary disc. In this thesis, I, with the help of my collaborators, investigated how the simultaneous formation of giant planets could impact their own growth and the protoplanetary disc structure. For this purpose, we used 2D isothermal hydrodynamical simulations to estimate the impact of giant planet formation at a global disc scale. We started by investigating the impact of runaway gas accretion on the gap formed by a single accreting planet in Chapter 3, before investigating the impact of the presence of a second planet on each planet growth in Chapter 4. Lastly, my collaborators and myself studied how the presence of multiple giant planets influence the disc structure by deriving synthetic ALMA images of protoplanetary discs hosting i) the Solar system giant planets or ii) a system of three planets of one Jupiter mass. Our last study brought an observational aspect to the influence of the presence of multiple giant planets on the disc structure by deriving synthetic ALMA images of a protoplanetary disc hosting the Solar system giant planets or a system of 3 giant planets. The conclusions of the different studies are an attempt to address the following questions:

How strongly do disc parameters influence the runaway gas accretion of giant planets ?

In this thesis, we mostly investigated the impact of two major disc parameters, namely the aspect ratio profile h and the turbulent viscosity α. These parameters govern the behavior of the gas in the vicinity of the planet, which is influenced by the formation of a gap by the planet and by the capacity of the gas to flow through this gap. The accretion rate formula that we investigated in Chapters 3 and 4 is directly dependent on the aspect ratio of the disc (see eq. 2.4): as it is more difficult for planets to create gaps in discs with larger aspect ratios, the planets stay longer in an accretion regime regulated by the Bondi accretion resulting in higher accretion rates. On the other hand, the turbulent viscosity dictates how efficiently the gas can diffuse through the planet gap, refilling the amount of gas present in the vicinity of the planet. A lower viscosity therefore results in lower gas accretion rates.

The competition between gap opening and gas accretion is highly dependent on the kinematic viscosity $\nu(\alpha, h)$ of the disc. As shown in Chapter 4, this competition dictates how the gas mass is distributed between two planets accreting within the same disc. Depending on the capacity of the gas to flow through the gaps, the inner planet can be quickly starved. Therefore, we found that the disc's kinematic viscosity is a key parameter governing planet gas accretion and planet growth.

Do accreting planets create characteristic observable features in the protoplanetary disc structure ?

Gas accretion can have an impact on two observable features influenced by the presence of planets: gap formation and stellar accretion. Indeed, it is possible to determine the stellar accretion rate from the UV excess in a star SED (Hartmann et al., 1994; Calvet & Gullbring, 1998). This accretion rate is directly linked to the amount of gas flowing towards the central star. In Chapters 3 and 4, we investigated the impact of the presence of accreting planets in the disc on the stellar accretion rate. We found that, after reaching the viscous time scale, the accretion onto the star is reduced by the presence of accreting planets, as they both accrete a fraction of the gas flowing to the inner part of the disc and repel another fraction of the gas via gap formation. However, even an efficiently accreting single planet could only reduce the stellar accretion by less than an order of magnitude (see Sect. 3.3.3 and 3.5.1). Adding a second planet in a disc with medium or high viscosity ($\alpha \gtrsim 10^{-3}$) barely influenced the stellar accretion rate compared to the impact induced by a single planet (see Sect. 4.4.2). Due to the uncertainties on the disc's viscosity which plays a major role in setting the stellar accretion rate, it is impossible to disentangle from the observed stellar accretion rate if the disc hosts accreting planets.

On the other hand, gas accretion has also an impact on the gap opening mass of the planets. In Chapter 3, we found that, in low viscosity discs, gas accretion can influence the gap opening mass by up to a factor of four. This means that, depending on the planetary gas accretion rate, different planet masses produce the same gap shape (as shown in Fig. 3.16). As gas accretion rates onto the planets are not well constrained yet, the impact it has on the gap opening mass complicates our understanding of protoplanetary disc observations.

To which extent can gas accretion impact the dynamical evolution of planetary systems hosting giant planets ?

Within our framework of studies, the most important impact that gas accretion can have on the dynamical evolution of single giant planets lies on its impact on the gap opening mass. Indeed, when a planet opens a gap, it switches from a fast type I migration to a slow type II migration (see Sect. 1.2.3 and 3.4.4). At low viscosities, gas accretion significantly impacts the mass at which the planet switches from one type of migration to the other. Moreover, in Chapter 4, we found that two planets accreting from the same disc quickly end up with similar masses. This will have an important impact on the dynamical evolution of the pair of planets. By staying longer or shorter (depending on the viscosity) in the type I migration regime, the relative speed between the planets then depends on their accretion rate, impacting their potential capture in resonance. Therefore, the whole system architecture can be impacted by the planet gas accretion.

Can we use the observed distribution of exoplanetary systems to constrain giant planet formation ?

In Chapter 4, we found that planets accreting from the same protoplanetary disc end up with similar masses. However, when we compare the resulting masses to the masses of the planets observed in exoplanetary systems, we find that it is complicated to reproduce the large mass ratios observed (see Fig. 4.12). This can be used to better constrain giant planet formation: from our study, it is clear that the runaway gas accretion onto the planets has to be quickly stopped once the second planet starts accreting in order to reach extreme mass ratios. If we consider that the accretion is stopped by the gas disc dispersal, then it is possible to time when runaway gas accretion occurred during the growth of embedded planets.

However, it is still unclear whether giant planets favourably form in the inner or in the outer regions of the disc. In one hand, observations of large bright protoplanetary discs, like in the DSHARP survey (Andrews et al., 2018), sustain the idea that giant planets form in the outer part of the discs before migrating inward to their final positions. This would explain the presence of the bright outer rings observed in the discs together with the planet distributions observed by different surveys (Lodato et al., 2019). However, this scenario relies on an efficient migration of the giant planets, requiring a high viscosity gas disc. Other disc observations tend to show that the disc's viscosity is low (e.g., Dullemond et al., 2018), too low to allow such an efficient migration (Ndugu et al., 2019).

On the other hand, giant planet formation can occur in the inner regions of the discs, where the orbital timescales favor planet formation and where a slower migration of the planets can still explain the observed giant distributions (Bitsch et al., 2020; Wang et al., 2021). However, as shown in Chapter 5, such systems would not produce the bright features in the outer part of the discs observed in the different surveys. Therefore, by combining the constraints derived from the observation of protoplanetary discs and the distribution of eccentric giant planets, it is possible to determine the birth location of some giant planets and some characteristics of their parental protoplanetary discs.

Do current facilities have the capacity to help better constrain giant planet formation during the gaseous disc phase ?

In Chapter 5, we concluded that high resolution observations of smaller discs can help us to unveil the initial conditions needed for giant planets to form in the inner or in the outer part of the discs (as discussed in the previous paragraph). We showed in Sect. 5.4.4 that ALMA theoretically has the capacity to reach a high enough resolution to show the most important features in the inner disc.

Can the presence of multiple giant planets significantly influence our interpretation of the substructures observed in dusty protoplanetary discs ?

As expected, the presence of multiple giant planets embedded in the same protoplanetary disc highly influences the gas distribution, especially at low viscosities. Multiple gaps and rings are formed, and the gas radial velocity is highly perturbed, partly due to the overlap of all the spiral density waves produced by the planets. As shown and discussed in Sect. 5.4.2 and 5.5.3, and detailed in appendix B.2, these gas radial velocity perturbations induce traffic jams, producing rings far from the planet locations. The presence of these traffic jams blurs even more the link between the number of planets and the number of rings observed in discs. The study presented in Chapter 5 clearly shows that the relation between observed substructures and eventual planets is even more complicated than previously assumed.

How to fit the Solar system in the broad picture of giant planet formation ?

The Solar system provides a multitude of planet formation constraints (see Sect. 1.2.1). Studying its formation can help us improve our global understanding of planet formation. This statement motivated the study presented in Chapter 5: by deriving synthetic ALMA images of the potential Solar system protoplanetary disc, we bring a new perspective on the analysis of the observed protoplanetary discs. We found that, considering realistic migration efficiency, the presence of bright rings located at large radii in large protoplanetary disc is inconsistent with the observations of giant planets distribution (e.g., like the Solar system). These bright rings are either produced by another mechanism than giant planet formation, or are consistent with a giant planet population that is not yet observed or under-represented in the different surveys.
Moreover, in Chapter 4, we found that in the majority of the observed planetary systems containing two giant planets, the outer planet is more massive than the inner one (see Sect. 4.7.4). However this is not the case of our Solar system. While the detection limits of the instruments observing exoplanetary systems might hide the smaller planets, the observed discrepancies between the Solar system and the majority of the observed planetary systems raise the question of the uniqueness of our system. Including theses differences in planet formation scenarios can bring us interesting insights on the initial formation conditions needed to reproduce the different planetary architectures. These initial conditions can be challenged by the constraints derived from the local analysis of our Solar system, impossible to undertake in exoplanetary systems (e.g., the chemical analysis of meteorites). Therefore, by placing the Solar system in perspective with respect to the observed planetary systems and protoplanetary discs, we improve our understanding of planet formation.

Outlook

Planet formation theories rely on our capacity to implement detailed physical processes in our simulations. With the increasing capacity of new computational centers, our understanding of the planet growth over several order of magnitudes will be improved as it will be increasingly possible to implement different processes that inter-depend on each other. Moreover, future high resolution observations will provide more constraints on the evolution pathways of planets. While many different aspects can be investigated, this section gathers some follow-up projects investigating giant planet formation.

The impact of planetary dynamics

In this thesis, it was mentioned several times (Sect. 3.5.3, 4.7.2 and 5.5.4) that implementing dynamically evolving accreting planets will highly impact our understanding of giant planet formation. I intend to develop this aspect in future projects. Using similar setups and methods as shown in this thesis (i.e., hydrodynamical simulations, dust evolution models and radiative transfer derivations), I intend to start by analysing the impact of the presence of a second planet on the migration behavior of a non accreting planet. The long-term goal is to investigate if the Grand Tack scenario can be reproduced taking planetary gas accretion into account. This study can help us constrain which formation scenario occurred in our own Solar system (see Sect. 1.2.1), and, if possible, determine if such formation pathway can produce characteristic observable features via the production of synthetic images.

Different disc structures

The gas equation of state can influence the disc structure and therefore the evolution of the growing planets. In this thesis, we considered a locally isothermal disc, with a constant aspect ratio in the discs with accreting planets. However, it was shown in previous studies that considering the stellar irradiation has an important impact on the disc structure (e.g., Dullemond et al., 2001; Bitsch et al., 2013). In this case, the disc aspect ratio present a bump in the inner region as the disc temperature switches from being dominated by stellar irradiation to being dominated by viscous heating.

As the gas accretion rate depends on the disc aspect ratio, the planet masses evolution will be impacted differently depending on their location in the disc. Therefore, I intend to investigate, as a first step, the accretion of multiple planets in flared discs and compare the mass ratio evolution of the planets to the mass ratios derived in Chapter 4. Due to computational cost, it will be difficult to implement a more complex thermodynamical description of the discs presented in the different chapters with `FARGO-2D1D`. However, it is possible to investigate the evolution of multiple gas accreting planets in radiative discs (i.e., heated by stellar irradiation in addition to the standard viscous heating) at the expense of the global disc description provided by the large grids of `FARGO-2D1D`. As these more complex descriptions are more computationally expensive, they have to be integrated over shorter timescales compared to the simulations in Chapter 4. However, with recent hydrodynamical codes such as `Fargo-3D`[1] (Benítez-Llambay & Masset, 2016), it is still possible to investigate the evolution of the planet masses and the disc structure during the first few ten thousands years, as in Chapter 3. A comparison between the different disc structure during this time ($\sim 10^4$ yrs) can already give us important insights on the importance of the disc structure on the evolution of the planet mass ratios.

Linking planet formation theories and observations

One of the challenges of planet formation theories is the lack of constraints. These constraints are derived from the different observations of both the birth environment of the planets, the protoplanetary discs, and of the resulting planetary architectures. As shown in Fig. 1.1, the information derived from these observations is therefore crucial to improve planet formation theories.

Many different studies aim at specifically reproducing observations of exoplanetary systems (e.g., Mordasini et al., 2012; Ndugu et al., 2019), or of protoplanetary discs (e.g., Baruteau et al., 2019; Mentiplay et al., 2019; Dullemond et al., 2020). While these studies are the most direct link between theory and observations, it is also primordial to investigate the impact of planet formation processes on observable features (e.g., impact on the shape of the pressure profiles as in Sect. 3.5.2 or on the stellar accretion rate as in Sect. 3.5.1 and 4.4.2); or to include simple comparisons with observations (e.g., comparisons with the observed exoplanetary systems as in Sect. 4.7.4) in theoretical works.

Investigating the observability of theoretical processes with these simple studies, coupled to the more extended studies mentioned earlier, will help us improve our global understanding of planet formation.

---

[1] http://fargo.in2p3.fr/

A Additional material to Chapter 4

This chapter contains additional information about the analysis presented in Chapter 4.

A.1 Surface density maps

In Sect. 4.3.1, we investigate the influence of the disc viscosity on the evolution of the planets growth. At low viscosity ($\alpha = 10^{-4}$ and $h = 0.05$), the Rossby Wave Instability (RWI, Lovelace et al., 1999; Li et al., 2001) is triggered at the edges of the different planet gaps, creating vortices. In Fig. A.1, we show the 2D perturbed surface density maps of the disc hosting two accreting planets in the 3:1 period ratio, at three different times, increasing from left to right. Polar plots of the density maps presented in the top row are shown in the bottom row. The vortices produce asymmetric over-densities that can be used to trace them (in yellow in Fig. A.1).

At the beginning of the simulation (at 500 inner planet orbits, left panel), we see that vortices are produced at three different locations in this configuration: at the outer edge of the outer planet gap, in between the planets and interior to the inner planet gap. Their presence impacts the flow of gas in the vicinity of the planets, creating oscillations in the planetary accretion rates (see Sect. 4.3.1). Quickly, the vortices located in between the planet and in the inner disc vanish (middle panel). The strongest vortex is the one located at the outer edge of the outer planet gap. It takes longer to dissipate and is completely vanished after 10^5 years (right panel). The strength of the vortices depends on the growth timescale of the planets (Hammer et al., 2017): if the planets accrete faster, the vortices would be stronger but would also vanish faster. This was observed in the previous chapter (see Sect. 3.4.2), where single planets with different accretion rates would produce different vortices with different lifetimes.

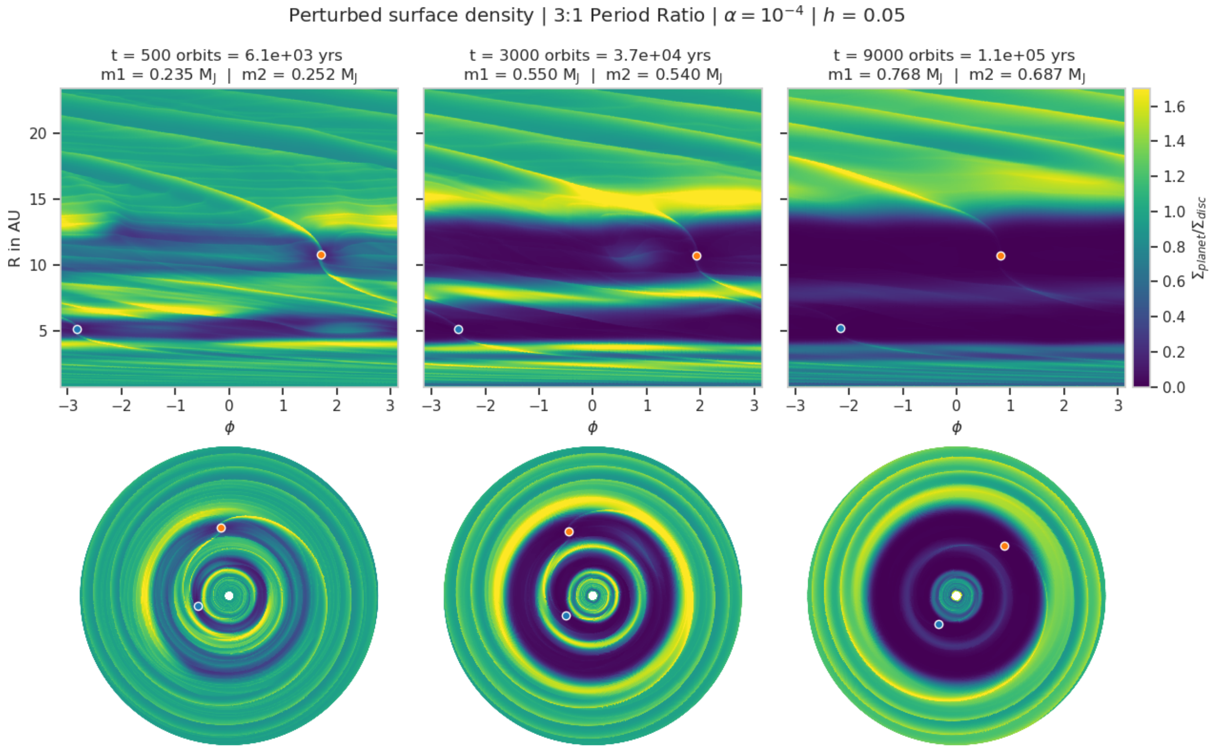

Figure A.1: 2D perturbed surface density maps at three different times: t = 500 (left), 3 000 (middle) and 9 000 (right) inner planet orbits. The over-densities (yellow asymmetries) are representative of vortices.

B Additional material to Chapter 5

This chapter contains additional information about the study presented in Chapter 5. We derived synthetic images of the potential natal protoplanetary disc of our Solar system. Here, we provide more information regarding the hydrodynamical simulations used.

B.1 Gas hydrodynamical profiles

As discussed in Sect. 5.2.2, we present in this section the outputs of the 2D hydrodynamical setups. In Figs. B.1, B.2, and B.4 we show the perturbed surface densities of the 2D grids of the discs, for the different configurations and disc parameters. Each row represents a configuration, and each column represents a different α viscosity, ranging from 10^{-4} to 10^{-2} from left to right. The two first figures represent the two different aspect ratios investigated: an MMSN-like aspect ratio in is shown in Fig. B.1 and a smaller aspect ratio, as described in Sect. 5.2.2, in Fig. B.2). In Fig. B.4 we present the perturbed surface densities for the different masses investigated in the Spread and Three-Giants configurations. In each of the panels of these three figures we see that the gas disc is axisymmetric after t = 12 500 orbits. The vortices triggered by some instabilities or planet growth that could form at low viscosity at the edges of the giant gaps have time to vanish (Hammer et al., 2017; Bergez-Casalou et al., 2020), meaning that we can take the azimuthal average needed as inputs for `TWO-POP-PY`.

In Figs. B.3 and B.5 we present the azimuthal and time average gas profiles used as inputs for the dust evolution model (Sect. 5.3). The profiles are time-averaged over 2 500 orbits. For each configuration and each viscosity, the profiles at each aspect ratio are plotted in the same panel: the MMSN-like aspect ratio is presented in solid line while the smaller aspect ratio is shown in dashed lines. Each planet's orbit is represented by a vertical dotted gray line.

These 2D surface densities show the importance of the viscosity. In the Solar System configurations (Figs. B.1 and B.2), Jupiter and Saturn create a common gap at low viscosity whereas only Jupiter is able to start to form a gap at high viscosity. Depending on the planet configuration, at $\alpha = 10^{-3}$, the two inner giants create different features: when they create a common gap in the Compact configuration, some gas is accumulated in between Jupiter and Saturn in the Spread configuration.

In the Compact configuration, at low viscosity and for both aspect ratios, Uranus and Neptune are massive enough to start creating a pileup of gas outside of Neptune's orbit. It is particularly visible with the small aspect ratio and in the 1D profiles (see Fig.

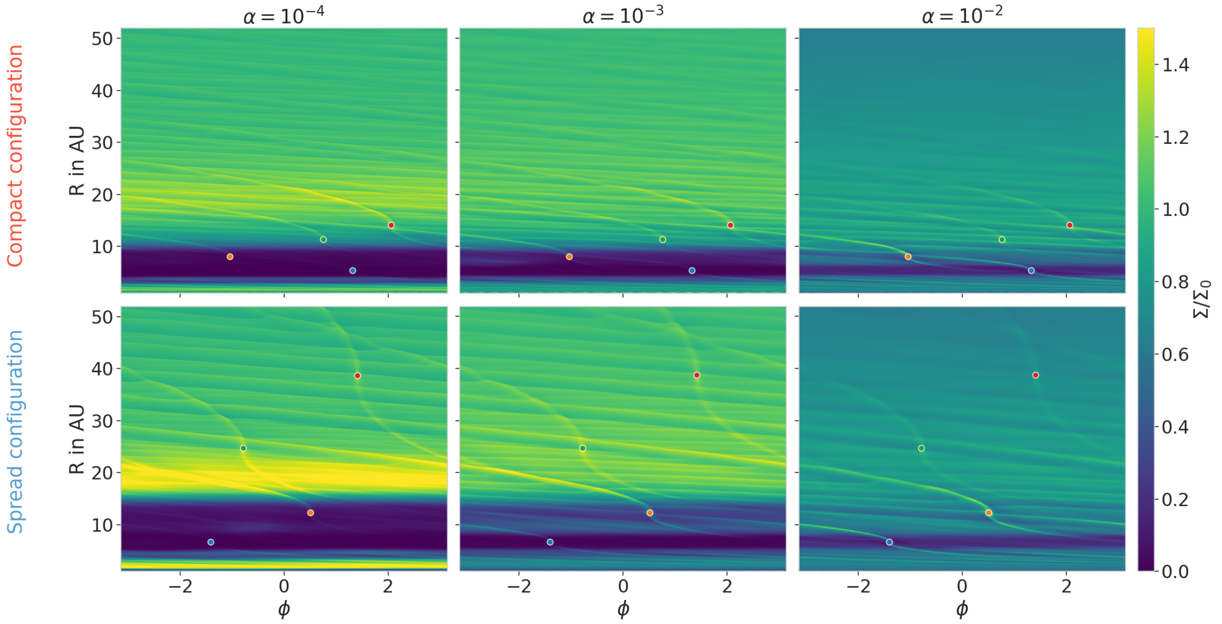

Figure B.1: Perturbed gas surface densities (Σ/Σ_0) for an MMSN-like aspect ratio at t = 12 500 orbits of the inner planet, in the Compact (first row) and Spread (second row) configurations. The positions of the planets are marked by dots in each panel (blue corresponds to Jupiter, orange to Saturn, green to Uranus, and red to Neptune). The discs can be considered axisymmetric, which is important for the dust evolution model that takes the 1D radial gas profile as an input.

B.3). When we compare these two panels to the two corresponding panels for the Spread configuration, we notice that Uranus and Neptune barely have an effect on the gas disc.

Regarding the planets of different mass and the Three-Giants configuration (Figs. B.4 and B.5), we see that the Three-Giants configuration always creates a deep common gap as the planets are close to one another. However, in the Spread configuration the amount of gas present between Jupiter and Saturn clearly create two different gaps when the planets have reduced masses.

We show in Sect. 5.3 that the velocities of the planets can create traffic jams that produce noticeable substructures. This is due to the fact that the gas disc is highly perturbed by multiple giant planets. In Figs. B.6 and B.7 we present the radial azimuthally and time-averaged profiles used in our simulations. We see that even after averaging the profiles for 2 500 orbits, the disc remain highly perturbed by the planets. In Fig. B.7 we clearly show that these perturbations are due to the planets as we see that they are stronger for more massive planets.

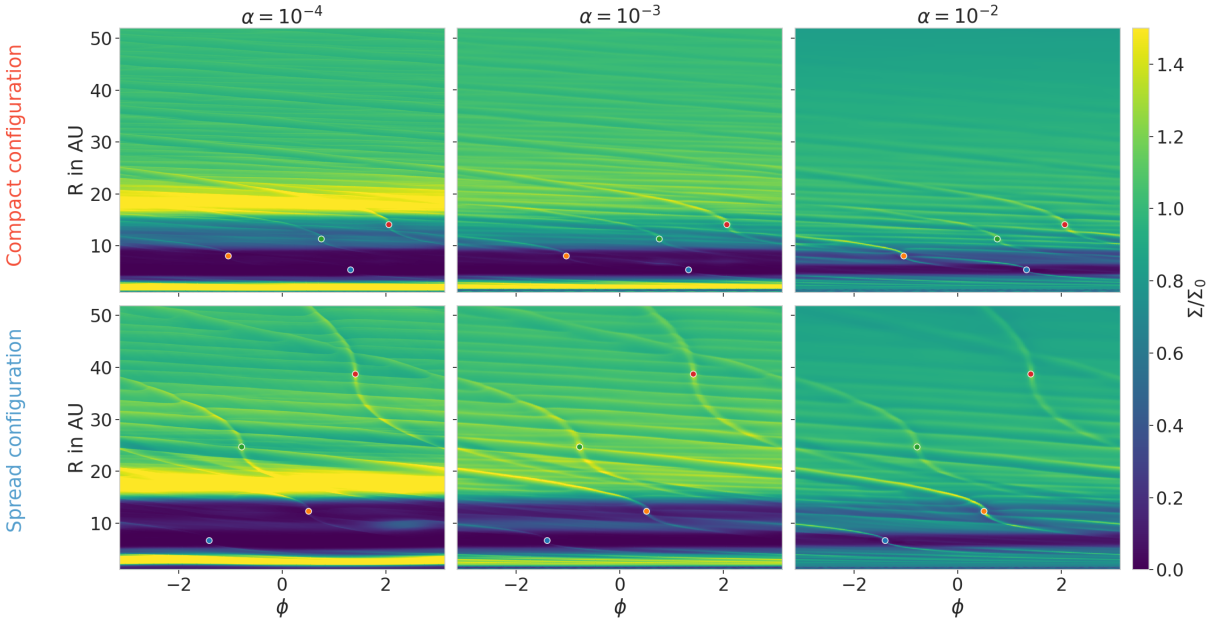

Figure B.2: Same as B.2 but for a smaller aspect ratio.

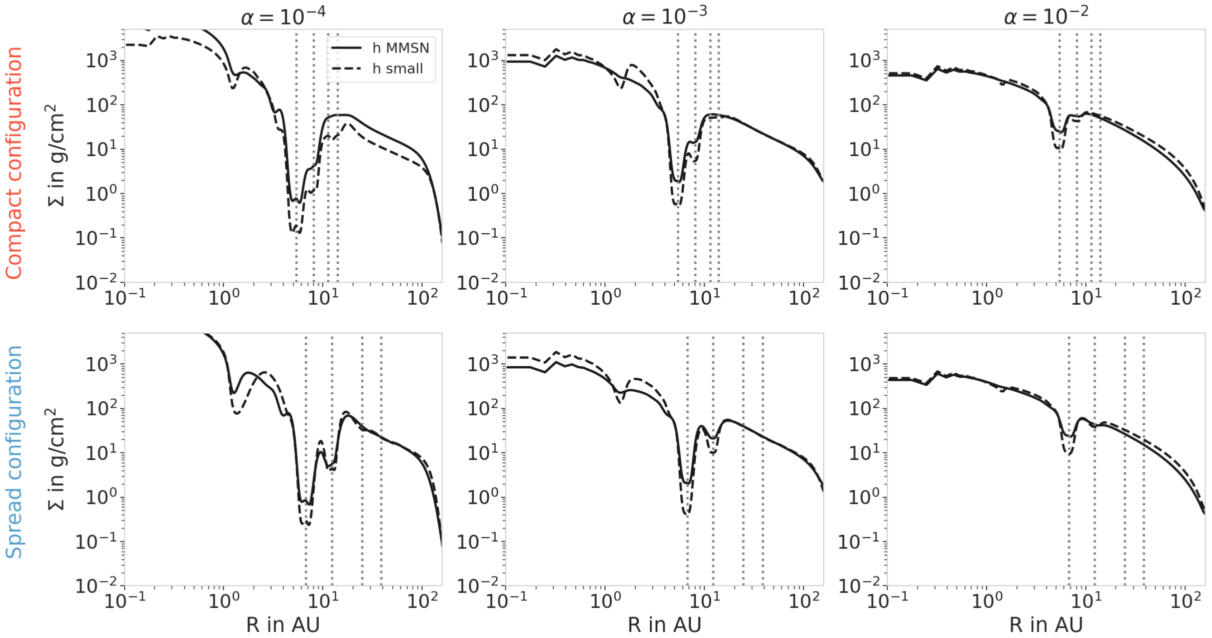

Figure B.3: Time- and azimuthal-averaged gas surface density profiles for each aspect ratio. Vertical dotted lines represent the positions of each planet. Jupiter and Saturn are the only ones creating substructures in the discs, except in the Compact configuration with a low α and small aspect ratio, where Uranus and Neptune create a small gap and an over-density outside of Neptune's gap.

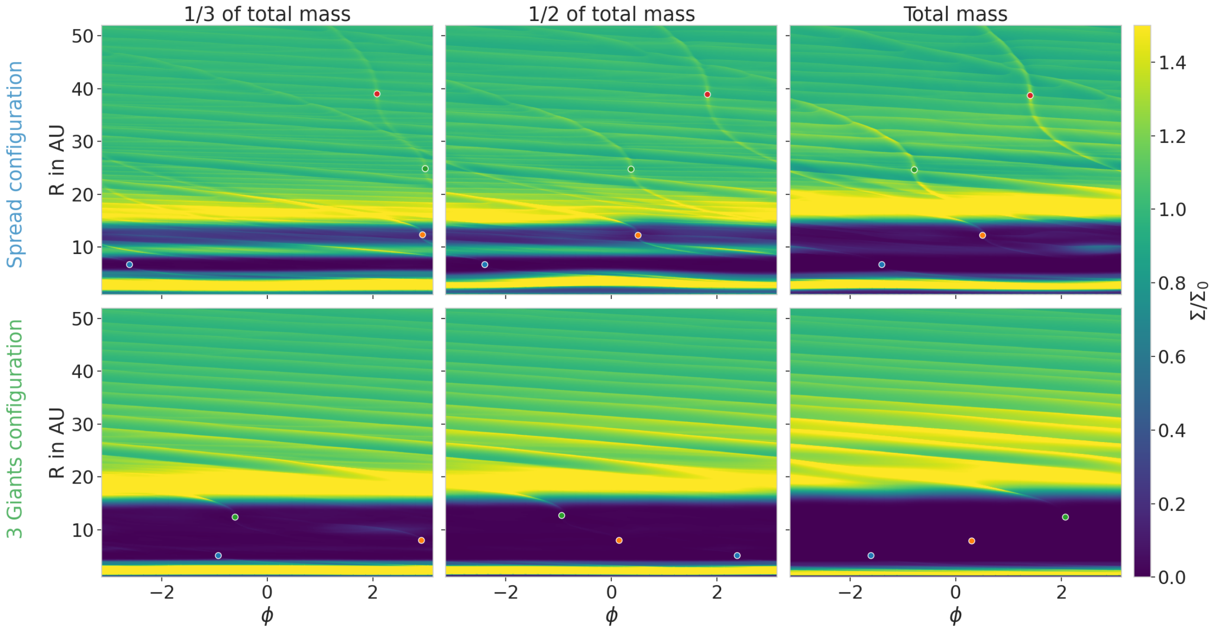

Figure B.4: Perturbed gas surface densities (Σ/Σ_0) at t = 12 500 orbits of the inner planet, in the Spread (first row) and Three Giants (second row) configurations. The discs have a small aspect ratio and low viscosity ($\alpha = 10^{-4}$). The masses of the planets are reduced by a factor of two-thirds (left panels) and one-half (middle panels). They can be compared to the total mass configuration in the right panels. As in Fig. B.1, the positions of the planets are marked by dots in each panel and the discs can be considered axisymmetric.

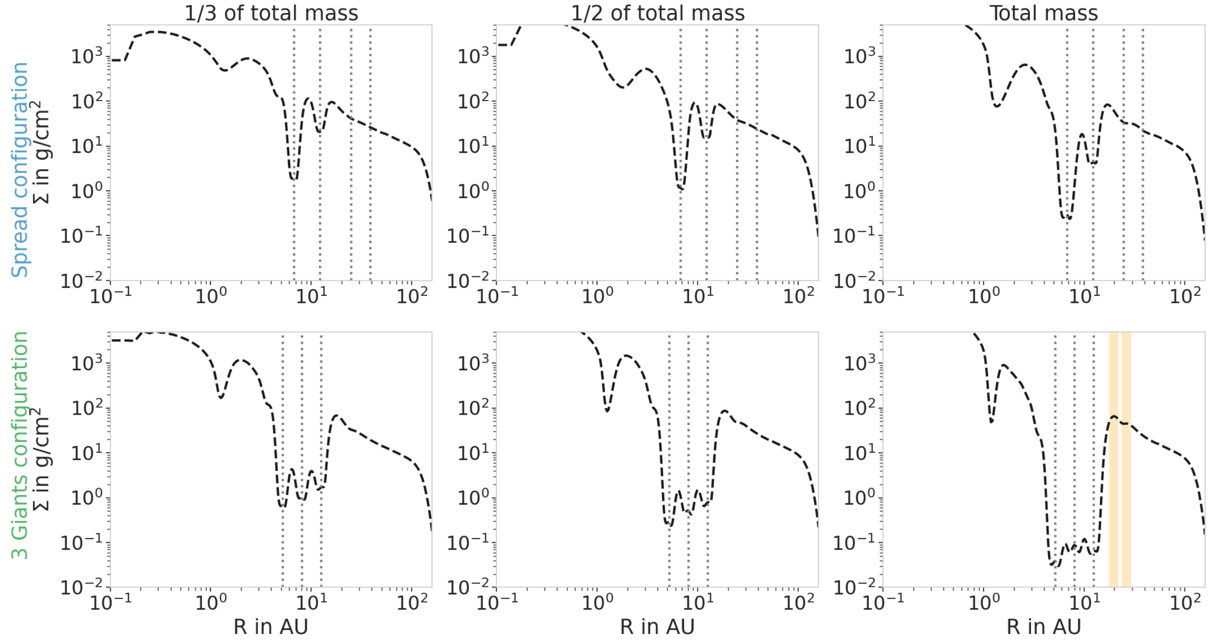

Figure B.5: Time- and azimuthal-averaged gas surface density profiles for the different configurations. Vertical dotted lines represent the positions of each planet. As expected, more massive planets create deeper gaps. In the Three-Giants case, the giants are close enough to one another to always create a common gap. The masses of the planets then dictate how deep the gap is and how much gas is present in the gap between them. The two orange vertical lines show the positions of the rings seen in the synthetic millimeter images (Fig. 5.6). We see that they do not correspond to strong features in the gas disc and are located far from the giants' orbits.

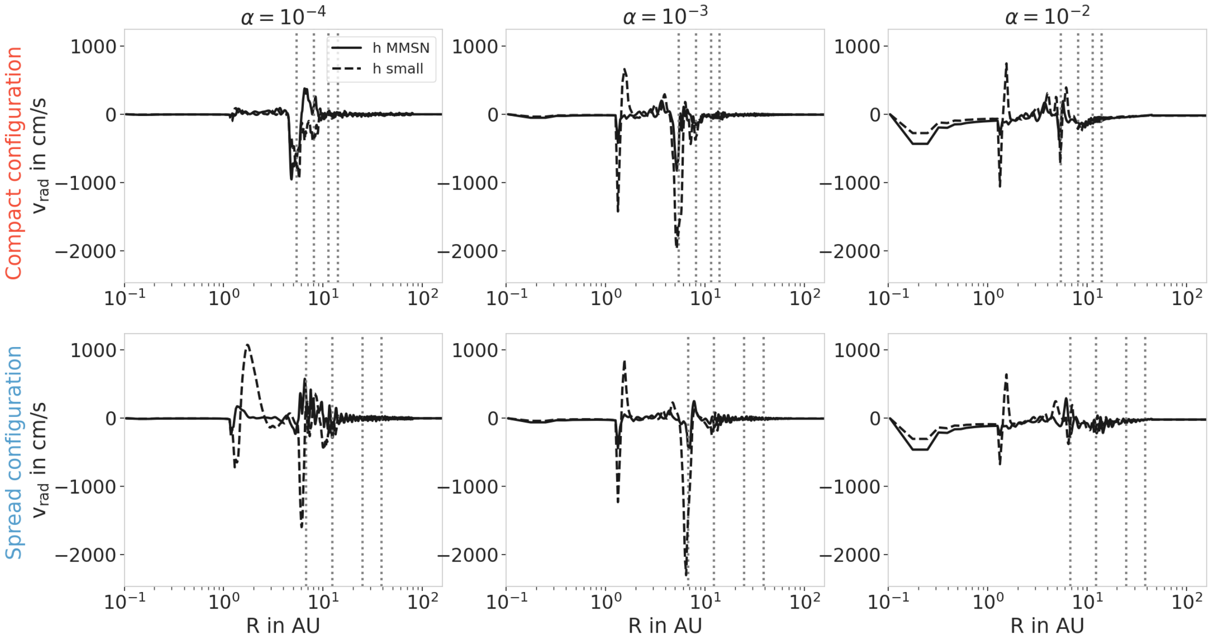

Figure B.6: Time- and azimuthal-averaged gas radial velocity profiles for the different configurations. Vertical dotted lines represent the positions of each planet. Multiple planets highly perturb the gas velocities, having an important impact on the dust distributions (see Sect. 5.3).

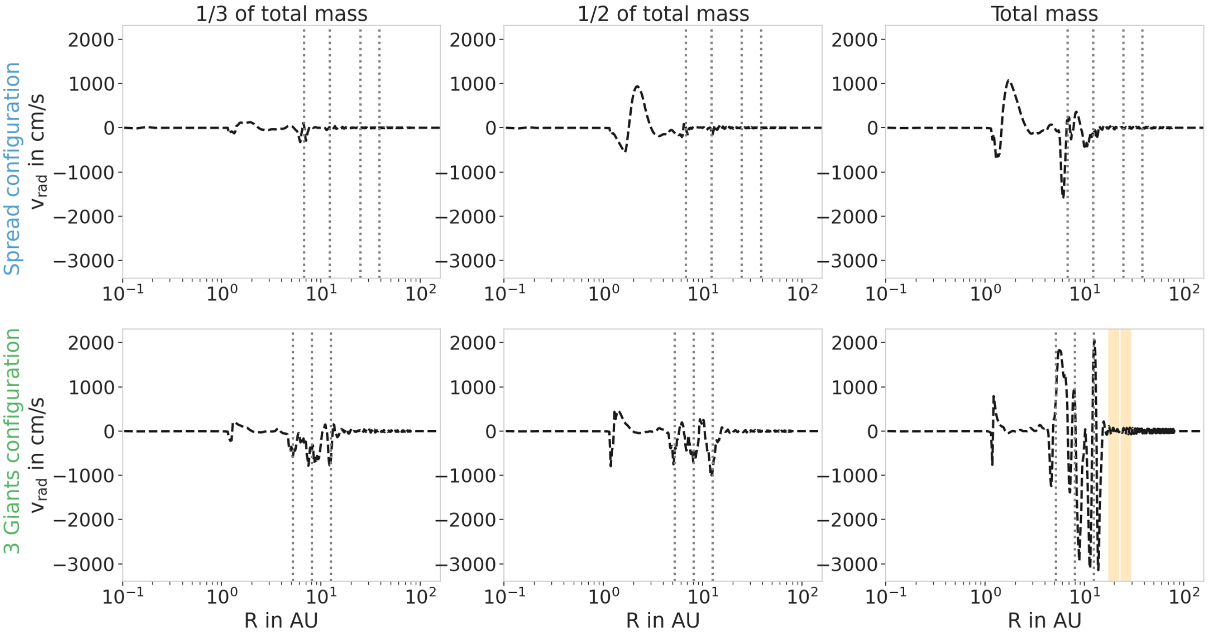

Figure B.7: Same as Fig. B.6 but for the Spread and Three-Giants configurations and different planet masses. The two orange vertical lines show the positions of the rings observed in Fig. 5.6.

B.2 Impact of the radial gas velocity on the dust distributions

In Sect. 5.3 some over-densities are observed at positions that are not directly related to the orbits of the planets or to any perturbations in the gas surface density. These over-densities originate in the radial velocity profile of the gas disc, highly perturbed by the presence of multiple giant planets. These perturbations create traffic jams, where the dust can accumulate without being trapped. In order to determine if these traffic jams are indeed producing such over-densities, we study the dust evolution distribution also with a gas radial velocity forced to be zero.

We take the example of the Three-Giants configuration as it produces the most perturbed disc. We present in Fig. B.8 the dust distributions in the case where the same gas surface density profile is given to the model but the radial velocity profiles are either averaged as in this paper (left panels) or set to zero (right panels). In the first row, we show the integrated dust surface density over all the grain sizes: these profiles allow us to see that the dust is distributed differently in both cases. When the radial gas profile is set to zero, the dust mostly accumulate in the pressure bumps present in the disc. Even if the gas surface density profile present a very slight bump located at 26 AU, creating a small over-density in the dust at this location, it is too small to create a noticeable feature in the observations. However, when the gas radial profile is taken into account, the dust gets stuck in these different traffic jams, explaining this spiky behavior. When compared to the positions of the rings observed specially in Fig. 5.10, represented in orange in this figure, we see that the second ring located at 26 AU is clearly originating in the strong traffic jam located at the same semi-major axis.

As these traffic jams can create noticeable substructures, we conclude that the gas radial velocity profile has a non-negligible impact on the dust distributions when multiple planets are present in the disc. This is important for the derivation of synthetic images but also for dust evolution models.

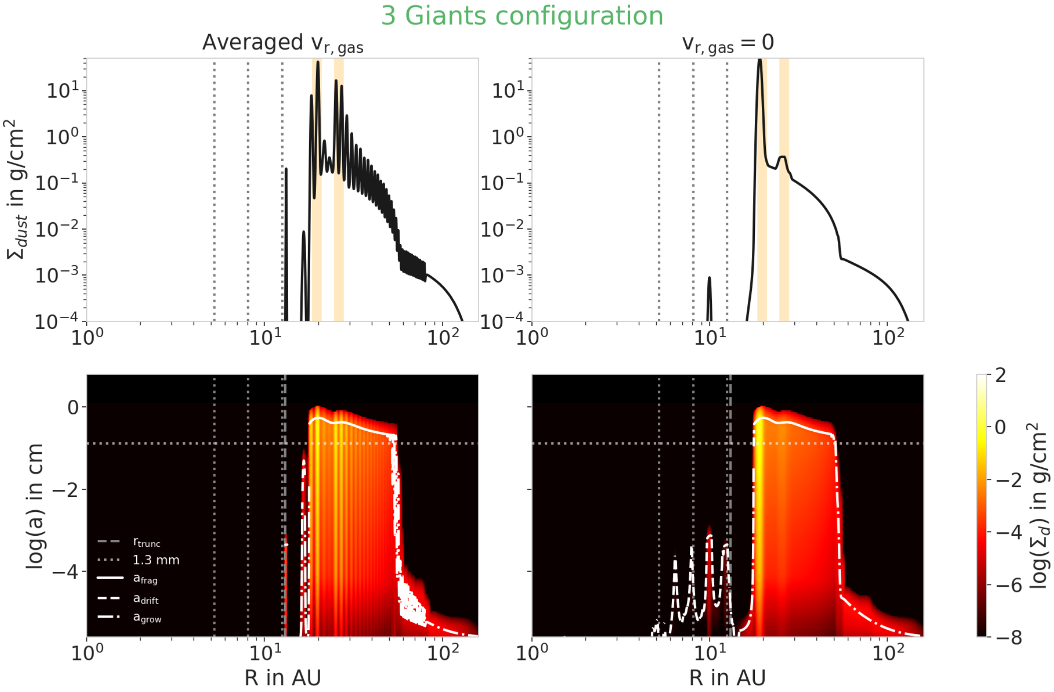

Figure B.8: Dust distributions in the Three-Giants configuration case: in the left panels, the velocity of the gas used as an input for the dust evolution model is the averaged velocity as presented in Fig. B.7; in the right panels, the gas velocity is taken to be null. The first row presents the integrated dust distribution along all the dust sizes, representing the total dust distribution in the disc, whereas the second row presents the classic dust distributions as in Sect. 5.3. The presence of spikes in the left panel shows that the radial gas velocities are indeed responsible for the dust accumulations in additional rings exterior to the positions of the planets.

B.3 Complementary images

B.3.1 Solar System images

We show in this section the images of the Solar System images corresponding to the normalized intensity profiles presented in Sect. 5.4.

B.3.2 Images of inclined discs

Here, we present the images of the discs with different inclinations in the Spread and Three-Giants configurations. These images correspond to the radial profiles presented in Fig. 5.8.

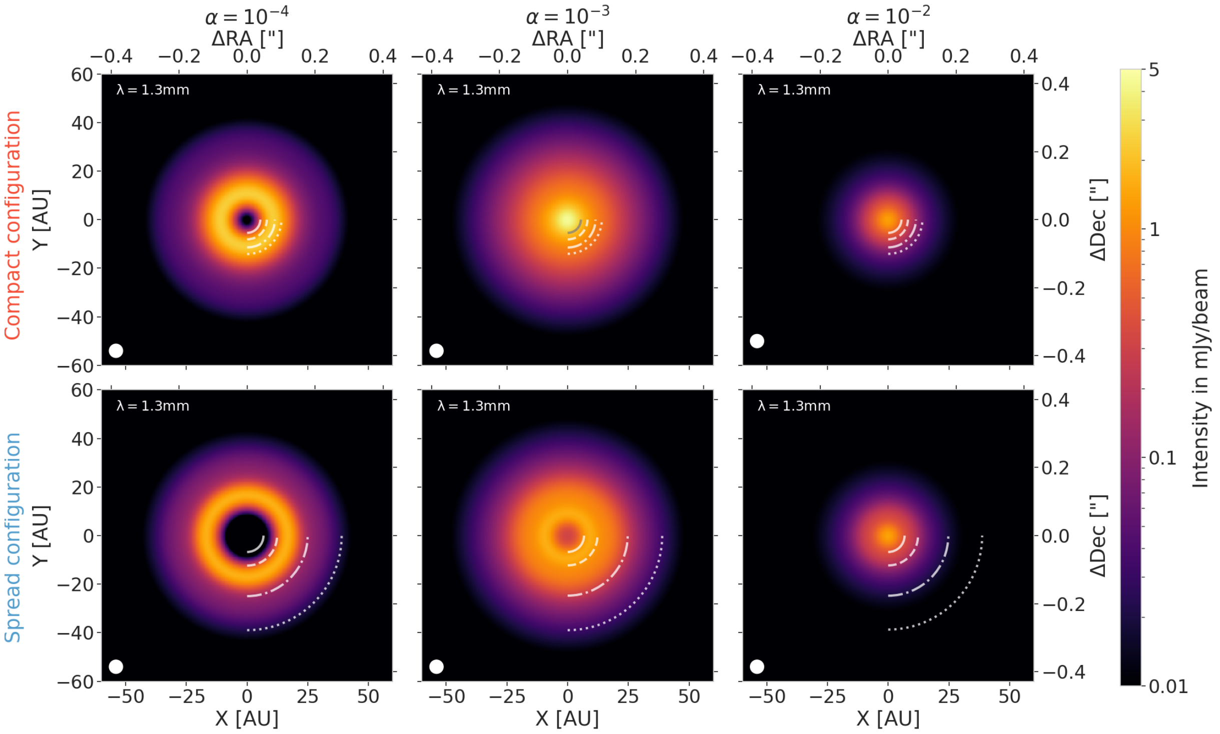

Figure B.9: Images at $\lambda = 1.3$ mm for each Solar System configuration for an MMSN-like aspect ratio. These are the images that correspond to the intensity profiles presented in Fig. 5.5. The beam is 0.04"×0.04" and is represented as the white circle in the lower-left corner of each panel. The white lines represent the distances of the different planets.

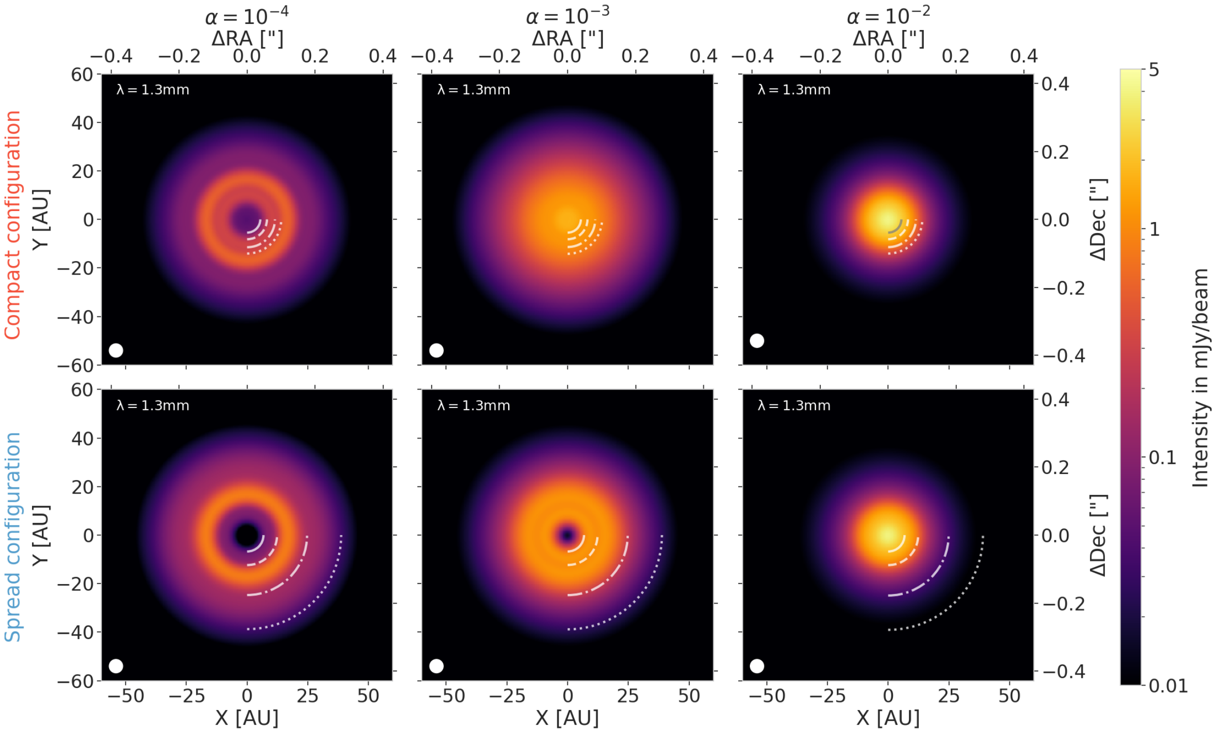

Figure B.10: Same as Fig. B.9 but for a smaller aspect ratio.

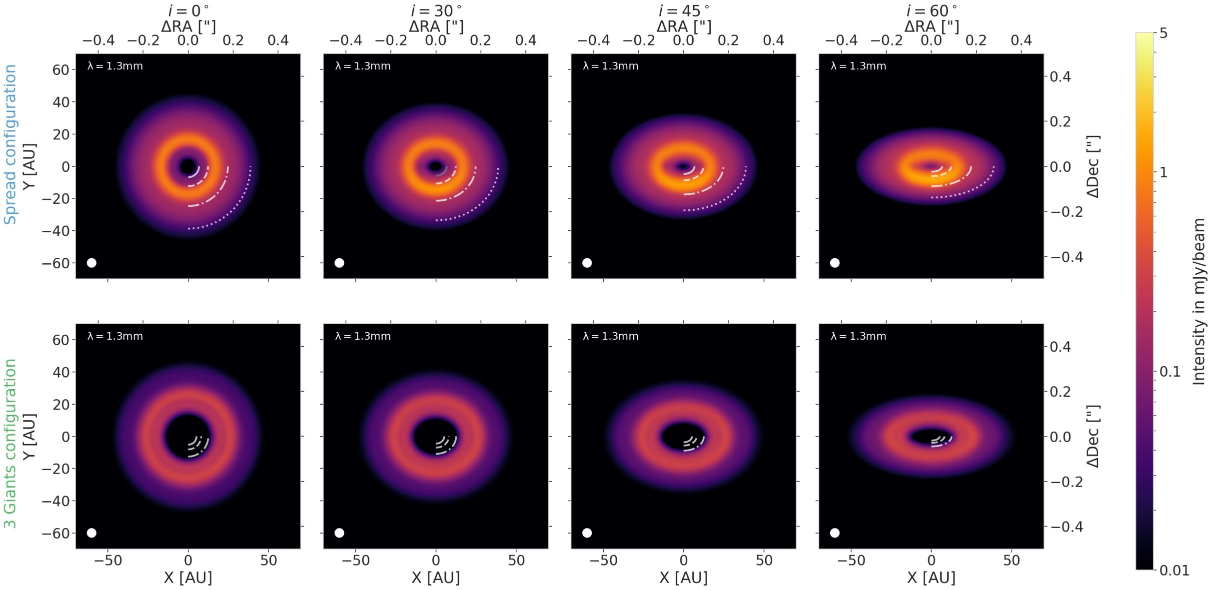

Figure B.11: Images at λ =1.3mm in the Spread (first row) and Three-Giants (second row) configuration, at low viscosity and low aspect ratio, for different inclinations. The inclination is increasing from left to right, going from a face-on disc ($i = 0°$) to a highly inclined disc ($i = 60°$). The white lines represent the positions of the different planets in each configuration.

List of Figures

1.1 Schematic of the connections between the different components and processes studied in this thesis. 2
1.2 Schematic of the geometries of an evolving star-disc system. 3
1.4 Inward radial velocity of a grain compared to the radial velocity of the gas for different stokes number (Brauer et al., 2008). 7
1.5 Radial dependence of the fragmentation, drift and growth limits 9
1.6 DSHARP and SPHERE images of protoplanetary discs at high resolution. . . . 13
1.7 Core accretion mass evolution Pollack et al. (1996) 15
1.8 Sketch of the horseshoe region 17
1.9 Possible Solar system formation scenarios 23
1.10 Known exoplanetary systems with multiple planets around Sun-like stars . . . 26

2.1 Sketch of the FARGO-2D1D grids 29

3.1 Grid setting single planet 37
3.2 Influence of gas accretion on the gap shape for a planet of m = 0.5 M_J and m = 1.5 M_J for $h = 0.05$ and $\alpha = 10^{-2}$ 39
3.3 Influence of different accretion rates 42
3.4 Pressure gradient in different gas accretion models for m = 0.5 M_J 43
3.5 Influence of planetary gas accretion on the stellar gas accretion for our fiducial disc parameters ($h = 0.05,\ \alpha = 10^{-2}$) 44
3.6 Influence of different planetary gas accretion rates on the stellar gas accretion for the fiducial disc parameters ($h = 0.05,\ \alpha = 10^{-2}$) 45
3.7 Influence of different aspect ratios with $\alpha = 10^{-2}$ and $m_{\mathrm{init}} = 20\ M_\oplus$ 47
3.8 Influence of different viscosities for $h = 0.05$ 49
3.9 Perturbed surface density at different times and different accretion rates, in discs with $\alpha = 10^{-4}$, $h = 0.05$ 50
3.10 Influence of different accretion rates on stellar gas accretion for $\alpha = 10^{-4}$ and $h = 0.05$ 51
3.11 Gap-opening mass as a function of the viscosity for different criteria and our simulations 53
3.12 Time needed for gap opening as a function of the planetary mass at two different viscosities 54
3.13 Migration maps for low-mass planets orbiting near our accreting planets . . . 56
3.14 Migration maps for low-mass planets orbiting near our accreting planets at low aspect ratio 56
3.15 Migration maps for $\alpha = 10^{-4}$ and $h = 0.05$ for low-mass planets orbiting near our accreting planets 57

3.16 Influence of gas accretion on the disc structure at the gap-opening mass for $\alpha = 10^{-4}$ and $h = 0.05$ 59

4.1 Grid setting two accreting planets 66
4.2 Planetary accretion rates and masses as a function of time for different α-viscosities for the planets in a 3:1 period ratio 68
4.3 Planetary accretion rates and masses as a function of time for different aspect ratios for the planets in a 3:1 period ratio 69
4.4 Mass ratio and perturbed density profiles as a function of time for different α-viscosities with the planets in the 3:1 period ratio. 70
4.5 Mass ratio and perturbed density profiles as a function of time for different aspect ratios with the planets in the 3:1 period ratio. 71
4.6 Comparison between single accreting planets and two simultaneously accreting planets. 73
4.7 Comparison of the mass ratios in the single planet and two accreting planets cases as a function of time and for different viscosities. 75
4.8 Influence of a second accreting planet on the stellar accretion rate at the inner edge of the disc (0.2 AU). 77
4.9 Mass ratio as a function of time for different α-viscosities and different period ratios. 79
4.10 Gap-opening mass as a function of the viscosity for different criteria and our simulations. 81
4.11 Mass ratio as a function of time for different delays of accretion on the inner or the outer planet. 83
4.12 Mass ratio evolution of the two accreting planets as a function of their period ratio compared to exoplanetary systems. 88

5.1 Hydro grid setting Solar System images 95
5.2 Dust densities distributions for the MMSN-like aspect ratio 100
5.3 Dust densities distributions for the small aspect ratio 101
5.4 Dust densities distributions with the planet masses reduced in the Spread configuration and in the Three-Giants configuration 103
5.5 Radial profile of convolved and unconvolved images at $\lambda = 1.3$ mm for both aspect ratios in the Compact and Spread configurations. 105
5.6 Radial profile of convolved and unconvolved images at $\lambda = 1.3$ mm with the planet masses reduced in the Spread configuration and in the Three-Giants configuration. 107
5.7 Images in total intensity at $\lambda = 1.3$ mm with the planet masses reduced in the Spread configuration and in the Three-Giants configuration. 108
5.8 Radial profile of convolved and unconvolved images at $\lambda = 1.3mm$ with different inclinations in the Spread and in the Three-Giants configuration 109
5.9 Radial profile of convolved and unconvolved images at $\lambda = 1.3$ mm with different beam sizes in the Spread and in the Three-Giants configurations. 110
5.10 Images in total intensity at $\lambda = 1.3$ mm in the Spread and in the Three-Giants configurations. 111
5.11 Images at λ =1.3mm of the different configurations, at low viscosity and low aspect ratio, at different times 114
5.12 Radial intensity profiles after 0.5 Myr, 1 Myr, 2Myrs, and 3 Myrs of evolution in each configuration with low viscosity and a low aspect ratio. 115

5.13 Masses of the dust discs for each configuration and each disc parameter derived from the dust evolution model 117
5.14 Observed dust masses for each configuration and each disc parameter. 119

A.1 2D perturbed surface density maps at three different times to trace the evolution of vortices 130

B.1 Perturbed gas surface densities for an MMSN-like aspect ratio at t = 12 500 orbits of the inner planet, in the Compact and Spread configurations. 132
B.2 Perturbed gas surface densities for a small aspect ratio at t = 12 500 orbits of the inner planet, in the Compact and Spread configurations. 133
B.3 Time- and azimuthal-averaged gas surface density profiles for each aspect ratio. 133
B.4 Perturbed gas surface densities at t = 12 500 orbits of the inner planet, in the Spread and Three Giants configurations. 134
B.5 Time- and azimuthal-averaged gas surface density profiles for the Spread and Three Giants configurations. 134
B.6 Time- and azimuthal-averaged gas radial velocity profiles for the Spread and Compact configurations 135
B.7 Time- and azimuthal-averaged gas radial velocity profiles for the Spread and Three Giants configurations 135
B.8 Dust distribution in the Three-Giants configuration case with our averaged gas velocity compared to a null gas velocity. 137
B.9 Images at $\lambda = 1.3$ mm for each Solar System configuration for an MMSN-like aspect ratio 138
B.10 Same as Fig. B.9 but for a smaller aspect ratio. 138
B.11 Images at λ =1.3mm in the Spread and Three-Giants configurations, at low viscosity and low aspect ratio, for different inclinations 139

List of Tables

1.1 Different gas accretion rates from the literature 16

2.1 Global gas disc parameters 31
2.2 Global dust evolution parameters 33
2.3 Global radiative transfer parameters 34

3.1 Single accreting planet: Gas disc parameters 38
3.2 Depth of the initial gap and time needed to reach the equilibrium as a function of the disc parameters 48

4.1 Semi-major axis of the different planet configurations considered in this Chapter. 65
4.2 Gas disc parameters two accreting planets 66

5.1 Semi-major axis and masses of the three different configurations considered here (Compact, Spread, and Three Giants). 94
5.2 Solar System images: Gas disc parameters 96
5.3 Solar System dust evolution parameters 98
5.4 Solar System images radiative transfer parameters 99
5.5 Dust masses calculated from the total integrated flux as in eq. 5.4. 120

Publication list

The following published papers are part of this thesis:

- **Bergez-Casalou, C.**, Bitsch, B., Pierens, A., Crida, A., Raymond, S. N., 2020

  Influence of planetary gas accretion on the shape and depth of gaps in protoplanetary discs, A&A, 643, A133

- **Bergez-Casalou, C.**, Bitsch, B., Kurtovic, N. T., Pinilla, P., 2022

  Constraining giant planet formation with synthetic ALMA images of the Solar system's natal protoplanetary disc, A&A, 659, A6

This thesis also includes a paper in preparation:

- **Bergez-Casalou, C.**, Bitsch, B., Raymond, S. N., *in prep*

  Influence of simultaneous gas accretion of multiple giant planets on their protoplanetary disc and on their own growth [Title subject to change]

I am also the co-author of the following paper, which is not included in this thesis:

- Asensio-Torres, R., Henning, Th., Cantalloube, F., Pinilla, P., Mesa, D., Garufi, A., Jorquera, S., Gratton, R., Chauvin, G., Szulágyi, J., van Boekel, R., Dong, R., Marleau, G. -D., Benisty, M., Villenave, M., **Bergez-Casalou, C.**, Desgrange, C., Janson, M., Keppler, M., Langlois, M., Ménard, F., Rickman, E., Stolker, T., Feldt, M., Fusco, T., Gluck, L., Pavlov, A., Ramos, J., 2021

  Perturbers: SPHERE detection limits to planetary-mass companions in protoplanetary disks, A&A, 652, A101

Bibliography

Alibert, Y. 2017, A&A, 606, A69

ALMA Partnership, Brogan, C. L., Pérez, L. M., et al. 2015, ApJ, 808, L3

Andrews, S. M., Huang, J., Pérez, L. M., et al. 2018, ApJ, 869, L41

Andrews, S. M., Rosenfeld, K. A., Kraus, A. L., & Wilner, D. J. 2013, ApJ, 771, 129

Andrews, S. M. & Williams, J. P. 2005, ApJ, 631, 1134

Ansdell, M., Williams, J. P., van der Marel, N., et al. 2016, ApJ, 828, 46

Armitage, P. J. 2010, Astrophysics of Planet Formation

Asensio-Torres, R., Henning, T., Cantalloube, F., et al. 2021, arXiv e-prints, arXiv:2103.05377

Ataiee, S., Baruteau, C., Alibert, Y., & Benz, W. 2018, A&A, 615, A110

Avenhaus, H., Quanz, S. P., Garufi, A., et al. 2018, ApJ, 863, 44

Ayliffe, B. A. & Bate, M. R. 2009, MNRAS, 393, 49

Bae, J. & Zhu, Z. 2018, ApJ, 859, 118

Baillié, K., Marques, J., & Piau, L. 2019, A&A, 624, A93

Baruteau, C., Barraza, M., Pérez, S., et al. 2019, MNRAS, 486, 304

Baruteau, C., Crida, A., Paardekooper, S. J., et al. 2014, in Protostars and Planets VI, ed. H. Beuther, R. S. Klessen, C. P. Dullemond, & T. Henning, 667

Baruteau, C. & Papaloizou, J. C. B. 2013, ApJ, 778, 7

Baruteau, C., Wafflard-Fernandez, G., Le Gal, R., et al. 2021, MNRAS, 505, 359

Beckwith, S. V. W., Sargent, A. I., Chini, R. S., & Guesten, R. 1990, AJ, 99, 924

Bell, K. R. & Lin, D. N. C. 1994, ApJ, 427, 987

Benisty, M., Bae, J., Facchini, S., et al. 2021, ApJ, 916, L2

Benítez-Llambay, P. & Masset, F. S. 2016, ApJS, 223, 11

Bergez-Casalou, C., Bitsch, B., Kurtovic, N. T., & Pinilla, P. 2022, A&A, 659, A6

Bergez-Casalou, C., Bitsch, B., Pierens, A., Crida, A., & Raymond, S. N. 2020, A&A, 643, A133

Bhandare, A. E. 2020, PhD thesis, Heidelberg University, Germany

Birnstiel, T., Andrews, S. M., Pinilla, P., & Kama, M. 2015, ApJ, 813, L14

Birnstiel, T., Dullemond, C. P., & Brauer, F. 2010, A&A, 513, A79

Birnstiel, T., Dullemond, C. P., Zhu, Z., et al. 2018, ApJ, 869, L45

Birnstiel, T., Klahr, H., & Ercolano, B. 2012, A&A, 539, A148

Bitsch, B., Crida, A., Morbidelli, A., Kley, W., & Dobbs-Dixon, I. 2013, A&A, 549, A124

Bitsch, B., Izidoro, A., Johansen, A., et al. 2019, A&A, 623, A88

Bitsch, B. & Kley, W. 2011, A&A, 536, A77

Bitsch, B., Lambrechts, M., & Johansen, A. 2015, A&A, 582, A112

Bitsch, B., Morbidelli, A., Johansen, A., et al. 2018, A&A, 612, A30

Bitsch, B. & Savvidou, S. 2021, A&A, 647, A96

Bitsch, B., Trifonov, T., & Izidoro, A. 2020, A&A, 643, A66

Bonnor, W. B. 1956, MNRAS, 116, 351
Brasser, R., Matsumura, S., Ida, S., Mojzsis, S. J., & Werner, S. C. 2016, ApJ, 821, 75
Brauer, F., Dullemond, C. P., & Henning, T. 2008, A&A, 480, 859
Brouwers, M. G. & Ormel, C. W. 2020, A&A, 634, A15
Budde, G., Burkhardt, C., & Kleine, T. 2019, Nature Astronomy, 3, 736
Calvet, N. & Gullbring, E. 1998, ApJ, 509, 802
Carrera, D., Gorti, U., Johansen, A., & Davies, M. B. 2017, ApJ, 839, 16
Carrera, D., Johansen, A., & Davies, M. B. 2015, A&A, 579, A43
Casassus, S., Marino, S., Lyra, W., et al. 2019, MNRAS, 483, 3278
Chambers, J. E., Wetherill, G. W., & Boss, A. P. 1996, Icarus, 119, 261
Chametla, R. O., D'Angelo, G., Reyes-Ruiz, M., & Sánchez-Salcedo, F. J. 2020, MNRAS, 243
Cieza, L. A., Ruíz-Rodríguez, D., Hales, A., et al. 2019, MNRAS, 482, 698
Clement, M. S., Kaib, N. A., Raymond, S. N., & Walsh, K. J. 2018, Icarus, 311, 340
Connelly, J. N., Bizzarro, M., Krot, A. N., et al. 2012, Science, 338, 651
Crida, A. & Bitsch, B. 2017, Icarus, 285, 145
Crida, A., Masset, F., & Morbidelli, A. 2009, ApJ, 705, L148
Crida, A., Morbidelli, A., & Masset, F. 2006, Icarus, 181, 587
Crida, A., Morbidelli, A., & Masset, F. 2007, A&A, 461, 1173
Cridland, A. J., Rosotti, G. P., Tabone, B., et al. 2021, arXiv e-prints, arXiv:2112.06734
D'Angelo, G. & Bodenheimer, P. 2013, ApJ, 778, 77
D'Angelo, G., Kley, W., & Henning, T. 2003, The Astrophysical Journal, 586, 540
de Juan Ovelar, M., Pinilla, P., Min, M., Dominik, C., & Birnstiel, T. 2016, MNRAS, 459, L85
Delage, T. N., Okuzumi, S., Flock, M., Pinilla, P., & Dzyurkevich, N. 2022, A&A, 658, A97
DeMeo, F. E. & Carry, B. 2014, Nature, 505, 629
Deng, H., Mayer, L., & Helled, R. 2021, Nature Astronomy, 5, 440
Disk Dynamics Collaboration, Armitage, P. J., Bae, J., et al. 2020, arXiv e-prints, arXiv:2009.04345
Dittrich, K., Klahr, H., & Johansen, A. 2013, ApJ, 763, 117
Dominik, C., Min, M., & Tazaki, R. 2021, Astrophysics Source Code Library, ascl:2104.010
Dong, R., Li, S., Chiang, E., & Li, H. 2018, ApJ, 866, 110
Draine, B. T. 2003, ARA&A, 41, 241
Drążkowska, J., Alibert, Y., & Moore, B. 2016, A&A, 594, A105
Drążkowska, J., Li, S., Birnstiel, T., Stammler, S. M., & Li, H. 2019, ApJ, 885, 91
Dullemond, C. P., Birnstiel, T., Huang, J., et al. 2018, ApJ, 869, L46
Dullemond, C. P. & Dominik, C. 2004, A&A, 421, 1075
Dullemond, C. P., Dominik, C., & Natta, A. 2001, ApJ, 560, 957
Dullemond, C. P., Isella, A., Andrews, S. M., Skobleva, I., & Dzyurkevich, N. 2020, A&A, 633, A137
Dullemond, C. P., Juhasz, A., Pohl, A., et al. 2012, RADMC-3D: A multi-purpose radiative transfer tool
Dullemond, C. P. & Penzlin, A. B. T. 2018, A&A, 609, A50
Dürmann, C. & Kley, W. 2015, A&A, 574, A52
Dürmann, C. & Kley, W. 2017, A&A, 598, A80
Dybczyński, P. A. 2006, A&A, 449, 1233
Ebert, R. 1955, ZAp, 37, 217

Ercolano, B. & Pascucci, I. 2017, Royal Society Open Science, 4, 170114

Espaillat, C., Muzerolle, J., Najita, J., et al. 2014, in Protostars and Planets VI, ed. H. Beuther, R. S. Klessen, C. P. Dullemond, & T. Henning, 497

Fabrycky, D. C., Lissauer, J. J., Ragozzine, D., et al. 2014, ApJ, 790, 146

Facchini, S., Benisty, M., Bae, J., et al. 2020, A&A, 639, A121

Fang, J. & Margot, J.-L. 2012, ApJ, 761, 92

Flaherty, K. M., Hughes, A. M., Teague, R., et al. 2018, ApJ, 856, 117

Flock, M., Dzyurkevich, N., Klahr, H., Turner, N. J., & Henning, T. 2011, ApJ, 735, 122

Flock, M., Ruge, J. P., Dzyurkevich, N., et al. 2015, A&A, 574, A68

Flores-Rivera, L., Flock, M., & Nakatani, R. 2020, A&A, 644, A50

Fu, W., Li, H., Lubow, S., & Li, S. 2014, ApJ, 788, L41

Fulton, B. J., Rosenthal, L. J., Hirsch, L. A., et al. 2021, ApJS, 255, 14

Fung, J., Shi, J.-M., & Chiang, E. 2014, ApJ, 782, 88

Gaia Collaboration, Brown, A. G. A., Vallenari, A., et al. 2018, A&A, 616, A1

Goldreich, P. & Tremaine, S. 1979, ApJ, 233, 857

Gomes, R., Levison, H. F., Tsiganis, K., & Morbidelli, A. 2005, Nature, 435, 466

Gonzalez, J. F., Laibe, G., & Maddison, S. T. 2017, MNRAS, 467, 1984

Güttler, C., Blum, J., Zsom, A., Ormel, C. W., & Dullemond, C. P. 2010, A&A, 513, A56

Gyeol Yun, H., Kim, W.-T., Bae, J., & Han, C. 2019, ApJ, 884, 142

Haffert, S. Y., Bohn, A. J., de Boer, J., et al. 2019, Nature Astronomy, 3, 749

Hammer, M., Kratter, K. M., & Lin, M.-K. 2017, MNRAS, 466, 3533

Hammer, M., Lin, M.-K., Kratter, K. M., & Pinilla, P. 2021, MNRAS, 504, 3963

Hansen, B. M. S. 2009, ApJ, 703, 1131

Hartmann, L., Hewett, R., & Calvet, N. 1994, ApJ, 426, 669

Haugbølle, T., Weber, P., Wielandt, D. P., et al. 2019, AJ, 158, 55

Hayashi, C. 1981, Progress of Theoretical Physics Supplement, 70, 35

Helled, R. & Stevenson, D. 2017, ApJ, 840, L4

Hendler, N., Pascucci, I., Pinilla, P., et al. 2020, ApJ, 895, 126

Henning, T. & Stognienko, R. 1996, A&A, 311, 291

Heyer, M. & Dame, T. M. 2015, ARA&A, 53, 583

Hildebrand, R. H. 1983, QJRAS, 24, 267

Howard, A. W., Marcy, G. W., Bryson, S. T., et al. 2012, ApJS, 201, 15

Huang, J., Andrews, S. M., Dullemond, C. P., et al. 2018a, ApJ, 869, L42

Huang, J., Andrews, S. M., Pérez, L. M., et al. 2018b, ApJ, 869, L43

Hubickyj, O., Bodenheimer, P., & Lissauer, J. J. 2005, Icarus, 179, 415

Isella, A., Testi, L., Natta, A., et al. 2007, A&A, 469, 213

Izidoro, A., Bitsch, B., & Dasgupta, R. 2021a, ApJ, 915, 62

Izidoro, A., Bitsch, B., Raymond, S. N., et al. 2021b, A&A, 650, A152

Izquierdo, A. F., Testi, L., Facchini, S., Rosotti, G. P., & van Dishoeck, E. F. 2021, A&A, 650, A179

Johansen, A., Klahr, H., & Henning, T. 2006, ApJ, 636, 1121

Johansen, A. & Lacerda, P. 2010, MNRAS, 404, 475

Johansen, A. & Lambrechts, M. 2017, Annual Review of Earth and Planetary Sciences, 45, 359

Jurić, M. & Tremaine, S. 2008, ApJ, 686, 603

Kanagawa, K. D. & Szuszkiewicz, E. 2020, arXiv e-prints, arXiv:2004.01063

Kanagawa, K. D., Tanaka, H., Muto, T., Tanigawa, T., & Takeuchi, T. 2015, MNRAS, 448, 994

Kanagawa, K. D., Tanaka, H., & Szuszkiewicz, E. 2018, ApJ, 861, 140

Kant, I. 1755

Keppler, M., Benisty, M., Müller, A., et al. 2018, A&A, 617, A44

Klahr, H. H. & Bodenheimer, P. 2003, ApJ, 582, 869

Kley, W. 1999, MNRAS, 303, 696

Kloster, D. & Flock, M. 2021, arXiv e-prints, arXiv:2105.11150

Kobayashi, H., Tanaka, H., & Okuzumi, S. 2016, ApJ, 817, 105

Kratter, K. & Lodato, G. 2016, ARA&A, 54, 271

Kresak, L. 1977, Bulletin of the Astronomical Institutes of Czechoslovakia, 28, 65

Kretke, K. A., Levison, H. F., Buie, M. W., & Morbidelli, A. 2012, AJ, 143, 91

Kruijer, T. S., Burkhardt, C., Budde, G., & Kleine, T. 2017, Proceedings of the National Academy of Science, 114, 6712

Kurtovic, N. T., Pinilla, P., Long, F., et al. 2021, A&A, 645, A139

Lada, C. J. 1987, in Star Forming Regions, ed. M. Peimbert & J. Jugaku, Vol. 115, 1

Lambrechts, M. & Johansen, A. 2012, A&A, 544, A32

Lambrechts, M., Johansen, A., & Morbidelli, A. 2014, A&A, 572, A35

Lambrechts, M., Lega, E., Nelson, R. P., Crida, A., & Morbidelli, A. 2019, A&A, 630, A82

Lega, E., Morbidelli, A., Bitsch, B., Crida, A., & Szulágyi, J. 2015, MNRAS, 452, 1717

Lega, E., Morbidelli, A., & Nesvorný, D. 2013, MNRAS, 431, 3494

Lenz, C. T., Klahr, H., & Birnstiel, T. 2019, ApJ, 874, 36

Lenz, C. T., Klahr, H., Birnstiel, T., Kretke, K., & Stammler, S. 2020, arXiv e-prints, arXiv:2006.08799

Levison, H. F., Thommes, E., & Duncan, M. J. 2010, AJ, 139, 1297

Li, H., Colgate, S. A., Wendroff, B., & Liska, R. 2001, ApJ, 551, 874

Lin, D. N. C. & Papaloizou, J. 1979, MNRAS, 188, 191

Lin, D. N. C. & Papaloizou, J. 1986, ApJ, 309, 846

Lissauer, J. J., Hubickyj, O., D'Angelo, G., & Bodenheimer, P. 2009, Icarus, 199, 338

Lissauer, J. J., Marcy, G. W., Rowe, J. F., et al. 2012, ApJ, 750, 112

Lodato, G., Dipierro, G., Ragusa, E., et al. 2019, MNRAS, 486, 453

Long, F., Pinilla, P., Herczeg, G. J., et al. 2020, ApJ, 898, 36

Long, F., Pinilla, P., Herczeg, G. J., et al. 2018, ApJ, 869, 17

Lovelace, R. V. E., Li, H., Colgate, S. A., & Nelson, A. F. 1999, ApJ, 513, 805

Lozovsky, M., Helled, R., Rosenberg, E. D., & Bodenheimer, P. 2017, ApJ, 836, 227

Lubow, S. H. & D'Angelo, G. 2006, ApJ, 641, 526

Lynden-Bell, D. & Pringle, J. E. 1974, MNRAS, 168, 603

Machida, M. N., Kokubo, E., Inutsuka, S.-I., & Matsumoto, T. 2010, MNRAS, 405, 1227

Manara, C. F., Mordasini, C., Testi, L., et al. 2019, A&A, 631, L2

Marcus, P. S., Pei, S., Jiang, C.-H., et al. 2015, ApJ, 808, 87

Marquis de Laplace, P.-S. 1796

Martinez-Brunner, R., Casassus, S., Pérez, S., et al. 2022, MNRAS, 510, 1248

Masset, F. 2000, A&AS, 141, 165

Masset, F. & Snellgrove, M. 2001, MNRAS, 320, L55

Masset, F. S., D'Angelo, G., & Kley, W. 2006a, ApJ, 652, 730

Masset, F. S., Morbidelli, A., Crida, A., & Ferreira, J. 2006b, ApJ, 642, 478

Masset, F. S. & Papaloizou, J. C. B. 2003, ApJ, 588, 494

Mayor, M., Marmier, M., Lovis, C., et al. 2011, arXiv e-prints, arXiv:1109.2497

Mayor, M. & Queloz, D. 1995, Nature, 378, 355

McKee, C. F. & Ostriker, E. C. 2007, ARA&A, 45, 565

Mentiplay, D., Price, D. J., & Pinte, C. 2019, MNRAS, 484, L130

Meru, F., Rosotti, G. P., Booth, R. A., Nazari, P., & Clarke, C. J. 2019, MNRAS, 482, 3678

Miguel, Y., Cridland, A., Ormel, C. W., Fortney, J. J., & Ida, S. 2020, MNRAS, 491, 1998

Millholland, S., Wang, S., & Laughlin, G. 2017, ApJ, 849, L33

Morbidelli, A. 2020, A&A, 638, A1

Morbidelli, A., Bottke, W. F., Nesvorný, D., & Levison, H. F. 2009, Icarus, 204, 558

Morbidelli, A. & Crida, A. 2007, Icarus, 191, 158

Morbidelli, A., Lambrechts, M., Jacobson, S., & Bitsch, B. 2015, Icarus, 258, 418

Morbidelli, A. & Nesvorny, D. 2012, A&A, 546, A18

Morbidelli, A., Nesvorny, D., Laurenz, V., et al. 2018, Icarus, 305, 262

Mordasini, C., Alibert, Y., Klahr, H., & Henning, T. 2012, A&A, 547, A111

Mulders, G. D., Pascucci, I., Apai, D., & Ciesla, F. J. 2018, AJ, 156, 24

Mulders, G. D., Pascucci, I., Manara, C. F., et al. 2017, ApJ, 847, 31

Muro-Arena, G. A., Dominik, C., Waters, L. B. F. M., et al. 2018, A&A, 614, A24

Musiolik, G. & Wurm, G. 2019, ApJ, 873, 58

Ndugu, N., Bitsch, B., & Jurua, E. 2018, MNRAS, 474, 886

Ndugu, N., Bitsch, B., & Jurua, E. 2019, MNRAS, 488, 3625

Ndugu, N., Bitsch, B., Morbidelli, A., Crida, A., & Jurua, E. 2021, MNRAS, 501, 2017

Nesvorný, D. 2011, ApJ, 742, L22

Nesvorný, D. 2015, AJ, 150, 73

Nesvorný, D. & Morbidelli, A. 2012, AJ, 144, 117

Nesvorný, D., Vokrouhlický, D., & Morbidelli, A. 2013, ApJ, 768, 45

Öberg, K. I. & Bergin, E. A. 2021, Phys. Rep., 893, 1

Öberg, K. I. & Wordsworth, R. 2019, AJ, 158, 194

Okuzumi, S., Momose, M., Sirono, S.-i., Kobayashi, H., & Tanaka, H. 2016, ApJ, 821, 82

Ormel, C. W. & Cuzzi, J. N. 2007, A&A, 466, 413

Ormel, C. W. & Klahr, H. H. 2010, A&A, 520, A43

Ormel, C. W., Vazan, A., & Brouwers, M. G. 2021, A&A, 647, A175

Paardekooper, S. J., Baruteau, C., & Kley, W. 2011, MNRAS, 410, 293

Paardekooper, S.-J. & Johansen, A. 2018, Space Sci. Rev., 214, 38

Paardekooper, S. J. & Mellema, G. 2006, A&A, 453, 1129

Paardekooper, S. J. & Papaloizou, J. C. B. 2009, MNRAS, 394, 2297

Pfalzner, S., Steinhausen, M., & Menten, K. 2014, ApJ, 793, L34

Pierens, A. & Lin, M.-K. 2018, MNRAS, 479, 4878

Pierens, A., Lin, M. K., & Raymond, S. N. 2019, MNRAS, 488, 645

Pierens, A. & Nelson, R. P. 2008, A&A, 482, 333

Pierens, A., Raymond, S. N., Nesvorny, D., & Morbidelli, A. 2014, ApJ, 795, L11

Pinilla, P., Benisty, M., & Birnstiel, T. 2012, A&A, 545, A81

Pinilla, P., de Juan Ovelar, M., Ataiee, S., et al. 2015, A&A, 573, A9

Pinilla, P., Lenz, C. T., & Stammler, S. M. 2021, A&A, 645, A70

Pinilla, P., Pérez, L. M., Andrews, S., et al. 2017a, ApJ, 839, 99

Pinilla, P., Pohl, A., Stammler, S. M., & Birnstiel, T. 2017b, ApJ, 845, 68

Pinte, C., Price, D. J., Ménard, F., et al. 2020, ApJ, 890, L9

Pinte, C., Price, D. J., Ménard, F., et al. 2018, ApJ, 860, L13

Pirani, S., Johansen, A., Bitsch, B., Mustill, A. J., & Turrini, D. 2019, A&A, 623, A169

Piso, A.-M. A. & Youdin, A. N. 2014, ApJ, 786, 21

Pohl, A. 2018, PhD thesis, Heidelberg University, Germany

Pollack, J. B., Hubickyj, O., Bodenheimer, P., et al. 1996, Icarus, 124, 62

Pringle, J. E. 1981, ARA&A, 19, 137

Rafikov, R. R. 2005, ApJ, 621, L69

Rafikov, R. R. 2016, ApJ, 831, 122

Rafikov, R. R. 2017, ApJ, 837, 163

Raymond, S. N., Armitage, P. J., & Gorelick, N. 2009a, ApJ, 699, L88

Raymond, S. N., Armitage, P. J., Moro-Martín, A., et al. 2011, A&A, 530, A62

Raymond, S. N., Barnes, R., Veras, D., et al. 2009b, ApJ, 696, L98

Raymond, S. N. & Izidoro, A. 2017, Science Advances, 3, e1701138

Raymond, S. N., Izidoro, A., & Morbidelli, A. 2020, in Planetary Astrobiology, ed. V. S. Meadows, G. N. Arney, B. E. Schmidt, & D. J. Des Marais, 287

Raymond, S. N., O'Brien, D. P., Morbidelli, A., & Kaib, N. A. 2009c, Icarus, 203, 644

Robert, C. M. T., Crida, A., Lega, E., Méheut, H., & Morbidelli, A. 2018, A&A, 617, A98

Rosenthal, M. M., Chiang, E. I., Ginzburg, S., & Murray-Clay, R. A. 2020, MNRAS, 498, 2054

Rosotti, G. P., Ercolano, B., & Owen, J. E. 2015, MNRAS, 454, 2173

Rosotti, G. P., Juhasz, A., Booth, R. A., & Clarke, C. J. 2016, MNRAS, 459, 2790

Safronov, V. S. 1969, Evoliutsiia doplanetnogo oblaka (English translation: Evolution of the protoplanetary cloud and formation of the earth and planets).

Sanchis, E., Picogna, G., Ercolano, B., Testi, L., & Rosotti, G. 2020, MNRAS, 492, 3440

Schneider, N., Wurm, G., Teiser, J., Klahr, H., & Carpenter, V. 2019, ApJ, 872, 3

Schulik, M., Johansen, A., Bitsch, B., & Lega, E. 2019, A&A, 632, A118

Segura-Cox, D. M., Schmiedeke, A., Pineda, J. E., et al. 2020, Nature, 586, 228

Shakura, N. I. & Sunyaev, R. A. 1973, in IAU Symposium, Vol. 55, X- and Gamma-Ray Astronomy, ed. H. Bradt & R. Giacconi, 155

Smirnov-Pinchukov, G. V., Semenov, D. A., Akimkin, V. V., & Henning, T. 2020, A&A, 644, A4

Smoluchowski, M. V. 1916, Zeitschrift fur Physik, 17, 557

Sotiriadis, S., Libert, A.-S., Bitsch, B., & Crida, A. 2017, A&A, 598, A70

Steinacker, J., Baes, M., & Gordon, K. D. 2013, ARA&A, 51, 63

Suzuki, D., Bennett, D. P., Sumi, T., et al. 2016, ApJ, 833, 145

Szulágyi, J. & Mordasini, C. 2017, MNRAS, 465, L64

Takahashi, S. Z. & Inutsuka, S.-i. 2016, AJ, 152, 184

Tanaka, H. & Ida, S. 1999, Icarus, 139, 350

Tanigawa, T. & Ikoma, M. 2007, ApJ, 667, 557

Tanigawa, T. & Tanaka, H. 2016, ApJ, 823, 48

Teague, R., Bae, J., Bergin, E. A., Birnstiel, T., & Foreman-Mackey, D. 2018, ApJ, 860, L12

Teague, R., Guilloteau, S., Semenov, D., et al. 2016, A&A, 592, A49

Thommes, E. W. 2005, ApJ, 626, 1033

Tominaga, R. T., Takahashi, S. Z., & Inutsuka, S.-i. 2020, ApJ, 900, 182

Toomre, A. 1964, ApJ, 139, 1217

Valletta, C. & Helled, R. 2020, ApJ, 900, 133

van der Marel, N., Williams, J. P., Ansdell, M., et al. 2018, ApJ, 854, 177

Visser, R. G. & Ormel, C. W. 2016, A&A, 586, A66

Walsh, K. J., Morbidelli, A., Raymond, S. N., O'Brien, D. P., & Mandell, A. M. 2011, Nature, 475, 206

Walsh, K. J., Morbidelli, A., Raymond, S. N., O'Brien, D. P., & Mandell, A. M. 2012, Meteoritics & Planetary Science, 47, 1941

Wang, J. J., Graham, J. R., Dawson, R., et al. 2018, AJ, 156, 192

Wang, S., Kanagawa, K. D., & Suto, Y. 2021, ApJ, 923, 165

Wang, X.-M. 2015, MNRAS, 449, 1084

Warren, S. G. & Brandt, R. E. 2008, Journal of Geophysical Research (Atmospheres), 113, D14220

Weber, P., Benítez-Llambay, P., Gressel, O., Krapp, L., & Pessah, M. E. 2018, ApJ, 854, 153

Weber, P., Pérez, S., Benítez-Llambay, P., et al. 2019, ApJ, 884, 178

Weidenschilling, S. J. 1977, MNRAS, 180, 57

Weiss, L. M., Isaacson, H. T., Marcy, G. W., et al. 2018, AJ, 156, 254

Wetherill, G. W. 1994, Ap&SS, 212, 23

Williams, J. P., Cieza, L., Hales, A., et al. 2019, ApJ, 875, L9

Wright, J. T., Upadhyay, S., Marcy, G. W., et al. 2009, ApJ, 693, 1084

Youdin, A. & Johansen, A. 2007, ApJ, 662, 613

Youdin, A. N. & Goodman, J. 2005, ApJ, 620, 459

Youdin, A. N. & Lithwick, Y. 2007, Icarus, 192, 588

Zhang, K., Blake, G. A., & Bergin, E. A. 2015, ApJ, 806, L7

Zhang, S., Zhu, Z., Huang, J., et al. 2018, ApJ, 869, L47

Zhu, W. 2022, arXiv e-prints, arXiv:2201.03782

Acknowledgements

What better way to end this thesis than by thanking all the people without whom I could not have gone through these four years. My time at MPIA was one of the best experience I have ever lived, learning a lot about science but also about others and myself.

I would like to start by thanking **Bertram Bitsch**, my supervisor. Thank you for believing in me, proving me that I have the capacities to do science. You taught me a lot and have an amazing capacity to adapt to people, and I will always be grateful for this.

I also wish to thank the persons who refereed this work, **Bertram Bitsch** and **Kees Dullemond**. It is an honour to be reviewed by you two. Thank you also to the two other members of my examination committee, **Henrik Beuther** and **Luca Amendola**, for the time you have given to this thesis.

Thank you to all my collaborators, and all the persons who showed interest in my work and helped me improve it. I cannot list all of you but I would like to particularly thank **Sean Raymond**, **Arnaud Pierens**, **Paola Pinilla**, **Nicolas Kurtovic** and **Aurélien Crida** for your trust and knowledge. It is a pleasure to work with you.

I would like to acknowledge also the efforts of **Christian Fendt** and **Huong Witte-Nguy** for guiding us in the IMPRS-HD structure. Your help is vital and I really appreciated the social gathering you organized, allowing us to meet incredible other students.

Thank you to all the people who took time to give me feedback on my manuscript, whether it was for proof reading the text or improving its science content: **Dhruv Muley**, **Alex Dimoff**, **Gabriele Pichierri**, **Jonas Syed**, **Caroline Gieser** and my father, **Jean-Pierre Bergez-Casalou**.

The four years of my PhD have been perturbed by the COVID-19 pandemic. This resulted in many different office changes (4 different offices so far) and in a clear-cut separation between the two first years and the end of my PhD. It definitely had an impact on my relation with my work environment.

First of all, I would like to thank, deeply, my very first office-mates from 216B: **Christos Vourellis**, thank you for making the office feel like home and being like a mentor to me; **Asmita Bhandare**, your dedication to your work but also to other people around you is always an inspiration to me; and **Riccardo Nanni**, thank you for all these conversations about cultural differences and so on.

Jonas Syed, you've been my office-mate in three of my different offices, from 216B to the Guest house. Thank you for all these conversations, science-wise but also life-wise (if this word exists). It was really nice to feel supported during these challenging times (and sorry for the many complaints that you had to endure). We will manage to deal with our future, I believe in us !

I had the chance to start my PhD with the best PhD "sister" that one could wish for. **Sofia Savvidou**, thank you for all these rooms shared in conferences, all these discussions that we had, ranging from complaining about how the Bachelor cluster was behaving to discussing the gender of the different countries in different languages, and including work management discussions. That was a pleasure to have you around, I promise to be here for your defense.

To the members of the "Best PhD support group": **Liz Flores**, **Marcelo Barraza**, **Timmy Delage**, **Nicolas Kurtovic**, **Riccardo Franceschi** and **Sofia Savvidou**. I will always keep in mind all these moments that we shared, from our week in Copenhagen playing Uno in greek to all the games of Werewolf that we played: "You can kill me tonight but first, hear me out !"

I had the chance to start my PhD in office 216B, that was originally the Student coffee office. There, I met many different people who really enlightened my days. For all these Student coffee moments spent discussing literally everything, thank you. I will try to list everyone, I hope I'm not forgetting anyone ! Therefore, whether you're not here or attending anymore: **Arianna Musso-Barcucci**, **Josha van Houdt**, **Johanna Coronado**, **Sara Rezaei**, **Christian Lenz**, **Felix Bosco**, **Paula Sarkis**, **Melanie Kaasinen**, **Vincent Carpenter**, **Hector Hiß**, **Alex Hygate**, **Neven Tomicic**, **Yulong Zhuang**; or that you're part of the new generation reviving student coffee after the pandemic: **Alex Dimoff**, **Dhruv Muley**, **Olga Borodina**, **Sid Deshmukh**, **Eric Rohr**, **Elise Lei**, **Molly Wells**, **Rhys Seeburger**, **Claudia Danti** ... Thank you.

I intentionally omitted some persons who are part of my generation, as I would like to thank them particularly. **Jacob Isbell**, **Giancarlo Mattia** and **Grigorii Smirnov-Pinchukov**, you're just the best, I'm really glad I spent all my PhD with you around. **Irina Smirnova-Pinchukova**, I hope we will never stop having these wild conversations about different personalities and how to deal with them. I'm really happy to count you as my friend, you and Greg. Of course, I do not forget all the other members of the 14th IMPRS generation with whom I got to spend some time: **Alina Boecker**, **Mischa Breuhaus**, **Samantha Brown Sevilla**, **Francesco Conte**, **Christoph Engler**, **Caroline Gieser**, **Oliver Voelkel** and **Thomas Jackson**, our rep with Jacob.

It is thanks to all these persons that I had my best time in Heidelberg. However, during the different lockdowns, I could count also on another set of people, whom I cherish a lot and helped me keep a decent mental health. I have to mention my wonderful baby cat here, **Mendeleiev**, whom really helped me feel less alone ! More seriously, to the best person I discovered during this time, **Faustine Cantalloube**, who pushed me to go outside, bake amazing dishes (la tartiflette, TMTC) and made me meet other awesome persons: **Rubén Asensio Torres**, **Evert Nasedkin**, **Erika Jurevičiūtė** and **Priyanshu Shukla**. I had an amazing time with you guys.

During my Bachelor in Bordeaux, I met the best group of girls, that we kept for all these time and on whom I could always count on (in particular during the pandemic or the moments of doubt linked to my PhD). To my best friend, **Isabeau Bertrix**, thank you for being just the best person ever. I won't write all the reasons why I'm so glad to have you in my life, you know them. Thank you to **Éléonore Geulin**, **Léa Fournasson** and **Marie-Élodie Placé**, I can't wait to see what will be our next adventures!

When I consider this girls' group as my second family, I also know that my actual family is composed of the best persons on Earth: **Patricia**, **Jean-Pierre** and **Jean-**

Michel Bergez-Casalou, I wish I could be there more often. You've always supported me and I owe you so much. I'm really glad to have such an amazing family.

I had to finish with the most amazing person I met during this PhD, thanks to my awesome best friend. You've changed my life (in a good way !), taught me that I can be loved for who I am, you enlighten my everyday life with all your jokes and caring thoughts ... **Julian Preveraud**, thank you for being who you are and supporting all my mood swings and moments of doubts. I love you.

After reading again and again these acknowledgments, I have the feeling that it only partially shows how grateful I am for all of you. No words could express how honoured I feel to have met you all. Yes, that sounds cheesy ... I become increasingly sensitive as I get older, I might have cried a little while writing this section. Don't worry, these were tears of joy.

To all of you, thank you.
I hope our paths will continue to cross !